UNIVERSIDAD COMPLUTENSE DE MADRID

FACULTAD DE CIENCIAS QUÍMICAS

TESIS DOCTORAL

Development of hybrid chitosan hydrogels: combined application in magnetic hyperthermia and drug delivery

MEMORIA PARA OPTAR AL GRADO DE DOCTOR

PRESENTADA POR

María Vanessa Zamora Mora

Directores

Carmen Mijangos Ugarte
Rebeca Hernández Velasco

Madrid, 2014

DEVELOPMENT OF HYBRID CHITOSAN HYDROGELS.

Combined application in magnetic hyperthermia and drug delivery.

PH.D THESIS, 2014
MARÍA VANESSA ZAMORA MORA

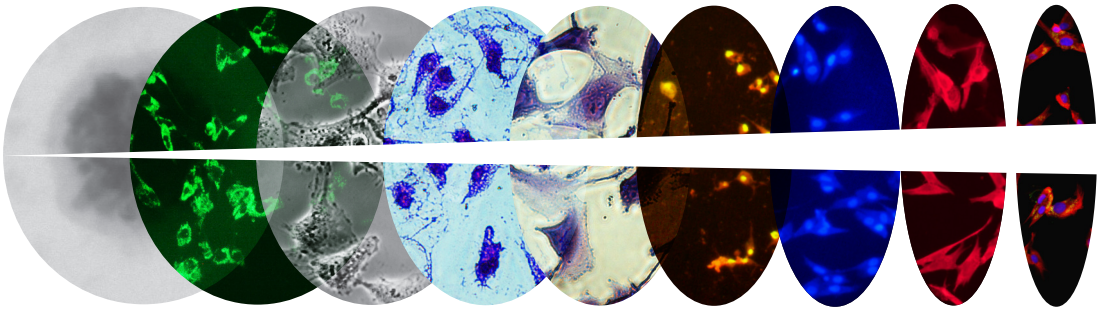

ICTP
Instituto de Ciencia y Tecnología de Polímeros

VNIVERSITAS COMPLVTENSIS MATRITENSIS

CSIC
CONSEJO SUPERIOR DE INVESTIGACIONES CIENTÍFICAS

Instituto de Ciencia y Tecnología de Polímeros

Ph.D Thesis, 2014

DEVELOPMENT OF HYBRID CHITOSAN HYDROGELS.

A COMBINED APPLICATION IN MAGNETIC HYPERTHERMIA AND DRUG DELIVERY

MARÍA VANESSA ZAMORA MORA

Supervisors:

Prof. Carmen Mijangos Ugarte

Rebeca Hernández Velasco

Resumen

El presente trabajo "***Development of hybrid chitosan hydrogels. A combined application in magnetic hyperthermia and drug delivery***", tiene como objetivo el desarrollo de hidrogeles híbridos a base de quitosano con el propósito de adquirir nuevos conocimientos y explorar aplicaciones potenciales de estos hidrogeles poliméricos en hipertermia magnética y liberación controlada de fármacos. Para el desarrollo de hidrogeles poliméricos con respuesta al pH se ha seleccionado un polímero de origen natural como es el quitosano, debido a sus propiedades intrínsecas de biodegradabilidad y biocompatibilidad. Con el fin de ampliar las aplicaciones de los hidrogeles de quitosano, se han preparado y caracterizado hidrogeles compuestos de quitosano/agarosa, como sistemas duales con respuesta al pH y a la temperatura para aplicaciones en liberación controlada de fármacos. Para aplicaciones en Hipertermia Magnética (MH), se han sintetizado hidrogeles de quitosano con partículas magnéticas encapsuladas. Con el fin de diversificar el campo de aplicación de los hidrogeles de quitosano, se ha llevado a cabo el desarrollo de geles a escala micro y nanométrica. Los microgeles de quitosano se han preparado mediante la técnica de microfluídica que ha permitido la obtención de microgeles monodispersos. Los nanogeles de quitosano se han preparado mediante un proceso de nanoprecipitación mediante el cual se han podido encapsular nanopartículas magnéticas y 5-Fluorouracil, fármaco modelo empleado en quimioterapia. De esta forma, se han desarrollado nano-transportadores para aplicaciones combinadas de hipertermia magnética y liberación de fármacos en terapias contra el cáncer. Por último, se ha realizado un estudio de las propiedades viscoelásticas de los macro y nanogeles mediante el cual se ha podido determinar la organización estructural de estos sistemas mediante la aplicación de modelos de escala.

Esta memoria describe en siete capítulos los objetivos parciales necesarios para conseguir el objetivo final. A continuación se describe el objetivo establecido para cada uno de ellos junto con las conclusiones derivadas del trabajo experimental realizado:

En el primer capítulo, "*Introdución general y objetivos"* se enmarca el trabajo de tesis doctoral dentro de las líneas de investigación del grupo donde se ha llevado a cabo y se describe el objetivo general de la tesis así como cada uno de los objetivos parciales y la metodología empleada para su consecución.

El segundo capítulo, *"Estado del arte",* resume el estudio bibliográfico llevado a cabo sobre los principales temas relacionados con el presente trabajo doctoral, en el cual se destaca: i) Las características principales del quitosano y su importancia como polímero natural para la obtención de materiales para aplicaciones biomédicas, ii) Hidrogeles a base de quitosano, macro y nanogeles y su caracterización reológica, iii) Sistemas de quitosano como nano-transportadores en terapias combinadas de hipertermia magnética y liberación de fármacos iv) la técnica de microfluídica como técnica avanzada de preparación de microgeles poliméricos.

El tercer capítulo, *"Macrogeles de quitosano. Estudio de sus propiedades"* describe la preparación y caracterización de diferentes geles físicos de quitosano: macrogeles de quitosano, macrogeles compuestos de quitosano/agarosa y macrogeles cargados con nanopartículas magnéticas. Los macrogeles de quitosano se obtienen por medio de la adicción de una disolución coagulante. Este mismo método es empleado para la síntesis de ferrogeles de quitosano mediante el cual se lleva a cabo la gelificación del quitosano y la preparación *in situ* de nanopartículas de óxido de hierro de forma simultánea. Los macrogeles compuestos de quitosano/agarosa se obtienen por gelificación de la agarosa en presencia de una disolución de quitosano y son evaluados como materiales para liberación controlada de fármacos. Estos macrogeles compuestos son cargados con diferentes concentraciones de ferrofluido y son evaluados como materiales para hipertermia magnética.

De acuerdo a los estudios realizados para todos los macrogeles, se observó que: i) los macrogeles de quitosano preparados por adicción de una disolución coagulante, deben su formación al establecimiento de enlaces de hidrógeno e interacciones hidrofóbicas y presentaron un comportamiento de tipo gel de acuerdo a su comportamiento reológico ii) mediante la síntesis *in situ* de nanopartículas de óxido de hierro en macrogeles de quitosano se obtuvieron ferrogeles de quitosano con mayor módulo elástico y estabilidad térmica que los macrogeles de quitosano, iii) con respecto a los macrogeles compuestos de quitosano/agarosa, la incorporación de quitosano dió lugar a materiales con módulos elásticos mayores y mayor estabilidad temporal (menor pérdida de peso con el tiempo) que los geles simples de agarosa, asimismo, iv) la incorporación de ferrofluido a los macrogeles compuestos de quitosano/agarosa mejoró la estabilidad térmica de los macrogeles resultantes aunque dio lugar a una disminución de sus propiedades mecánicas, finalmente, v) los macrogeles quitosano/agarosa se

evaluaron como materiales para aplicaciones en hipertermia magnética y liberación controlada de 5-Fluorouracil.

El cuarto capítulo, *"Microgeles de quitosano preparados a través de microfluídica"*, está enfocado a la preparación de diferentes tipos de microgeles de quitosano a través de la técnica de microfluídica. Se incluye la fabricación de diferentes dispositivos y la influencia de diferentes parámetros experimentales tales como velocidad de flujo y concentración de las fases orgánica y acuosa en el proceso de emulsificación del quitosano y en la formación final de microgeles.

Del estudio de estos sistemas se puede concluir que: i) se ha logrado la emulsificación en gotas de disoluciones de quitosano en los dos dispositivos empleados, "T-junction" y "flow-focusing", ii) se ha logrado el entrecruzamiento de las gotas de quitosano dentro del dispositivo de microfluidos empleando el tripolifosfato de sodio (TPP) como agente entrecruzante, iii) se han preparado microgeles compuestos de quitosano/agarosa por la técnica de microfluídica, iv) de acuerdo a los diferentes experimentos, la concentración de agarosa y la velocidad de flujo tuvieron un efecto directo sobre los tamaños de los microgeles, por último, v) se ha podido encapsular un ferrofluido en microgeles compuestos de quitosano/agarosa utilizando microfluídica.

El quinto capítulo, *"Nanopartículas de quitosano cargadas con ferrofluido"* da inicio al desarrollo de nanopartículas de quitosano obtenidas por medio de entrecruzamiento físico del quitosano con el tripolifosfato de sodio (TPP). Este método de preparación ha permitido además la obtención de nanopartículas de quitosano cargadas con ferrofluido que han sido evaluadas para aplicaciones en hipertermia magnética.

Los resultados obtenidos han permitido establecer las siguientes conclusiones: i) la reacción de entrecruzamiento entre el quitosano y el TPP depende de la concentración de quitosano y de TPP y de la proporción en volumen de quitosano/TPP, ii) las nanopartículas cargadas con ferrofluido presentaron una morfología tipo capa-núcleo (`core-shell´), un tamaño entre los 192-259 nm y todas las muestras presentaron carga superficial positiva, iii) La aplicación de teorías de escala y el análisis fractal obtenido a partir de los resultados reológicos ha permitido entender el tipo de uniones que suceden en la dispersión de los nanogeles de quitosano en función de la concentración de dichas dispersiones, iv) se evaluó la citotoxicidad de los materiales sintetizados sobre células

de tipo fibroblasto observándose que la viabilidad celular depende de la concentración de nanopartículas empleada y que además, disminuye en función del contenido de ferrofluido, y finalmente v) las nanopartículas de quitosano cargadas con ferrofluido pueden ser empleadas como agentes de hipertermia por su capacidad para calentarse al ser sometidas a un campo magnético.

En el sexto capítulo, *"Estudio in vitro de nanopartículas magnéticas de quitosano cargadas con 5-fluorouracil para aplicaciones en hipertermia magnética"*, se describe la preparación y caracterización de nanopartículas de quitosano cargadas con un fármaco empleado en quimioterapia, 5- Fluorouracilo (5-FU) y con un ferrofluido. Además se han evaluado sus propiedades para ser utilizadas como nano-transportadores en terapias combinadas de hipertermia magnética y liberación controlada.

De los estudios realizados se puede extraer que: i) 5-FU y ferrofluido fueron encapsulados exitosamente dentro de las nanopartículas de quitosano, ii) los tamaños nanométricos (140-200 nm) obtenidos para dichas nanopartículas, fueron adecuados para su internalización en células tipo fibroblasto y células cancerígenas (A-172), iii) el perfil de liberación de 5-FU puede ser modulado en función del pH y del contenido en ferrofluido de los nanogeles de quitosano, iv) los estudios de citotoxicidad permitieron determinar una menor viabilidad celular para células cancerígenas con respecto a células de tipo fibroblasto y v) los estudios de Hipertermia Magnética llevados a cabo en un equipo diseñado por el laboratorio (INA, Universidad de Zaragoza) permitieron determinar daños celulares, cambios morfológicos en las células y una reducción en la viabilidad celular tras la aplicación de un ciclo de hipertermia magnética, sin embargo, vi) no se observaron diferencias significativas sobre la viabilidad celular trás un segundo tratamiento de hipertermia magnética, por último, viii) las células cancerígenas (A-172) fueron más sensibles al tratamiento de hipertermia magnética que las células de tipo fibroblasto.

TABLE OF CONTENT

NANOPARTICLES

Chapter 1

GENERAL INTRODUCTION AND OBJECTIVES

The present work "***Development of hybrid chitosan hydrogels. A combined application in magnetic hyperthermia and drug delivery"***, aims to bring new insights in the framework of the research line *"**polymer gels"***, in which the group `Nanostructured Polymers and gels´ has been working for the last years, by searching new objectives. As a continuation of the significant efforts put on this topic, we proposed to develop a general study about hybrid hydrogels based on chitosan with the aim of getting deep knowledge and exploring potential applications of these polymer hydrogels. In order to accomplish this aim, the following strategy has been adopted:

Chitosan has been selected as a biopolymer obtained from natural resources with intrinsic properties of biodegradability and biocompatibility for the development of pH responsive polymer hydrogels for biomedical applications. In order to broaden the applications of chitosan hydrogels, chitosan/agarose composite hydrogels have also been investigated as materials with dual pH and temperature response to be employed in controlled drug delivery. In addition, to achieve chitosan hydrogels for magnetic **hyperthermia** applications, magnetic nanoparticles loaded chitosan hydrogels have been investigated. In order to diversify the range of applications of the chitosan gels**, two other size scales** have been studied, micro and nanogels. In relation to chitosan microgels, **microfluidics methods** have been applied to obtain monodisperse microgels. This technique was not settled up in our laboratory, neither in any other laboratories of CSIC or Spanish Universities, so a new collaboration was established with the team of Prof. E. Kumacheva (U. Toronto), pioneer in the field of microfluidics. On the other hand, chitosan nanogels have been prepared and characterized as nano-carriers for magnetic nanoparticles and a model chemotherapy drug, 5-Fluorouracil for combined hyperthermia treatment and drug delivery in **cancer treatment.** For these materials, in addition to the determination of the cytotoxicity, a thorough *in vitro* study of the effect of the application of magnetic field on fibroblasts and cancer cells loaded with the prepared materials is presented. Finally, the traditional rheological characterization strategy followed in other PhD thesis developed in our group has been applied to the study of the rheological behaviour of all the materials prepared. In this way a relationship between the rheological behaviour and the structural organization of polymer hydrogels and aqueous dispersions of polymer nanogels can be established which allows for the development of their applications.

In order to accomplish the general objective of this thesis "***Development of hybrid chitosan hydrogels. A combined application in magnetic hyperthermia and drug delivery"*** the thesis is structured in seven chapters, each of them corresponding to selected targets as described below:

The first chapter, "*General Introduction and objectives"*, is intended to establish the scientific framework in which the present work is carried out.

The second chapter, "*Brief state of the art"*, summarizes the results found in literature about specific features related to the aims of this thesis. It includes, i) the main characteristics of chitosan macro, micro and nanogels; ii) a general description of the microfluidics as innovative technique for the preparation of microgels; iii) a description of the rheological characterization of gels and aqueous colloidal polymer dispersions as a tool to establish the structure/properties relationship for these materials; iv) finally, the role of chitosan as nanocarriers for biomedical applications is studied, specifically for drug delivery and magnetic hyperthermia

The third chapter, "*Chitosan macrogels. Study of their properties"* includes the preparation of different types of chitosan macrogels: chitosan, chitosan/agarose and magnetically loaded chitosan macrogels and the characterization of their morphological, chemical and crystalline structure. Moreover, the temporal stability of the gels measured as the mass loss as a function of weight and the rheological properties are determined. Finally, the viability of chitosan hydrogels as precursors of biomedical applications in magnetic hyperthermia and controlled drug delivery is described.

The fourth chapter, "*Chitosan microgels prepared through microfluidics"*, gives a detailed description of the fabrication of microfluidic devices and the obtention of chitosan microparticles. The results are discussed on the basis of different device geometries, number of inlets and flow rates and concentrations of the continuous and the dispersed phases. It includes results and discussion about the effect of the different experimental parameters on the droplet size and the final particle size obtained.

The fifth chapter, entitled "*Ferrofluid loaded chitosan nanoparticles"* is aimed to the preparation and characterization of magnetic ferrofluid loaded chitosan

nanoparticles and evaluation for hyperthermia applications. It includes the optimization of the experimental parameters employed for the preparation of the chitosan nanoparticles by ionic crosslinking with sodium tripolyphosphate (TPP). Then, chitosan nanoparticles loaded with ferrofluid were prepared by simultaneous crosslinking and encapsulation of the ferrofluid and characterized by morphological studies, structural analysis, thermal stability, rheological studies, and cytotoxicity. Finally, chitosan nanoparticles loaded with ferrofluid were evaluated for hyperthermia applications through the evaluation of their heating in response to an alternating magnetic field.

The sixth chapter *"In vitro study of magnetic chitosan nanoparticles loaded with 5-fluorouracil for magnetic hyperthermia applications"* describes the preparation of chitosan nanoparticles loaded with ferrofluid and a model chemotherapeutic drug, 5-fluorouracil and their evaluation as materials for cancer therapy. The drug release profile of 5-fluorouracil was determined as a function of pH and ferrofluid content. All magnetic chitosan nanoparticles prepared have been assessed for *in vitro* magnetic hyperthermia applications following two different protocols designed in this thesis. Finally, cellular damage was analyzed though crystal violet staining and acridine orange and propidium iodide (AO/PI).

In the seventh chapter, the manuscript ends with a summary of the most general conclusions and future perspectives.

The manuscript includes a large number of references (more than 250), distributed among the different chapters which report the most relevant and updated results related to chitosan hydrogels, rheology models, microfluidics methods, and biomedical (hyperthermia and drug delivery) chitosan applications.

Finally, during the realization of this PhD work and related to this, new challenges have been set up (opened) in our group, which made us undertake new specific projects in the same line of research, carried out in parallel. For instance, we are involved in several projects regarding the employment of chitosan and additional natural polymers such as alginate, poly (lactic acid) and nanocellulose for the preparation of biodegradable polymer nanoparticles for the controlled release of active agents. As a continuation of the development of applications of polymer hydrogels in

magnetic hyperthermia, we are currently focused on the preparation of polymer hydrogels based on natural polymers employing a `layer-by-layer´ technique as a means to obtain nanostructured materials in which the magnetic response of the resulting materials can be controlled.

Chapter 2

BRIEF STATE OF THE ART

The present chapter summarizes the results found in literature about specific features related to the aims of this thesis. It includes, i) the main characteristics of chitosan macro and nanogels; ii) a description of the rheological characterization of gels and dispersions of polymer micro and nanogels as a tool to establish the structure/properties relationship for these materials; iii) the role of chitosan nanogels as nanocarriers for biomedical applications is studied, specifically for drug delivery and magnetic hyperthermia; iv) finally, a general description of microfluidics as innovative technique for the preparation of microgels is provided

2.1 CHITOSAN: A NATURAL POLYMER

Chitosan is the most important derivative of chitin, which is the second most abundant polysaccharide in nature after cellulose. Chitin was first isolated from fungi by Braconnot in 1811, but the name chitin which means tunic or cover was given by Odier, who in 1923 isolated it from the elytrum of the cockchafer beetle by treatment with hot alkaline solutions.[1] This is considered the beginning of modern carbohydrate polymers science. Chitin is generally represented as a linear polysaccharide composed of β (1 → 4) linked units of N -acetyl-2- amino-2-deoxy- d -glucose and it acts as structural support and defense materials in living organisms[1, 2]. The chemical structure of chitin is represented in Figure 2.1. Chitin is the most abundant organic component of the skeletal structure of many classes comprising the group of invertebrates, such as arthropods, mollusks and annelids. It is also found as a major polymeric constituent of the cell wall of fungi and algae. Therefore, chitin constitutes an important material obtained from a renewable natural resource.[2]

Chitosan is obtained by partial deacetylation of chitin in the solid state under alkaline conditions (concentrated NaOH) or by enzymatic hydrolysis in the presence of chitin deacetylase[2]. It is a copolymer of β (1 → 4) linked 2-aceta-mido-2-deoxy-D-glucopyranose and 2-amino-2-deoxy-D-glucopyranose[3]. The chemical structure of chitosan is represented in Figure 2.1.[4] The physicochemical properties of chitosan are defined mainly by the degree of acetylation (or deacetylation) and the molecular mass [3, 4]. Both parameters vary with the biological source of the raw material and the

preparation method. They also dictate the physicochemical, functional and biological properties of chitosan, essential to fit an application or end product. Solubility, pK, viscosity, gelling capacity, among other properties, are all dependent on these parameters. The molecular weight and its distribution affect the physical, chemical and biological properties of chitosan, such as (i) the mechanical properties of hydrogels, (ii) the pore size of membranes, scaffolds and microcapsules, (iii) the particle size and drug release properties of nanoparticles, (iv) the effect of chitosan on the permeability of epithelial cells and (v) its antimicrobial activity. Therefore, degree of acetylation and the molecular mass affects directly the performance of chitosan in biotechnology, food, pharmaceutical, biomedical and biological applications.[4]

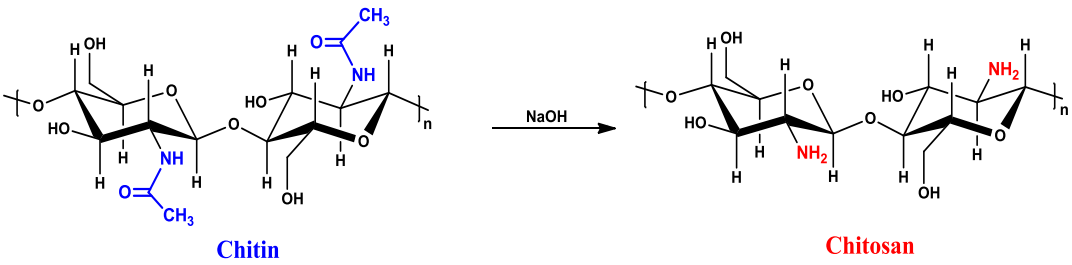

Figure 2.1. *Chemical structure of chitin (blue) and chitosan (red)*

The great variety of applications of chitosan in the field of biomaterials is due to its biocompatibility, biodegradability and low toxicity [5, 6]. Also, it presents excellent properties when interacting with the human body such as bioactivity, antimicrobial activity, immunostimulation, chemotactic action, enzymatic biodegradability, mucoadhesion and epithelial permeability which support the adhesion and proliferation of different cell types. Chitosan has the advantage that can be biodegraded by a number of enzymes, such as lysozyme, di-N-acetylchitobiase, N-acetyl-beta-D-glucosaminidase and chitiotriosidase, which are present in human mucosas and other physiological fluids. [7]. Current chitosan is used as a generally regarded as safe (GRAS) material [1, 7].

Nowadays, chitosan can be found it in a verity of different forms such as gels [8-10], membranes [11, 12], nanofibers[13, 14], beads[15-17], microparticles[18, 19], nanoparticles[20-22], scaffolds [2, 23, 24]. The above forms provide a wide variety of

biomedical applications in tissue engineering, wound dressing, cancer drug delivery, targeting and preventing bacterial adhesion [2, 4].

2.2 CHITOSAN HYDROGELS.

Hydrogels are defined as three-dimensional crosslinked, hydrophilic, polymeric networks capable to retain large amounts of water, or biological fluids [25]. In the swollen state, these gel networks are characterized by a soft and rubbery consistence, being thus similar with living tissues[26]. Specifically, chitosan hydrogels are extensively employed for biomedical applications since they are inherently biodegradable and biocompatible and also they provide response to pH due to the fact that its amine group is protonated under acidic conditions which confer positive charges. The pKa value always lies between 6.3 and 6.7. In this section it is presented the current knowledge about the development of chitosan macrogels and nanogels employed in biomedical applications. The preparation and characteristics of chitosan microgels prepared through microfluidics tecniques will be detailed in a separate section of this chapter.

2.2.1 Chitosan macrogels

Chitosan macrogels can be divided in many ways, but in this work, they are divided into two classes depending on the nature of the crosslinking, namely covalently crosslinked networks (irreversible covalent links) and networks formed by physical interactions (reversible links).

Chitosan chemical macrogels (Figure 2.2-a) are formed by irreversible covalent links. Some crosslinkers agents, as for example glutaraldehyde, present high toxicity and therefore it is a necessary a purification step, being a drawback for biomedical applications and therefore, the development of alternative types of hydrogels is desirable.

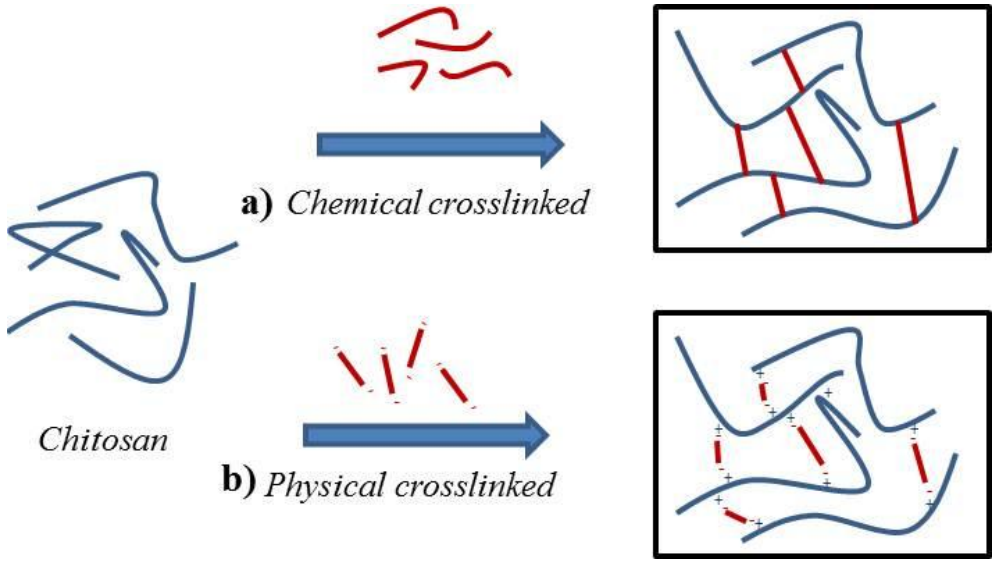

Figure 2.2. *Types of hydrogels networks, ab) chemical crosslinked and b) physical crosslinked.*

Chitosan physical macrogels (Figure 2.2-b) can be formed thanks to the polycationic nature of the chitosan in acidic medium by interaction with polyanions, leads to the formation of chitosan hydrogels via electrostatic interactions [6]. The ionic interactions can be divided into three groups depending on the type of crosslinker used, anions, anionic molecules or polymers with negative charge, commonly known it as polyelectrolyte complexes (PEC) [6]. According to the literature, the most common crosslinkers employed are: Mo(VI) or Pt(II) as ionic crosslinkers, among anionic molecules, phosphate-bearing groups, such as β-glycerophosphate and particularly tripolyphosphate salts and for PEC the alginate, pectin, xanthan and some proteins, such as collagen[3]. It is also possible to obtain chitosan physical macrogels without any crosslinking agent just by solubilisation of chitosan in an acidic aqueous medium and subsequent neutralization of $–NH_2$ groups. In this way, the repulsion between chitosan chains is blocked thus resulting in the formation of hydrogels through hydrophobic interactions, chitosan crystallinity and hydrogen bonding [6].

The method of preparation of physical chitosan macrogels is usually simple and these materials present several advantages such as a high pH-response due to modification of the global charge densities of chitosan, which can be useful for pH-controlled drug delivery.[3] Nevertheless, physical gels can be disintegrated by changes in the environment conditions such as ionic strength, pH, and temperature.[25]

It is well known that single-network hydrogels have weak mechanical properties and slow response at swelling.[25] To enhance the mechanical strength and/or properties such as swelling/deswelling response, multicomponent hydrogels have been designed.

From a biomedical perspective chitosan macrogels can be used for tissue engineering [27-29], drug delivery [30-33], and template for magnetic hyperthermia applications[34].

2.2.2 Chitosan nanogels

The preparation of chitosan nanogels can be accomplished with chemical or physical crosslinking methods as in the case of chitosan macrogels. The processes employed are emulsification, coacervation (nanoprecipitation) and shear break-up. One of the most well-known methods for the preparation of chitosan nanogels is crosslinking through the addition of an ionic crosslinker. [35]. Chitosan nanogels by ionic crosslinking can be assigned some key advantages: (i) they form under very mild conditions; (iii) they can stabilize encapsulated proteins against denaturation; (iv) their salt- and pH-sensitive ionic groups make them responsive to external stimuli; and (v) their properties can easily be enhanced by either coating their surface with polymers, nanoparticles and proteins, or covalently conjugating active molecules to their functional groups.[35]

Among the ionic crosslinkers, sodium tripolyphosphate (TPP) is generally employed for the preparation of chitosan nanogels for biomedical applications, because it is non-toxic, a quick gelling ability[36] and it is categorized as being GRAS (generally recognized as safe) by the FDA.[31] Chitosan nanoparticles crosslinked with TPP are formed mainly through the electrostatic interaction between positively charged amine from chitosan in acidic medium and negatively charged TPP molecules.[37]

Chitosan nanogels provide interesting opportunities as nanocarriers for drug delivery applications due to the fact they can protect the encapsulated molecule while facilitating its transport to the different sites [38]. Also, it can act in a controlled manner while preserving the ability to interact with mucosal surfaces, in summary chitosan nanocarriers can improve the pharmacological and therapeutic effects in terms of

reducing their toxic side effects. That is why chitosan nanocarriers have been broadly studied for a variety of biomedical applications, such as drug delivery [39-41], gene therapy [42], and carriers for magnetic nanoparticles for applications in magnetic hyperthermia [43-45]. The employment of chitosan nanocarriers for cancer therapy based on magnetic hyperthermia will be described in a separate section of this chapter.

2.2.3. Rheological studies of polymer macrogels and dispersions of nanogels

One important topic in this work is the study of the rheological properties of chitosan macrogels and dispersions of chitosan nanogels in order to determine the structure-properties relationship for these materials in order to develop the proposed final applications of these materials. The determination of the viscoelastic properties of these materials allows for the determination of their structural organization by means of fractal models applied to the rheological results.

i. Fundamentals of Rheology.

Rheology has been defined as a branch of physics which concerns itself with the mechanism of deformable bodies and flow of matter. However, rheological experiments do not merely reveal information about flow behavior of liquids but also about deformation behavior of solids. The connection here is that a large deformation produced by shear forces causes many materials to flow. All kinds of shear behavior, which can be described rheologically in a scientific way, can be viewed as being in between two extremes: flow of ideally viscous liquids on the one hand and deformation of ideally elastic solids on the other.[46] Behavior of all real materials is based on the combination of both a viscous and an elastic portion and therefore, they are considered as viscoelastic.

Nowadays, modern rheometers allow the precise measurement of a complex material's response to an applied force (stress) or deformation (strain). Linear oscillatory rheology subjects the material to a small oscillatory strain (or stress) of the form:

$$\gamma = A\sin(\omega t) \qquad \text{Equation 2.1}$$

where γ is the strain, A is the amplitude of the oscillation and ω is the frequency of oscillation. The resulting response of the material is measured. For a purely elastic solid, the stress required to impose the deformation is proportional to the strain whereas for a viscous liquid, the stress is proportional to the strain rate

$$\gamma = A\omega \cos(\omega t) \qquad \text{Equation 2.2}$$

Viscoelastic solids such as gels will have a response that is somewhere between the two extremes. The complex shear modulus G* can be separated into the fraction that is in-phase with the deformation and the part that is out-of-phase with the deformation. These are generally represented in terms of the elastic G' and viscous G" shear moduli:

$$G' \propto \sin(\omega t), \quad G'' \propto \cos(\omega t), \quad G^* = \left(G'^2 + G''^2\right)^{1/2}, \quad \tan(\delta) = \frac{G''}{G'}$$

Equation 2.3

The phase angle δ shows the relative importance of the liquid-like viscous modulus G" with respect to the solid-like elastic modulus G'.

Oscillatory rheology is a powerful characterization tool in polymer science because by varying the amplitude and frequency of the applied strain, a wide range of timescales and behaviors can be studied and that allows the characterization of the viscoelastic behavior of polymer materials. In the case of polymers gels, oscillatory experiments are carried out within the linear viscoelastic regime which allows an investigation of the gel response without disruption of the gel structure. In addition, the determination of the viscoelatic behaviour of polymer gels allows the study of their structural organization. In fact, the structures of gels are highly disordered, but there is much experimental evidence that in certain length scales they are often self-similar and can be described in terms of fractal geometry employing models based on scaling laws [47].

ii. Fractal analysis of gels.

The viscoelastic properties of gels can be analyzed using the theoretical model based on the scaling approach which relates modulus to concentration following the relation described in Equation 2.4. [48, 49]:

$$G \approx C^n \qquad \text{Equation 2.4}$$

where C is the polymer concentration and n is an exponent which depends upon the conformation of the chain linking junction points. The exponent n is related to the fractal dimension, ν^{-1}. There are several theoretical models for the determination of n. For a monodisperse solution of polymer with dimension ν^{-1} gives a viscoelastic exponent n defined in the next equation:

$$n = \frac{\nu^{-1}}{\nu^{-1} + 2} \qquad \text{Equation 2.5}$$

However, for not entanglement system, n is given by:

$$n = \frac{\nu^{-1}}{\nu^{-1} + 2}(r - 1) \qquad \text{Equation 2.6}$$

where r is scaling exponent that describes the size distribution. Muthukamar proposed other theoretical model and n values is given by:

$$n = \frac{d\left(d + 2 - 2\nu^{-1}\right)}{2\left(d + 2 - \nu^{-1}\right)} \qquad \text{Equation 2.7}$$

According the equation 2.7, all n values ($0<n<1$) are possible with a fractal dimension of $1<\nu^{-1}<3$.

iii. Fractal analysis of aqueous dispersions of polymer nanogels

Aqueous dispersions of polymer nano or microgels are very similar to polymer macrogels in that they both behave as viscoelastic materials. Aqueous dispersions os

polymer nano or microgels aggregate given rise to colloidal gels whereas polymer macrogels are formed by polymerization and/ or crosslinking, both of which are aggregation process. Taking into account this fact, scaling theories are developed to account for the elastic properties of colloidal gels by applying the scaling concepts which have been proved to be successful with polymer macrogels. Figure 2.3 shows a schematic representation of possible intra or inter interaction among microgels in dispersion.

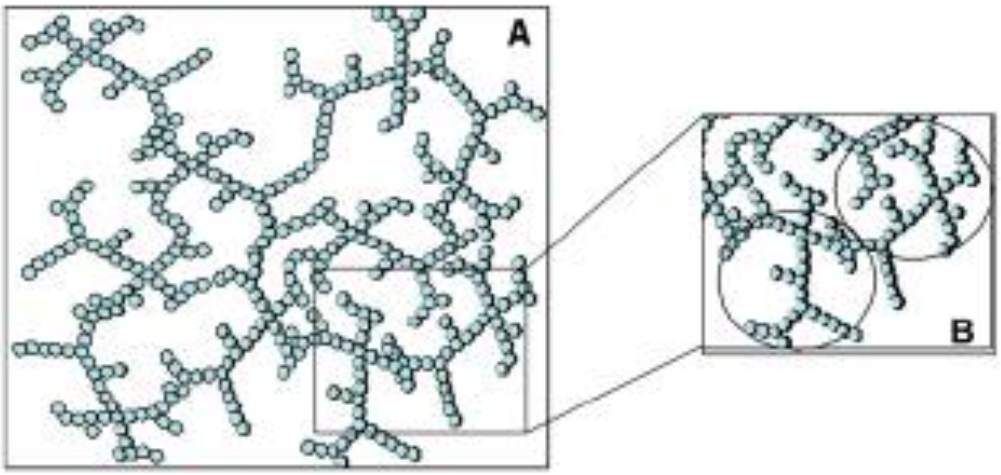

Figure 2.3 *A) Schematic representation of microgels dispersions agglomerated, B) Formation of agglomerates composed of fractal microgels. Adapted from the Coro Echeverria Zabala thesis.*

Several theories have been developed for studying the structure of a gel from rheological measurements, however, nowadays there are two main theories that will be explained ahead, Shi *et al*[50] and Wu and Morbidelli[47].

- **Shi *et al* model**

First, it is important to remark that for these scaling theories by assuming a certain structure for colloidal gels, simple but systematic scaling theory for both the elastic constant and the limit of linearity of colloidal gels that are well above the gelation threshold can be derived. The scaling of the elastic properties of colloidal gels under such conditions is dominated by the fractal nature of the flocs.

In this model, Shi and coworkers have developed a scaling model by defining two separate regimes: the strong-link regime and weak-link regime. The strong-link regime may be achieved by allowing the individual flocs to grow very big is that each

flocs is very weak spring, therefore it is presents at low particle concentrations. In this regime the links among flocs (interfloc links) have a higher elastic constant that those of the flocs, consequently the breaking of bonds occurs within a floc[50]. On the other hand, weak-link regime is presents at high particle concentrations, consequently with very small flocs. These small flocs are stronger springs compared to large flocs.

In this model, it is assumed that the structure of gels is constituted by fractal flocs, which during gelation aggregate with each other. The elastic properties of a flocs are dominated by its effective backbone, which can be approximated as a linear chain of springs. In the strong-link regime, where the interfloc links are stronger than the intrafloc links, the macroscopic elasticity of the gel is given by that of intralinks. In this case, it is possible to derive two relationships relating the fractal dimension of the flocs (d_f) and the fractal dimension of the backbones (x) to the storage modulus ($G´$) and the limit of linearity (γ_0):

$$G´ \propto \varphi^{A} \qquad \text{Equation 2.8}$$

$$\gamma_0 \propto \varphi^{B} \qquad \text{Equation 2.9}$$

where φ is the volume fraction and the exponents, A and B, have the form

$$A = (d + x)/(d - d_f) \qquad \text{Equation 2.10}$$

$$B = -(1 + x)/(d - d_f) \qquad \text{Equation 2.11}$$

where d is the Euclidean dimension of the system.

On the other hand, the weak-link regime is defined where the flocs are more rigid than the interfloc links, the elasticity of the interfloc links determines the elasticity of the gel. For this regime are employed the same equations for $G´$ and γ_0 previously described, but with different expressions for the exponents:

$$A = B = 1/(d - d_f) \qquad \text{Equation 2.12}$$

Therefore with this model only to regimes are considered and the transition from one to the other with the change in particle concentration must be continuous, leading to intermediate situations where both inter- and intrafloc links contribute to the gel's overall elasticity. Therefore, Wu and Morbidelli includes a new regime as it will be explained below.

- **Wu and Mobidelli model**

Wu and Mobidelli proposed a modification of the scaling model of Shi et al. that relates the structure parameters of the gel to its elastic properties and is valid not only for the strong- and the weak-link regimes but also for the intermediate regimes. In this model the structure of a colloidal gel (network) is considered as a collection of flocs. The flocs are fractal objects with average size ξ and fractal dimension d_f. It is well known that the size of the flocs that constitute a gel is in the range from one to hundreds of microns. Thus the flocs can be considered as microscopic elements that built the macroscopic gel.

Moreover, a macroscopic gel system is divided into two levels of structure: intramicrostructure characterizing structure within a floc and intermicrostructure characterizing the collection of flocs. Thus, the macroscopic elasticity of a gel must be related to both intra- and intermicroscopic elasticity.

Briefly, the relation between the macroscopic elastic constant and the particle volume fraction in terms of the microstructure parameters is given by

$$K \propto \varphi^{A} \qquad \text{Equation 2.13}$$

where

$$A = \beta / (d - d_f) \qquad \text{Equation 2.14}$$

and

$$\beta = (d - 2) + (2 + x)(1 - \alpha) \qquad \text{Equation 2.15}$$

where α is a constant in the range [0, 1], which depends on the given range of K_ξ/K_l. Moreover, x represents the backbone fractal dimension or tortuosity of the network, whose value for a colloidal gel is in the range of 1-1.3. Therefore, β is a constant, which for a three-dimensional system (d = 3) ranges between 1, for α = 1, and 3 + x, for α = 0.

On the other hand, Wu and Morbidelli extends the approach above to derive a scaling model for the limit of linearity, γ_0, following an approach originally proposed by Shih *et al*. The limit of linearity (γ_0) is defined as the situation where the weakest bonds break and the linear elastic behavior vanishes. These are generally the singly connected bonds and is given by

$$\gamma_0 = \frac{\Delta L}{L} \propto \xi^{(2+x)(1-\alpha)-1} = \xi^{\beta-d+1} \propto \varphi^B \qquad \text{Equation 2.16}$$

where

$$B = (d - \beta - 1)/(d - d_f) \qquad \text{Equation 2.17}$$

Thus, from the experimental values of γ_0 as a function of the particle volume fraction φ, one can estimate the exponent B, which together with the value of A in equation X allows us to determine the values of both β and d_f.

2.3 CHITOSAN NANOGELS AS NANOCARRIERS FOR CANCER THERAPY BASED ON MAGNETIC HYPERTHERMIA.

In recent years much attention has been focused on development of polymer nanogels and nanoparticles that can respond to external stimuli and act as drug nano-carrier, as well[51] for their employment in cancer therapy. [51]. In this way, their synergistic effect will improve the cancer therapy, resulting in less dose for the same therapeutic effects or the same dose with much higher therapeutic effects and less side effects.

2.3.1 Magnetic Hyperthermia.

Hyperthermia is defined as a kind of heat therapy which makes body tissue exposed to high temperatures. This treatment can be applied local, regional and whole body hyperthermia depending on the location of disease[52]. According to the degree of temperature raise, hyperthermia treatment can be classified into different types. In thermo ablation, a tumor is subjected to high temperatures of heat >46 °C (up to 56 °C) causing cells to undergo direct tissue necrosis, coagulation or carbonization. Moderate hyperthermia (41 °C < T < 46 °C) has various effects both at the cellular and tissue levels. The latter kind usually is named as hyperthermia treatment. This kind of hyperthermia can damage and kill cancer cells, while cause minimal injury to normal tissues. [51] After a hyperthermia treatment, cells can present a serial of changes and/or damages as: activation and/or initiation of many intra and extracellular degradation mechanisms like protein denaturation, protein folding, aggregation and DNA cross linking, induction and regulation of apoptosis, signal transduction, multidrug resistance and heat shock protein (HSP) expression.[52] Some recent studies are reported that cancer cells may present thermotolerance due to the existence of a class of heat-shock proteins (HSPs). Hyperthermia treatment would increases the expression of HSPs in cancer cells, which leads to higher resistance to hyperthermia therapy.[51]

Magnetic materials for hyperthermia applications have been broadly employed, because have the possibility to convert dissipated magnetic energy into thermal energy, the application of magnetic materials for hyperthermia treatment of cancer was first proposed in 1957[52]. Magnetic nanoparticles (MNPs) include metallic, bimetallic, and superparamagnetic iron oxide nanoparticles, which have reactive surface that can be coated with biocompatible polymers and loaded with therapeutic agents. [53] However, iron oxides are often used as hyperthermia agent because of their high biocompatibility and their heat response to the applied magnetic field.[51]

Specifically, for iron oxides when they are submitted to an alternating magnetic field at a specified frequency, they can produce enough heat for cancer treatment due to its high specific absorption rate (SAR) or specific loss power (SLP) [51]. This term is used to define the absorption efficiency of any material to generate heat due to AMF.[54] The heat generation mechanism can be attributed to two different phenomena: relaxation and hysteresis loss. The former mechanism (relaxation) is of two

types: Néel and Brownian relaxations. Heat generation through Néel relaxation is due to rapidly occurring changes in the direction of magnetic moments relative to crystal lattice (internal dynamics). In the case of Brownian relaxation is due to physical rotation of particles within a medium in which they are placed (external dynamics) and is hindered by the viscosity that tend to counter the movement of particles in the medium.[54] Usually, SPA values depend on parameters such as MNPs structure (size, shape and crystal structure), magnetic properties (magnetic anisotropy and temperature dependence of magnetizations) and amplitude (H) and frequency (*f*) of AMF, polydispersity of MNPs, and the surrounding environment, that means for those particles internalized within the cells.[54]

Magnetic nanoparticles (MNPs) based hyperthermia treatment has a number of advantages compared to conventional hyperthermia treatment, as example: i) cancer cells absorb MNPs thereby increasing the effectiveness of hyperthermia by delivering therapeutic heat directly to them, ii) MNPs can be targeted through cancer specific binding agents making the treatment much more selective and effective, iii) MNPs can also effectively cross blood-brain barrier (BBB) and hence can be used for treating brain tumors, iv) effective and externally stimulated heating can be delivered at cellular levels through alternating magnetic field (AMF), v) MNPs used for hyperthermia are only few tens of nanometer in size and therefore, allows easy passage into several tumors whose pore sizes are in 380–780 nm range, vi) MNP-based hyperthermia can also be utilized for controlled delivery of drugs.

Chitosan has the capacity to form complexes with metal ions, particularly with transition and post-transition metal ions. This fact is explained by the presence of the amino groups in the structural unit of chitosan, it is definitely the main cause of its complexing capacity, but the binding mechanism of metal ions to chitosan is not yet completely understood. Various processes such as adsorption, ion exchange and chelation have been considered as the mechanisms responsible for complex formation between chitosan and metal ions. The type of the interaction prevailing depends on the metal ion, its chemistry and the pH. [4] Chitosan has attracted intense attention as an important biopolymer to effectively stabilize colloidal dispersions of superparamagnetic iron oxide nanoparticles, conferring them an increased biocompatibility and chemical functionality and giving rise to materials for applications in magnetic hyperthermia [55, 56].

2.3.2 Combined treatments for cancer therapy

One of the trends employed in cancer therapy is the combination of two or more treatments with the aim to diminish the side effects of conventional treatments that are actually employed such as chemotherapy. The drug delivery for cancer therapy includes a huge number of drugs that are used for different kind of cancers. The most commonly employed drugs for chemotherapy reported in the literature are Doxorubician (DOX)[53], Placlitaxel[57, 58] and 5-Fluorouracil[43, 59, 60]. To this end, hyperthermia therapy, may be combined with well-developed therapeutics such as chemotherapy, irradiation, surgery, gene therapy, and immunotherapy in order to enhance its efficacy [52].

The use of nanoparticles loaded with anti-cancer drug have the advantages that are able to penetrate tumors due to their small size and the leaky nature of tumor microvasculature[53], therefore the efficacy of the treatment would improve the quality of life of cancer patients, particularly those who are end-staged and too weak to withstand harsh therapy. It is well known that tumor cells present low pH values, such as pH 5.5, that fact is generated by the anaerobic glucose metabolism. After targeting of nanoparticles to the tumor site drug release starts at the acidic microenvironment of the tumor tissue [53]. pH responsive chitosan nanoparticles would be expected to have an effective drug release in the tumor microenvironment since the drug release rate can be suddenly accelerated with lower pH.

2.4 CHITOSAN MICROGELS BY MICROFLUIDICS.

Microfluidics techniques arise as a powerful potential technique for the preparation of microgels with controlled dimensions. It is considered a promising strategy for the generation of microgels via rapid, high-throughput production of highly monodisperse droplets, which can be subsequently gelled to form microgels with tunable compositions and mechanical properties[61]. Moreover, microfluidic strategies offer a control over the shapes, morphologies, and size distribution of polymer colloids [62, 63]. It is worth pointing the importance of particle size and particle size distribution on pharmaceutical uses such as drug encapsulation [64] and controlled drug delivery

[65]. MF platforms can also provide precise control of mixing of reagents, residence time and reaction temperature of the diverse methods of synthesis of microparticles [66].

2.4.1 Fundamentals of MF.

Microfluidics technique is related to a set of technologies for the manipulation of small fluid volumes in the range of mL, µL, nL, pL, within artificially fabricated microsystems. Microfluidic systems enable generic and consistent miniaturization, integration, automation and parallelization of different chemical processes. [67]. In polymer science, the control over the dimensions of microfluidic channels in microfluidic devices allows for the generation of polymer microgels of controlled particle size.

The synthesis of microgels by MF can be explained in two main steps. The first step consists in the emulsification of polymer solutions, an oligomer or monomers in an immiscible non-polar liquid. The second step is based on the gelation of the precursor droplets.

The emulsification in MF devices can occur via different mechanisms as previously reported by E. Kumacheva *et. al.*[62], which depend on the geometry of the MF device, the macroscopic properties of the liquids, the flow rates of the liquids, viscosity ratio, gas pressure, and channel wettability. [68] With regard to the geometry, different routes to microfluidic emulsification have been reported in order to generate polymer particles[62]. As can be observe in Figure 2.4, there are several geometries that and currently employed for the generation of droplets. Most of the geometries employed for the generation of polymer microgels are limited to T-junction and flow-focusing geometries fabricated into a poly(dimethylsiloxane) (PDMS) slab, because they are the most frequently exploited to produce droplets with narrow size distribution.

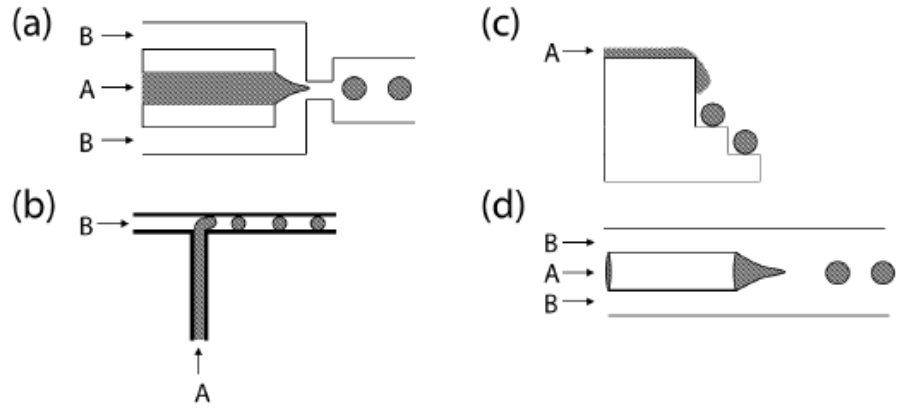

***Figure 2.4**. Schematic drawings of various types of microfluidic droplet generators the (a) flowfocusing, (b) T-junction, (c) terrace-like, and (d) and co-flowing stream geometries. The droplet and the disperse phases are labeled as A and B, respectively. Adapted from the Ethan Tumarkin thesis.*

In the flow-focusing droplet generator (Figure 2.4-a), an aqueous phase and a nonpolar liquid (labeled as A and B, respectively) are introduced to the central and side channels, respectively. A stream of the aqueous droplet phase is focused in the narrow orifice by the shear force imposed by the stream of the continuous phase. A highly periodic break-up of the thread of the disperse phase yields droplets with narrow size distribution. In this kind of geometry the size of the droplets is controlled by the ratio of the flow rates of the continuous to droplets phases, that is, the diameters of the droplets decrease with the increase in the ratio of the flow rates [69]. On the other hand, in the T-junction droplet generator (Figure 2.4-b) the droplet phase flows into the junction, the continuous phase forms a thin film layer between the disperse phase and the walls of the device, causing an increase in pressure which ‘‘squeezes’’ the disperse phase to form a droplet.[62] In this case, the droplets are usually considering as plugs that are droplets that span over the entire width of the channel, as it is shown in Figure 2.4-b. The size of the plugs is controlled by the ratio of flow rates of the continuous to droplets phases: with increasing flow rates ratio, the droplets become smaller.

The dimensions of microgels, their morphologies and shapes are determined by the corresponding properties of the precursor droplets. These final microgels can be obtained by on-chip or off-chip gelation of the precursor droplets. It is important to define that on-chip gelation, means that the gelation process occurs in the droplets

during their residence in the microchannels. [62] Off-chip gelation referes to gelation occurring outside of the microfluidic device.

Despite the advantages previously mentioned, the generation of microgels by MF technique has important challenges as for example the control of the viscosity of the precursor solutions once they are gelled. In fact, the small dimensions of MF reactors require fast gelation, so that the microgels emerging from the reactor should be sufficiently strong to keep their integrity, especially upon their transfer into an aqueous phase and to avoid collisions of gelling droplets in the microchannels.[62]

The transformations of precursor droplets into polymer particles is achieved by either chemical or physical mechanisms, such as crosslinking polymerization , thermally induced gelation, self-assembly, evaporation of the solvent from the droplets, or phase separation. [61]

2.4.2 Chitosan microgels by microfluidics and applications.

The use of biopolymers for the preparation of microgels by MF lies at the forefront because they are inherently scalable for bulk production and possess low environmental impact, providing new options for more distributed networks and utility for such systems in environmental and human health applications. [70] Also, microgels from biopolymers obtained by MF such as agarose[71, 72], collagen[73], alginate[74] and chitosan[75], presented several advantages related with the intrinsic properties of the biomaterial such as their stimuli responsive nature, the ease with which their surfaces can be functionalized, and their capacity to encapsulate and release functional species. [76].

Specifically for chitosan microgels, different methods have been reported for their preparation with MF employing different geometries and crosslinking processes. Xu *et al* [77] have prepared chitosan microgels employing T-junction geometry and by off-chip crosslinking with glutaraldehyde. These microgels are applied in the field of protein drug controlled release and immobilization lipases. Also, chitosan microgels have been synthesized using a double T-junction channel geometry on a microfluidic chip to generate droplets and separate satellite droplets from parent droplets and then microgels were off-chip crosslinking with sodium tripolyphosphate. [75] Some studies

are reported in the literature employing flow-focusing devices. Yan et al[78] used MF for generating TPP-chitosan microparticles using a cross-flow microfluidic chip coupled with external crosslinking reaction for pharmaceutical applications.

Very few studies are reported based on the gelation of chitosan solutions without the use of crosslinkers by MF. Chen *et al*[63] reported the preparation of chitosan/cytosine-phosphodiester-guanine oligodeoxynucleotide (CpG ODN) nanoparticles as potential immunostimulatory adjuvants, yielding a decrease in particle size and size range, an increase in loading efficiency with regard to bulk synthesis. Zhang *et al* [79] reported the synthesis of microgels from a triple interpenetrating network (3XN), based on partially oxidized dextran (Odex), Teleostean, and N-carboxyethyl chitosan (CEC). In this case, a chitosan derivative is employed.

The MF technique has also been employed for the encapsulation of bio-molecules or cells and functional nanoparticles. Jiang et al [80] prepared chitosan droplets obtained by T-junction MF device that are interfacially crosslinked with glutaraldehyde. These microparticles were loaded with various payloads, such as magnetic nanoparticles and/or fluorescent dyes and then semiflexible chains were prepared. Such microparticles could find applications as microfluidic mixers, delivery vehicles, microscale sensors, or miniature biomimetic robots. Xi Lu et al [81] synthesized soft dimer capsules based on chitosan, that are like Janus particles. They prepared dimmers wherein one lobe encapsulates paramagnetic Fe_2O_3 nanoparticles and the other is composed by chitosan.

2.5 REFERENCES

[1] Muzzarelli RAA. Chemical and Technological Advances in Chitins and Chitosans Useful for the Formulation of Biopharmaceuticals. Chitosan-Based Systems for Biopharmaceuticals: John Wiley & Sons, Ltd; 2012. p. 1-21.

[2] Jayakumar R, Menon D, Manzoor K, Nair SV, Tamura H. Biomedical applications of chitin and chitosan based nanomaterials - A short review. Carbohydrate Polymers. 2010;82:227-32.

[3] Berger J, Reist M, Mayer JM, Felt O, Gurny R. Structure and interactions in chitosan hydrogels formed by complexation or aggregation for biomedical applications. European Journal of Pharmaceutics and Biopharmaceutics. 2004;57:35-52.

[4] Peniche C, Argüelles-Monal W, Goycoolea FM. Chapter 25 - Chitin and Chitosan: Major Sources, Properties and Applications. In: Belgacem MN, Gandini A, editors. Monomers, Polymers and Composites from Renewable Resources. Amsterdam: Elsevier; 2008. p. 517-42.

[5] Kadib AE, Bousmina M, Brunel D. Recent progress in chitosan bio-based soft nanomaterials. J Nanosci Nanotechnol. 2014;14:308-31.

[6] Shukla SK, Mishra AK, Arotiba OA, Mamba BB. Chitosan-based nanomaterials: A state-of-the-art review. Int J Biol Macromol. 2013;59:46-58.

[7] Garcia-Fuentes M, Alonso MJ. Chitosan-based drug nanocarriers: Where do we stand? J Control Release. 2012;161:496-504.

[8] Pujana MA, Pérez-Álvarez L, Iturbe LCC, Katime I. Water soluble folate-chitosan nanogels crosslinked by genipin. Carbohydrate Polymers. 2014;101:113-20.

[9] Berger J, Reist M, Mayer JM, Felt O, Peppas NA, Gurny R. Structure and interactions in covalently and ionically crosslinked chitosan hydrogels for biomedical applications. European Journal of Pharmaceutics and Biopharmaceutics. 2004;57:19-34.

[10] Borzacchiello A, Ambrosio L, Netti PA, Nicolais L, Peniche C, Gallardo A, et al. Chitosan-based hydrogels: Synthesis and characterization. J Mater Sci Mater Med. 2001;12:861-4.

[11] Liu Y, Wang J, Zhang H, Ma C, Liu J, Cao S, et al. Enhancement of proton conductivity of chitosan membrane enabled by sulfonated graphene oxide under both hydrated and anhydrous conditions. Journal of Power Sources. 2014;269:898-911.

[12] Karim Z, Mathew AP, Grahn M, Mouzon J, Oksman K. Nanoporous membranes with cellulose nanocrystals as functional entity in chitosan: Removal of dyes from water. Carbohydrate Polymers. 2014;112:668-76.

[13] Sarkar SD, Farrugia BL, Dargaville TR, Dhara S. Physico-chemical/biological properties of tripolyphosphate cross-linked chitosan based nanofibers. Materials Science and Engineering: C. 2013;33:1446-54.

[14] Jayakumar R, Prabaharan M, Nair SV, Tamura H. Novel chitin and chitosan nanofibers in biomedical applications. Biotechnology Advances.28:142-50.

[15] Zhang L, Xue J, Zhou X, Fei X, Wang Y, Zhou Y, et al. Adsorption of molybdate on molybdate-imprinted chitosan/triethanolamine gel beads. Carbohydrate Polymers. 2014;114:514-20.

[16] Trifković KT, Milašinović NZ, Djordjević VB, Krušić MTK, Knežević-Jugović ZD, Nedović VA, et al. Chitosan microbeads for encapsulation of thyme (Thymus serpyllum L.) polyphenols. Carbohydrate Polymers. 2014;111:901-7.

[17] Copello GJ, Villanueva ME, González JA, López Egües S, Diaz LE. TEOS as an improved alternative for chitosan beads cross-linking: A comparative adsorption study. Journal of Applied Polymer Science. 2014;131.

[18] Shrestha N, Shahbazi MA, Araújo F, Zhang H, Mäkilä EM, Kauppila J, et al. Chitosan-modified porous silicon microparticles for enhanced permeability of insulin across intestinal cell monolayers. Biomaterials. 2014;35:7172-9.

[19] Mantripragada VP, Jayasuriya AC. IGF-1 release kinetics from chitosan microparticles fabricated using environmentally benign conditions. Materials Science and Engineering C. 2014;42:506-16.

[20] Peniche H, Peniche C. Chitosan nanoparticles: A contribution to nanomedicine. Polym Int. 2011;60:883-9.

[21] Lien C-F, Molnár É, Toman P, Tsibouklis J, Pilkington GJ, Górecki DC, et al. In Vitro Assessment of Alkylglyceryl-Functionalized Chitosan Nanoparticles as Permeating Vectors for the Blood–Brain Barrier. Biomacromolecules. 2012;13:1067-73.

[22] Almalik A, Donno R, Cadman CJ, Cellesi F, Day PJ, Tirelli N. Hyaluronic acid-coated chitosan nanoparticles: Molecular weight-dependent effects on morphology and hyaluronic acid presentation. Journal of Controlled Release. 2013;172:1142-50.

[23] Gnavi S, Barwig C, Freier T, Haastert-Talini K, Grothe C, Geuna S. Chapter One - The Use of Chitosan-Based Scaffolds to Enhance Regeneration in the Nervous System. In: Stefano Geuna IPPT, Bruno B, editors. International Review of Neurobiology: Academic Press; 2013. p. 1-62.

[24] Muzzarelli RAA. Chitins and chitosans for the repair of wounded skin, nerve, cartilage and bone. Carbohydrate Polymers. 2009;76:167-82.

[25] Dragan ES. Design and applications of interpenetrating polymer network hydrogels. A review. Chemical Engineering Journal. 2014;243:572-90.

[26] Samanta HS, Ray SK. Controlled release of tinidazole and theophylline from chitosan based composite hydrogels. Carbohydrate Polymers. 2014;106:109-20.

[27] Nguyen MK, Alsberg E. Bioactive factor delivery strategies from engineered polymer hydrogels for therapeutic medicine. Prog Polym Sci. 2014;39:1235-65.

[28] Farshi Azhar F, Olad A, Salehi R. Fabrication and characterization of chitosan–gelatin/nanohydroxyapatite–polyaniline composite with potential application in tissue engineering scaffolds. Designed Monomers and Polymers. 2014;17:654-67.

[29] Wang L, Stegemann JP. Thermogelling chitosan and collagen composite hydrogels initiated with [beta]-glycerophosphate for bone tissue engineering. Biomaterials.31:3976-85.

[30] Foley PL, Ulery BD, Kan HM, Burks MV, Cui Z, Wu Q, et al. A chitosan thermogel for delivery of ropivacaine in regional musculoskeletal anesthesia. Biomaterials. 2013;34:2539-46.

[31] Ur-Rehman T, Tavelin S, Gröbner G. Chitosan in situ gelation for improved drug loading and retention in poloxamer 407 gels. International Journal of Pharmaceutics. 2011;409:19-29.

[32] Ruel-GariÃ©py E, Leclair G, Hildgen P, Gupta A, Leroux JC. Thermosensitive chitosan-based hydrogel containing liposomes for the delivery of hydrophilic molecules. Journal of Controlled Release. 2002;82:373-83.

[33] Sun P, Li P, Li Y-M, Wei Q, Tian L-H. A pH-sensitive chitosan-tripolyphosphate hydrogel beads for controlled glipizide delivery. Journal of Biomedical Materials Research Part B: Applied Biomaterials.97B:175-83.

[34] Hernández R, Zamora-Mora V, Sibaja-Ballestero M, Vega-Baudrit J, López D, Mijangos C. Influence of iron oxide nanoparticles on the rheological properties of hybrid chitosan ferrogels. Journal of Colloid and Interface Science. 2009;339:53-9.

[35] Lapitsky Y. Ionically crosslinked polyelectrolyte nanocarriers: Recent advances and open problems. Current Opinion in Colloid & Interface Science. 2014;19:122-30.

[36] Gan Q, Wang T, Cochrane C, McCarron P. Modulation of surface charge, particle size and morphological properties of chitosan-TPP nanoparticles intended for gene delivery. Colloids and Surfaces B: Biointerfaces. 2005;44:65-73.

[37] Shah S, Pal A, Kaushik VK, Devi S. Preparation and characterization of venlafaxine hydrochloride-loaded chitosan nanoparticles and in vitro release of drug. Journal of Applied Polymer Science. 2009;112:2876-87.

[38] de la Fuente M, Raviña M, Paolicelli P, Sanchez A, Seijo B, Alonso MJ. Chitosan-based nanostructures: A delivery platform for ocular therapeutics. Advanced Drug Delivery Reviews. 2010;62:100-17.

[39] Papadimitriou S, Bikiaris D, Avgoustakis K, Karavas E, Georgarakis M. Chitosan nanoparticles loaded with dorzolamide and pramipexole. Carbohydrate Polymers. 2008;73:44-54.

[40] Chen M-C, Mi F-L, Liao Z-X, Hsiao C-W, Sonaje K, Chung M-F, et al. Recent advances in chitosan-based nanoparticles for oral delivery of macromolecules. Advanced Drug Delivery Reviews. 2013;65:865-79.

[41] Agnihotri SA, Mallikarjuna NN, Aminabhavi TM. Recent advances on chitosan-based micro- and nanoparticles in drug delivery. Journal of Controlled Release. 2004;100:5-28.

[42] Nahaei M, Valizadeh H, Baradaran B, Nahaei MR, Asgari D, Hallaj-Nezhadi S, et al. Preparation and characterization of chitosan/beta-cyclodextrin nanoparticles containing plasmid DNA encoding interleukin-12. Drug research. 2013;63:7-12.

[43] Zhang L-y, Zhu X-j, Sun H-w, Chi G-r, Xu J-x, Sun Y-l. Control synthesis of magnetic Fe3O4-chitosan nanoparticles under UV irradiation in aqueous system. Current Applied Physics. 2010;10:828-33.

[44] Huang H-Y, Shieh Y-T, Shih C-M, Twu Y-K. Magnetic chitosan/iron (II, III) oxide nanoparticles prepared by spray-drying. Carbohydrate Polymers.81:906-10.

[45] Zhao D-L, Wang X-X, Zeng X-W, Xia Q-S, Tang J-T. Preparation and inductive heating property of Fe3O4-chitosan composite nanoparticles in an AC magnetic field for localized hyperthermia. Journal of Alloys and Compounds. 2009;477:739-43.

[46] Vicente JD. Rheology. Croatia2012.

[47] Wu H, Morbidelli M. A Model Relating Structure of Colloidal Gels to Their Elastic Properties. Langmuir. 2001;17:1030-6.

[48] Gennes PG. Scaling concepts in polymer physics. New York: Cornell University Press; 1979.

[49] Lopez D, Mijangos C, Munoz ME, Santamaria A. Viscoelastic Properties of Thermoreversible Gels from Chemically Modified PVCs&#x2020. Macromolecules. 1996;29:7108-15.

[50] Shih W-H, Shih WY, Kim S-I, Liu J, Aksay IA. Scaling behavior of the elastic properties of colloidal gels. Physical Review A. 1990;42:4772.

[51] Mi Y, Liu X, Zhao J, Ding J, Feng S-S. Multimodality treatment of cancer with herceptin conjugated, thermomagnetic iron oxides and docetaxel loaded nanoparticles of biodegradable polymers. Biomaterials. 2012;33:7519-29.

[52] Kumar CSSR, Mohammad F. Magnetic nanomaterials for hyperthermia-based therapy and controlled drug delivery. Advanced Drug Delivery Reviews. 2011;63:789-808.

[53] Unsoy G, Khodadust R, Yalcin S, Mutlu P, Gunduz U. Synthesis of Doxorubicin loaded magnetic chitosan nanoparticles for pH responsive targeted drug delivery. European Journal of Pharmaceutical Sciences. 2014;62:243-50.

[54] Kumar CSSR, Mohammad F. Magnetic nanomaterials for hyperthermia-based therapy and controlled drug delivery. Advanced Drug Delivery Reviews.63:789-808.

[55] Dias AMGC, Hussain A, Marcos AS, Roque ACA. A biotechnological perspective on the application of iron oxide magnetic colloids modified with polysaccharides. Biotechnology Advances. 2011;29:142-55.

[56] Nicolás P, Saleta M, Troiani H, Zysler R, Lassalle V, Ferreira ML. Preparation of iron oxide nanoparticles stabilized with biomolecules: Experimental and mechanistic issues. Acta Biomaterialia. 2013;9:4754-62.

[57] Koo H, Min KH, Lee SC, Park JH, Park K, Jeong SY, et al. Enhanced drug-loading and therapeutic efficacy of hydrotropic oligomer-conjugated glycol chitosan nanoparticles for tumor-targeted paclitaxel delivery. Journal of Controlled Release. 2013;172:823-31.

[58] Wei W, Lv P-P, Chen X-M, Yue Z-G, Fu Q, Liu S-Y, et al. Codelivery of mTERT siRNA and paclitaxel by chitosan-based nanoparticles promoted synergistic tumor suppression. Biomaterials. 2013;34:3912-23.

[59] Nagarwal RC, Nath Singh P, Kant S, Maiti P, Pandit JK. Chitosan Nanoparticles of 5-Fluorouracil for Ophthalmic Delivery: Characterization, in-Vitro and in-Vivo Study. Chemical and Pharmaceutical Bulletin. 2011;59:272-8.

[60] Tigli Aydin RS, Pulat M. 5-Fluorouracil Encapsulated Chitosan Nanoparticles for pH-Stimulated Drug Delivery: Evaluation of Controlled Release Kinetics. Journal of Nanomaterials. 2012;2012:10.

[61] E. Kumacheva PG. Microfluidic Reactors for Polymer Particles 2011.

[62] Tumarkin E, Kumacheva E. Microfluidic generation of microgels from synthetic and natural polymers. Chemical Society Reviews. 2009;38:2161-8.

[63] Chen S, Zhang H, Shi X, Wu H, Hanagata N. Microfluidic generation of chitosan/CpG oligodeoxynucleotide nanoparticles with enhanced cellular uptake and immunostimulatory properties. Lab on a Chip. 2014;14:1842-9.

[64] Lee HY, Chan LW, Heng PWS. Influence of partially cross-linked alginate used in the production of alginate microspheres by emulsification. Journal of Microencapsulation. 2005;22:275-80.

[65] Bala I, Hariharan S, Kumar MNVR. PLGA nanoparticles in drug delivery: The state of the art. Critical Reviews in Therapeutic Drug Carrier Systems. 2004;21:387-422.

[66] Luo G, Du L, Wang Y, Lu Y, Xu J. Controllable preparation of particles with microfluidics. Particuology. 2011;9:545-58.

[67] Halldorsson S, Lucumi E, Gómez-Sjöberg R, Fleming RMT. Advantages and challenges of microfluidic cell culture in polydimethylsiloxane devices. Biosensors and Bioelectronics. 2015;63:218-31.

[68] Huerre A, Miralles V, Jullien M-C. Bubbles and foams in microfluidics. Soft Matter. 2014;10:6888-902.

[69] Garstecki P, Stone HA, Whitesides GM. Mechanism for Flow-Rate Controlled Breakup in Confined Geometries: A Route to Monodisperse Emulsions. Physical Review Letters. 2005;94:164501.

[70] Domachuk P, Tsioris K, Omenetto FG, Kaplan DL. Bio-microfluidics: Biomaterials and Biomimetic Designs. Advanced Materials. 2010;22:249-60.

[71] Kumachev A, Tumarkin E, Walker GC, Kumacheva E. Characterization of the mechanical properties of microgels acting as cellular microenvironments. Soft Matter. 2013;9:2959-65.

[72] Kumachev A, Greener J, Tumarkin E, Eiser E, Zandstra PW, Kumacheva E. High-throughput generation of hydrogel microbeads with varying elasticity for cell encapsulation. Biomaterials. 2011;32:1477-83.

[73] Hegde M, Jindal R, Bhushan A, Bale SS, McCarty WJ, Golberg I, et al. Dynamic interplay of flow and collagen stabilizes primary hepatocytes culture in a microfluidic platform. Lab on a Chip. 2014;14:2033-9.

[74] Zhang H, Tumarkin E, Peerani R, Nie Z, Sullan RMA, Walker GC, et al. Microfluidic Production of Biopolymer Microcapsules with Controlled Morphology. Journal of the American Chemical Society. 2006;128:12205-10.

[75] Yang C-H, Lin Y-S, Huang K-S, Huang Y-C, Wang E-C, Jhong J-Y, et al. Microfluidic emulsification and sorting assisted preparation of monodisperse chitosan microparticles. Lab on a Chip. 2009;9:145-50.

[76] Fiddes LK, Young EWK, Kumacheva E, Wheeler AR. Flow of microgel capsules through topographically patterned microchannels. Lab on a Chip - Miniaturisation for Chemistry and Biology. 2007;7:863-7.

[77] Xu J-H, Zhao H, Lan W-J, Luo G-S. A Novel Microfluidic Approach for Monodispersed Chitosan Microspheres with Controllable Structures. Advanced Healthcare Materials. 2012;1:106-11.

[78] Yang C-H, Huang K-S, Lin P-W, Lin Y-C. Using a cross-flow microfluidic chip and external crosslinking reaction for monodisperse TPP-chitosan microparticles. Sensors and Actuators B: Chemical. 2007;124:510-6.

[79] Zhang H, Betz A, Qadeer A, Attinger D, Chen W. Microfluidic formation of monodispersed spherical microgels composed of triple-network crosslinking. Journal of Applied Polymer Science. 2011;121:3093-100.

[80] Jiang K, Xue C, Arya C, Shao C, George EO, Devoe DL, et al. A new approach to in-situ "micromanufacturing": Microfluidic fabrication of magnetic and fluorescent chains using chitosan microparticles as building blocks. Small. 2011;7:2470-6.

[81] Lu AX, Jiang K, DeVoe DL, Raghavan SR. Microfluidic Assembly of Janus-Like Dimer Capsules. Langmuir. 2013;29:13624-9.

Chapter 3

CHITOSAN MACROGELS.

STUDY OF THEIR PROPERTIES

In this chapter chitosan macrogels were prepared through two different methods. The first one consists in the preparation of alkali chitosan macrogels by adding coagulant solution. This method allows for the *in situ* synthesis of iron oxide nanoparticles. Another route is based on the preparation of composite chitosan/agarose, where the gelation process is achieved by the feature of agarose to gel at low temperatures (8–17 ºC). This method enables the encapsulation of ferrofluid. The preparation, characterization and development of biomedical application, Magnetic Hyperthermia and drug release, are detailed in the following sections.

3.1. INTRODUCTION

Hydrogels are defined as three-dimensional polymer networks that are able to retain a large amount of water in their swollen state[1]. Specifically, hydrogels obtained from natural polymers are currently the focus of considerable scientific research for the development of biomedical applications due to their inherent biocompatibility, biodegradability and also they are susceptible to enzymatic degradation [2, 3][4]. As stated in the introduction, an example of natural polymers commonly employed for the preparation of hydrogels is chitosan. Chitosan is soluble in certain acidic aqueous solutions, owing to the protonation of the primary amine groups. Due to the pH-responsiveness and inherent biocompatibility, chitosan gels are attractive for biomedical applications [5-7] and specially, as materials for controlled drug delivery [8-11].

Chitosan hydrogels are accomplished either by physical associations, such as secondary forces (hydrogen, ionic, or hydrophobic bonding) and physical entanglements and by covalent crosslinkages [2]. It is known that chitosan aqueous solution can to become a gel in alkaline solution without any chemical crosslinkers. This kind of gel is achieved when the pH of chitosan solution is high and consequently the positive charges of chitosan molecules are neutralized and under goes coacervation-phase inversion, and chitosan gels [12]. This material can be used for controlled release not only in acidic but also in basic media, for rapid release by dissolution and as thermogelling systems[13].

Another route for the preparation of chitosan hydrogels consists in ionic crosslinking, which is a simple and mild method for preparing chitosan hydrogels. This kind of hydrogel is obtained thanks to the cationic amino groups of chitosan that can interact with negatively charged molecules, anions and polyelectrolytes, such as polysaccharides, proteins and synthetic polymers.[2] This method presents advantages for biomedical applications because it is not necessary the use of organic precursors, catalysts, or reactive agents.

In order to broaden the applications of chitosan hydrogels, researchers have developed composite hydrogels, where chitosan is blended with others biopolymers e.g. collagen[14], gelatin[15] and agarose[16]. In particular, agarose, an alternating copolymer found in some seaweeds consisting of 1, 4-linked 3, 6-anhydro-α-l-galactose and 1, 3-linked β-d-galactose derivatives is a neutral polysaccharide that forms thermoreversible gels upon cooling agarose aqueous solutions. The mechanical and thermal properties of agarose hydrogels depend on polymer concentration, pH and solvent type [17-19]. The biocompatibility of agarose and the mild conditions of its gelation make agarose suitable for applications in tissue engineering [20], however, agarose hydrogels exhibit low cell adhesiveness [21] and slow degradation rate [22]. To overcome these disadvantages, agarose can be chemically functionalized [23] or blended with others biopolymers such as gelatin [24, 25]. In particular, the combination of chitosan and agarose in composite gels has improved the mechanical and cell-adhesive properties of agarose [26, 27].

The complex formation of chitosan with transition metal ions is another method to obtain ionic crosslinked chitosan. This process has been widely studied and the existence of intra- or intermolecular complexes has been reported depending on parameters such as the nature of the ion, pH and relative chitosan/ion concentration [28-30]. Specifically, the ferric ion has been shown to coordinate with two chitosan residues, three molecules of water and one chloride ion [31]. Iron oxide particles such as magnetite, Fe_3O_4, have been *in situ* synthesized into a chitosan matrix to obtain magnetic chitosan materials. Another method to preparer magnetic chitosan hydrogels consist in the encapsulation of magnetic nanoparticles into chitosan matrix. These materials present the advantage that they can be employed in biomedical applications involving magnetic fields.

Therefore, in this chapter two different chitosan macrogels were prepared. On the one hand, alkali chitosan macrogels were prepared by the addition of coagulant solution (alkali solution). Then, *in situ* iron oxide nanoparticles were prepared into chitosan matrix and they were fully characterized trough FT-IR, thermal analysis, XRD and viscoelastic properties. On the other hand, composite chitosan/agarose macrogels were prepared taking into account the capacity of agarose of forming gels a low temperature. Their final viscoelastic properties and temporal stability were evaluated. Composite chitosan/agarose macrogels loaded with ferrofluid were synthesized and evaluated by heating performance, when macrogels are submitted to an alternating magnetic field. There are few studies that report a combination of hydrogels with micro- and/or nanomagnetic particles (e.g., γ-Fe_2O_3, Fe_3O_4, $CoFe_2O_4$) have been implemented as materials able to heat up target tumors remotely through an external magnetic field [32, 33]. In addition composite chitosan/agarose macrogels were loaded with drug model chemotherapy, 5-Fluorouracil (5-FU), and their drug release profile were evaluated as a function of pH and temperature. 5-Fluorouracil is one of the most widely used agents for the treatment of cancer and presented a broad activity against many cancer, for example, breast, head and neck, adrenal, pancreatic, gastric, colon, rectal, esophageal, liver and G-U (bladder, penile, vulva, prostate), as well as skin cancers (basal cell and keratosis) by topical application[34]. According to the literature, there are few systems reported based on composite chitosan/agarose as drug delivery carrier[35] or hyperthermia applications.

3.2. EXPERIMENTAL PART

3.2.1 Materials

Chitosan employed in this work was isolated from shrimp's shell (*Heterocarpus vicarious*) and supplied by Polymers Laboratory, National University, Costa Rica. Chitosan has a deacetylation degree of 65% as determined by potentiometric titration

and a molecular weight of 362 KDa as determined by viscosity method (ASTM D 2857). Ultra-low gelling temperature agarose (gelling temperature in the range of 8–17 ºC and melting point in the range of 40-50 ºC) was purchased from SeaPrep (Lonza, Switzerland, www.lonza.com). Oleic-acid-coated iron oxide nanoparticles dispersed in water as a ferrofluid (density =1.08 g/mL), NGAP FeO-05#4, were provided by Nanogap Subnmparticles, Spain.

Phosphate buffer saline (PBS, pH=7.4) (Gibco-BRL, Rockville, MD), acetate buffer (pH 5.2), 5-Fluorouracil (5-FU), acetic acid, ferrous chloride ($FeCl_2 \cdot 4H_2O$), ferric chloride ($FeCl_3 \cdot 6H_2O$), sodium hydroxide, methanol 80% were purchased from Sigma Company (Sigma Company, St. Louis, MO, USA) and used as received. The deionised water was obtained from the Millipore Milli-Q water purification system.

3.2.2 Preparation of alkali chitosan macrogels

i. Alkali chitosan macrogels

Chitosan solutions (1.5-4.0% w/v) were prepared by dissolving chitosan powder in 100 ml of acetic acid solution at 1% (v/v) (pH=3.8). Chitosan solutions were cast on teflon moulds and alkali chitosan macrogels were prepared by adding coagulant solution (H_2O:MeOH: NaOH) (4:5:1w/w)[36] to the chitosan solutions at room temperature.

ii. Chitosan ferrogels (*in situ* synthesis of iron oxide nanoparticles)

An aqueous solution (20 mL) of iron ions was prepared by mixing 0.21g of $FeCl_2 \cdot 4H_2O$ and 0.58 g of $FeCl_3 \cdot 6H_2O$ under constant N_2 bubbling with ultrasonication. After 30 minutes, the aqueous solution of iron ions was added under vigorous stirring to a chitosan solution (4% w/v) in a N_2 atmosphere to obtain a final chitosan concentration of 3% and 2% w/v.

Finally, each solution was cast on a teflon mould and carefully immersed in a 1 M sodium hydroxide solution in a N_2 atmosphere. The immersion time was varied from 30 minutes to 2 hours.

3.2.3 Preparation of composite chitosan/agarose macrogels

Macrogels based on composite chitosan/agarose macrogels were prepared at a fixed concentration of chitosan and three different concentrations of agarose. Their preparation is described below:

i. Composite chitosan/agarose macrogels.

For the preparation of composite chitosan/agarose macrogels, different amounts of agarose were dissolved at 60 °C in 0.5% (w/v) aqueous chitosan solutions containing 1% (v/v) of acetic acid. The concentration of agarose in the mixed solution was 1.0, 1.5 and 2.0% (w/v). The samples were designated as chitosan/agarose-1, chitosan/agarose-1.5 and chitosan/agarose-2. The chitosan-free sample was used as a control, for this sample agarose was dissolved in acetic acid 1% (v/v) and was labeled as agarose-1.5 (Table 3.1).

Table 3.1. Concentrations of agarose and chitosan in precursor solutions.

Sample	Agarose (% w/v)	Chitosan (% w/v)
Agarose-1.5	1.5	0
Chitosan/agarose-1	1	0.5
Chitosan/agarose-1.5	1.5	0.5
Chitosan/agarose-2	2	0.5

Mixed solutions were poured in Teflon moulds and maintained overnight at 4 ºC to allow the mixtures to gel. Teflon moulds with two different diameters (~4 and 8 mm) and ~5 mm in height were employed.

ii. Composite chitosan macrogels loaded with ferrofluid.

Composite chitosan/agarose macrogels and agarose macrogels were loaded with two different concentrations of ferrofluid in water (2% and 5% w/v). The concentrations of agarose and chitosan solutions were the same as reported in Table 3.1. The ferrofluid solutions were mixed under vortex agitation with the corresponding chitosan/agarose solutions in a volume ratio of 6:1, until getting homogeneous samples. Then, mixed solutions were poured in Teflon moulds and maintained overnight at 4 ºC to allow the mixtures to gel. As an example, samples were designed as chitosan/agarose-1+FeX, where X corresponds to the ferrofluid concentration, 2% or 5% (w/v).

iii. Composite chitosan/agarose macrogels loaded with 5-Fluorouracil.

Composite chitosan/agarose-1.5 macrogels and agarose-1.5 macrogels were loaded with a model anticancer drug 5-Fluorouracil (5-FU) at a concentration 0.5% (w/v). 5-FU was dissolved directly in chitosan/agarose solution and stirred at 60 ºC. The procedure of the preparation of 5-FU loaded chitosan/agarose macrogel was identical to that used for the preparation of 5-FU free composite macrogels. Final mixed solutions were poured in Teflon moulds and maintained overnight at 4 ºC to allow the mixtures to gel. Composite chitosan/agarose-1.5 loaded with 5-FU was designated as chitosan/agarose-1.5+FU. The chitosan-free sample was used as a control and was named as agarose-1.5+FU.

3.2.4 Characterization of macrogels.

i. Morphological studies.

- Transmission Electron Microscopy (TEM)

Samples were dried to form films and the morphology of thin films prepared by ultra-microtome was observed by transmission electron microscope (TEM, 200Kv Philips Tecnai). Thin films were cut perpendicular to the surface direction and laid on a copper grid.

- Scanning Electron Microscopy (SEM).

The surface and cross section of all macroscopic gel samples was examined using an SEM (XL30 ESEM, Philips). All the gels under study were freeze-dried. Subsequently the dried sample was coated with an ultrathin coating of gold deposited on the sample by high-vacuum metallization. Analysis of the pore structure was done using Image Pro 5.0 (media Cybernetics, USA) software.

ii. Study of the chemical structure by Attenuated Total Reflection Fourier Transformed Infra-Red Spectroscopy (ATR-FTIR)

Attenuated Total Reflection Fourier Transformed Infra Red Spectroscopy (ATR-FTIR) experiments were carried out on freeze-dried samples using a Perkin Elmer spectrometer. The spectra were acquired in the wave number range of 600-4000 cm^{-1} at a 4 cm^{-1} resolution.

iii. Temporal stability (mass loss).

To examine temporal stability (mass loss as a function of time) of the composite chitosan/agarose macrogels, the samples were immersed at 37 ºC in buffer solutions at pH 7.4 or 5.2 for various time intervals. Mass loss was determined as $(m_t-m_o)/m_o$, where m_t is the mass of the sample after a given time interval and m_o the mass of the `as prepared´ gel. Before weighing, the gel samples were quickly dried with a filter paper to remove excess water from the surface.

iv. Thermal stability by thermogravimetric analysis (TGA).

Dried alkali chitosan macrogels and composite chitosan/agarose macrogels were evaluated by thermogravimetric analysis (TGA) performed on a Q500 TA Instruments TGA, using a nitrogen stream as purge gas, at a heating rate of 10 ºC/min. Specifically

for chitosan macrogels the range of temperature employed was 40-950 ºC and for composite chitosan/agarose macrogels was 25–700 ºC

v. Determination of crystallinity by X-ray diffraction measurements (XRD).

X-ray diffraction measurements were performed on powdered samples in a Bruker Advance D8 equipment by using CuKα radiation (λ=1.2418 Å) in the range 2θ=5-65º.

vi. Rheological properties by dynamic oscillatory measurements.

The viscoelastic properties of alkali chitosan macrogels, composite chitosan/agarose macrogels and composite chitosan/agarose macrogels loaded with ferrofluid were carried out in an AR-G2 rheometer (TA Instruments, USA) using the 20 mm-diameter steel parallel plates. Two different experiments were performed: frequency sweeps between 0.1 and 10 Hz at 20 ºC and the temperature sweeps were performed from 5 to 80 ºC at 10 ºC/min and at 1 Hz frequency. All the experiments were carried out at a fixed torque in the linear viscoelastic regime. The linear viscoelastic region was located with the aid of a torque sweep. All the viscoelastic measurements were performed on hydrogels swelled to equilibrium.

3.2.5 Composite chitosan macrogels as precursors for biomedical applications.

i. Determination of Magnetic Remote Heating.

The specific power absorption (SPA) of the ferrofluid loaded chitosan/agarose-1.5 macrogels with two concentration of ferrofluid (2% and 5% w/v) were measured with a commercial AC field applicator (DM100 by nB nanoscale Biomagnetics, Spain) working at f=580 kHz and 24 kA/m (300 Oe). Figure 3.1 shows a scheme of the hyperthermia experiments. Experiments were carried out within a thermally-insulated working space of about 1 cm^3, using a closed container of 1.0 mL volume. All gels were prepared directly in the vial. This experiment was carried out in the Universidade Nova de Lisboa, FCT-UNL, Caparica, Portugal.

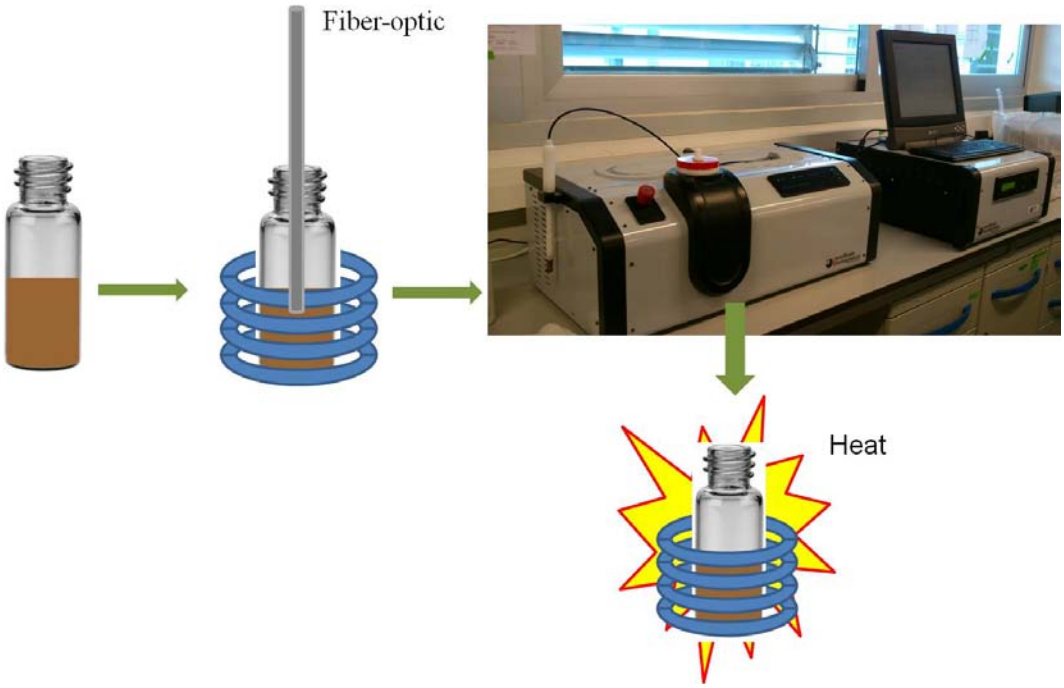

Figure 3.1*. a) Schematic representation of hyperthermia experiments.*

ii. Evaluation of *in vitro* drug release.

To study the *in vitro* release of 5-FU loaded from chitosan/agarose-1.5 macrogels at different pH values, the following procedure was used. Macroscopic gel samples were placed in vials containing 10 mL of buffer at pH of 5.0 (acetate buffer) or 7.4 (PBS buffer), both at 37 ºC, and stirred. An aliquot of 1 mL of the solution was periodically withdrawn to determine the concentration of 5-FU using UV/Vis spectrometry (Perkin Elmer Instrument Lambda 35 UV/VIS spectrometer, wavelength of 265 nm). The solution medium was replaced with the same volume of fresh medium.

3.3 RESULTS AND DISCUSSION

Two kinds of chitosan macrogels have been prepared. The first one consists in alkali chitosan macrogels. Then, iron oxide nanoparticles have been successfully synthesized in the presence of chitosan using an *in situ* coprecipitation method. This

method allows obtaining chitosan ferrogels. Secondly, composite chitosan/agarose macrogels were elaborated, taking into account the capacity of agarose to gel at low temperatures. Then, it has been developed composite chitosan/agarose macrogels loaded with ferrofluid. Finally, both system loaded with magnetic particles were evaluated for magnetic hyperthermia. Therefore, chitosan/agarose macrogels were loaded with a model anticancer drug 5-Fluorouracil and its release profile was analyzed as a function of pH and temperature. Next, it is described all the results obtained for both chitosan macrogels prepared.

3.3.1 Chitosan macrogels

i. Preparation of alkali chitosan macrogels.

In the process of formation of physical chitosan macrogels due to a pH increase by the addition of the coagulant solution, there is a balance between hydrogen bonding and hydrophobic interactions responsible for the formation of physical junctions. Alkali chitosan macrogel is shown in Figure 3.2. For degrees of acetylation lower than 40 %, the physical junctions are mainly composed of hydrogen bonding counterbalancing the low amount of acetyl groups in favour of hydrophobic interactions[37]. The formation of hydrogen bonds requires the deprotonation of the amine sites achieved by dissolving the raw chitosan in acetic acid.

Figure 3.2. *Visual appearance of chitosan ferrogels: (a) alkali chitosan hydrogel (2% w/v).*

The direct addition of NaOH to a chitosan solution would result in the local precipitation of chitosan[38]. To avoid this, MeOH is added to the coagulating solution in order to participate in the formation of hydrophobic junctions between polymer chain segments and therefore favour the formation of the gel[39].

ii. Preparation of chitosan ferrogels: *in situ* synthesis of iron oxide nanoparticles.

The synthesis of iron oxide nanoparticles inside chitosan macrogels involves two steps. As a first step, the chitosan is dissolved in an acid solution containing Fe^{2+} and Fe^{3+}, it has been reported that each iron ion is chelated with two moles of amino groups and four moles of oxygen[40, 41]. As a second step, the solutions are carefully immersed in a NaOH solution to simultaneously gel the chitosan solution and oxidize the iron cations to yield iron oxide nanoparticles. A schematic representation of the procedure is shown in Figure 3.3.

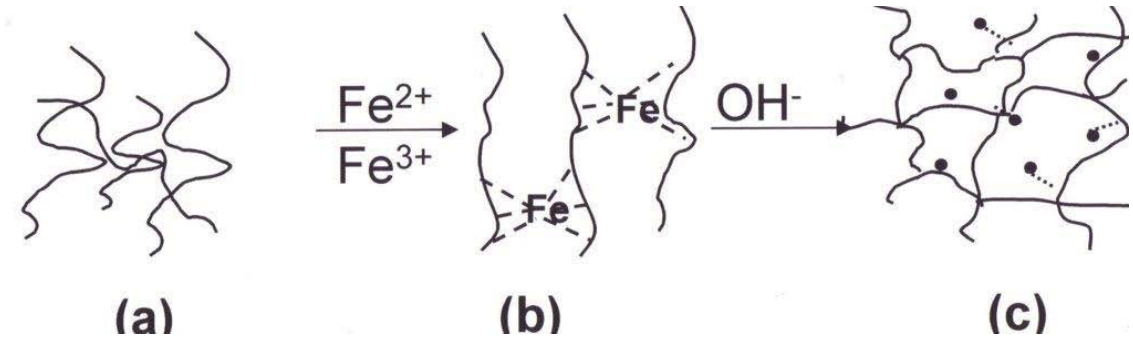

Figure 3.3. *Schematic representation of the synthesis of iron oxide in the presence of a chitosan solution: (a) neat chitosan; (b) formation of a complex Fe–chitosan and (c) chitosan ferrogel (black dots represent iron oxide nanoparticles).*

Due to the fact that chitosan dissolves in acidic mediums such as the one provided by the aqueous Fe^{3+}/Fe^{2+} solutions, it was not possible to repeat the number of oxidation cycles to increase the amount the iron oxide nanoparticles [42, 43]. Instead, the immersion time in NaOH solution was varied.

The formation of iron oxide nanoparticles is highly dependent on the chitosan concentration. Figure 3.4 shows that ferrogels obtained from a 2% (w/v) chitosan solution present a dark brown colour after 1 hour immersion time in NaOH which is characteristic of magnetite. Furthermore they are responsive to a 1T magnetic field. Interestingly, attempts to prepare a magnetite polymer gel hybrid by *in situ* oxidation of 3% (w/v) chitosan solutions were unsuccessful. Rather than the development of the black coloration characteristic of magnetite, the gel turned red/orange in colour possibly due to the formation of iron(III) oxyhydroxides [44]. One possible explanation for the absence of magnetite is that the higher viscosity of the 3% (w/v) chitosan solution with respect to the 2% (w/v) chitosan solution restricts the extent of oxidation by hindering the diffusion of NaOH. In fact it has been reported that, in the formation of iron oxide by coprecipitation of iron chlorides with bases, the slow addition of the base may lead to the formation of a brown nonmagnetic precipitate, probably hydroxides[45].

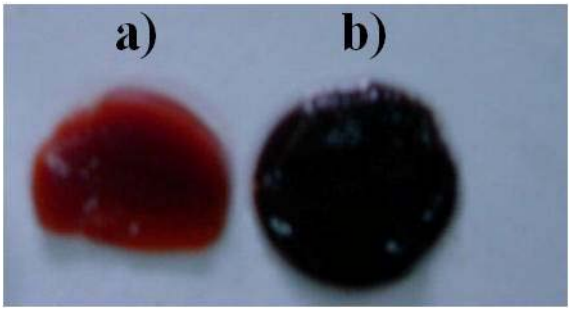

Figure 3.4. *Visual appearance of chitosan ferrogels: a) chitosan ferrogel subjected to 1 h immersion time in NaOH (3% w/v) and b) chitosan ferrogel subjected to 1 h immersion time in NaOH (2% w/v).*

iii. Morphological study.

Figure 3.5 shows the TEM images corresponding to alkali chitosan macrogels prepared with two concentration of chitosan: 2% and 3 (w/v). A good dispersion of spherical iron oxide nanoparticles was observed in the 2% (w/v) chitosan matrix with an average size of 10 nm. This result confirmed the successful *in situ* formation of iron oxide nanoparticles. Meanwhile the nanoparticles synthesized inside the 3% (w/v)

chitosan gel presented a very fine needle like morphology which is typical of hydroxides[46].

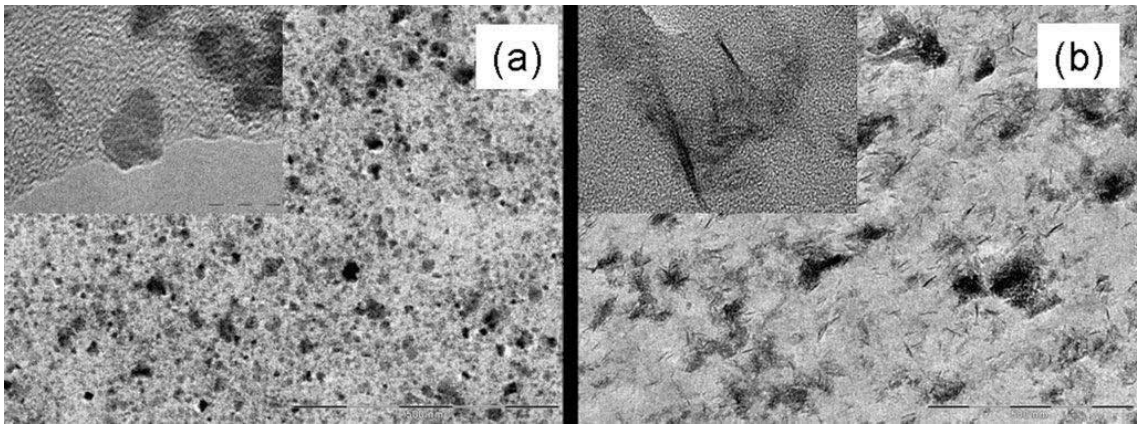

Figure 3.5. *Transmission electron microscopy corresponding to: (a) 2% (w/v) chitosan ferrogel and (b) 3 % (w/v) chitosan ferrogel subjected to 30 min immersion time in NaOH (bar = 500 nm). Inset shows iron oxide nanoparticles at a higher magnification (bar = 10 nm).*

iv. Determination of crystallinity by X-ray diffraction measurements (XRD)

The crystalline phase of the iron oxides was confirmed through XRD and the results are presented in Figure 3.6. Pure chitosan (Figure 3.6-a) exhibits two characteristic peaks at 2θ=9.7º (020) and 19.9º (110 and 040) [28].

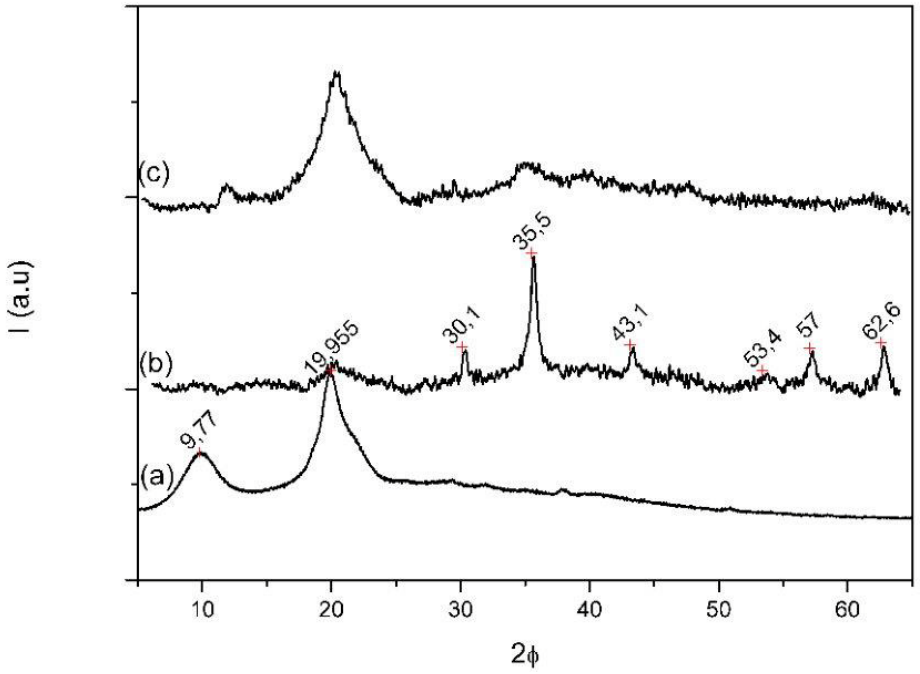

Figure 3.6. *Wide angle X-ray diffractograms of: (a) pure chitosan; (b) 2% (w/v) chitosan ferrogel immersed in NaOH for 1 h and (c) 3% (w/v) chitosan ferrogel immersed in NaOH for 1 h.*

The diffractogram corresponding to the 2% (w/v) chitosan ferrogel immersed for 1 hour in a NaOH solution (Figure 3.6-b) present six characteristic peaks at 30.1º (220), 35.5º (311), 43.1º (400), 53.4º (422), 57.0º (511) and 62.6º (440), which are consistent with standard diffraction data for magnetite[29]. Only the peak located at 2θ=19.9º corresponding to pure chitosan is slightly visible in this diffractogram which indicates almost complete disruption of the chitosan crystalline domains. The diffractogram corresponding to the 3% (w/v) chitosan ferrogel (Figure 3.6-c) does not present appreciable peaks corresponding to magnetite which corroborates the absence of magnetic, crystalline, iron oxide species in this sample. Furthermore, in this sample, the peak located at 2θ=19.9º indicates only slight disruption of the chitosan crystalline domain.

v. Analysis of the chemical structure.

The interaction of the chitosan matrix and the iron oxide nanoparticles was elucidated through FT-IR experiments presented in Figure 3.7.

Raw chitosan (Figure 3.7-a) presents two strong vibrations located at 1650 cm^{-1} that has previously been assigned to the amide I and at 1584 cm^{-1} attributed to the amine groups bending vibration overlapped with the amide II vibration respectively [31, 47]. Nitrogen atoms corresponding to the amine group hold a free electron doublet that is responsible for the uptake of metal ions by a chelation mechanism [48, 49]. However the overlapping of the bands assigned to the amide II and the amine groups prevent the observation of the interaction of the amine groups with the iron ions. Instead, the presence of amino complexes is corroborated by the appearance of a new band located at 800 cm^{-1} attributed to ν_{NH2} and ρ_{NH2}. This band has been observed in chitosan metal complexes with Cu^{2+}, Mn^{2+} and Zn^{2+}[30, 50].

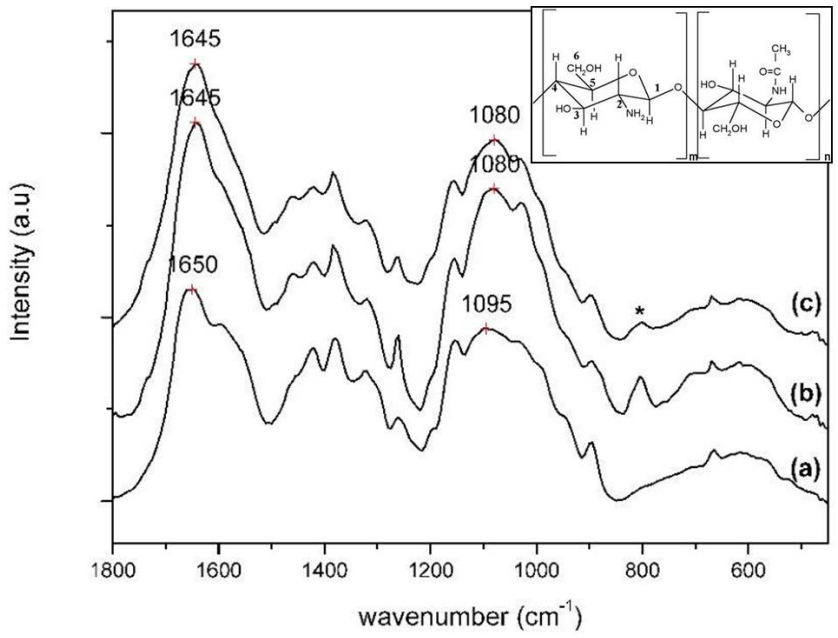

Figure 3.7*. FT-IR spectra of: (a) raw chitosan; (b) 2% (w/v) chitosan ferrogel and (c) 3% (w/v) chitosan ferrogel after 2 h immersion time in NaOH. The inset image shows the structure of partially acetylated chitosan constituted by (m) glucosamine units and (n) N-acetylglucosamine units.*

The acetyl groups remaining from chitin may also participate in the interaction with iron nanoparticles as denoted by the shift to lower frequency numbers of the 1650 cm^{-1} band corresponding to the amide I vibrations observed for the spectra containing iron oxide.

The absorption bands in the region of 1000-1100 cm^{-1} in the raw chitosan spectrum owe their origin to C-O stretching vibrations primarily in the alcohol groups[51]. Specifically, the band at 1095 cm^{-1} assigned to the C_3-O stretching in the spectrum corresponding to raw chitosan shifts to 1080 cm^{-1} in the spectra corresponding to the samples containing iron oxide nanoparticles (Figures 3.7-b and 3.7-c) whereas the peak located at 1020 cm^{-1} assigned to the C_6-O in Figure 3.7-a does not move in the samples containing iron oxide nanoparticles which indicates the existence of interactions involving the C_3 hydroxyl groups in agreement with theoretical studies[52].

It is worth of remark that even if the formation of magnetite nanoparticles is not achieved in the case of the 3% (w/v) chitosan ferrogels as shown by TEM images (Figure 3.5) and XRD (Figure 3.6), the FT-IR spectrum corresponding to this sample immersed for 2 hours in NaOH (Figure 3.7-c) presents the same features as the spectrum corresponding to the 2% (w/v) chitosan samples subjected to the same treatment (Figure 3.7-b). This indicates that the coordination of the iron cations to the chitosan matrix does take place for 3% (w/v) chitosan ferrogels and that it is the slow diffusion of the OH- species in the viscous medium provided by the 3% (w/v) chitosan what hinders the formation of the magnetite nanoparticles. These results will be further corroborated by rheological measurements.

vi. Analysis of the thermal degradation of the samples under study.

The iron oxide content in 2% (w/v) chitosan ferrogels was determined through TGA experiments and the results are shown in Figure 3.8.

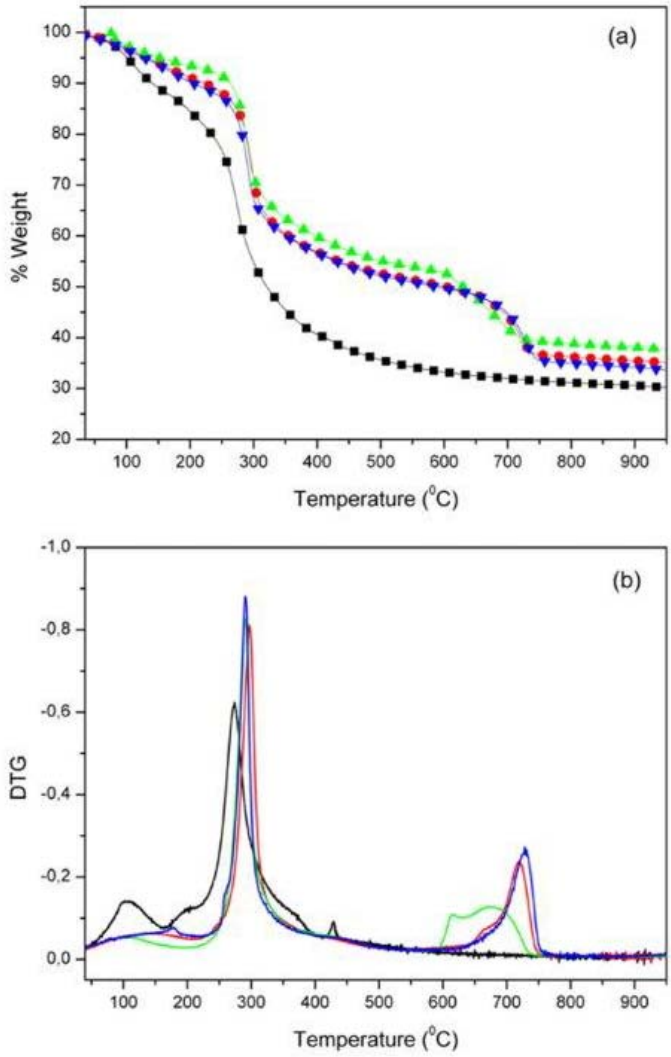

Figure 3.8. *(a) Thermogravimetric analysis and (b) differential thermogravimetric curves of 2% (w/v) chitosan ferrogels subjected to different inmersion times. (black) Neat chitosan; (red) 30 min; (green) 1 h; (blue) 2 h.*

The peak degradation temperatures obtained from the DTG curves and the residue at 950 ºC are given in Table 3.2.

Table 3.2. Temperature of the maximum weight loss rate, T_p and associated weight loss for neat chitosan and 2% (w/v) chitosan ferrogels.

	First range (50-200)		Second range (200-575)		Third range (575-785)		Fe_3O_4 (%w/v)
	T_P (ºC)	Weight loss (%)	T_P (ºC)	Weight loss (%)	T_P (ºC)	Weight loss (%)	
Neat chitosan	102	14.7	274	45.7			
Chitosan ferrogels (2% w/v)							
30 min	105	8	297	34.3	719	13.9	13.8
1 h	110	8	290	33.7	672	13.9	14.2
2 h	110	8	291	33.6	728	14.8	14.2

For neat chitosan, the first degradation stage ranges between 90 and 200 ºC and shows about 14.7% loss in weight. This may correspond to the loss of adsorbed and bound water. The second stage of weight loss starts at 200 ºC and continues up to 575 ºC and it is due to dehydration, depolymerisation and decomposition of the acetylated and deacetylated units of the chitosan[53]. This stage left about 30 % (w/w) solid residue in the neat chitosan.

The TGA of the iron-containing chitosan showed three degradation steps instead of the two observed for the starting chitosan. The amount of adsorbed water occurring during the first degradation range decreases to 8 % (w/w) for the three samples. The peak degradation corresponding to the second degradation range shifts to higher temperatures which indicate an increase of the thermal stability associated to the samples containing iron oxide. A third degradation range is observed in the samples containing iron oxide at temperatures 575-785 ºC. This may imply the attachment of the iron particles to the hydrogel networks [54, 55]. In addition, leakage of iron oxide nanoparticles from the swollen hydrogels in water was not observed at room temperatures for periods up to three months. This is a further indication of the attachment of the iron particles to the polymer network.

The iron oxide content was calculated assuming that the ratio between the weight of the residue at 950 ºC and the weight loss in the interval of 200-575 ºC for

pure chitosan is the same for chitosan in the ferrogels [56]. Therefore, the weight percentage of magnetite, M, in the ferrogels can be calculated as follows:

$$\frac{Rq}{\Delta W_q} \times \Delta W_m + M = R \qquad \text{Equation 3.1}$$

where R_q is the residue (% w/w) at 950 ºC of the starting chitosan; ΔW_q and ΔW_m are the weight loss percentages in the interval of 200-575 ºC for starting chitosan and chitosan ferrogels respectively and R is the residue at 950 ºC for the chitosan ferrogels.

In Table 3.2, it can be seen that the iron oxide concentration is independent from the immersion time in NaOH. The results are in agreement with reports in which it was determined that the chitosan-induced synthesis of iron oxide nanoparticles hardly depended on the iron ion concentration [57].

vii. Viscoelastic properties of alkali chitosan macrogels.

Before of analysis the viscoelastic properties of the samples, first it has been determined the Linear Viscoelastic Regions (LVR), defined as the region in which the elastic modulus and loss modulus are independent of the applied deformation. As an example, Figure 3.9 shows a strain sweep of alkali chitosan macrogels. From the experiments a value of 1% strain was employed for the rest of the rheological experiments.

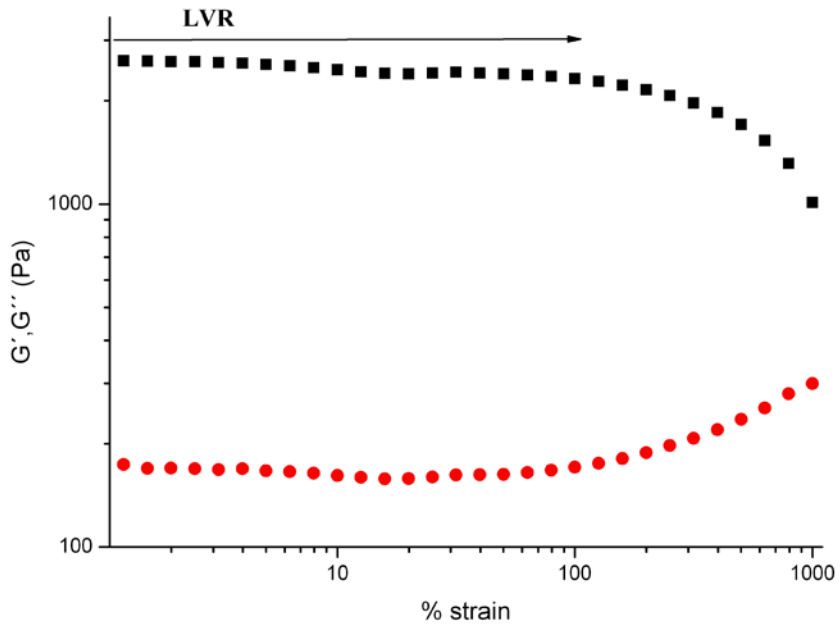

Figure 3.9. *Strain sweep for the determination of the Linear Viscoelastic Region (LVR) of chitosan/agarose-2.(■) Elastic modulus (G´) and (●) loss modulus (G´´).*

We have examined the rheological behaviour of chitosan gels precipitated in an alkali coagulating solution (H_2O:MeOH:NaOH: 4:5:1, w/w)[36].

Figure 3.10 shows a representative plot of the frequency dependence of G´ and G´´ for a 2% (w/v) chitosan hydrogel formed by neutralizing an acidic solution of chitosan with an alkali coagulating solution.

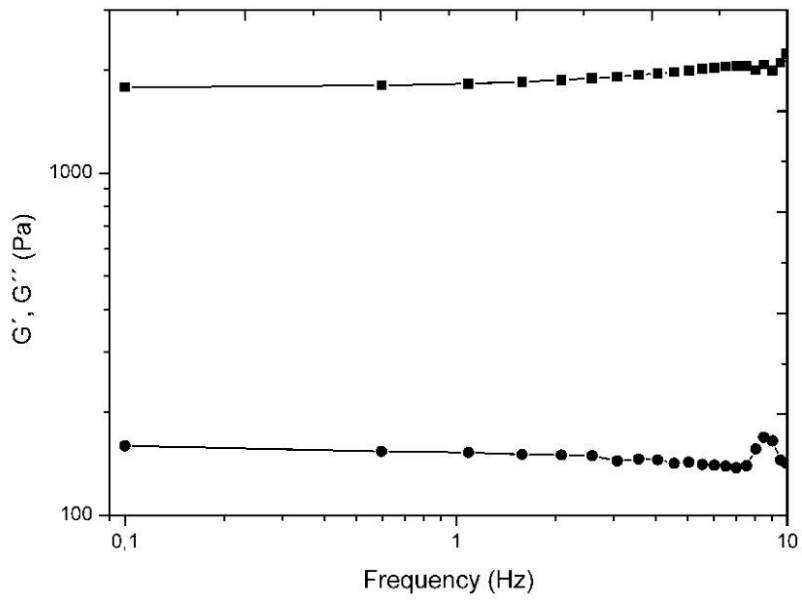

Figure 3.10 . *(■) Elastic modulus (G´) and (●) loss modulus (G´´) as a function of frequency for 2% (w/v) alkali chitosan hydrogels.*

As can be observed, G´ is much higher than G´´ over the entire frequency range and both modules are essentially frequency independent, a behaviour that is typical of hydrogels [58, 59]. The same conclusions are reached for other chitosan hydrogels obtained by raising the pH [60, 61].

The storage modulus as a function of frequency for chitosan hydrogels of varying chitosan concentrations are presented in Figure 3.11. All the samples present a typical gel behaviour in which the dynamic elastic modulus (G´) is relatively independent of the frequency of deformation. Moreover the elastic modulus increases with the chitosan concentration. Similar results have been reported for chitosan hydrogels obtained by treating chitosan solutions with gaseous NH_3. The increase of the elastic modulus with the chitosan concentration has been attributed to the presence of more polymer chains responsible for more entangled junctions[37].

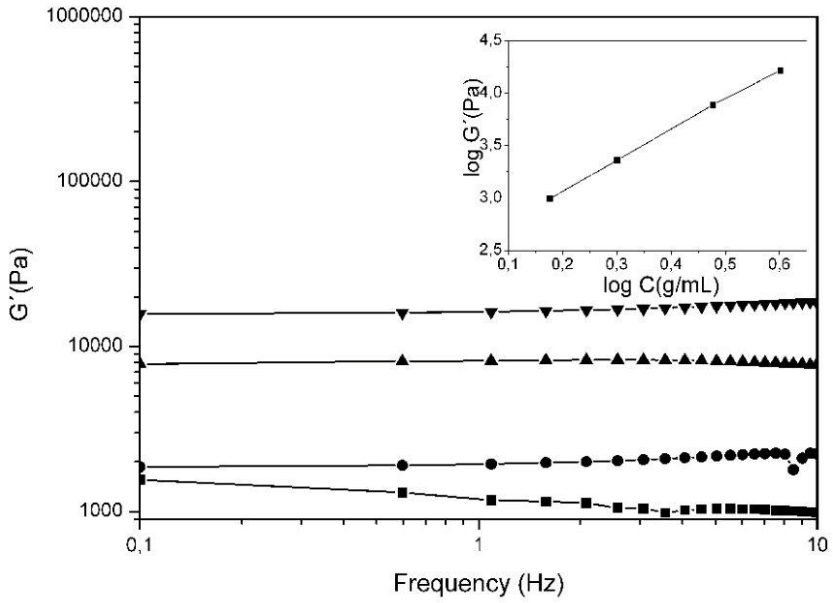

Figure 3.11. *Elastic modulus (G´) as a function of frequency for alkali chitosan hydrogels (■) 1.5% (w/v); (●) 2% (w/v); (▲) 3% (w/v); (▼) 4% (w/v) (inset: double logarithmic plot of storage modulus versus polymer concentration).*

The viscoelastic results have been analyzed using the theoretical model based on the scaling approach which relates modulus to concentration following the relation described in Equation 3.2. [62, 63]:

$$G \approx C^{n} \qquad \text{Equation 3.2}$$

where C is the polymer concentration and *n* is an exponent which depends upon the conformation of the chain linking junction points.

The double logarithmic plot of G´ versus concentration is shown in the inset of Figure 3.11. From this figure and making use of equation 3.2 a value of the exponent of 3 is obtained. The exponent n is related to the fractal dimension, ν^{-1}, of the object between the junctions as:

$$G \approx C^{3\nu/(3\nu-1)} \qquad \text{Equation 3.3}$$

Therefore, the fractal dimension, ν^{-1}, obtained from the exponent n is 2, which is characteristic of flexible systems with elasticity predominantly of entropic origin. This result indicates that these gels present a structure more similar to chemical gels than to

physical gels in the sense that they are constituted of flexible chains linked each other either through the formation of cooperative hydrogen bonds or by chemical crosslinking.

- Influence of iron oxide nanoparticles over viscoelastic properties of alkali chitosan macrogels.

It was evaluated the influence of the formation *in situ* of iron oxide nanoparticles in the rheological behaviour of chitosan hydrogels. Figure 3.12-a shows the evolution of the storage modulus as a function of frequency for 2% (w/v) chitosan ferrogels subjected to different immersion times. The *in situ* synthesis of iron oxide nanoparticles results in an increase of the elastic modulus of the chitosan ferrogels with respect to the neat alkali chitosan hydrogels, however, the increase of the NaOH immersion time does not entail an increase in the elastic modulus. On the contrary, the storage modulus corresponding to the gels immersed for 1 and 2h in NaOH are lower with respect to the gels after 30 minutes immersion time. This is more clearly seen in Figure 3.12-b where the storage modulus, G´ at 1 Hz is represented as a function of the immersion time in NaOH. To explain these results two factors have to be taken into account, on the one hand, the incorporation of metal nanoparticles onto polymer hydrogels will generally improve the mechanical properties of the systems[64]. According to this, an increase in the magnetite content would result in an increase of the storage modulus. Therefore, at immersion times longer than 1 h, the storage modulus, G´ becomes independent from the immersion time may be explained by the fact that the magnetite content remains constant as determined by TGA experiments (Figure 3.8) and thus an increase of the NaOH immersion time does not entail a reinforcement of the network.

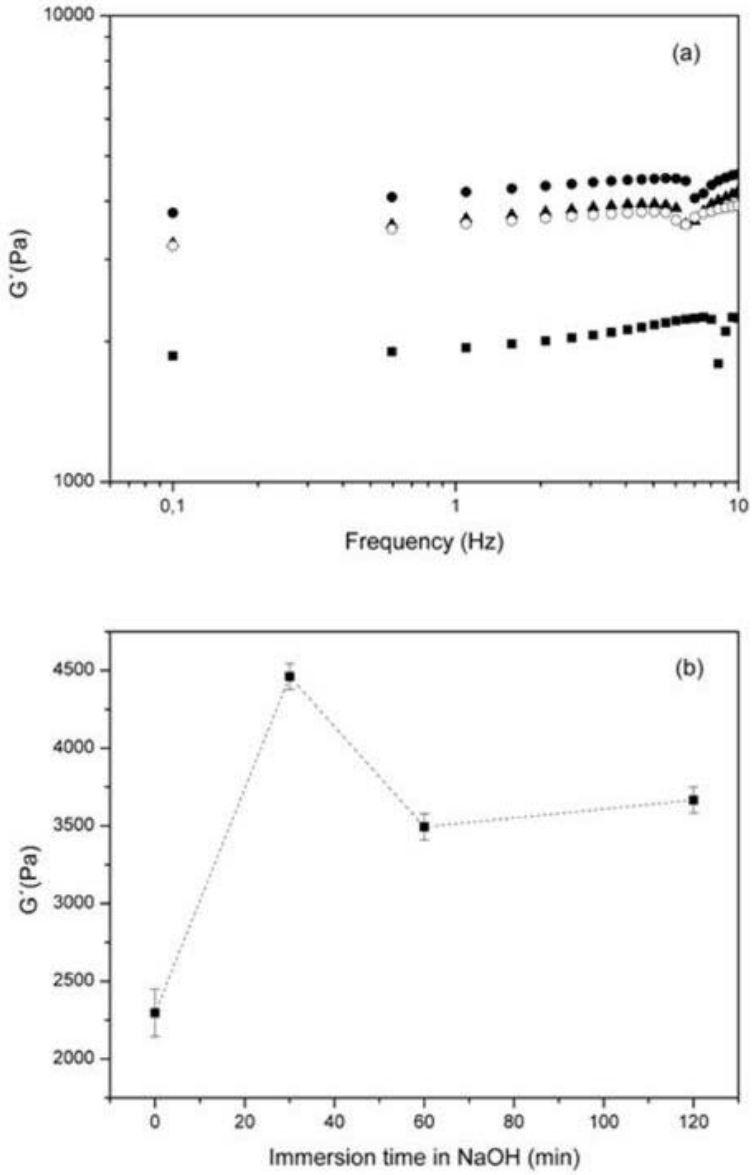

***Figure 3.12**. (a) Log of the elastic modulus (G´) as a function of frequency for 2% (w/v) chitosan ferrogels subjected to different immersion times in NaOH. (■) 0; (●) 30 min; (▲) 1 h; (○) 2 h. (b) Elastic modulus, G´, at 1 Hz as a function of immersion time in NaOH.*

On the other hand, the interaction of the iron cations with the amine groups and the hydroxyl groups in the chitosan matrix demonstrated through FT-IR (Figure 3.7) prevents the establishment of hydrogen bonding involving these groups. At the same time, the acetyl groups responsible for the establishment of hydrophobic interactions also interact with the iron cations and thus it is reasonable to assume that the effectiveness of these interactions are also reduced.

Figure 3.13-a shows the storage modulus as a function of frequency for 3% (w/v) chitosan hydrogels. For these samples, the immersion time in NaOH does not result in an increase of the modulus with respect to the neat chitosan hydrogels. In fact, as can be observed in Figure 3.13-b, the storage modulus remains unchanged for NaOH immersion times equal or shorter than 1 hour with respect to the neat chitosan.

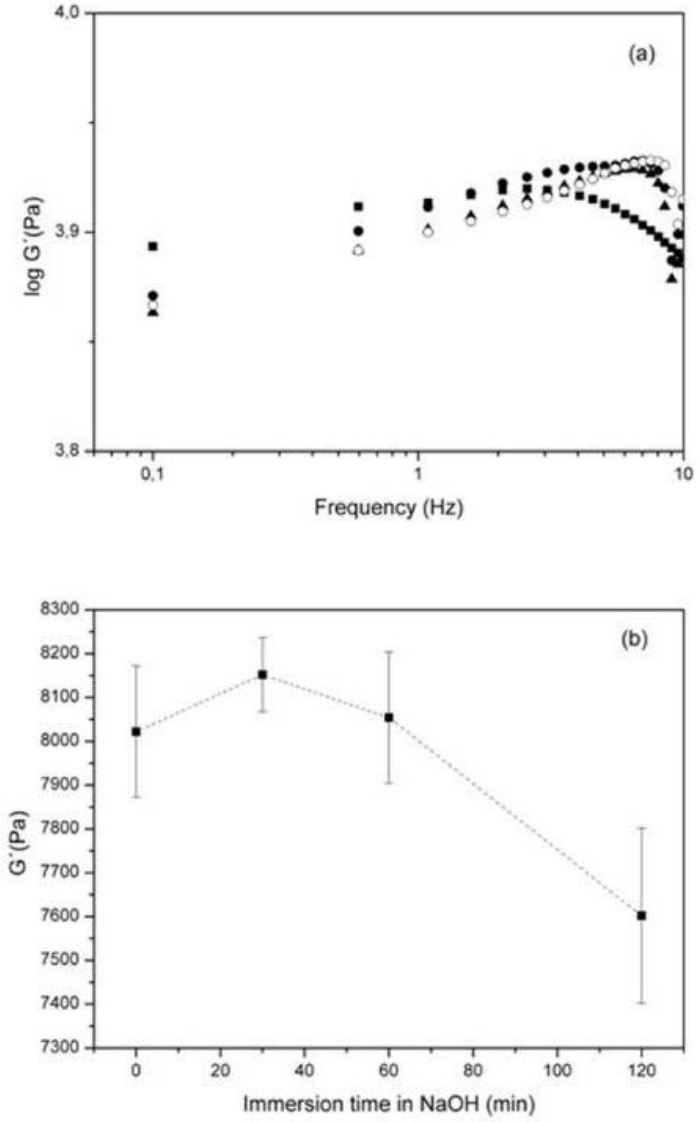

***Figure 3.13**. Log of the elastic modulus (G^0) as a function of frequency for 3% (w/v) chitosan ferrogels subjected to different immersion times in NaOH. (■) 0; (●) 30 min; (▲) 1 h; (○) 2 h (b) Elastic modulus, G´, at 1 Hz as a function of immersion time in NaOH.*

These results are in good agreement with the fact that magnetite nanoparticles are not formed in this case; instead the formation of hydroxides takes place which does

not induce the reinforcement of the network. At immersion times longer than 1 hour the storage modulus is lower than the corresponding to neat chitosan due to the fact that the interaction between iron cations and the polymer matrix prevent the formation of interactions between the polymer groups responsible for the formation of chitosan hydrogels.

3.3.2 Composite chitosan/agarose macrogels.

i. Preparation of composite chitosan/agarose macrogels.

Chitosan/agarose macrogels were prepared changing agarose content in the precursor chitosan/agarose solutions with three different concentrations. Figure 3.14-a shows a schematic representation of composite chitosan/agarose macrogels. The control agarose-1.5 looks transparent, as can be observed in Figure 3.14-b. The composite chitosan/agarose macrogels retained a transparency in the hydrated state, which suggested uniform distribution of chitosan in the host agarose matrix, without noticeable phase separation, as shown in Figure 3.14.

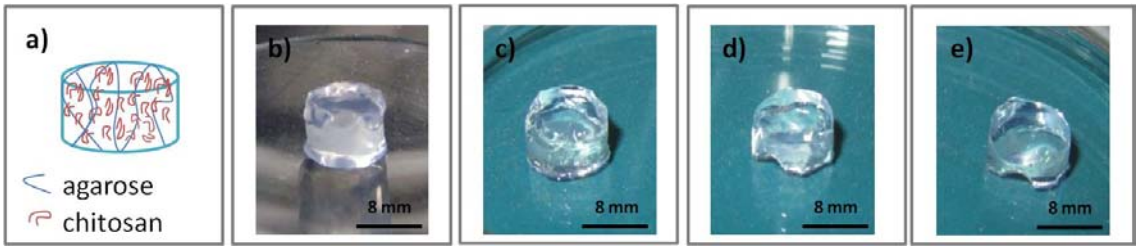

Figure 3.14. *(a) Schematic representation of chitosan/agarose macrogels. Photographs of b) agarose-1.5, c) chitosan/agarose-1 d) chitosan/agarose-1.5 and e) chitosan/agarose-2 macrogels.*

ii. Morphological study

The microstructure of the agarose-1.5 and composite chitosan/agarose macrogels was examined using scanning electron microscopy (SEM) after lyophilization of the samples. The structure of the surface and cross-section of the agarose-1.5 and chitosan/agarose macrogels are shown in Figure 3.15-a and 3.15-b respectively. Both

types of macrogels had a similar a sponge-like structure and porosity. Representative images of the pore size corresponding to agarose-1.5 and chitosan/agarose-2 gels determined from SEM images taken on the cross section (Figure 3.15-b) was 73±16 µm and 102±39 µm respectively. The individual agarose and chitosan domains were not distinguishable in the composite macrogels.

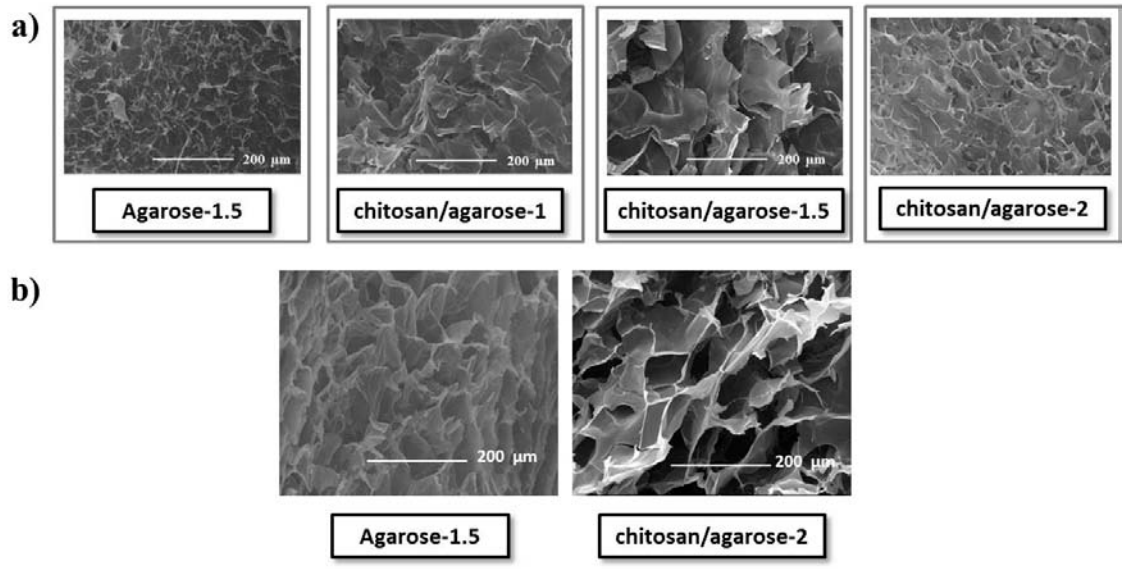

Figure 3.15. *(a) SEM images corresponding to the surface of agarose-1.5 and composite chitosan/agarose macroscopic gels. (b) Cross sections of agarose-1.5 and chitosan/agarose-2.*

iii. Analysis of the chemical structure.

The presence of interactions between chitosan and agarose in the composite gels was examined by ATR-FTIR spectroscopy experiments. The ATR-FTIR spectrum of agarose-1.5 (Figure 3.16-a) shows the peak at 1046 cm^{-1} for C-O (characteristic of axial deformation), 1371 cm^{-1} ascribed to C-C bending, 890 cm^{-1} attributed to C-H angular deformation of anomeric carbon, and 931 cm^{-1} assigned to 3,6-anhydrogalactose [22]. The chitosan spectrum exhibited the band at 1579 cm^{-1} corresponding to the N-H bending vibration overlapping the amide II vibration and the band at 1649 cm^{-1} that corresponds to the amide I vibration (Figure 3.16-b). Absorption bands at 1153 cm^{-1} (antisymmetric stretching C-O-C bridge), 1089 cm^{-1} and 1033 cm^{-1} (skeletal vibrations involving the C-O stretching) were characteristic of the CS saccharide structure [65].

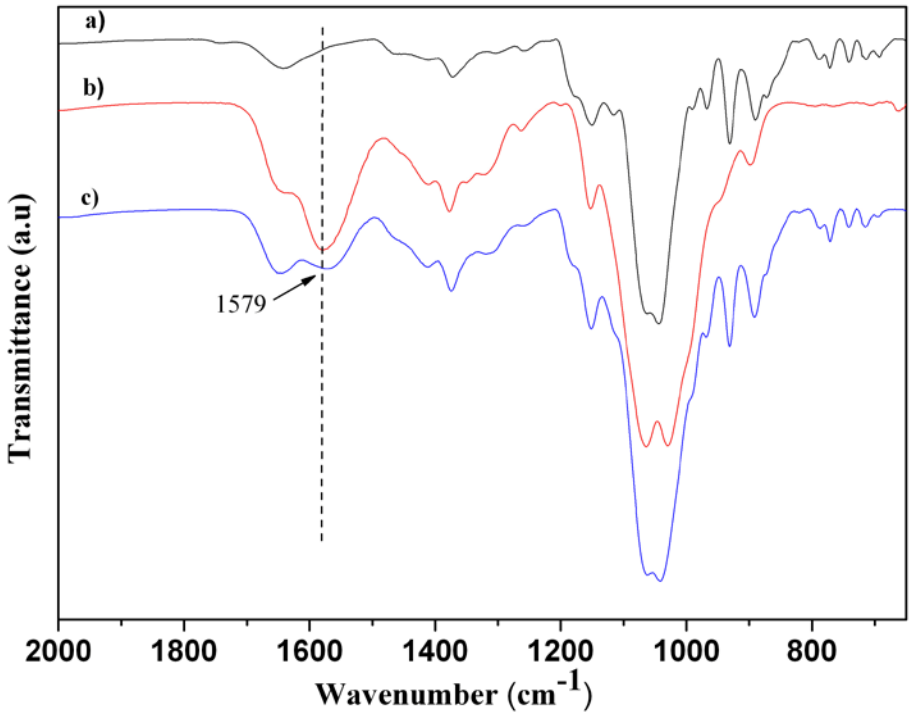

Figure 3.16. *ATR-FTIR spectra of (a) agarose-1.5, (b) chitosan, (c) chitosan/agarose-1.5*

The ATR-FTIR spectrum corresponding to the sample chitosan/agarose-1.5 (Figure 3.16-c) showed the characteristic bands of each polymer, however, the band located at 1579 cm^{-1} in chitosan (Figure 3.16-b) shifted to 1568 cm^{-1} (Figure 3.16-c), suggesting intermolecular hydrogen bonding between the chitosan amino groups and agarose hydroxyl groups. In addition, band broadening indicated interaction between the polymers.

iv. Temporal stability

In vitro stability of the composite chitosan/agarose macrogels was measured as their temporal mass loss at physiological temperature and pH 7.4 (Figure 3.17). The study was extended to pH=5.2, in order to simulate acidic tumor environment [66] and a 45 ºC, to analyze the effect of the temperature. First, the comparison among agarose-1.5 and chitosan/agarose-1.5 was analyzed, with the objective to study the addition of chitosan into the macrogel. Then, it will be reported the stability as function of agarose concentration, specifically for chitosan/agarose-2.

At physiological temperature of 37 ºC and pH 7.4, composite chitosan/agarose-macrogels have a significantly weaker mass loss than agarose-1.5 gels (Figure 3.17-a). This fact could be explained by two factors: the addition of chitosan to the system and the medium employed for the preparation of agarose solution. Agarose gels are known to be stable at physiological temperature and pH. Generally, they are prepared by dissolving agarose in water or PBS buffer and subsequently gelling the solution under reduced temperatures. In this work, agarose-1.5 gel was prepared by dissolving agarose in an aqueous 1% (v/v) acetic acid solution (pH=3.5), which could promote the light hydrolysis of 1-4 glucosidic links and decrease the stability of agarose gels. At pH=5.2 the increase in stability in chitosan/agarose gels, in comparison with agarose samples was evident (Figure 3.17-b). Therefore, the hydrolysis of agarose polymer was hindered in the presence of chitosan which led to an enhanced stability of the composite gels.

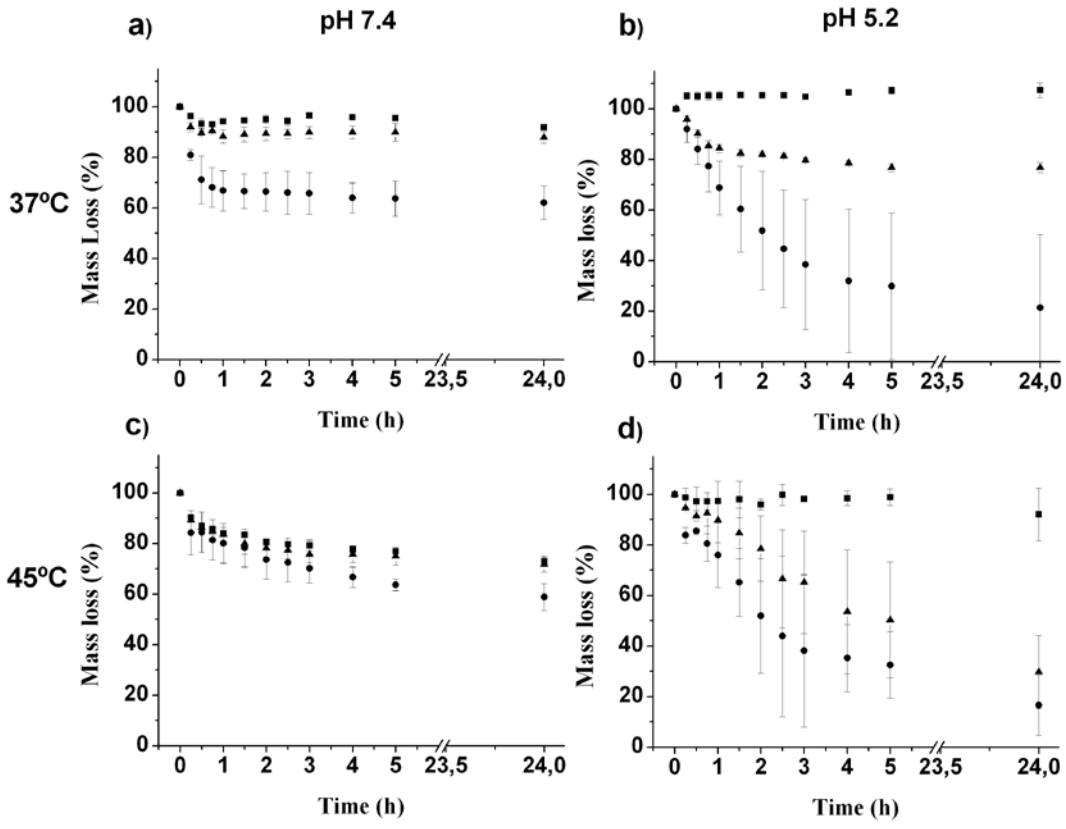

Figure 3.17. *Kinetics of stability of chitosan/agarose-2 macrogels (■), chitosan/agarose-1.5 macrogels (▲) and agarose-1.5 macrogel (●) at T=37 ºC and pH 7.4 (a) and at pH 5.2(b) and at T=45 ºC at pH 7.4 (c) and pH 5.2 (d).*

It is important to recall that agarose can gel below 17 ºC and melts in the range of 40-50 ºC. These transitions depend on the degree of hydroxyethylation of agarose component of the hydrogel. In order to determine the effect of chitosan on stability of the composite gels above agarose melting temperature, it is determined mass loss at 45 ºC at pH 7.4 and at pH 5.2. After 24 h, at pH 7.4 the mass loss was ~28% and ~41% for both composite chitosan/agarose gels and agarose-1.5 gel, respectively (Figure 3.17-c). Whilst, at pH 5.2 it is observed an important diminishing of the mass loss for all the samples under study, where composite chitosan/agarose macrogels were more stable than agarose gels. Thus, it can be concluded that at T=45 ºC, the stability of the gels was lower than at T=37 ºC as a consequence of partial melting of the agarose gel, yet, it was higher in the presence of chitosan.

In general, to compare the influence of agarose concentration in composite chitosan/agarose macrogels, it is possible to conclude that macrogels with higher agarose concentration were more stable at both pHs and temperatures. This results suggest that chitosan/agarose-2 presented a higher melting point than chitosan/agarose-1.5, for this reason there was no an important difference on function of temperature. The improvement of stability can be related with more hydrogen bonding among polymers, this fact was confirmed trough ATR-FTIR spectroscopy. Considering this hypothesis, composite chitosan/agarose-2 is less sensitive to pH and their degradation as it was mentioned before can be controlled on functions of agarose concentration, as well.

As Figure 3.18 shows, despite of the better stability of composite macrogels, an evident change on its appearance was observed. This fact may suggest a slow hydrolysis process of agarose, because samples turned white at pH 5.2 and after 24 h. It is important to highlight that this effect was the same for agarose-1.5 with the difference that this was observed a shorter times and finally the gel was broken in small pieces.

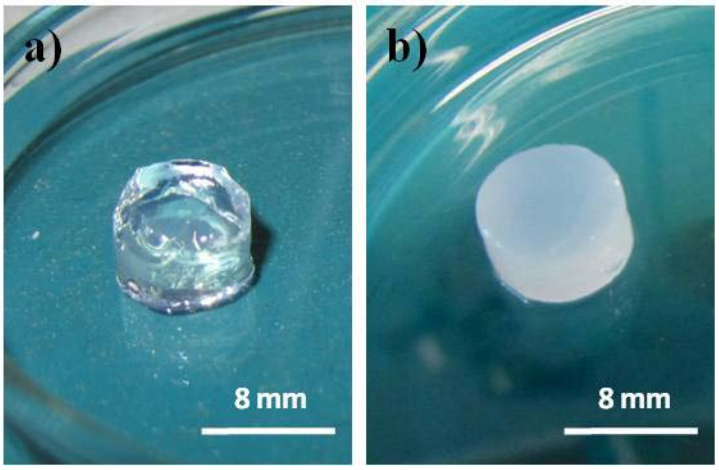

Figure 3.18. *Representative photograph of chitosan/agarose-1.5, a) before the experiment and b) 24 h latter at pH 5.2.*

v. Viscoelastic properties of composite chitosan/agarose macrogels.

The variation in the elastic modulus of the composite chitosan/agarose macrogels as a function of temperature is shown in Figure 3.19. No variation in the elastic modulus G'_e was observed below the melting temperature of the gel, T_m. Above T_m, the value of G'_e dramatically decreased and ultimately reached the second plateau at ~70 ^oC, above which the agarose network completely melted down. The value of T_m increased with agarose concentration from 57±1 ^oC (chitosan/agarose-1) to 62±1 ^oC (chitosan/agarose-2). The elastic modulus of the composite gels increased with agarose concentration, reaching the value of 1 kPa at 20 ^oC for chitosan/agarose-2. In addition, composite gels had a higher elastic modulus than agarose gels (G' = 824 ±10 Pa for the sample chitosan/agarose-1.5 and G´ = 540±44 Pa for agarose-1.5).

The dependence of the elastic modulus on agarose concentration in the chitosan/agarose macrogels was analyzed using the scaling approach [67]. For that, it was employed the equation 3.2. Individual agarose chains are intrinsically rigid and, on cooling, they form bundles (nanofibrils), which assemble in a gel [68]. Jones and Marques theory [69] relates the exponent *n* to the longitudinal fractal dimensions of the fibrils as [70]

$$G' \sim C^{(3\upsilon+1)/(3\upsilon-1)} \qquad \text{Equation 3.4}$$

where the constant υ is the inverse of the fractal dimension.

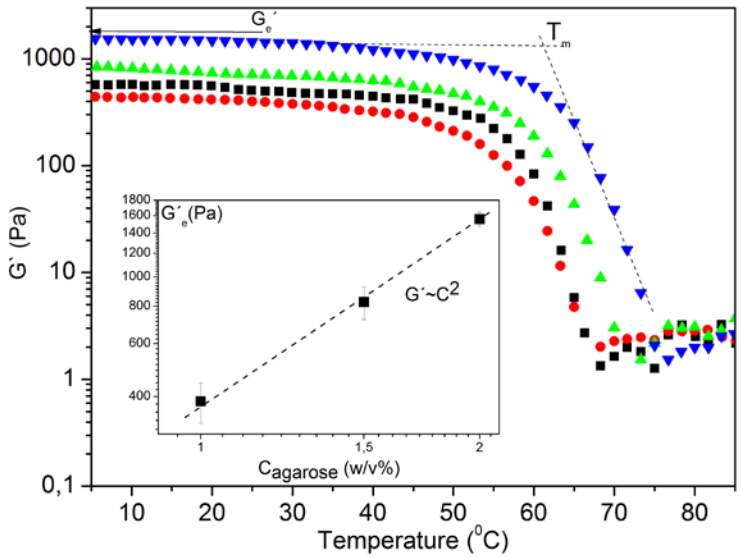

Figure 3.19. *Variation in elastic modulus, G`, plotted as a function of temperature, for agarose-1.5 (■), chitosan/agarose-1 (●), chitosan/agarose-1.5 (▲) macrogel and chitosan/agarose-2 (▼) macrogels. Dashed lines show the determination of the melting point, T_m, of the gel. Insert shows the variation in G' as a function of agarose concentration. The black dashed line corresponds to the linear fit of the data.*

The double logarithmic dependence of G'_e *vs.* agarose concentration for the composite gels is shown in the inset of Figure 3.19. The elastic modulus of the composite gel increased with agarose concentration, in agreement with the reported changes for agarose gel[17, 71]. The linear fitting of the data plotted in the inset of Figure 3.19 yielded a slope of ~2. A relation of $G' \sim C^2$ and the fractal dimension $1/\upsilon \sim 1$ obtained for the chitosan/agarose macrogels indicated that agarose gels with embedded chitosan chains were composed of rigid nanofibrils identical to those in pure agarose gels. [70, 72] This result was in agreement with the earlier measurements of the elastic modulus of agarose gels, which gave a power law dependence of G' corresponding to a longitudinal fractal dimension $1/\upsilon \approx 1.1$ [73, 74]. From these results, it is possible to infer a close similarity between the structural organization of agarose fibrils in the chitosan-free and chitosan/agarose macrogels.

The increase in the elastic modulus of the composite chitosan/agarose gels with respect to agarose gels could be caused by the hydrogen bonding between the chitosan

chains and the agarose network, as it was reported for agarose mixed with collagen [75, 76], κ-carrageenan, [77] or xylans [78].

3.3.3 Composite chitosan/agarose macrogels loaded with ferrofluid.

i. Preparation of composite chitosan/agarose macrogels loaded with ferrofluid.

In this section, composite chitosan/agarose macrogels were loaded with two concentrations of ferrofluid, 2% and 5% (w/v) and after an extended characterization were evaluated for hyperthermia applications. Figure 3.20, shows photograph corresponding to composite chitosan/agarose-1.5 and their respective ferrofluid loaded macrogels and a schematic representation of the materials obtained. As can be observed the encapsulation of ferrofluid was successful for both concentrations employed.

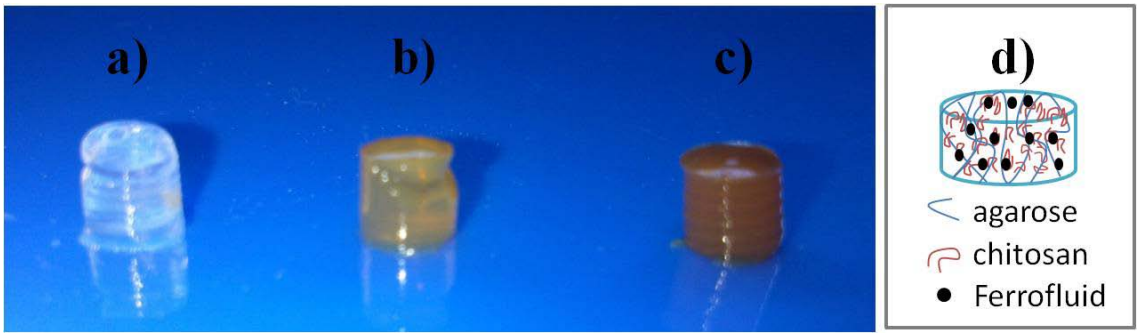

Figure 3.20. *Photographs of a) chitosan/agarose-1.5,b) chitosan/agarose-1.5+Fe2%, c) chitosan/agarose-1.5+Fe5% and d) schematic representation of chitosan/agarose macrogels loaded with ferrofluid.*

ii. Morphological study

Figure 3.21 shows the SEM images corresponding to the surface morphology (a) and cross section (b) of agarose-1.5 and chitosan/agarose-1.5, both loaded with ferrofluid at 2% and 5% (w/v). The SEM photographs of all surfaces presented roughness and their respective cross section corroborated the porous microstructure of all the samples.

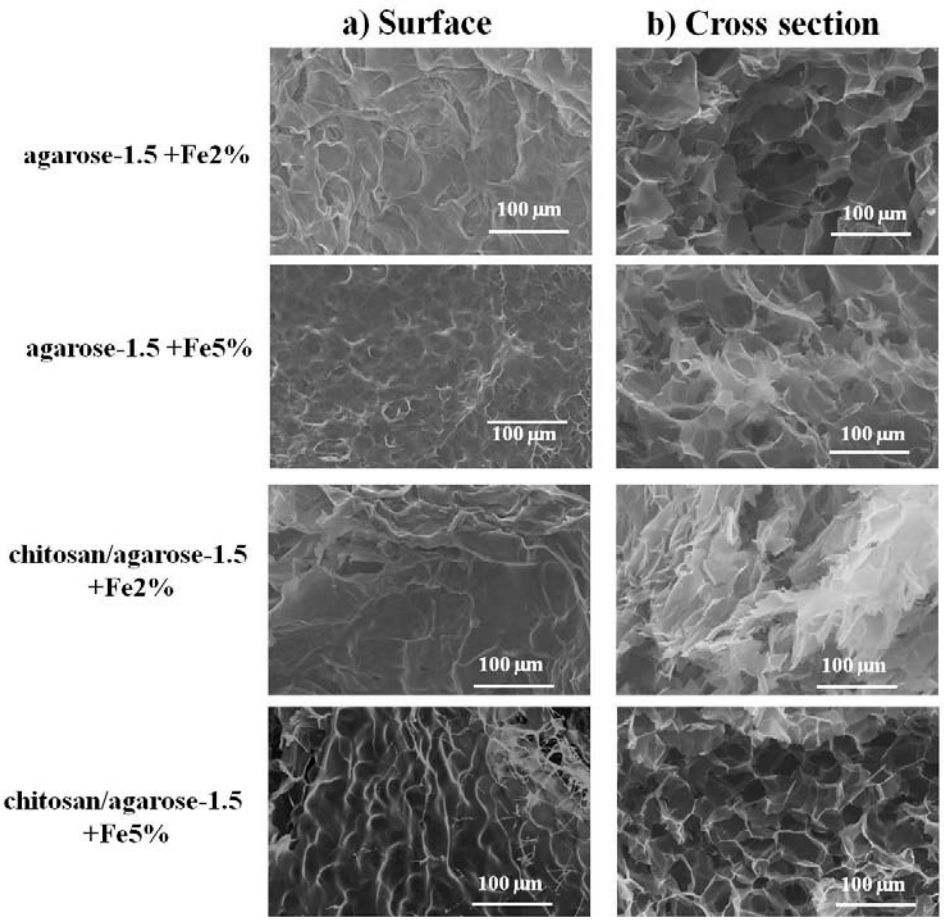

Figure 3.21. *SEM images corresponding to the a) surface and b) cross sections of agarose-1.5and chitosan/agarose-1.5, both loaded with ferrofluid at 2% and 5% (w/v).*

iii. Study of the chemical structure.

Figure 3.22 shows ATR-FTIR spectra of chitosan/agarose-1.5 and chitosan/agarose-1.5+Fe5%. Previously, it was described the spectra of chitosan/agarose-1.5 (Figure 3.16-c) where it was remarked the band of N-H bending vibration at 1568 cm^{-1} and also it was observed the band corresponding to C=O located at 1648 cm^{-1}. In this ATR-FTIR study, it was analyzed the shifts of the main bands of chitosan/agarose-1.5+Fe5% to regard at chitosan/agarose-1.5 without ferrofluid.

Chitosan/agarose-1.5+Fe5% spectrum (Figure 3.22-b) presents the band of N-H bending and C=O at 1557 cm^{-1} and 1635 cm^{-1}. Both bands are shifted a lower frequency with regard to chitosan/agarose-1.5 (Figure 3.22-a) that appears at 1568 cm^{-1} and 1648 cm^{-1}, respectively. These results suggest intermolecular hydrogen bonding between the chitosan and ferrofluid.

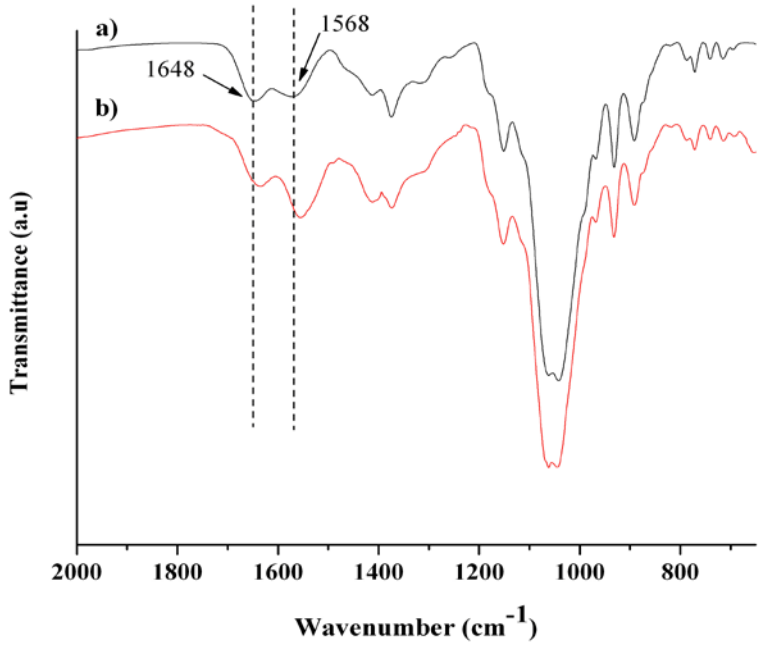

Figure 3.22. *ATR-FTIR spectra of (a) chitosan/agarose-1.5 and b) chitosan/agarose-1.5+Fe5%.*

No changes were observed as a function of ferrofluid content. Chitosan/agarose-1.5+Fe2% presented the same spectra as chitosan/agarose-1.5+Fe5% (results not shown).

iv. Thermal stability by TGA.

Thermal stability of chitosan/agarose-2 macrogels loaded with ferrofluid at 2% and 5% (w/v) was studied through thermogravimetric analysis. The results are shown in Figure 3.23.

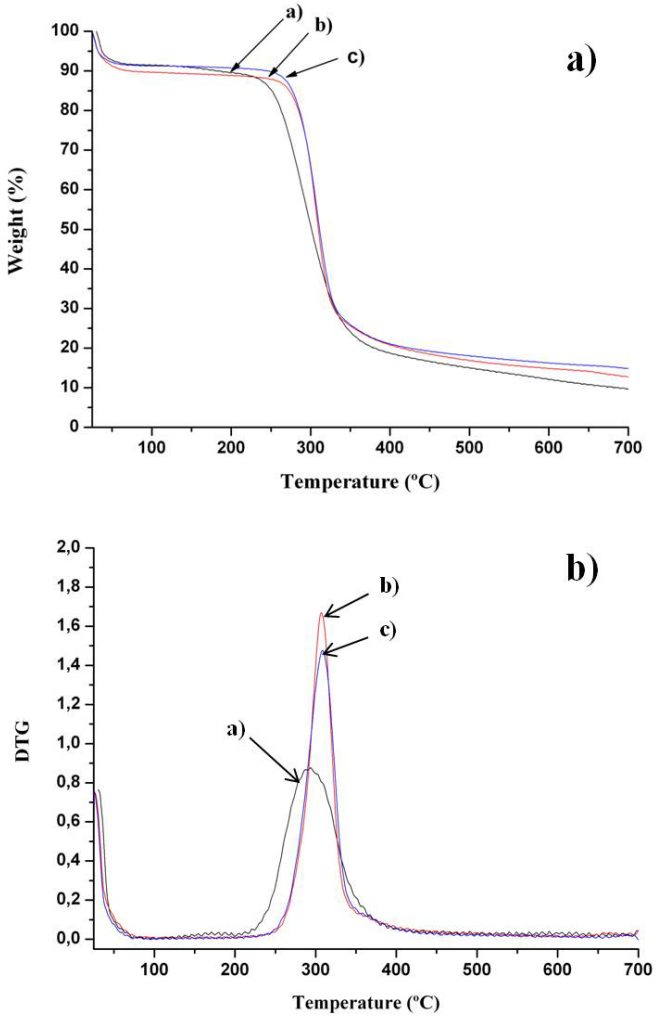

Figure 3.23. *a) Thermal degradation and b) differential thermogravimetric curves of (a) chitosan/agarose-2 and b) chitosan/agarose-2+Fe2% and c) chitosan/agarose-2+Fe5%.*

All samples presented a first weight loss between 25-80 ºC, which is attributed to the evaporation of superficial water, the weight loss (%) for chitosan/agarose-2, chitosan/agarose-2+Fe2% and chitosan/agarose-2+Fe5% were 8%, 10% and 8%, respectively.

Then, the second weight loss stage in the range of 150-500 ºC is due to the decomposition of the organic chains of polymers, chitosan[53] and agarose[22]. According to the derivative of TGA (Figure 3.23-b), the degradation temperature for chitosan/agarose-2, chitosan/agarose-2+Fe2% and chitosan/agarose-2+Fe5% were 294, 307 and 308 ºC, with weight loss 79%, 74% and 75%, respectively. The thermal stability increases with the ferrofluid content. This fact can be attributed to the

establishment of interactions among polymer matrix and the ferrofluid as determined through ATR-FTIR analysis.

The residue obtained for chitosan/agarose-2, chitosan/agarose-2+Fe2% and chitosan/agarose-2+Fe5% at 600 ºC were 12%, 15% and 16%, respectively. Taking into account these values, the residue obtained increases with the encapsulation of the ferrofluid content.

v. Viscoelastic properties of composite chitosan/agarose macrogels loaded with ferrofluid.

Figure 3.24 shows the variation in elastic modulus, G` with the temperature of chitosan/agarose macrogels loaded with ferrofluid at 5% (w/v) for different concentrations of agarose. As can be observing, the elastic modulus increases as a function on agarose content, keeping the same tendency as chitosan/agarose macrogels. With respect to melting temperature (T_m) was determined as shown in Figure 3.24. The T_m of macrogels loaded with ferrofluid is in the range of 48-50 ºC, which increased slightly as a function of agarose content. These T_m values were lower than composite chitosan/agarose macrogels, which can be explained by their low degree of crosslinking and therefore samples melts at lower temperatures.

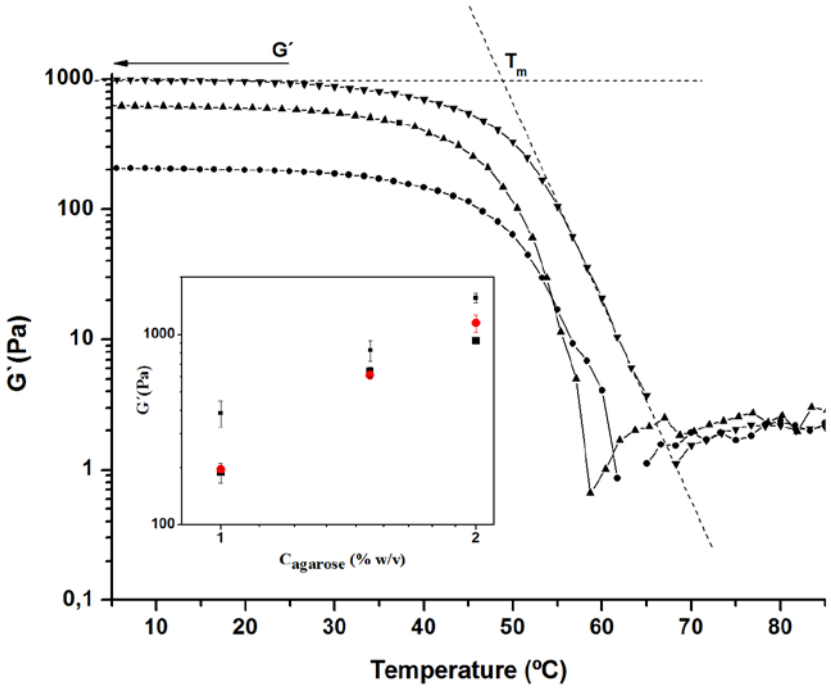

Figure 3.24. *Variation in elastic modulus, G`, plotted as a function of temperature, for chitosan/agarose-1+Fe5% (●), chitosan/agarose-1.5+Fe5% (▲) and chitosan/agarose-2+Fe5% (▼) macrogels. Dashed lines show the determination of the melting temperature, T_m, of the gel. Inset image corresponds to the variation in G' as a function of agarose concentration for macrogels loaded with both concentrations of ferrofluid (2% and 5% w/v).*

Comparing the G` values obtained in this experiment with chitosan/agarose macrogels without ferrofluid, it is observed that elastic modulus G´ were lower than chitosan/agarose macrogels, reaching the value of 1150 Pa at 20 ^{o}C for chitosan/agarose-2+Fe5%. This fact can be related with the new interactions among polymers-ferrofluid, which reduce the interactions of the network components, chitosan and agarose. Therefore, there is a low degree of crosslinking and consequently their mechanical properties diminish. However, ferrofluid loaded chitosan/agarose macrogels had a higher elastic modulus than ferrofluid loaded agarose macrogels, keeping the same tendency as chitosan/agarose macrogels (G' ~600 Pa for the sample chitosan/agarose-1.5+Fe5% and G´ ~300 Pa for agarose-1.5+Fe5%).

The inset image of Figure 3.24 exhibits the variation in G' as a function of agarose concentration for macrogels loaded with two concentrations of ferrofluid (2% and 5% w/v). Taking into account this result, there was not significant contribution of ferrofluid over the viscoelastic properties of chitosan/agarose macrogels loaded with ferrofluid.

3.3.4 Composite chitosan/agarose macrogels as precursors for biomedical applications.

Composite chitosan/agarose macrogels were assessed as precursors for two biomedical applications, hyperthermia applications and drug delivery. The results obtained are describes below.

i. Application in Magnetic Hyperthermia.

Figure 3.25 shows the results obtained for chitosan/agarose-1.5 loaded with two concentrations of ferrofluid (2% and 5% w/v). There was an evident increase of temperature as a function of ferrofluid content. Macrogels loaded with 5% (w/v) of ferrofluid presented a higher temperature change than macrogels loaded with 2% (w/v). Chitosan/agarose-1.5+Fe2% and chitosan/agarose-1.5+Fe5% presented an increase of the temperature (ΔT) of 2.5 and 1.5, respectively at 300 s.

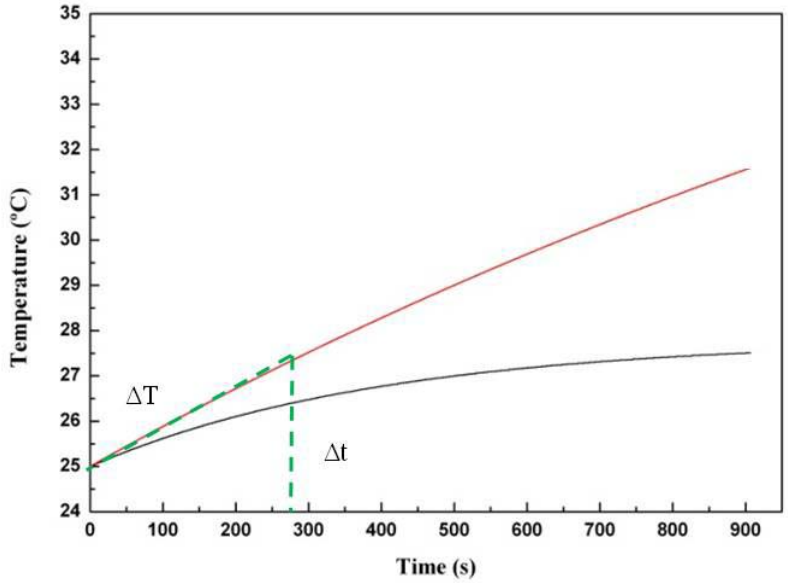

Figure 3.25. *Time dependence of the temperature of chitosan/agarose-1.5 macrogel loaded with ferrofluid at 2% (w/v) (black line) and 5% (w/v) (red line) for at f =580 kHz and 24 kA/m.*

The capacity on heat generation of chitosan/agarose macrogels loaded with ferrofluid when are submitted to an alternating magnetic field were assessed. Specific power absorption (SPA) was determined from the initial slope of the temperature vs time curves (Figure 3.25). The temperature increase (ΔT) of a given mass of ferrofluid diluted in the system during the time interval (Δt) of the experiment. SPA was calculated by the following equation[79]

$$SPA = \frac{P}{m_{NPs}} = \frac{(c_{LIQ}m_{LIQ} + c_{NPs}m_{NPs})}{m_{NPs}} \frac{\Delta T}{\Delta t} \qquad \text{Equation 3.5}$$

where c_{LIQ} and c_{NPs} are the specific heat capacities of the liquid carrier, whereas we can approximate $c_{LIQ}m_{LIQ} + m_{NPs}\, c_{NPs} \sim c_{LIQ}m_{LIQ}$ and write Eq. 3.6 as

$$SPA = \frac{c_{LIQ}m_{LIQ}}{m_{NPs}} \frac{\Delta T}{\Delta t} \qquad \text{Equation 3.6}$$

The SPA values listed in Table 3.3 show the variation of SPA as a function of ferrofluid content, specifically for the two samples under study.

Table 3.3. Specific power absorption of the samples under study.

Samples	ΔT/Δt	SPA (W/g)
chitosan/agarose-1.5+Fe2%	0.007	1.5
chitosan/agarose-1.5+Fe5%	0.009	0.8

ii. Controlled release of 5-FU from composite chitosan/agarose macrogels.

- Preparation of composite chitosan/agarose macrogels loaded with 5-Fluorouracil.

Composite chitosan/agarose-1.5 macrogels and agarose-1.5 loaded with 5-Fluorouracil (5-FU) were prepared as matrixes for drug delivery. The gel formation was successful, even in presence of 5-FU. As can be observed in Figure 3.26, agarose-1.5+5-FU and chitosan/agarose-1.5+5-FU, looks transparent as 5-FU-free composite chitosan/agarose macrogels.

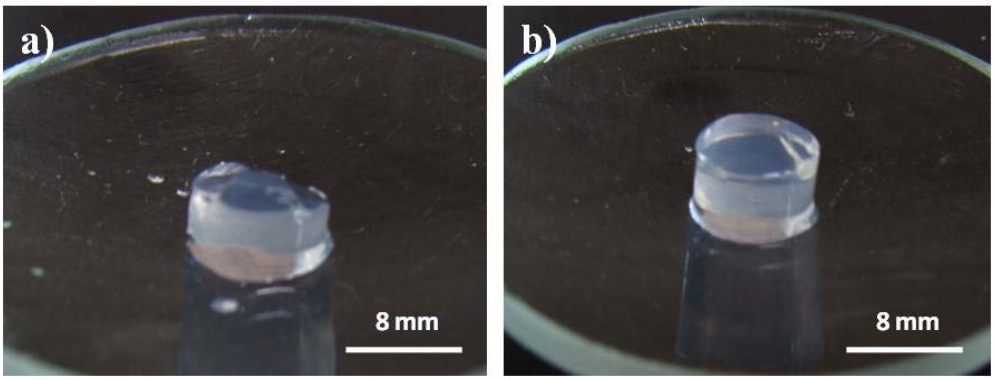

Figure 3.26. *(a) Photographs of a) agarose-1.5+5-FU, b) chitosan/agarose-1.5+5-FU.*

- Study of drug-polymer matrix interactions by ATR-FTIR spectroscopy.

The loading of 5-Fluorouracil in the agarose and chitosan/agarose macrogels was confirmed in ATR-FTIR experiments. The inset image in Figure 3.27 shows, the characteristic absorption bands of 5-Fluorouracil located at 1651 cm^{-1}, corresponding to C=O stretching of the N-acetyl group (amide I band), 1501 cm^{-1} assigned to N-H amide II band, N-H stretching of amide at 1429 cm^{-1}, 1244 cm^{-1} for C-F and 804 cm^{-1} for C-H out of plane deformation.

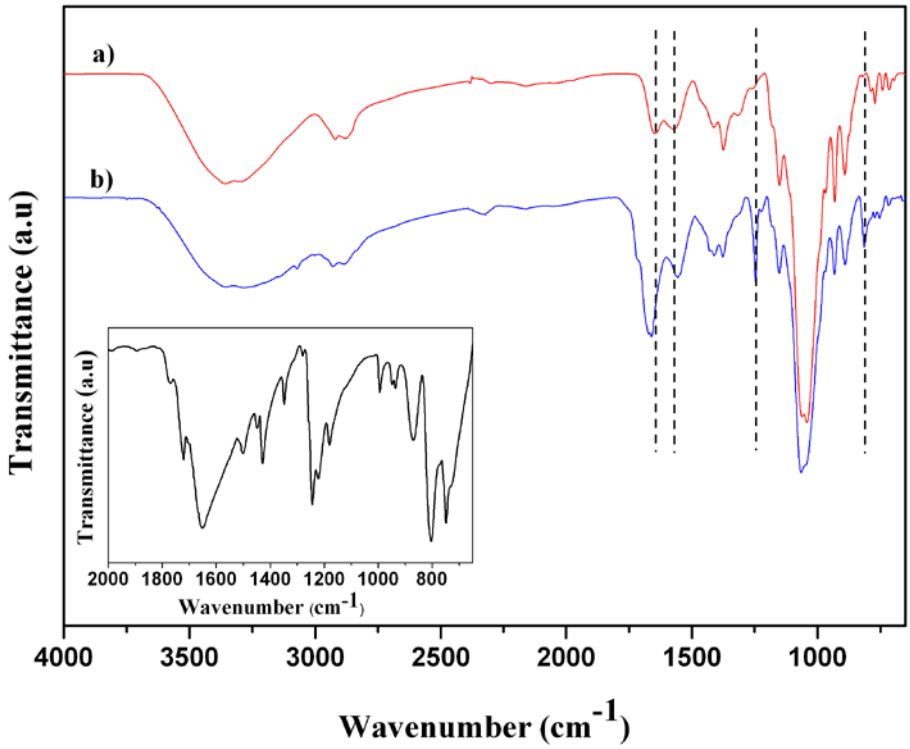

Figure 3.27. *ATR-FTIR spectra of a) chitosan/agarose-1.5 and b) chitosan/agarose-1.5+5-FU. The insert image correspond to the ATR-FTIR spectra of 5-FU.*

After 5-Fluorouracil loading in chitosan/agarose macrogel, the absorption peak located at 1569 cm^{-1} and at 1648 cm^{-1} in the composite gel (Figure 3.27-a) shifted to 1555 cm^{-1} and 1664 cm^{-1}, respectively (Figure 3.27-b), which suggested hydrogen bonding between the polar functional groups in 5-Fluorouracil and NH_2 groups of chitosan. Furthermore, the band located at 804 cm^{-1} and at 1244 cm^{-1} in 5-FU shifted to 814 cm^{-1} and 1248 cm^{-1}, when the drug was encapsulated in the composite chitosan/agarose gel (Figure 3.27-B) [80, 81], which suggested hydrogen bonding between the polar functional groups in 5-Fluorouracil and NH_2 groups of chitosan.

- Drug delivery of 5-FU from composite chitosan macrogels on function of pH.

The drug release was evaluated for chitosan/agarose-1.5 and agarose-1.5 macrogels in buffered solutions at pH 7.4 and 5.2 and at 37º C. For chitosan/agarose-1.5+5-FU (Figure 3.28, full symbols), it can be observed that at pH=7.4, the cumulative

release of 5-Fluorouracil was ~50% within 96 h, whereas at pH=5.2 it was ~33%. In the initial period (~3 h) high release rates of 5-Fluorouracil were measured, due to the localization of the drug at or near the gel surface and a stronger relative mass loss of the gels after a short time interval, as shown in Figure 3.28. After 5 h, the drug release rate did not change with time. At pH of 7.4 and 5.2, part of the 5-Fluorouracil remained trapped in the hydrogel as a result of drug-polymer interactions, as demonstrated by ATR-FTIR spectra.

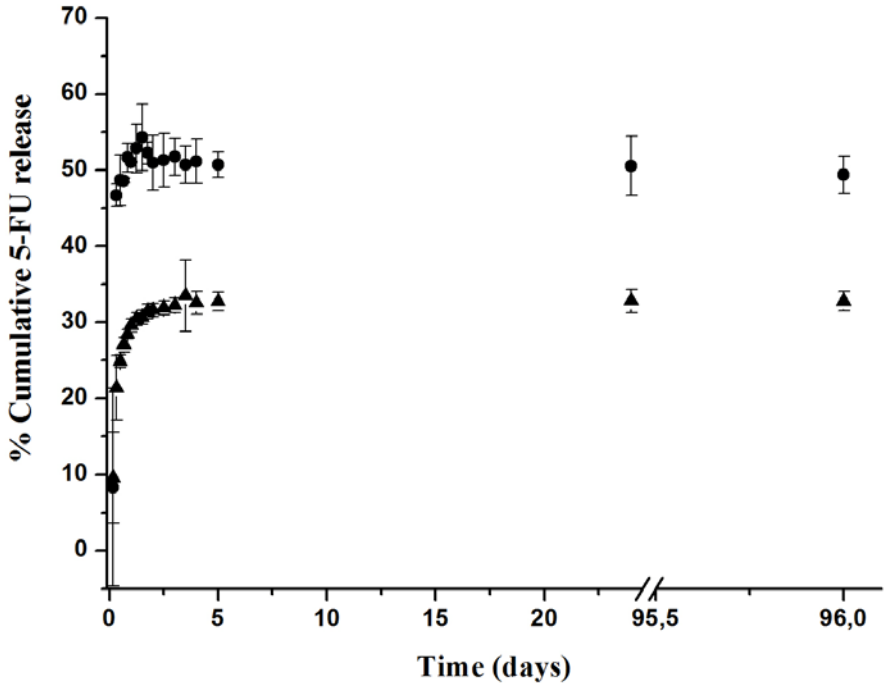

Figure 3.28. *In vitro release of 5-FU from the composite gel chitosan/agarose-1.5 at pH=7.4 (●) and pH=5.2 (▲) at 37 ºC.*

In principle, due to the ionic nature of 5-Fluorouracil, its electrostatic interactions with chitosan in chitosan/agarose composite gels could affect drug release, however the enolic hydroxyl groups of 5-Fluorouracil ionize at pK of 8.1,[82] and at pH values studied, 5-Fluorouracil remained uncharged. The main reason for the difference in release profiles at different pH values could result from the varying solubility of 5-Fluorouracil: in alkaline media the solubility of 5-Fluorouracil is higher than that in acidic conditions [83]. According to the release profiles shown in Figure 3.28, chitosan/agarose1.5+5-FU gels allow a fast drug delivery of 5-FU in short time period, which is appropriate because 5-FU has a half-life of 10-20 min. On the other hand, for a

local application (cream or subcutaneous injection), chitosan/agarose gels would allow controlled 5-FU delivery in a single dose thus avoiding cycles of treatment and consequently side effects. Therefore, chitosan/agarose gels assure that 5-FU will be released along time under the conditions employed in this work.

3.4. CONCLUSIONS

After the preparation by two different methods and characterization of chitosan macrogels, the following conclusions can be drawn.

Chitosan ferrogels can be prepared by simultaneous coprecipitation of iron ions in alkali media and chitosan gelation. As a first step, chitosan amine groups interact with iron ions and this step depends neither on the iron ions nor on the chitosan concentration. As a second step the simultaneous coprecipitation and chitosan gelation in alkali media is achieved. The iron oxide crystalline phase was seen to depend on the chitosan concentration. For the highest chitosan concentration (3% w/v), the formation of non magnetic iron hydroxides avoids the reinforcement of the chitosan hydrogel. The slow diffusion of OH-species through the polymer matrix was proposed as possible explanation for this behavior. For the lowest chitosan concentration (2% w/v), magnetite nanoparticles are formed that reinforces the chitosan hydrogels as viewed by the increase of the viscoelastic modulus. Nevertheless, this reinforcement effect is counterbalanced by the disruption of hydrogen bonding as a consequence of the coordination of iron ions with chitosan amine groups.

A second method of preparation consisted of composite chitosan/agarose macrogels, which have presented good transparency and mechanical stability. Chitosan/agarose macrogels had a higher elastic modulus than agarose macrogels due to the reinforcement of the composite chitosan/agarose gels, in comparison with agarose gels. The introduction of chitosan in agarose gels reduced mass loss of the chitosan/agarose gels, in comparison with agarose gels, at 37 ºC and pH=7.2. The increase in the stability of the chitosan/agarose gels was more evident at pH=5.2. This result has an important implication for the utilization of these gels as drug delivery matrixes in areas where the pH is lower than the pH of the blood plasma (7.4) such as

the acidic stomach or tumoral tissues. Composite chitosan/agarose gels loaded with ferrofluid, presented a higher thermal stability, however, their mechanical properties decreased in presence of ferrofluid. Ferrofluid loaded chitosan/agarose gels, can be considered as agent for hyperthermia applications due to their response to an alternating magnetic field. The release of 5-Fluorouracil from chitosan/agarose macrogels at pH 7.4 and 5.2 under physiological temperature demonstrated the feasibility of these hydrogels for drug delivery applications. Therefore composite chitosan/agarose gels can be useful for biomedical applications as cancer treatment.

3. 5 REFERENCES

[1] Buwalda SJ, Boere KWM, Dijkstra PJ, Feijen J, Vermonden T, Hennink WE. Hydrogels in a historical perspective: From simple networks to smart materials. Journal of Controlled Release. 2014;190:254-73.

[2] Bhattarai N, Gunn J, Zhang M. Chitosan-based hydrogels for controlled, localized drug delivery. Advanced Drug Delivery Reviews.62:83-99.

[3] Majedi FS, Hasani-Sadrabadi MM, Emami SH, Taghipoor M, Dashtimoghadam E, Bertsch A, et al. Microfluidic synthesis of chitosan-based nanoparticles for fuel cell applications. Chemical Communications. 2012;48:7744-6.

[4] Dang JM, Leong KW. Natural polymers for gene delivery and tissue engineering. Advanced Drug Delivery Reviews. 2006;58:487-99.

[5] Muzzarelli RAA, Boudrant J, Meyer D, Manno N, DeMarchis M, Paoletti MG. Current views on fungal chitin/chitosan, human chitinases, food preservation, glucans, pectins and inulin: A tribute to Henri Braconnot, precursor of the carbohydrate polymers science, on the chitin bicentennial. Carbohydrate Polymers. 2012;87:995-1012.

[6] Muzzarelli RAA, Muzzarelli C. Chitosan Chemistry: Relevance to the Biomedical Sciences. In: Heinze T, editor. Polysaccharides I: Springer Berlin Heidelberg; 2005. p. 151-209.

[7] Dash M, Chiellini F, Ottenbrite RM, Chiellini E. Chitosan—A versatile semi-synthetic polymer in biomedical applications. Progress in Polymer Science. 2011;36:981-1014.

[8] Park JH, Saravanakumar G, Kim K, Kwon IC. Targeted delivery of low molecular drugs using chitosan and its derivatives. Advanced Drug Delivery Reviews. 2010;62:28-41.

[9] Puga AM, Lima AC, Mano JF, Concheiro A, Alvarez-Lorenzo C. Pectin-coated chitosan microgels crosslinked on superhydrophobic surfaces for 5-fluorouracil encapsulation. Carbohydrate Polymers. 2013;98:331-40.

[10] Zhang H, Mardyani S, Chan WCW, Kumacheva E. Design of Biocompatible Chitosan Microgels for Targeted pH-Mediated Intracellular Release of Cancer Therapeutics. Biomacromolecules. 2006;7:1568-72.

[11] Wei L, Cai C, Lin J, Wang L, Zhang X. Degradation controllable biomaterials constructed from lysozyme-loaded Ca-alginate microparticle/chitosan composites. Polymer. 2011;52:5139-48.

[12] Dobashi T, Tomita N, Maki Y, Chang CP, Yamamoto T. An analysis of anisotropic gel forming process of chitosan. Carbohydrate Polymers.In Press, Corrected Proof.

[13] Berger J, Reist M, Mayer JM, Felt O, Peppas NA, Gurny R. Structure and interactions in covalently and ionically crosslinked chitosan hydrogels for biomedical applications. European Journal of Pharmaceutics and Biopharmaceutics. 2004;57:19-34.

[14] Wang L, Stegemann JP. Thermogelling chitosan and collagen composite hydrogels initiated with [beta]-glycerophosphate for bone tissue engineering. Biomaterials.31:3976-85.

[15] Farshi Azhar F, Olad A, Salehi R. Fabrication and characterization of chitosan–gelatin/nanohydroxyapatite–polyaniline composite with potential application in tissue engineering scaffolds. Designed Monomers and Polymers. 2014;17:654-67.

[16] Miguel SP, Ribeiro MP, Brancal H, Coutinho P, Correia IJ. Thermoresponsive chitosan–agarose hydrogel for skin regeneration. Carbohydrate Polymers. 2014;111:366-73.

[17] Guenet JM. Thermoreversible Gelation of Polymers and Biopolymers. London: Academic Press; 1992.

[18] Ramzi M, Rochas C, Guenet JM. Structure-properties relation for agarose thermoreversible gels in binary solvents. Macromolecules. 1998;31:6106-11.

[19] Fernández E, López D, Mijangos C, Duskova-Smrckova M, Ilavsky M, Dusek K. Rheological and thermal properties of agarose aqueous solutions and hydrogels. Journal of Polymer Science Part B: Polymer Physics. 2008;46:322-8.

[20] Kong H, Dumitriu S. Polysaccharide-based hydrogels in tissue engineering Polysaccharides : Structural Diversity and Functional Versatility2004.

[21] Lin P-W, Wu C-C, Chen C-H, Ho H-O, Chen Y-C, Sheu M-T. Characterization of cortical neuron outgrowth in two- and three-dimensional culture systems. Journal of Biomedical Materials Research Part B: Applied Biomaterials. 2005;75B:146-57.

[22] Zhang LM, Wu CX, Huang JY, Peng XH, Chen P, Tang SQ. Synthesis and characterization of a degradable composite agarose/HA hydrogel. Carbohydrate Polymers. 2012;88:1445-52.

[23] Luo Y, Shoichet MS. A photolabile hydrogel for guided three-dimensional cell growth and migration. Nature Materials. 2004;3:249-53.

[24] Tripathi A, Kathuria N, Kumar A. Elastic and macroporous agarose–gelatin cryogels with isotropic and anisotropic porosity for tissue engineering. Journal of Biomedical Materials Research Part A. 2009;90A:680-94.

[25] Imani R, Emami SH, Moshtagh PR, Baheiraei N, Sharifi AM. Preparation and characterization of agarose-gelatin blend hydrogels as a cell encapsulation matrix: An in-vitro study. Journal of Macromolecular Science, Part B: Physics. 2012;51:1606-16.

[26] Cao Z, Gilbert RJ, He W. Simple Agarose–Chitosan Gel Composite System for Enhanced Neuronal Growth in Three Dimensions. Biomacromolecules. 2009;10:2954-9.

[27] Gómez-Mascaraque LG, Méndez JA, Fernández-Gutiérrez M, Vázquez B, San Román J. Oxidized dextrins as alternative crosslinking agents for polysaccharides: Application to hydrogels of agarose–chitosan. Acta Biomaterialia. 2014;10:798-811.

[28] Guibal E. Heterogeneous catalysis on chitosan-based materials: a review. Progress in Polymer Science. 2005;30:71-109.

[29] Ng JCY, Cheung WH, McKay G. Equilibrium Studies of the Sorption of Cu(II) Ions onto Chitosan. Journal of Colloid and Interface Science. 2002;255:64-74.

[30] Varma AJ, Deshpande SV, Kennedy JF. Metal complexation by chitosan and its derivatives: a review. Carbohydrate Polymers. 2004;55:77-93.

[31] Nieto JM, Peniche-Covas C, Del Bosque J. Preparation and characterization of a chitosan-Fe(III) complex. Carbohydrate Polymers. 1992;18:221-4.

[32] Hernandez R, Sacristan J, Nogales A, Fernandez M, Ezquerra TA, Mijangos C. Structure and viscoelastic properties of hybrid ferrogels with iron oxide nanoparticles synthesized in situ. Soft Matter. 2010;6:3910-7.

[33] Li Y, Huang G, Zhang X, Li B, Chen Y, Lu T, et al. Magnetic Hydrogels and Their Potential Biomedical Applications. Advanced Functional Materials. 2013;23:660-72.

[34] Tomoiaga AM, Cioroiu BI, Nica V, Vasile A. Investigations on nanoconfinement of low-molecular antineoplastic agents into biocompatible magnetic matrices for drug targeting. Colloids and Surfaces B: Biointerfaces. 2013;111:52-9.

[35] Hu Z, Li S, Yang L. Preparation of berbamine loaded chitosan-agarose microspheres and in vitro release study. Polímeros. 2012;22:422-6.

[36] Chatterjee S, Chatterjee S, Chatterjee BP, Das AR, Guha AK. Adsorption of a model anionic dye, eosin Y, from aqueous solution by chitosan hydrobeads. Journal of Colloid and Interface Science. 2005;288:30-5.

[37] Montembault A, Viton C, Domard A. Rheometric Study of the Gelation of Chitosan in Aqueous Solution without Cross-Linking Agent. Biomacromolecules. 2005;6:653-62.

[38] Cairns P, Miles MJ, Morris VJ, Ridout MJ, Brownsey GJ, Winter WT. X-ray fibre diffraction studies of chitosan and chitosan gels. Carbohydrate Research. 1992;235:23-8.

[39] Montembault A, Viton C, Domard A. Physico-chemical studies of the gelation of chitosan in a hydroalcoholic medium. Biomaterials. 2005;26:933-43.

[40] Bhatia SC, Ravi N. A Magnetic Study of an Fe−Chitosan Complex and Its Relevance to Other Biomolecules. Biomacromolecules. 2000;1:413-7.

[41] Bhatia SC, Ravi N. A Mössbauer Study of the Interaction of Chitosan and d-Glucosamine with Iron and Its Relevance to Other Metalloenzymes. Biomacromolecules. 2003;4:723-7.

[42] Cendoya I, López D, Alegría A, Mijangos C. Dynamic mechanical and dielectrical properties of poly(vinyl alcohol) and poly(vinyl alcohol)-based nanocomposites. Journal of Polymer Science Part B: Polymer Physics. 2001;39:1968-75.

[43] Hernández R, Mijangos C. In situ Synthesis of Magnetic Iron Oxide Nanoparticles in Thermally Responsive Alginate-Poly(<I>N</I>-isopropylacrylamide) Semi-Interpenetrating Polymer Networks. Macromolecular Rapid Communications. 2009;30:176-81.

[44] Montes Atenas G, Mielczarski E, Mielczarski JA. Composition and structure of iron oxidation surface layers produced in weak acidic solutions. Journal of Colloid and Interface Science. 2005;289:157-70.

[45] Horák D, Babiccaron M, Macková H, Benescaron MJ. Preparation and properties of magnetic nano- and microsized particles for biological and environmental separations. Journal of Separation Science. 2007;30:1751-72.

[46] Pattanayak J, Rao VS, Maiti HS. The hydrolysis product of ferric nitrate in sodium hydroxide. Journal of Materials Science. 1990;25:2245-8.

[47] Lawrie G, Keen I, Drew B, Chandler-Temple A, Rintoul L, Fredericks P, et al. Interactions between Alginate and Chitosan Biopolymers Characterized Using FTIR and XPS. Biomacromolecules. 2007;8:2533-41.

[48] Chang Y-C, Chen D-H. Adsorption Kinetics and Thermodynamics of Acid Dyes on a Carboxymethylated Chitosan-Conjugated Magnetic Nano-Adsorbent. Macromolecular Bioscience. 2005;5:254-61.

[49] Bhattarai SR, Bahadur K.C R, Aryal S, Khil MS, Kim HY. N-Acylated chitosan stabilized iron oxide nanoparticles as a novel nano-matrix and ceramic modification. Carbohydrate Polymers. 2007;69:467-77.

[50] Hernández RB, Yola OR, Mercê ALR. Chemical equilibrium in the complexation of first transition series divalent cations Cu2+, Mn2+ and Zn2+ with chitosan. Journal of the Brazilian Chemical Society. 2007;18:1388-96.

[51] F. G. Pearson, Marchessault RH, Liang CY. Infrared spectra of crystalline polysaccharides. V. Chitin. Journal of Polymer Science. 1960;43:101-16.

[52] Webster A, Halling MD, Grant DM. Metal complexation of chitosan and its glutaraldehyde cross-linked derivative. Carbohydrate Research. 2007;342:1189-201.

[53] Peniche-Covas C, Argüelles-Monal W, San Román J. A kinetic study of the thermal degradation of chitosan and a mercaptan derivative of chitosan. Polymer Degradation and Stability. 1993;39:21-8.

[54] Goiti E, Salinas MM, Arias G, Puglia D, Kenny JM, Mijangos C. Effect of magnetic nanoparticles on the thermal properties of some hydrogels. Polymer Degradation and Stability. 2007;92:2198-205.

[55] Sahiner N. In situ metal particle preparation in cross-linked poly(2-acrylamido-2-methyl-1-propansulfonic acid) hydrogel networks. Colloid & Polymer Science. 2006;285:283-92.

[56] Peniche H, Osorio A, Acosta N, Campa A, Peniche C. Preparation and characterization of superparamagnetic chitosan microspheres: Application as a support for the immobilization of tyrosinase. Journal of Applied Polymer Science. 2005;98:651-7.

[57] Wang Y, Li B, Zhou Y, Jia D. Chitosan-induced synthesis of magnetite nanoparticles via iron ions assembly. Polymers for Advanced Technologies. 2008;19:1256-61.

[58] Nishinari K. Rheological and DSC study of sol–gel transition in aqueous dispersions of industrially important polymers and colloids. Colloid & Polymer Science. 1997;275:1093-107.

[59] Fernández E, López D, López-Cabarcos E, Mijangos C. Viscoelastic and swelling properties of glucose oxidase loaded polyacrylamide hydrogels and the evaluation of their properties as glucose sensors. Polymer. 2005;46:2211-7.

[60] Chenite A, Buschmann M, Wang D, Chaput C, Kandani N. Rheological characterisation of thermogelling chitosan/glycerol-phosphate solutions. Carbohydrate Polymers. 2001;46:39-47.

[61] Chenite A, Gori S, Shive M, Desrosiers E, Buschmann MD. Monolithic gelation of chitosan solutions via enzymatic hydrolysis of urea. Carbohydrate Polymers. 2006;64:419-24.

[62] Gennes PG. Scaling concepts in polymer physics. New York: Cornell University Press; 1979.

[63] Lopez D, Mijangos C, Munoz ME, Santamaria A. Viscoelastic Properties of Thermoreversible Gels from Chemically Modified PVCs&#x2020. Macromolecules. 1996;29:7108-15.

[64] Hernández R, Sarafian A, López D, Mijangos C. Viscoelastic properties of poly(vinyl alcohol) hydrogels and ferrogels obtained through freezing-thawing cycles. Polymer. 2004;45:5543-9.

[65] Zamora-Mora V, Fernández-Gutiérrez M, Román JS, Goya G, Hernández R, Mijangos C. Magnetic core–shell chitosan nanoparticles: Rheological characterization and hyperthermia application. Carbohydrate Polymers. 2014;102:691-8.

[66] Kim B, Lee E, Kim Y, Park S, Khang G, Lee D. Dual Acid-Responsive Micelle-Forming Anticancer Polymers as New Anticancer Therapeutics. Advanced Functional Materials. 2013;23:5091-7.

[67] de Gennes PG. Scaling concepts in polymer physics. London1979.

[68] Guenet JM, Rochas C. Agarose sols and gels revisited. Macromolecular Symposia. 2006;242:65-70.

[69] Jones JL, Marques CM. Rigid polymer network models. Journal de Physique. 1990;51.

[70] Guenet JM. Polymer-solvent molecular compounds: Elsevier; 2008.

[71] te Nijenhuis K. Agarose. Thermoreversible Networks: Springer Berlin Heidelberg; 1997. p. 194-202.

[72] Fernández E, Hernández R, Teresa Cuberes M, Mijangos C, López D. New hydrogels from interpenetrated physical gels of agarose and chemical gels of polyacrylamide: Effect of relative concentration and crosslinking degree on the viscoelastic and thermal properties. Journal of Polymer Science Part B: Polymer Physics. 2010;48:2403-12.

[73] Rochas C, Brulet A, Guenet J-M. Thermally reversible Gelation of Agarose in Water/Dimethyl Sulfoxide Mixtures. Macromolecules. 1994;27:3830-5.

[74] Ramzi M, Rochas C, Guenet J-M. Structure−Properties Relation for Agarose Thermoreversible Gels in Binary Solvents. Macromolecules. 1998;31:6106-11.

[75] Ulrich TA, Jain A, Tanner K, MacKay JL, Kumar S. Probing cellular mechanobiology in three-dimensional culture with collagen–agarose matrices. Biomaterials. 2010;31:1875-84.

[76] Lake SP, Hald ES, Barocas VH. Collagen-agarose co-gels as a model for collagen–matrix interaction in soft tissues subjected to indentation. Journal of Biomedical Materials Research Part A. 2011;99A:507-15.

[77] Amici E, Clark AH, Normand V, Johnson NB. Interpenetrating Network Formation in Agarose−κ-Carrageenan Gel Composites. Biomacromolecules. 2002;3:466-74.

[78] Meena R, Lehnen R, Schmitt U, Saake B. Physicochemical and rheological properties of agarose/xylans composite hydrogel materials. Polymer Composites. 2013;34:978-88.

[79] Lima Jr E, Torres TE, Rossi LM, Rechenberg HR, Berquo TS, Ibarra A, et al. Size dependence of the magnetic relaxation and specific power absorption in iron oxide nanoparticles. Journal of Nanoparticle Research. 2013;15:1-11.

[80] Ganguly K, Aminabhavi TM, Kulkarni AR. Colon Targeting of 5-Fluorouracil Using Polyethylene Glycol Cross-linked Chitosan Microspheres Enteric Coated with

Cellulose Acetate Phthalate. Industrial & Engineering Chemistry Research. 2011;50:11797-807.

[81] Zhu L, Ma J, Jia N, Zhao Y, Shen H. Chitosan-coated magnetic nanoparticles as carriers of 5-Fluorouracil: Preparation, characterization and cytotoxicity studies. Colloids and Surfaces B: Biointerfaces. 2009;68:1-6.

[82] Ojugo ASE, McSheehy PMJ, Stubbs M, Alder G, Bashford CL, Maxwell RJ, et al. Influence of pH on the uptake of 5-fluorouracil into isolated tumour cells. British Journal of Cancer. 1998;77:873-9.

[83] Rao KSVK, Chung I, Reddy KM, Ha C-S. PMMA-based microgels for controlled release of an anticancer drug. Journal of Applied Polymer Science. 2009;111:845-53.

Chapter 4

CHITOSAN MICROGELS THROUGH MICROFLUIDICS

This chapter describes the preparation and characterization of chitosan microgels through microfluidics. It includes the design and fabrication of two types of microfluidics droplets generator, T-junction and flow-focusing. It also describes the microfluidics emulsification and generation of three kinds of droplets: chitosan, composite chitosan/agarose and ferrofluid loaded chitosan/agarose, by means of different crosslinking processes.

4.1 INTRODUCTION

It is currently well-established that continuous microfluidic (MF) synthesis and assembly of polymer particles offers a facile approach to the generation of microgels with dimensions in the range of tens to hundreds of micrometres[1]. The distinct features of these particles include their very narrow polydispersity and controllable size, compositions and morphologies.[1-7] Microfluidic preparation of microgels have been explored for a broad spectrum of biopolymers, including alginate[8], gelatin[9], chitosan [10-13], agarose,[14-18] and κ-carrageenan and carboxymethylcellulose[19]. Nowadays, research in this field is developing toward well-defined applications of microgel particles prepared by the MF means, which is sometimes challenging when a microgel is formed from a single polymer. Microparticles preparation from single based precursor, usually presents several drawbacks, as for example: systems require potentially cytotoxic crosslinkers or photo-initiators and generally have poor mechanical properties[13]. Taking into account these drawbacks, this kind of microparticles could be discarded for biomedical applications.

Combining several polymers in microgel particles enables the realization of synergetic properties among the two or more polymers[20]. Concerning composite chitosan, although, they could be interesting for many applications, until the present few works has been carried out in the literature. For instance, monodispersed microgels from a triple interpenetrating network (3XN) based on partially oxidized dextran (Odex), Teleostean, and N-carboxyethyl chitosan (CEC) had been prepared by MF[13]. Moreover, blending of chitosan with agarose, a neutral polysaccharide that forms hydrogel at low temperatures, allows chitosan to retain its response to pH and, at the

same time, it allows to get termoreversible materials as a consequence of the response to temperature of the agarose gels[21]. For thus, chitosan and agarose has attracted keen interest for its dual (pH and temperature) response properties attributed to each of the constituent polymers. Although, in the literature have been reported different methods of preparation as a suspension crosslinking method[22] and water-in-oil emulsion technique[23], but this system has never been prepared by microfluidics.

The general objective of this work is to investigate the viability of microfluidics technique to prepare monodispersed chitosan microgels and composite chitosan/agarose microgels. It includes the selection, design and preparation of microfluidics devices and the generation of different types of chitosan microgels. In order to achieve the objectives, different factor were evaluated: crosslinking reactions of chitosan (off and on chip), different geometries and some parameters such as concentrations and flow rates.

Three kinds of chitosan microgels by MF emulsification have been explorer: rough chitosan microgels, composite chitosan/agarose microgels and ferrofluid chitosan/agarose microgels. Then, it is studying the subsequent gelation of the precursor droplets, in order to obtain particles of controlled size and with narrow polydispersity. Three composite chitosan/agarose microgels were prepared varying the agarose concentrations, which were selected based on the good properties of composite macrogels observed in the chapter 3.

4.2 EXPERIMENTAL PART

4.2.1 Materials

Chitosan, ultra-low gelling temperature agarose and ferrofluid employed in this work were the same described in chapter 3. Non-ionic surfactant Span-80, acetic acid, sodium tripolyphosphate, phosphate buffered saline (PBS), pH 7.4, hexane and mineral oil (viscosity 30 cPs) were supplied by Aldrich-Sigma (Canada) and used as received.

Photoresist resin (SU-8 50, 3050) was purchased from Microchem Co. (MA, USA). Sylgard 184 Silicon Elastomer kit was received from Dow Corning Corp. (Midland, MI) and was mixed with the curing agent containing a crosslinker (dimethyl-methylhydrogen siloxane, Aldrich) and an inhibitor (tetramethyltetravinyl cyclotetrasiloxane, Aldrich) at 10:1 (w/w) ratio. The poly(dimethylsiloxane) (PDMS) elastomer was prepared from Sylgard® 184 (Dow Corning Cop., USA). The deionized water was obtained from the Millipore Milli-Q water purification system.

4.2.2 Fabrication of microfluidics devices.

Microfluidic devices were fabricated trough soft lithography. For soft lithography, moulds are fabricated through photolithography which is a well-established and widely used process for patterning structures out of a photoresist on a substrate (typically a silicon wafer). All the devices were prepared in Department of Chemistry, University of Toronto, Canada, in collaboration with Kumacheva's Group. To achieve the different devices, the following methodology and steps were performed.

i. Mask design

Masks (or photomasks) of microfluidic channels of microdevice were previously designed using AutoCad 2007® (Autodesk Inc., USA) software. Different designs were printed on high-resolution transparencies (Pacific Arts and Designs Inc., Markham, Canada) using ultra-high resolution printers with a resolution of 20,000 dpi. In this work different types of mask have been designed and will be reports in the next section 4.2.3.

ii. Microfabrication of Negative Masters: Silicon Masters

Silicon (Si) negative masters, who serve as a mold for PDMS to be performed in the next step[24], were prepared in a level 6 cleanroom facility (Bahen Center) at the University of Toronto. Si subtract masters consist of a positive bas-relief of photoresist on a silicon wafer.

Fabrication of the negative masters with microchannel features was carried out with SU-8 photoresist (SU-8 50) deposited on 10 cm diameter silicon (Si) wafer[25]. Previously, the Si wafers were washed several times with acetone and methanol. The surface of the substrate was dried by blowing dry N_2 gas. Then, spin coating with SU-8 photoresist at a typical spin rate of 2000 rpm on the Si wafer, enabled the formation of 50 μm height features. After the spin-coating process, the photoresist layer was thermally baked to evaporate the solvent, γ-butyrolactone. Silicon wafers required only a single spin-coated layer of the photoresist prior to the generation of the microchannel patterns.

In the next step, the photomask was placed overtop the photoresist layer/ Si wafers, and the system was exposed to UV-light (Karl Suss MA6 mask aligner, λ=365~405 nm) (Figure 4.1) to cure the photoresist and create the patterned microchannels (Figure 4.2, step I). A typical exposure time was approximately 30 sec.

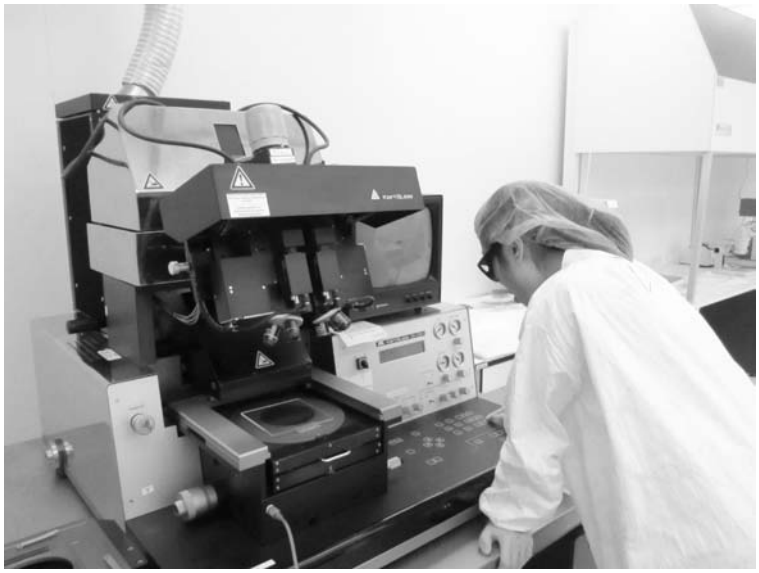

Figure 4.1. *Equipment for UV exposure (into the clean room).*

Following UV exposure, a post-bake process was conducted to enhance the crosslinking of the UV-exposed areas of the photoresist. The post-baked wafers with the crosslinked patterns of the microchannels were immersed during 10 min in a developer solution (1-methoxy-2-propanol acetate) to remove the non-crosslinked regions of the

photoresist. The substrates with the microchannel patterns were rinsed several times with isopropanol and methanol and dried under a gentle stream of nitrogen (Figure 4.2, step II).

iii. Fabrication of Microfluidic Devices: PDMS Microfluidic Devices

Microfluidic (MF) devices were fabricated in poly(dimethylsiloxane) (PDMS) elastomer using a standard soft-lithographic procedure[24]. The PDMS elastomer was prepared from Sylgard® 184, which contains vinyl-terminated dimethylsiloxane oligomers, a platinum catalyst, and a silica filler (dimethylvinylated and trimethylated silica)[26].

The base polymer was mixed with the curing agent containing a crosslinker (dimethyl-methylhydrogen siloxane) and an inhibitor (tetramethyltetravinyl cyclotetrasiloxane) at 10:1 (w/w) ratio. Air was removed from the mixture under vacuum (Isotemp* Model 282A Vacuum Oven, Fisher Scientific*) during 20 min.

The mixture was poured onto the silicon negative master and baked at 75 °C in an oven (Mechanical Convection Oven DKN 400, Yamatp Scientific America Inc.) for at least 4 h. (Figure 4.2, step III). After curing, the PDMS replica was obtaining by peeling from the master, (Figure 4.2, step IV) and holes were created with a blunt-tipped needle at the designated positions, which correspond to the inlets connections of the dispersed and oil phases and outlet tubing of the MF device. Next, in order to close the circuit (Figure 4.2, step V) the PDMS replica and a plane PDMS sheet were oxidized in a plasma cleaner chamber (PDC-3XG, Harrick, USA) for 90 sec. and after the plasma-treatment the replica and the plane PDMS sheet were brought in contact and sealed immediately. Both, plasma-treatment and sealing process will be explained in detail ahead.

Finally, polytetrafluoroethylene tube of 0.05 cm outer diameter, Small Parts, USA) was forced tightly into the holes and then the system is ready to carry out the experiment by microfluidic device.

iv. Plasma Cleaner Operation

The plasma cleaner operation goes as follows: once PDMS is peeled off from the master, it is cleaned with a tape to ensure that there is no dust on the surfaces. Then, PDMS samples are placed into the chamber of plasma cleaner (using a quartz tray) with the bonding surfaces facing up. Once the plasma cleaner door is closed, the Plasma-Flow has to be turn on in order to reach the desired vacuum pressure inside the chamber ~80Pa. Once the desire pressure is reached the plasma cleaner is turned on and the PDMS samples are let inside the chamber during 90 sec. Finally PDMS samples are sealed carefully avoiding bubbles between the surfaces sealed.

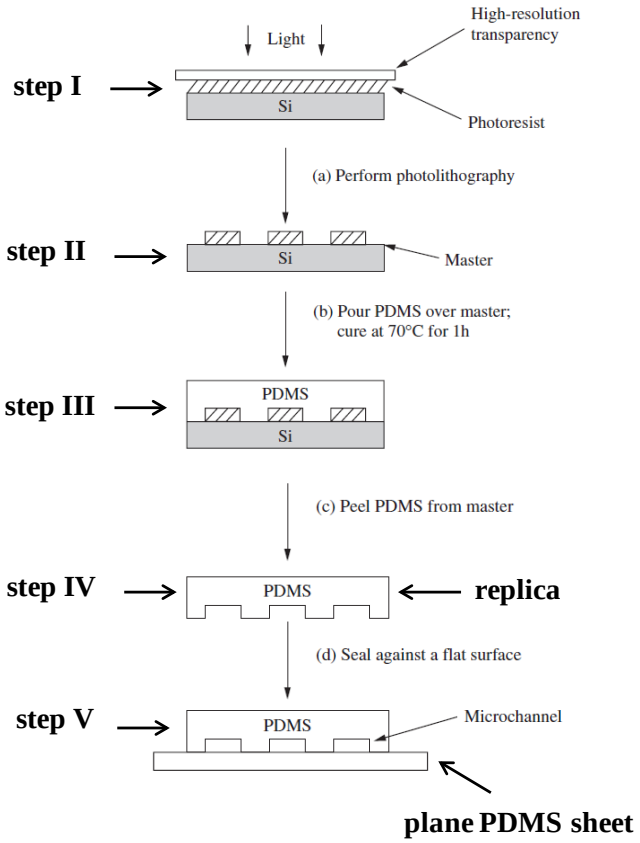

Figure 4.2. *Schematic representation of the steps involved in the preparation of the microfluidic device.*

v. Sealing

One advantage of PDMS is that it can seal to itself, or to other surfaces, reversibly or irreversibly and without distortion of the channels [27, 28]. Sealing of

PDMS channels is substantially simpler than sealing channels in glass, silicon, or thermoplastics[28-30]. PDMS that has been molded against a smooth surface can conformally contact other smooth surfaces, even if they are nonplanar, because PDMS is elastomeric. A reversible seal provided by simple van der Waals contact is watertight but cannot withstand pressures greater than ~0.35 Pa[27]. Adhesive tapes-silicone or cellophane also seal the PDMS channels reversibly[31].

In order to form an irreversible seal both PDMS surfaces were exposed to air plasma for 90 sec. Oxygen plasma surface treatment is one of several techniques that exist for bonding cured PDMS pieces. This treatment generates silanol groups (Si-OH) on the surface of the PDMS by the oxidation of methyl groups [32]. Surface-oxidized PDMS can seal to itself, glass, silicon, polystyrene, polyethylene, or silicon nitride, provided that these surfaces have also been exposed to air plasma. This sealing process, while simple and reproducible, requires technical agility. After surface activation, the two surfaces must be brought into contact quickly (<1 min) after oxidation, because the surface of the oxidized PDMS reconstructs in air [33, 34]. Contact with water or polar organic solvents maintains the hydrophilic nature of the surface indefinitely[35].

4.2.3. Device design

Devices with different geometries were designed with the aim to achieve stable and controlled conditions for the generation of chitosan droplets with narrow size distribution. These requirements can be precisely achieved by passive ways through tuning the geometry of microfluidic devices. In this work, two types of microfluidics generator of droplets, T-junction and flow-focusing were selected. In flow focusing geometry different number of inlets was employed. Therefore, T-junction and flow-focusing droplet generators were classified as a function of the number of inlets. In this section, we will describe the main features of each droplet generator.

i. T-junction droplet generator (two inlets).

Figure 4.3 shows a T-junction geometry device employed for droplet generation. Briefly, T-junction geometry consists of a horizontal channel and a perpendicular channel resembling the two branches of a "T", where the continuous and dispersed phases are introduced, respectively. This device was designated as device 1.

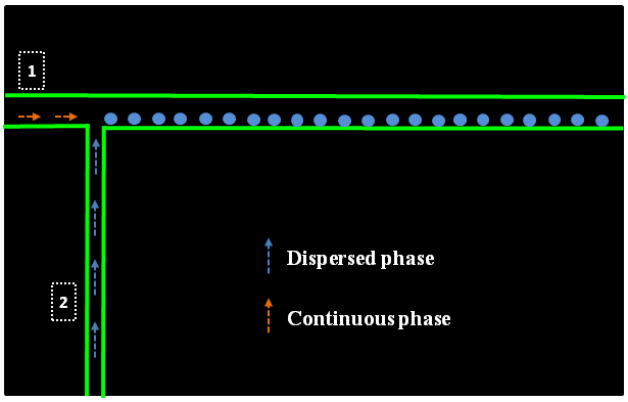

Figure 4.3. *T-junction geometry employed for droplets generation (device 1).*

This geometry (Figure 4.3) was only employed for emulsification of chitosan solutions. The device was fabricated with the follows dimension: 80 µm for main channel (1) and 37 µm perpendicular channel (2).

ii. Flow-focusing droplet generator.

Three different flow focusing droplets generator were employed, depending on the number of inlets. Next, we describe all the geometries:

- Droplet generator by flow-focusing (two inlets).

The flow-focusing geometry employed for droplets generation with two inlets, one for the dispersed phase and the other for the continuous phase, is shown in Figure 4.4. Briefly, the continuous phase was supplied by the inlet and then splitted in two branches (sides) of the device; the liquid stream corresponding to the dispersed phase

was supplied from a central channel. The continuous phase surrounds the inner, immiscible liquid so that the inner thread becomes unstable and breaks in the orifice in a periodic manner to release droplets into the outlet channel.

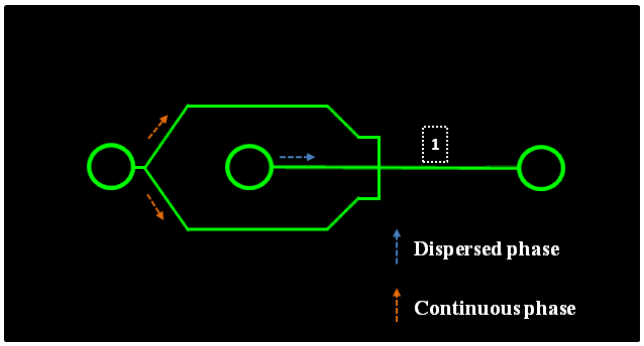

Figure 4.4. *Flow-focusing droplet generator with two inlets (device 2).*

The height of the channel was 50 µm. The width of the horizontal channel supplying the continuous phase and dispersed phase were 70 µm. The length of the mixing channel was 1.02 cm. The device was named as device 2.

- Droplet generator by flow-focusing (three inlets).

In this case, the principle of droplet generation is similar to that of device 2, but with some changes: First, it was included another inlet, which was used for the incorporation of a second dispersed phase, as will explain ahead. The device was named as device 3. Moreover, at the point where the formation of the droplets takes place (★), three design were used.

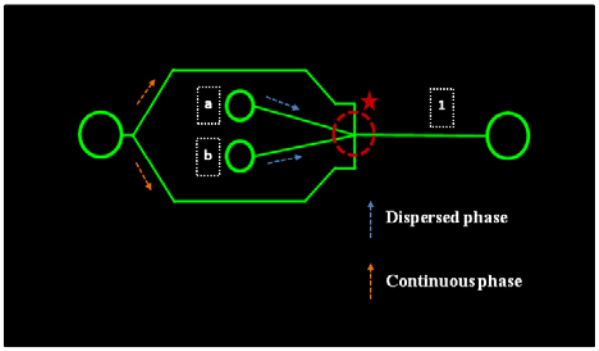

Figure 4.5. *Flow-focusing droplet generator with three inlets (device 3).*

- Droplet generator by flow-focusing (four inlets).

Device 4 (Figure 4.6) included a fourth inlet (middle inlet) for another dispersed phase. Moreover, this device includes two serpentines, the first one was used to improve the interaction between all dispersed phases, and the second one was used to improve the crosslinking process of the microgels obtaining trough microfluidics.

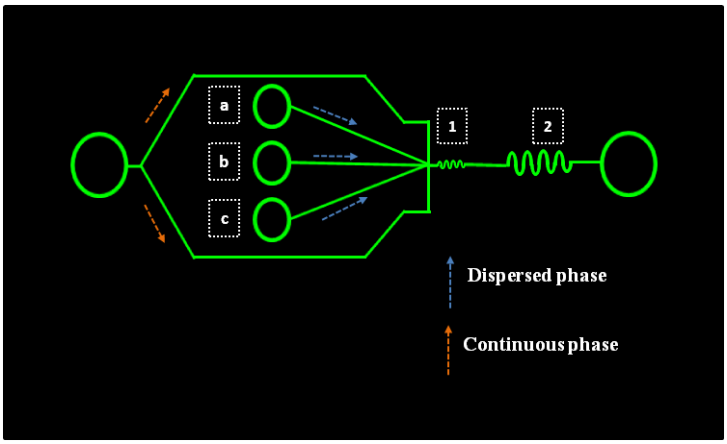

Figure 4.6. *Flow-focusing droplet generator with four inlets (device 4).*

4.2.4. Generation of chitosan and composite chitosan droplets by microfluidic emulsification.

In general, microfluidic approaches for making droplets involve the injection of one liquid phase (the dispersed phase) into another immiscible liquid phase (the continuous phase) through a specially designed microfluidic device[36]. Droplets are sheared off at the junction where the two phases meet. In this work the most common geometries were employed T-junction and flow focusing as droplet generators.

In this section, we assessed the possibility of emulsification of different solutions (chitosan, agarose and chitosan+Fe) by microfluidics, as well the formation of chitosan microgels by studying different crosslinking processes. The respective conditions and concentration it will be detailed in each experiment.

4.2.4.1 Generation of chitosan droplets.

The generation of chitosan droplets was studied by two different droplets generators, as it is detailed below:

i. Chitosan droplets by T-junction droplet generator.

Chitosan 0.5% (w/v) solution was used as dispersed phase for this experiment (see Table 4.1). For that, chitosan powder for a final concentration of 0.5% (w/v) was dissolved in acetic acid 1% (v/v) and used as dispersed phase. Mineral oil containing 3% (w/v) of the non-ionic surfactant Span 80 was used as continuous phase and was injected in the second inlet. Device 1 was employed for this experiment (Figure 4.3). The dispersed phase and mineral oil were supplied to the T-junction droplet generator, using two independent syringe pumps (Harvard Apparatus 33 Dual Syringe Pump, USA). The experiment was carried at room temperature. Volumetric flow rate, Q_o, of the oil phase was 2.0, 2.1, 2.3 and 2.5 mL/h, while the flow rate of the dispersed phase, Q_d, was fixed at 0.1 mL/h.

ii. Chitosan droplets by flow-focusing droplet generator.

Chitosan droplets were also generated employing three different flow-focusing droplets generators, corresponding to devices 2-4.

- Droplet generation by flow-focusing. Crosslinking reaction off-chip (two inlets).

Crosslinked reaction is a key issue for chitosan microgels formation trough microfluidics, for this reason this first experiments is based on chitosan emulsification and then the crooslinked reaction off-chip. A device with two inlets (device 2) was employed for this experiment (Figure 4.4). In this case, an aqueous chitosan solution 0.5% (w/v) was employed as dispersed phase and continuous phase was mineral oil + Span 80 (3% w/v). Both phases were supplied to the flow focusing droplet generator, using two independent syringe pumps. After, chitosan emulsification, the droplets were collected in a reservoir containing 5 mL of a mixture of sodium tripolyphosphate (TPP) solution with a concentration at 5% (w/v) and hexane in a volume ratio of 1/1. Volumetric flow rate, Q_o, of the oil phase was 1.2 and 1.6 mL/h, while the flow rate of the dispersed phase, Q_d, was 0.5 and 0.2 mL/h respectively. The experiment was carried out at room temperature. The emulsion collected in the reservoir was centrifuged at 14000 rpm for 10 min (Eppendorf Microcentrifuge, Model 5430R) in order to recover the resulting chitosan microgels.

- Droplet generation by flow-focusing. Crosslinking reaction on-chip (three inlets).

In this case, it is studied the viability of a crosslinking reaction on-chip. For that TPP solution with a concentration of 0.5% (w/v) was employed as the second dispersed phase (see Figure 4.5), and the other dispersed phase was the aqueous chitosan solution 0.5% (w/v), see Table 4.1. Mineral oil + Span 80 (3% w/v) was employed as continuous phase. Moreover, at the junction point where the formation of the droplets takes place, three different designs were employed that will be discussed in the Results and Discussion part. The experiment was carried at room temperature. Their dimensions were the same to those reported for the geometry shown in previous example of

crosslinking off-chip (Figure 4.4), the width of channels were 70 µm. Volumetric flow rates, Q_o, of the oil phase was 0.4 mL/h, while the flow rates corresponding to the chitosan solution and the TPP solution were set to 0.5 mL/h and 0.25 mL/h, respectively.

- Droplet generation by flow-focusing. Crosslinking reaction on- chip (four inlets).

This experiment is based on the previous experiment with some modifications. First, a third dispersed phase was included consisting of acetic acid 1% (v/v) in order to reduce the interaction among polymer-crosslinking agent. Moreover, chitosan and TPP solutions concentrations were changed. Chitosan solution was prepared with a final concentration of 0.25% (w/v) in acidic acid 1% (v/v) and TPP solution to a final concentration of 0.05% (w/v), see Table 4.1. Mineral oil + Span 80 (3% w/v) was employed as continuous phase. Volumetric flow rates, Q_o, of the oil phase was 0.4, 0.55 and 0.7 mL/hr, while the flow rate of chitosan solution, was 0.3 mL/h, for TPP solution was 0.4 mL/h and for acidic acid was 0.5 mL/h. The experiment was carried at room temperature.

Table 4.1. Precursor solutions employed in microfluidic emulsification and generation of chitosan droplets experiments.

Geometry	**Device employed**	**Dispersed phase**	**Type of Crosslinking**
T-junction	1	chitosan 0.5% (w/v)	*
Flow-Focusing	2	chitosan 0.5% (w/v)	Off-chip
	3	chitosan 0.5% (w/v) and TPP 0.5%(w/v)	On-chip
	4	chitosan 0.25% (w/v), TPP 0.05% (w/v) and acetic acid 1% (v/v)	On-chip

* Only emulsification through microfluidics was prepared.

**For all samples, the continuous phase was Mineral oil+Span80.

4.2.4.2 Generation of composite chitosan/agarose microgels trough flow-focusing regime.

Composite chitosan/agarose microgels were prepared by varying agarose concentration, which was controlled by changing agarose content in the precursor chitosan/agarose solution. Different amounts of agarose were dissolved at 60 °C in 0.5% (w/v) aqueous chitosan solutions containing 1% (v/v) of acetic acid. This concentration was selected because viscosity of solution was appropriate for microfluidics experiments. The concentration of agarose in the mixed solution was 1.0, 1.5 and 2.0% (w/v). The samples were designated as chitosan/agarose-1, chitosan/agarose-1.5 and chitosan/agarose-2 (Table 4.2). The chitosan-free sample was used as a control and was labeled as agarose-1.5. These concentrations are the same used for composite macrogels.

Aqueous chitosan/agarose solution and mineral oil containing 3 w/v % of the non-ionic surfactant Span 80 heated to 37 ºC were supplied to the flow-focusing MF droplet generator (Figure 4.4) using two independent syringe pumps. Following MF emulsification, the droplets travelled through the downstream channel and exited the device through the outlet tubing. Volumetric flow rate, Q_o, of the oil phase was varied from 0.05 to 0.3 mL/h, while the flow rate of the chitosan/agarose solution, Q_d, was fixed at 0.05 mL/h.

The outlet tubing was enclosed within a hose connected to a water circulator cooled to 4 ºC by a 1:4 vol/vol mixture glycerol and water. The droplets moved through the cooled tubing, where they gelled and were collected in a 15 mL vial containing PBS solution (pH 7.4). The vial was placed on an ice bath for 45 min to ensure complete gelation of the composite microgels. The resulting suspension was centrifuged at 14000 rpm for 30 min (Eppendorf Microcentrifuge, Model 5430R), then washed with a PBS buffer, and transferred into a PBS buffer (pH 7.4).

4.2.4.3 Microfluidic emulsification and generation of the ferrofluid loaded chitosan/agarose microgels (device 2).

For this experiment, composite chitosan/agarose with an agarose concentration of 1.5% (w/v) (Chitosan/agarose-1.5) was selected, and the same procedure explained before was used. Then, two different ferrofluid concentrations (2% and 5 % (w/v) were dispersed in Milli-Q water. Each of this ferrofluid solution was mixed under vortex agitation with chitosan/agarose-1.5 in a volume ratio of 6:1, until to get a homogeneous sample. Also, ferrofluid 5% (w/v) loaded agarose-1.5 was prepared following the same procedure. The samples were designated as chitosan/agarose-1.5+Fe2%, chitosan/agarose-1.5+Fe5% and agarose-1.5+Fe5% (Table 4.2). Each dispersed solution and mineral oil containing 3% (w/v) of the non-ionic surfactant Span 80 was heated to 37 ºC and supplied to the flow-focusing MF droplet generator (Device 2), using two independent syringe pumps. Volumetric flow rate, Q_o, of the oil phase was varied from 0.05 to 0.4 mL/h, while the flow rate of the chitosan/agarose solution, Q_d, was 0.05 mL/h.

Table 4.2. Concentrations of agarose and chitosan in precursor solutions.

Sample	Agarose (% w/v)	Chitosan (% w/v)	Fe (%w/v)
Agarose-1.5	1.5	0	0
Chitosan/agarose-1	1	0.5	0
Chitosan/agarose-1.5	1.5	0.5	0
Chitosan/agarose-2	2	0.5	0
Agarose-1.5+Fe5%	1.5	0	5
Chitosan/agarose-1.5+Fe2%	1.5	0.5	2
Chitosan/agarose-1.5+Fe5%	1.5	0.5	5

4.2.5 Characterization of chitosan droplets and chitosan/agarose microgels.

The diameters of the precursor droplets and the corresponding microgels were determined by analyzing optical microscopy images of 20 droplets or microgels using Image Pro 5.0 (media Cybernetics, USA) software. For composite chitosan microgels, precursor droplets and the corresponding microgels were determined by analyzing optical microscopy images of 100 droplets or microgels. The polydispersity is expressed as the coefficient of variance (CV) and it is defined as CV (%) = (σ/D) x 100, where σ is the standard deviation of droplet diameter (μm) and D is the mean diameter of the droplets (μm).

4.3 RESULTS AND DISCUSSION

In this work, microfluidics has been used as technique that allows studying the transformation of chitosan precursor droplets into microgels. This fact was achieved mainly by two physicals mechanisms. On the one hand, electrostatic interactions among chitosan and TPP allow the preparation of chitosan microgels. On the other hand, composite chitosan/agarose microgels were obtained by thermally induced gelation. It is important to highlight the versatility of MF technique because offers the possibility of changing easily the configuration geometry. In this work four different designs were prepared and comparatively analyzed by employing T-junction and flow focusing geometries, in order to prepare chitosan and composite chitosan microparticles.

4.3.1 Generation of chitosan droplets by microfluidic emulsification.

In this section different chitosan droplets were obtained. For that, different droplets generators, T-junction and flow-focusing were employed.

i. Generation of chitosan droplets with T-junction geometry (device 1).

First, in this work was assessed the emulsification of chitosan, which the mechanism of droplet formation results from the competition between the shear stress imposed by the flow of the continuous phase and the interfacial force[37]. The emulsification of chitosan was obtained using T-junction geometry (device 1). Figure 4.7 shows the formation of chitosan droplets in T-junction point (Figure 4.7-a) and the variation in its size, plotted as a function of the flow rate of the continuous oil phase Q_0 and constant Q_d= 0.1 mL/h, obtained by MF (Figure 4.7-b).

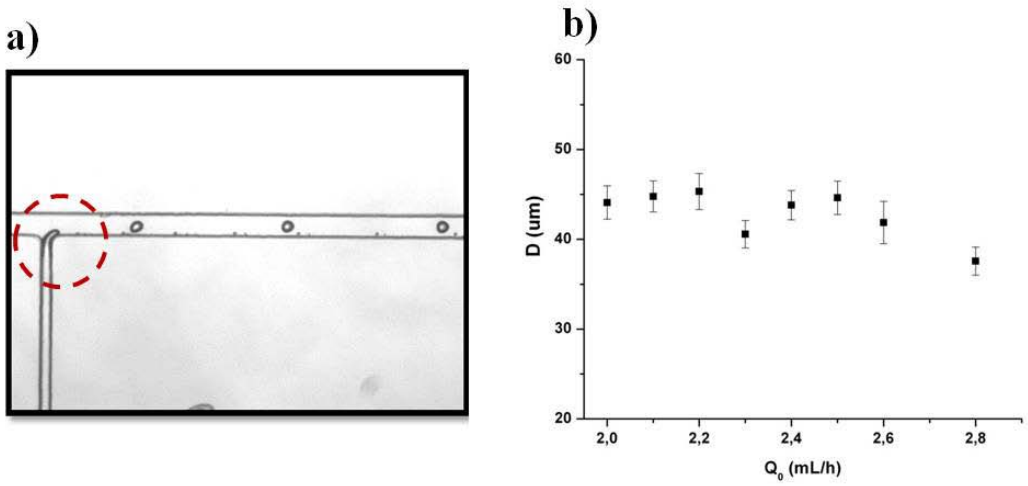

Figure 4.7. *a) Optical microscopy images of the T-junction generator of chitosan 0.5%. b) Variation in the mean diameter, D, of droplets formed by T-junction MF emulsification of chitosan0.5% (■).*

As can be observed in the Figure 4.7-a, chitosan droplets presented almost spherical shape. However, a jetting transition was observed, when the flow is very slow and therefore it is difficult overcome the surface tension. This kind of effect is always unstable for droplets formation. Figure 4.7-b shows, the variation of the mean diameter D, as a functions of flow rate of the continuous phase. However, the droplet size changed in a random way with the increase of the flow rate of the continuous phase (Q_o). Therefore, the control over the droplets size was very difficult to keep and the polydispersity increased.

After checking up the emulsification of chitosan employing a T-junction droplet generator, unstable conditions and high polydispersity were obtained. Moreover, cross-

linked reaction arises as key question to obtain chitosan microgels. For that, we propose some alternatives to achieve chitosan microgels.

ii. Generation of chitosan droplets with flow-focusing geometry. Crosslinking reaction off-chip (device 2).

Figure 4.8 shows the optical images corresponding to the formation of chitosan droplets inside a flow-focusing device with two-inlets. In this case, a chitosan solution 0.5% (w/v) was employed as dispersed phase. As can be observed in Figure 4.8, chitosan emulsification was achieved and the average diameter calculated for chitosan droplets was 16 μm with a CV of 4.6%, which indicates that chitosan droplets are nearly monodisperse.

As it is well known, two different regimes can occur during the emulsification process, the dripping and the jetting regime [38]. A jetting regime can be observed in the formation of chitosan droplets in Figure 4.8. This regime is obtained when a continuous thread of the dispersed phase extends into the outlet channel and breaks far downstream of the orifice [38]. This kind of regime is no desirable, because it is unstable and the droplets obtained are usually considerable smaller than the width of the orifice. In fact, droplets obtained under jetting regime are accompanied of satellite droplets, which increase their CV, even if in our system we did not observe the formation of satellite droplets.

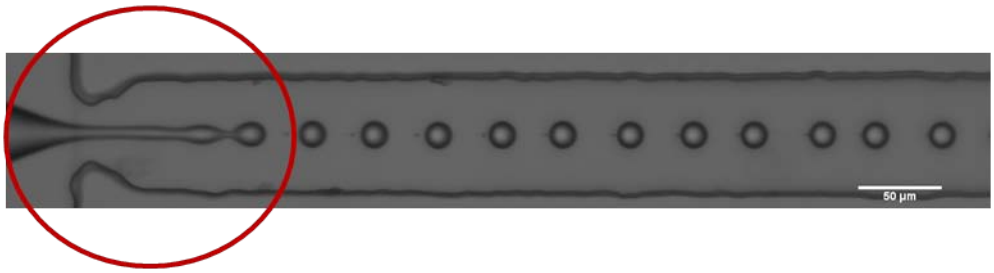

Figure 4.8. *Formation of chitosan droplets with flow- focusing device with two-inlets.*

The droplets moved through the downstream channel and they were collected off-chip in a reservoir containing a mixture of TPP solution+hexane, in order to achieve the crosslinking of chitosan droplets. This process takes place when the droplets

gradually solidify from the surface to the inside[12]. However, it was observed chitosan droplets immersed into a hexane/TPP solution in the reservoir, therefore, it is difficult to ensure an appropriate contact with the TPP. On the other hand, the resulting microgels could not be separated by centrifugation due to their small size (16 µm) and a homogeneous crosslinking process for chitosan droplets was difficult to achieve. Although previous investigations reported the achieving of chitosan microparticles and chitosan droplets off-chip [12], however, the sizes obtained were ~300 µm. In order to improve the crosslinking process maintaining the size of the particles <100 µm, we decided to change the protocol of fabrication of chitosan microgels to ensure the interaction among the chitosan droplets and the crosslinking agent (TPP) by a three inlets flow-focusing device, described below.

iii. Generation of chitosan droplets with flow-focusing geometry. Crosslinking reaction on-chip with TPP (device 3).

In order to prepare chitosan microgels and to ensure their crosslinking reaction, TPP solution was included as a second dispersed phase, enabling chitosan-TPP interaction inside the microfluidic device. For this experiment, it was employed a device with three inlets (device 3), shown in Figure 4.5. Figure 4.9 shows the main results obtained for this experiment. As a first step, a serpentine prior to the junction was added to the geometry device in order to increase the time of chitosan-TPP interaction and thus facilitate the crosslinking of chitosan prior to droplet formation. The results shown in Figure 4.9-a allow to observe fiber formation at the junction point where chitosan droplets are formed. The following conditions were employed: chitosan and TPP concentration of 0.5% (w/v) and flow rate of the oil phase of Q_o 0.4 mL/hr, while the flow rates corresponding to the chitosan solution and the TPP solution were set to 0.5 mL/h and 0.25 mL/h, respectively. In fact, only a few seconds are necessary to achieve the crosslinking reaction of chitosan with TPP, therefore it is very hard to overcome the surface tension of the final fiber.

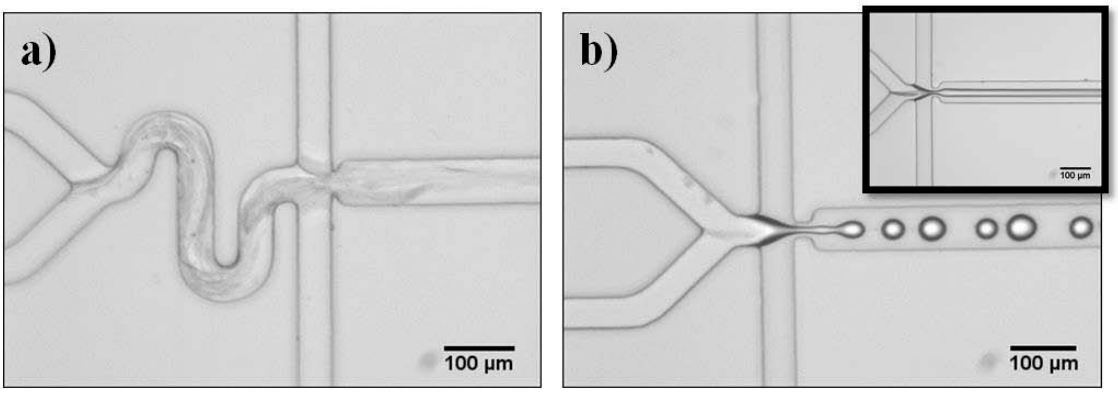

Figure 4.9. *Images corresponding at two designs of the three-inlets flow focusing microfluidic device. The inset in Figure 4-b shows the fiber formation.*

In order to reduce time of chitosan-TPP interaction, a second geometry device was designed in which the serpentine prior to the flow focusing junction was eliminated and the results are shown in Figure 4.9-b. In this case, unstable droplets were obtained which also gave rise to fiber formation (see the inset image in Figure 4b).

According to the results shown in Figure 4.9, a three-inlets flow focusing MF device does not allow the generation of chitosan droplets and, instead, fiber formation is observed.

iv. Generation of chitosan droplets with flow-focusing geometry. Crosslinking reaction on-chip with TPP (device 4).

In order to avoid the formations of the fiber obtained in the section 4.3.1-iii, a four-inlet device was designed, with the objective to reduce the interaction among chitosan and TPP. The fourth inlet consists in an aqueous solution of acetic acid. In this way, as chitosan is dissolved in acetic acid, the chitosan-TPP interaction should diminish. Figure 4.10 shows that the incorporation of the fourth inlet (central channel) for acidic acid 1% (v/v) the keeping concentrations of chitosan 0.25% (w/v) and TPP 0.05% (w/v), the fiber formation was avoided. In order to improve the mixing of chitosan and TPP, a first serpentine was included immediately after the emulsification of chitosan. With the objective to increase the residence time and therefore the interaction between chitosan and TPP and in the last term to promote hardening of the resulting chitosan microgels, a second serpentine was included in the outlet channel.

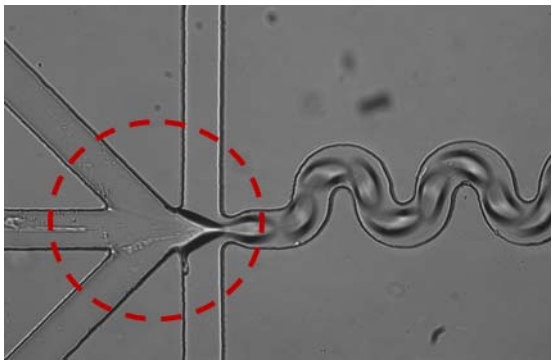

Figure 4.10. *Optical image for crosslinking reaction on-chip in a four-inlet flow focusing microfluidic device (device 4).*

Figure 4.11 shows optical images corresponding to chitosan droplets formed across different parts of the four-inlet device. Three different flow rates of the oil phase were employed: 0.4, 0.55 and 0.7 mL/h. The flow rates of the three dispersed phases, chitosan, TPP and acidic acid were fixed at 0.3 mL/h, 0.4 mL/h and 0.5 mL/h, respectively. This geometry allows mixing chitosan with TPP, mainly in the first serpentine (left column, Figure 4.11). The successful formation of chitosan microgels under these conditions demonstrates that the stability of the system is improved with respect to the experiment performed within the three-inlet device (Figure 4.9) and that the concentrations employed were appropriate. Besides, the fiber formation was avoided for all the flow rates of the oil phase under study. The second serpentine was added to the design in order to increase the residence time of the chitosan microgels within the microfluidic device and hence to promote hardening of the resulting chitosan microgels (center column, Figure 4.11). Finally, chitosan microgels exited the device through the outlet tubing as shown in the images on the right column.

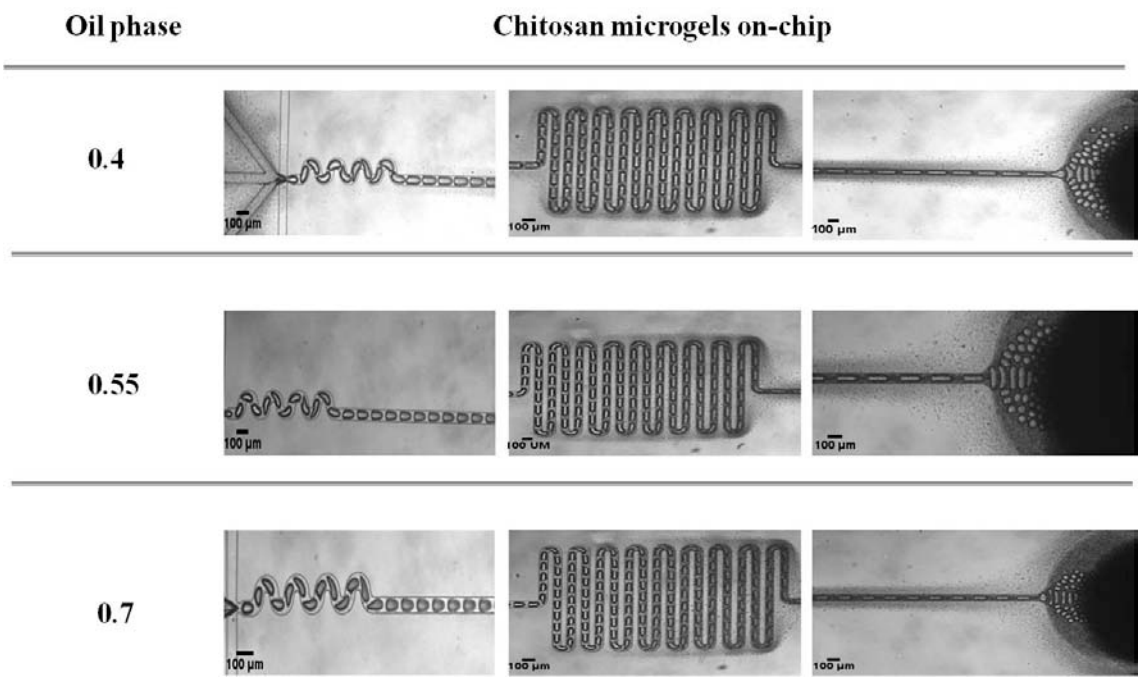

Figure 4.11. *Optical images of chitosan droplets obtained at different flow rates of the oil phase in a four-inlets flow focusing microfluidic device. Images on the left column correspond to chitosan microgels moving downstream into the first serpentine, images in the center column correspond to chitosan microgels into the second serpentine and images on the right column correspond to chitosan microgels exiting the device through the outlet tubing (on-chip chitosan microgels).*

It is important to note that the microgel shape within the MF channel is not spherical due to geometry constrictions which give rise to elongated microgel shapes which are known as plugs[39]. This is mainly observed in the images corresponding to chitosan microgels into the first and the second serpentine (left and center columns in Figure 4.11 respectively). Once chitosan microgels exit the device through the outlet tubing they get a spherical shape as can be observed in the images shown in the right column in Figure 5. From analysis of these optical images, the average diameter of the chitosan microgels on-chip decreased with the flow rate of the oil phase being 68, 57 and 42 μm for Q_o of 0.4, 0.55 and 0.7 mL/h.

Figure 4.12-a shows an optical micrograph corresponding to the chitosan microgels off-chip (outside the MF device) prepared with a flow rate, Q_o of 0.55 mL/h. (Figure 4.11) which presented a spherical shape. The distribution of diameters corresponding to chitosan microgels on-chip (before exiting the device) and off-chip (outside the device) is shown in Figure 13-b.

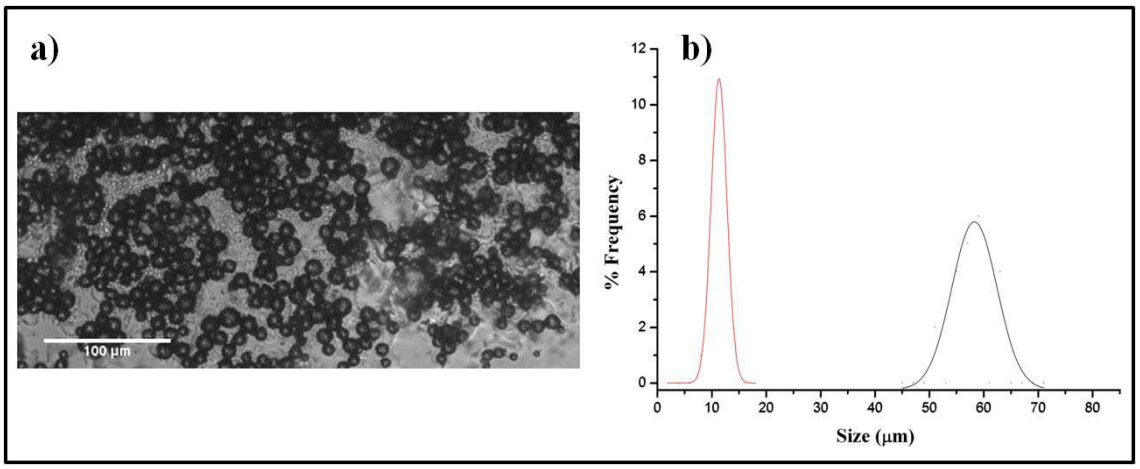

Figure 4.12. *a) Optical micrographs for chitosan microgels, b) The black curve corresponds to the distribution of the diameters of chitosan microgels before exiting the device and the red curve corresponds to the distribution of the diameters of chitosan microgels outside the device, for a flow rate of the continuous phase, Q_o of 0.55 mL/h. The experimental data points were fitted to Gaussian distribution.*

As can be observed in Figure 12-b, there is an important difference regarding the average diameter obtained for chitosan microgels before and after exiting the outlet tubing of the MF device. The average diameter corresponding to the chitosan microgels off-chip is 10 µm which presented an important reduction with respect to their size inside the device being 60 µm. The fact that the mean diameter decreases in the final chitosan microgels with respect to the chitosan microgels on-chip suggests the possibility to tune the final particle size diameter by varying the residence time of the chitosan microgels in the MF device. Also, it could be due to partial expulsion of water from the microgels when complete gelation occurred. This can be achieved by adjusting several experimental parameters such as the flow rate of the oil phase.

Although, to keep all streams working at good conditions is a very difficult task and in some cases, the fiber formation was obtained, nevertheless chitosan microparticles of controlled and monodispersed size can be obtained by varying the geometry of MF devices and flow rates. In order to develop multifunctional microparticles two other systems have been investigated. For that, was included a second polymer with interesting properties, agarose. It is a neutral polysaccharide that

forms thermoreversible gels upon cooling agarose aqueous solutions. Taking into account this property, we proposed chitosan/agarose microgels trough microfluidics.

4.3.2 Microfluidic preparation of chitosan/agarose microgels in a two inlets flow focusing microfluidic device.

Chitosan/agarose microgel particles were prepared by the technique of microfluidics employing the equipment shown on Figure 4.13. The incorporation of a chamber was necessary, with the aim to keep the appropriated temperature (37 °C) for the experiments. A zoom in the Figure 4.13 allows observing in detail the equipment and the device employed. In this study, a flow-focusing droplets generator with two inlets was employed.

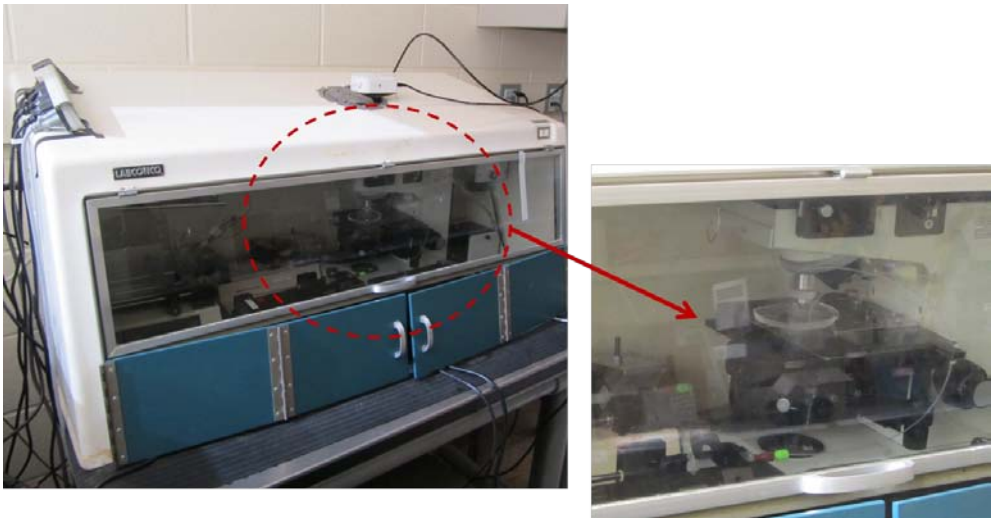

Figure 4.13. *Microfluidics equipment employed for chitosan/agarose microgels preparation.*

Different compositions of chitosan/agarose aqueous solutions and mineral oil containing 3% (w/v) of Span 80, were forced into the orifice of the MF device, as shown in Figure 4.14. Volumetric flow rate of the oil phase, Q_o, was varied from 0.05 to

0.3 mL/h, while the flow rate of the dispersed phase, chitosan/agarose solution, Q_d, was fixed at 0.05 mL/h.

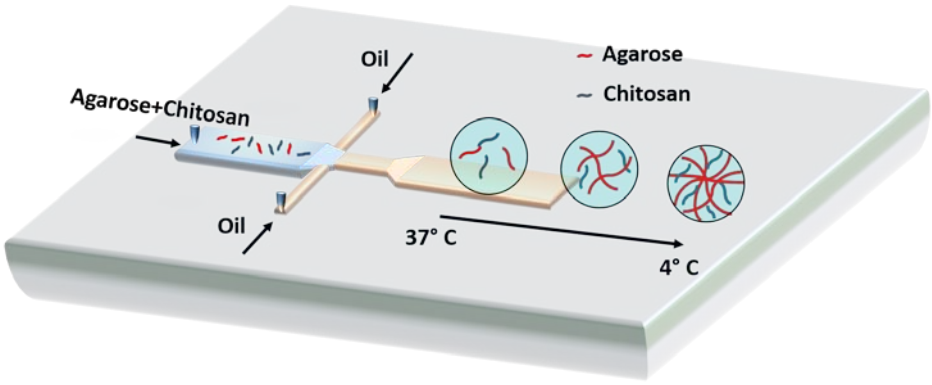

Figure 4.14. *Schematic of the MF preparation of microgels from chitosan/agarose solutions. Emulsification of the chitosan/agarose solution at 37 ºC in a flow-focusing droplet generator is followed by crosslinking of the precursor droplets upon cooling to 4 ºC. The height of the channel was 50 µm. The width of the horizontal channel supplying the mineral oil and the chitosan/agarose solution were 70 µm. The length of the mixing channel was 1.02 cm.*

The stream of the chitosan/agarose solution periodically broke up to release droplets. The formation of droplets occurred in the flow-focusing regime[40] at a frequency of 1,200 s^{-1}. The formation of primary droplets was accompanied by the formation of small ~3 µm diameter satellite droplets (not show here). This kind of droplets (satellite droplets) are byproducts in the droplet formation process for the preparation of uniform microparticles[12]. With increasing volumetric flow rate, Q_o, of the oil phase from 0.05 to 0.30 mL/h, the diameter of primary droplets is reduced (Figure 4.15-a). This fact is due to the increasing of shear stress imposed by the oil phase on the aqueous stream.

This tendency was corroborated in the study of the variation of the mean diameter D of the droplets formed from the others mixed solutions, chitosan/agarose-1, chitosan/agarose-1.5, chitosan/agarose-2 and agarose-1.5, as a function of the flow rate of the oil phase (Figure 4.15-b). The average diameter of droplets was tuned from 42 to 18 µm by varying Q_o from 0.05 to 0.3 mL/h, while maintaining constant the flow rate of the chitosan/agarose solution, Q_d, at 0.05 mL/h.

Moreover, it was also analyzed the influence of agarose concentration for a particular Q_o. It was observed that the diameter of droplets increases with increasing agarose concentration in the chitosan/agarose solutions for a specific Q_o. This fact can be explained by the increasing in viscosity of the solution[41, 42]. A similar trend was observed for the droplets of chitosan/agarose-1.5 solution, compared to the droplets of agarose-1.5 solution. For all the chitosan/agarose and agarose solutions, MF emulsification produced primary droplets with polydispersity not exceeding 1.5%.

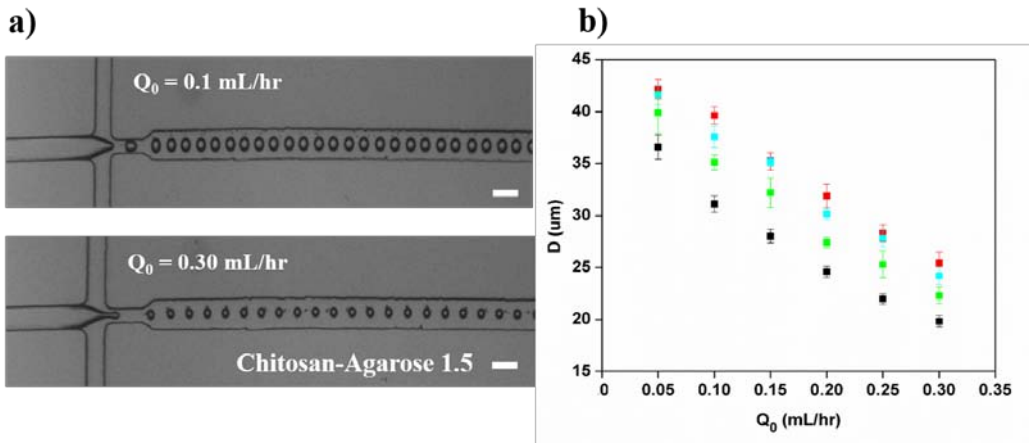

Figure 4.15. *a) Optical microscopy images of the chitosan/agarose-1.5 droplets obtained at Q_0 of 0.1 mL/hr (top) and 0.35 mL/hr (bottom) at Q_d=0.05 mL/h. The scale bar is 70 μm. b) Variation in the mean diameter, D, of droplets formed by MF emulsification of chitosan/agarose-1 (■), chitosan/agarose-1.5 (■), chitosan/agarose-2 (■) and agarose-1.5 (■) solutions, plotted as a function of the flow rate of the continuous oil phase. Q_d=0.05 mL/h.*

The precursor droplets exiting the MF device were cooled down in the outlet tubing to induce agarose gelation, while the chitosan molecules were distributed within the agarose network. These droplets were collected in PBS solutions at low temperature. Additional off-chip post-gelation yielded transparent microgels with a well-defined round shape and polydispersity below 1.5 %. A representative image of chitosan/agarose-1 microgels generated at Q_o=0.20 mL/hr and Q_d=0.05 mL/h, which were transferred in PBS solution, was shown in Figure 4.16. The average diameter of the microgels was 18.4±2.3 μm, ~30% smaller than the diameter of the corresponding precursor droplets, owing to microgel shrinkage upon gelation.

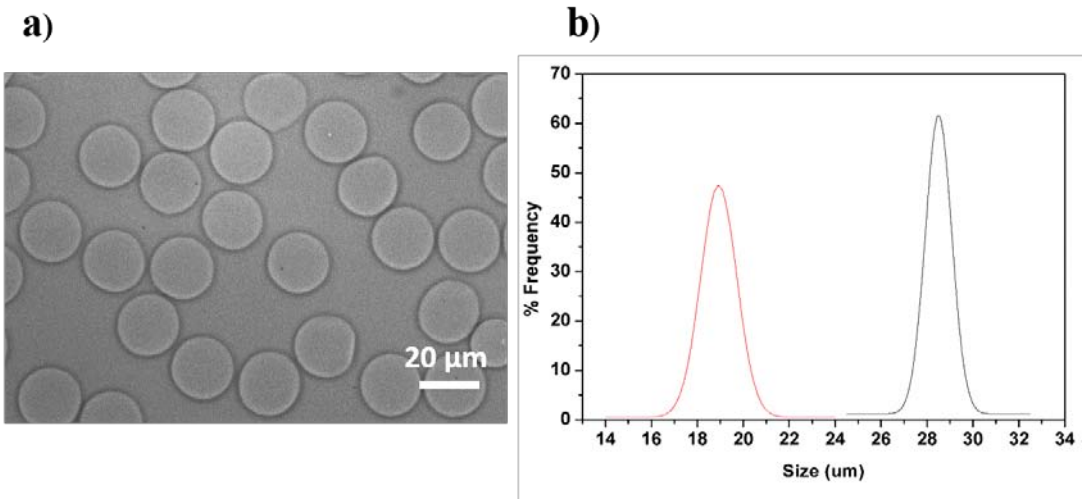

Figure 4.16. *a) Optical microscopy image of chitosan/agarose-1 microgel in the PBS buffer at 25 °C. The droplets were generated at Q_o= 0.20 mL/h and Q_d = 0.05 mL/h, transferred in PBS solution and post-gelled at 4 °C. b) Distribution of the diameters of droplets of chitosan/agarose-1 solution (black curve) and of the corresponding microgels (red curve). The experimental data points were fitted to Gaussian distribution.*

4.3.3Microfluidic emulsification and generation of the ferrofluid loaded chitosan/agarose microgels in a two inlets flow focusing microfluidic device.

In this section, we propose a ferrofluid loaded chitosan/agarose microgel through microfluidics. Some magnetic chitosan microparticles[43] have been prepared trough microfluidics; however, for the best of our knowledge this is the first time that is reported ferrofluid loaded composite chitosan/agarose microgels through microfluidics with flow-focusing droplet generator.

Chitosan/agarose-1.5 solution was select to study the incorporation of ferrofluid (2 and 5% w/v) and consequently the microgel formation through MF. Agarose-1.5 loaded with ferrofluid at 5% (w/v) was used as a control. Figure 4.17 shows the variation in the mean diameter of droplet on function of the flow rate of the oil phase for samples under study, which a higher flow rate of the oil phase, the diameter of droplets reduced for all the samples.

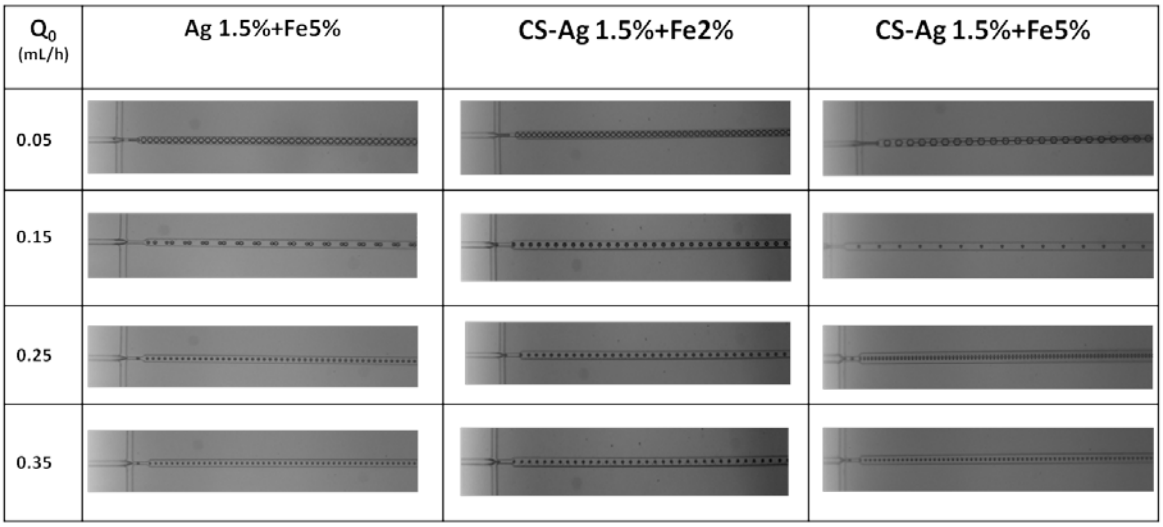

Figure 4.17. *Optical microscopy images of magnetic droplets obtained at Q_0 of 0.05, 0.15, 0.25 and 0.35 mL/h at Q_d=0.05 mL/h. The scale bar is 70 µm.*

Figure 4.18 shows the mean diameter D, of the droplets formed from chitosan/agarose-1.5+Fe2%, chitosan/agarose-1.5+Fe5%, and agarose-1.5+Fe5% solutions, plotted as a function of the flow rate of the oil phase. As can be observed, at low flow rate of the oil phase (0.05 mL/h) it was observed a significant different of droplet size among all the samples under study. Chitosan/agarose-1.5 presented a droplet size around 46 µm, whilst chitosan/agarose-1.5+Fe2%, chitosan/agarose-1.5+Fe5%, and agarose-1.5+Fe5% presented a droplet size of 51 µm, 70 µm and 56 µm, respectively. This change on their droplets size as a function of ferrofluid content, at Q_o of 0.05 mL/h, could be explained for a slight increase of their respective viscosity. Therefore, break up the stream of samples loaded with ferrofluid was more difficult, consequently their droplet size increased. Moreover, Figure 4.18 shows that a higher Q_o, the droplet size decreased for all the samples under study, being the droplets size independent of ferrofluid content, even for agarose1.5+Fe5%.

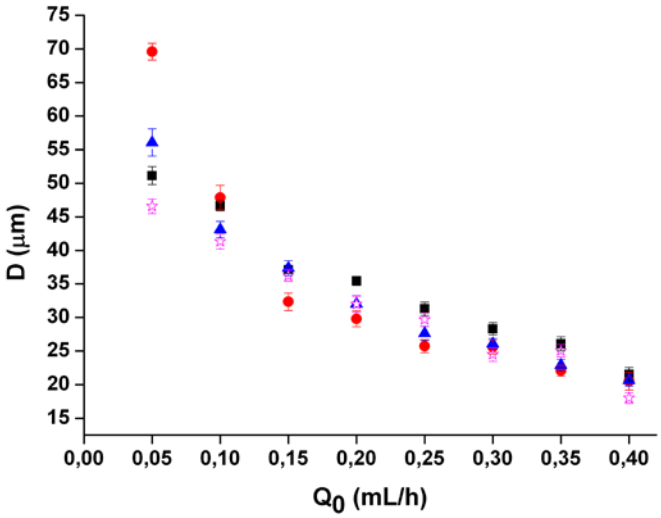

Figure 4.18. *Variation in the mean diameter, D, of droplets formed by MF emulsification of chitosan/agarose-1.5+Fe2% (■), chitosan/agarose -1.5+Fe5% (•), agarose-1.5+Fe5% (▼) and chitosan/agarose-1.5 (☆) solutions, plotted as a function of the flow rate of the continuous oil phase. Q_d=0.05 mL/h.*

Figure 4.19 shows the optical microscopy image of agarose-1.5+Fe5% microgel in the PBS buffer at 25 ºC. These microgels present a well defined spherical shape and with a good polydispersity, their average diameter calculated was 28 µm with a CV of 7%.

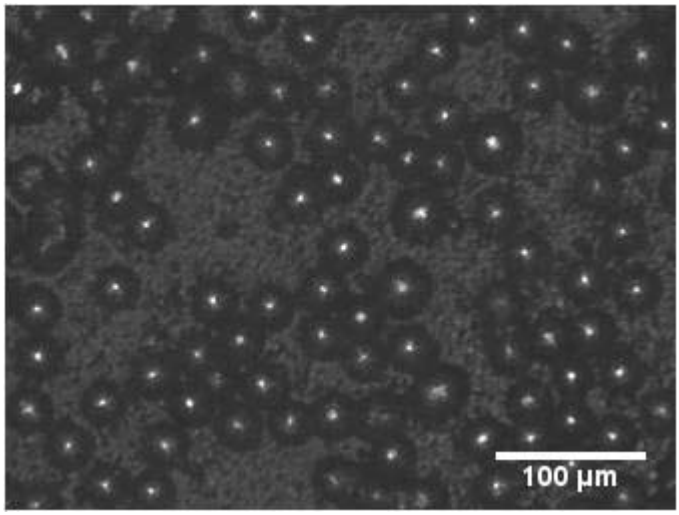

Figure 4.19. *Optical microscopy image of agarose-1.5+Fe5% microgel.*

Composite chitosan/agarose and ferrofluid loaded chitosan/agarose microgels were successfully prepared by microfluidics. Taking into account, the results obtained in the chapter 3 related with composite chitosan/agarose macrogels, can be suggest that these microgels presented as well good properties as their respective macrogels. However, it is important corroborate this hypothesis.

4.4 CONCLUSIONS

In the study of preparation of different protocols for chitosan microgels through microfluidics, the following conclusions can be drawn:

For the generation of chitosan droplets was necessary change several parameters such as geometry, concentrations and crosslinking reaction.

In this work, we set up a microfluidic device in order to achieve crosslinking of chitosan with TPP on-chip as an alternative to crosslinking off-chip that does not assure homogenous crosslinking. Crosslinking reaction on-chip among chitosan and TPP was very fast and presented some drawbacks such as fiber formation. This fact prevented droplet formation and high polydispersity of the droplets. For this reason, a four-inlet MF device was designed that allowed to obtain chitosan microgels with sizes around 10 microns and a CV lower than 13%. It is important to note that the final size of chitosan microgels could be tuned by varying the residence time of the chitosan microgels inside the chip. The microfluidics technique allows to easily change the geometry configuration, and to control several experimental parameters such as the flow rates of the aqueous and the organic phase at the same time.

Finally, our work provides a useful strategy for the preparation of composite chitosan/agarose microgels and ferrofluid loaded chitosan/agarose microgels by the MF method as a means to obtain colloidal materials with narrow particle size distribution and potential candidates for their employment in controlled drug release applications or another biomedical application.

4.5 REFERENCES

[1] Tumarkin E, Kumacheva E. Microfluidic generation of microgels from synthetic and natural polymers. Chemical Society Reviews. 2009;38:2161-8.

[2] Xu S, Nie Z, Seo M, Lewis P, Kumacheva E, Stone HA, et al. Generation of Monodisperse Particles by Using Microfluidics: Control over Size, Shape, and Composition. Angewandte Chemie International Edition. 2005;44:3799-.

[3] E. Kumacheva PG. Microfluidic Reactors for Polymer Particles 2011.

[4] Nie Z, Xu S, Seo M, Lewis PC, Kumacheva E. Polymer Particles with Various Shapes and Morphologies Produced in Continuous Microfluidic Reactors. Journal of the American Chemical Society. 2005;127:8058-63.

[5] Utada AS, Lorenceau E, Link DR, Kaplan PD, Stone HA, Weitz DA. Monodisperse Double Emulsions Generated from a Microcapillary Device. Science. 2005;308:537-41.

[6] Sugiura S, Nakajima M, Tong J, Nabetani H, Seki M. Preparation of Monodispersed Solid Lipid Microspheres Using a Microchannel Emulsification Technique. Journal of Colloid and Interface Science. 2000;227:95-103.

[7] Dendukuri D, Tsoi K, Hatton TA, Doyle PS. Controlled Synthesis of Nonspherical Microparticles Using Microfluidics. Langmuir. 2005;21:2113-6.

[8] Fang A, Cathala B. Smart swelling biopolymer microparticles by a microfluidic approach: Synthesis, in situ encapsulation and controlled release. Colloids and Surfaces B: Biointerfaces. 2011;82:81-6.

[9] Huang KS, Lu K, Yeh CS, Chung SR, Lin CH, Yang CH, et al. Microfluidic controlling monodisperse microdroplet for 5-fluorouracil loaded genipin-gelatin microcapsules. Journal of Controlled Release. 2009;137:15-9.

[10] Xu J-H, Zhao H, Lan W-J, Luo G-S. A Novel Microfluidic Approach for Monodispersed Chitosan Microspheres with Controllable Structures. Advanced Healthcare Materials. 2012;1:106-11.

[11] Yang C-H, Huang K-S, Lin P-W, Lin Y-C. Using a cross-flow microfluidic chip and external crosslinking reaction for monodisperse TPP-chitosan microparticles. Sensors and Actuators B: Chemical. 2007;124:510-6.

[12] Yang C-H, Lin Y-S, Huang K-S, Huang Y-C, Wang E-C, Jhong J-Y, et al. Microfluidic emulsification and sorting assisted preparation of monodisperse chitosan microparticles. Lab on a Chip. 2009;9:145-50.

[13] Zhang H, Betz A, Qadeer A, Attinger D, Chen W. Microfluidic formation of monodispersed spherical microgels composed of triple-network crosslinking. Journal of Applied Polymer Science. 2011;121:3093-100.

[14] Kumachev A, Greener J, Tumarkin E, Eiser E, Zandstra PW, Kumacheva E. High-throughput generation of hydrogel microbeads with varying elasticity for cell encapsulation. Biomaterials. 2011;32:1477-83.

[15] Kumachev A, Tumarkin E, Walker GC, Kumacheva E. Characterization of the mechanical properties of microgels acting as cellular microenvironments. Soft Matter. 2013;9:2959-65.

[16] Velasco D, Tumarkin E, Kumacheva E. Microfluidic encapsulation of cells in polymer microgels. Small. 2012;8:1633-42.

[17] Wan J. Microfluidic-Based Synthesis of Hydrogel Particles for Cell Microencapsulation and Cell-Based Drug Delivery. Polymers. 2012;4:1084-108.

[18] Chung BG, Lee KH, Khademhosseini A, Lee SH. Microfluidic fabrication of microengineered hydrogels and their application in tissue engineering. Lab on a Chip - Miniaturisation for Chemistry and Biology. 2012;12:45-59.

[19] Zhang H, Tumarkin E, Peerani R, Nie Z, Sullan RMA, Walker GC, et al. Microfluidic Production of Biopolymer Microcapsules with Controlled Morphology. Journal of the American Chemical Society. 2006;128:12205-10.

[20] Huang G, Zhang X, Xiao Z, Zhang Q, Zhou J, Xu F, et al. Cell-encapsulating microfluidic hydrogels with enhanced mechanical stability. Soft Matter. 2012;8:10687-94.

[21] Buckley CT, Thorpe SD, O'Brien FJ, Robinson AJ, Kelly DJ. The effect of concentration, thermal history and cell seeding density on the initial mechanical properties of agarose hydrogels. Journal of the Mechanical Behavior of Biomedical Materials. 2009;2:512-21.

[22] Xue Z-X, Yang G-P, Wang G-C, Niu J-F, Cao X-Y. Preparation of porous chitosan/agarose microsphere and its R-phycoerythrin release properties. Journal of Applied Polymer Science. 2007;103:2759-66.

[23] Hu Z, Li S, Yang L. Preparation of berbamine loaded chitosan-agarose microspheres and in vitro release study. Polímeros. 2012;22:422-6.

[24] Xia Y, Whitesides GM. Soft lithography. Annual Review of Materials Science. 1998;28:153-84.

[25] Wallraff GM, Hinsberg WD. Lithographic Imaging Techniques for the Formation of Nanoscopic Features. Chemical Reviews. 1999;99:1801-22.

[26] Oláh A, Hillborg H, Vancso GJ. Hydrophobic recovery of UV/ozone treated poly(dimethylsiloxane): adhesion studies by contact mechanics and mechanism of surface modification. Applied Surface Science. 2005;239:410-23.

[27] McDonald JC, Duffy DC, Anderson JR, Chiu DT, Wu H, Schueller OJ, et al. Fabrication of microfluidic systems in poly(dimethylsiloxane). Electrophoresis. 2000;21:27-40.

[28] Duffy DC, McDonald JC, Schueller OJA, Whitesides GM. Rapid Prototyping of Microfluidic Systems in Poly(dimethylsiloxane). Analytical Chemistry. 1998;70:4974-84.

[29] Martynova L, Locascio LE, Gaitan M, Kramer GW, Christensen RG, MacCrehan WA. Fabrication of plastic microfluid channels by imprinting methods. Anal Chem. 1997;69:4783-9.

[30] Anderson JR, Chiu DT, Jackman RJ, Cherniavskaya O, McDonald JC, Wu H, et al. Fabrication of Topologically Complex Three-Dimensional Microfluidic Systems in PDMS by Rapid Prototyping. Analytical Chemistry. 2000;72:3158-64.

[31] McDonald JC, Chabinyc ML, Metallo SJ, Anderson JR, Stroock AD, Whitesides GM. Prototyping of microfluidic devices in poly(dimethylsiloxane) using solid-object printing. Anal Chem. 2002;74:1537-45.

[32] Owen MJ, Smith PJ. Plasma treatment of polydimethylsiloxane. Journal of Adhesion Science and Technology. 1994;8:1063-75.

[33] Kim J, Chaudhury MK, Owen MJ. Hydrophobic Recovery of Polydimethylsiloxane Elastomer Exposed to Partial Electrical Discharge. Journal of Colloid and Interface Science. 2000;226:231-6.

[34] Morra M, Occhiello E, Marola R, Garbassi F, Humphrey P, Johnson D. On the aging of oxygen plasma-treated polydimethylsiloxane surfaces. Journal of Colloid and Interface Science. 1990;137:11-24.

[35] McDonald JC, Whitesides GM. Poly(dimethylsiloxane) as a Material for Fabricating Microfluidic Devices. Accounts of Chemical Research. 2002;35:491-9.

[36] Zhao C-X. Multiphase flow microfluidics for the production of single or multiple emulsions for drug delivery. Advanced Drug Delivery Reviews. 2013;65:1420-46.

[37] Khan IU, Serra CA, Anton N, Vandamme T. Microfluidics: A focus on improved cancer targeted drug delivery systems. Journal of Controlled Release. 2013;172:1065-74.

[38] Nie Z, Seo M, Xu S, Lewis PC, Mok M, Kumacheva E, et al. Emulsification in a microfluidic flow-focusing device: Effect of the viscosities of the liquids. Microfluidics and Nanofluidics. 2008;5:585-94.

[39] Song H, Bringer MR, Tice JD, Gerdts CJ, Ismagilov RF. Experimental test of scaling of mixing by chaotic advection in droplets moving through microfluidic channels. Appl Phys Lett. 2003;83:4664-6.

[40] Anna SL, Bontoux N, Stone HA. Formation of dispersions using “flow focusing” in microchannels. Applied Physics Letters. 2003;82:364-6.

[41] Nie Z, Seo M, Xu S, Lewis P, Mok M, Kumacheva E, et al. Emulsification in a microfluidic flow-focusing device: effect of the viscosities of the liquids. Microfluidics and Nanofluidics. 2008;5:585-94.

[42] Wang Y, Tumarkin E, Velasco D, Abolhasani M, Lau W, Kumacheva E. Exploring a direct injection method for microfluidic generation of polymer microgels. Lab on a Chip. 2013;13:2547-53.

[43] Jiang K, Xue C, Arya C, Shao C, George EO, Devoe DL, et al. A new approach to in-situ "micromanufacturing": Microfluidic fabrication of magnetic and fluorescent chains using chitosan microparticles as building blocks. Small. 2011;7:2470-6.

Chapter 5

FERROFLUID LOADED CHITOSAN NANOPARTICLES

This chapter described first the preparation of chitosan nanoparticles by electrostatic interaction among positively charged chitosan and negatively charged sodium tripolyphosphate (TPP) molecules, which act as crosslinking agent. It also includes, the optimization of the protocols used for chitosan nanoparticles preparation. Secondly, this section describes the synthesis of chitosan nanoparticles loaded with ferrofluid. After that, all chitosan nanoparticles were characterized by morphological studies, structural analysis, thermal stability, rheological studies, and cytotoxicity. Finally, chitosan nanoparticles loaded with ferrofluid were evaluated for hyperthermia applications.

5.1. INTRODUCTION

In recent years, the preparation of magnetic chitosan nanoparticles has attracted a great attention in the research community in order to develop thermoseeds for magnetic hyperthermia that can be injected for localized therapy [1-3]. This challenge with the fact that sodium tripolyphosphate (TPP) is a polyanion categorized as being GRAS (generally recognized as safe) by the FDA (Food and Drug administration)[4]. It has made chitosan nanoparticles crosslinked with TPP, be applied for many biomedical applications, as gene delivery[5], to immobilize enzymes[6] and drug delivery[7-10]. Also, the crosslinking reaction of chitosan with TPP constitutes a mild and efficient method to achieve chitosan nanoparticles [11, 12]. Because, chitosan particles are formed mainly through the electrostatic interaction between positively charged chitosan and negatively charged TPP molecules. Magnetic chitosan nanoparticles can be prepared *in situ* with tiny pools of water-in-oil microemulsion containing chitosan and ferrous salt as micro-reactors by adding the basic precipitant, NaOH, into the micro-emulsion[13]. The encapsulation of preformed iron oxide nanoparticles can be stabilized by crosslinking chitosan with glutaraldehyde[14] or tripolyphosphate salts (TPP).

The understanding of the macroscopic rheological properties of the resulting aqueous colloidal dispersions is of paramount importance for the design of biomedical applications[15]. In a recent report, the packing of chitosan nanoparticles to form microgels from aqueous suspensions was ascertained through rheological measurements for samples with different particle sizes obtained by varying the chitosan to TPP ratio. It is well known, that nanoparticles can aggregate to form clusters that are mass fractal objects, these clusters would then interconnect, leading to a liquid-like to solid-like transition, that means can be considered as gel[16]. In order to study the packing of chitosan nanoparticles and try to understand if the elastic properties are consequence of the intrinsic elasticity of the particles or, on the contrary, by interactions among particles, fractal analysis rises as suitable tool to study the colloidal structure of chitosan nanoparticles dispersion. There are many scaling theories that can be applied for fractal analysis as was described in the introduction. However in this work, we study the gel behavior of chitosan nanoparticles when we apply a shear rate to the system and then will be analyzed if chitosan nanoparticles are able to overcome the repulsive interaction energy barrier, leading to the formation of a gel. Specifically, Wu and Morbidelli model, is based on previous models[17] where the scaling model is defined by two separate regimes: the strong-link regime at low particle concentrations and the weak-link regime at high particle concentrations.[18] But the main feature is that Wu and Morbidelli model includes a third regime, the intermediate regime, which considerer the elastic contributions of both inter- and intrafloc links. Even the interest of magnetic chitosan nanoparticles to be applied into the body as injectable system and where it has not been reported in the literature a deeply study of the correlation of composition, rheology and application.

In this chapter, first the preparation of chitosan nanoparticles is described and then the encapsulation of ferrofluid nanoparticles into chitosan nanoparticles crosslinked with TPP. This work has as objective, to answer to requirements if the chitosan nanoparticles can be considered as injectable material. For that, the rheological properties of the aqueous dispersions were investigated through dynamic rheological measurements. The rheological characterization will allow determining the structural organization of these materials by relating their linear viscoelastic properties to their properties in dispersion by means of scaling laws [19, 20]. The work extends to a study

on remote heating by a magnetic field and the study of cytotoxicity to evaluate the application of the materials obtained in magnetic hyperthermia treatment.

5.2. EXPERIMENTAL PART

5.2.1 Materials

Chitosan supplied by Polymers Laboratory, National University, Costa Rica and ferrofluid, were the same previously described in chapter 3.

Acetic acid (Aldrich) and sodium tripolyphosphate (Aldrich) were used as received. For the biological tested were used fibroblasts of human embryonic skin (HFB, Innoprot). The culture medium was Dulbecco's modified Eagle's medium enriched with4500 mg/mL of glucose (DMEM, Sigma) and supplemented with 10% fetal bovine serum (GIBCO, Life Technologies, Spain), 200 mMl-glutamine, 100 units/mL penicillin and 100 mg/mL streptomycin,modified with HEPES (Sigma, Spain). The Alamar Blue (AB) was provided by Serotec, Spain.

5.2.2 Preparation of chitosan–sodium tripolyphosphate nanoparticles (CS+TPP).

Chitosan nanoparticles were prepared as reported elsewhere[12] with some modifications. In this experiment, different parameters involved in chitosan nanoparticles preparation were assessed such as, concentrations of chitosan and sodium tripolyphosphate (TPP) and chitosan:TPP volumetric ratios. First, chitosan solutions of different concentrations (0.05, 0.2 and 0.5% (w/v) were prepared by dissolving the appropriate amount of chitosan in 1% (w/v) acetic acid solution. Then, sodium tripolyphosphate (TPP) was dissolved in Milli-Q water to a final concentration of 0.05% and 0.5% (w/v). Chitosan nanoparticles were formed instantly at room temperature by

dropwise addition of TPP solution into a 30 mL of chitosan stock solution under severe magnetic stirring (8600 rpm). The nanoparticles were formed at selected chitosan:TPP volumetric ratios of 20:1, 5:1, 2.5:1, 2:1 and 1.7:1.

Finally, chitosan nanoparticles are collected by centrifugation and washed one time with distilled water. Aqueous dispersions of CS+TPP nanoparticles were centrifuged at 5000 rpm, for 20 min. The residue containing the big particles is discarded and the supernatant, where the small CS+TPP nanoparticles remain, is collected. The supernatant was separated and then it was dried by lyophilization. Table 5.1, shows all the samples prepared in this section and their respectives names.

Table 5.1. All chitosan nanoparticles prepared and their respective names.

TPP		**Concentrations of chitosan % (w/v)**		
Concentration % (w/v)	**Ratios CS:TPP**	**0,05%**	**0,20%**	**0,50%**
0,05%	20:1	x	x	x
	5:1	x	x	x
	2.5:1	x	x	x
	2:1	x	x	x
	1.7:1	x	x	x
0,50%	20:1	x	x	x
	5:1	x	x	**0.5CS-0.5TPP**
	2.5:1	x	x	x
	2:1	x	x	x
	1.7:1	x	x	x

Samples were named as follow: *x*CS-*y*TPP, where *x* represents the concentration of chitosan and *y* the concentration of TPP employed.

5.2.3 Preparation of ferrofluid loaded chitosan nanoparticles (NP+Fe).

First, for this study was selected a chitosan and TPP concentration of 0.5% (w/v). The method of preparation for these solutions was the same described in the previous section.

Chitosan nanoparticles loaded with three different ferrofluid contents (NP+Fe) were prepared by the following steps: firstly, a determined amount of pure ferrofluid was dispersed in 5 mL of Mili-Q water in order to yield final concentrations of 0.5, 2 and 5% (w/v). The resulting ferrofluid solution (5 mL) was added under vigorous stirring to 30 mL of a chitosan solution (0.5% w/v, pH=3.5) in 1% (v/v) acetic acid in a N_2 atmosphere. Secondly, an aqueous TPP solution (0.5% w/v, pH=9.2) was dropped into the chitosan solution containing ferrofluid nanoparticles (final pH~4, for all the samples). This step allowed encapsulating ferrofluid nanoparticles into CS+TPP nanoparticles, as will be demonstrated. Finally, aqueous dispersions of NP+Fe nanoparticles were washed one time with distilled water and were centrifuged at 5000 rpm, for 20 min. As in the previous section the supernatant of NP+Fe was separated and subjected to freeze-drying and storage.

The ferrofluid concentration in the chitosan nanoparticles was determined through UV spectroscopy. Samples were digested in HNO_3 and HCl 6M and iron concentration was measured spectrophotometrically at the λ_{max} of 478 nm. Ferrofluid loaded chitosan nanoparticles were named NP+Fex, where x correspond to 1, 3.2 and 5.6% (w/v) of ferrofluid, determined by UV spectroscopy, see Table 5.2.

Table 5.2. Chitosan nanoparticles loaded with ferrofluid and the control.

Sample	**Chitosan (% w/v)**	**TPP (% w/v)**	**Fe (% w/v)***
CS+TPP	0.5	0.5	-
NP+Fe1%	0.5	0.5	1
NP+Fe3.2%	0.5	0.5	3.2
NP+Fe5.6%	0.5	0.5	5.6

* Determined by UV spectroscopy.

5.2.4 Characterization

i. Determination of particle size and zeta potential of chitosan nanoparticles by Dynamic Light Scattering

Dynamic light scattering (DLS, Malvern Nanosizer Nano S) was employed for the determination of electrophoretic mobility (surface charge) and hydrodynamic diameter of chitosan nanoparticles and ferrofluid loaded chitosan nanoparticles dispersed in Mili-Q water at 25 °C, the resulting pH of the dispersions was 4.5. For hydrodynamic diameter determinations, a backscattering detection angle of 173° was employed. The electrophoretic mobility was transformed into zeta potential using the Smoluchowski equation. All measurements were repeated three times and the average of three runs was taken as the result.

ii. Morphological studies

- Scanning Electron Microscopy (SEM) and Scanning Electron Microscopy with electron transmission (FESEM)

The morphologies of the chitosan nanoparticles were observed with SEM (XL30 ESEM, Philips). One drop of chitosan nanoparticles dispersion was dropped on a flat microscopy glass. All samples were kept at room temperature overnight to dry the sample by evaporation of the water. Subsequently the dried sample was coated with an ultrathin coating of gold deposited on the sample by high-vacuum metallization.

Micrographs of the chitosan nanoparticles loaded with ferrofluid were taken using a FESEM Hitachi model SU8000 HRSEM used in the TE (electron transmission) detector bright field mode and SE operated at 0.5-30 KV. One drop corresponding to aqueous dispersions of each of the samples under study was deposited on the Formvar carbon-coated Cu grid.

- Atomic Force Microscopy (AFM)

AFM images of CS+TPP were obtained with a Multimode Scanning probe microscope (di NanoScope IVa Controller, Veeco) in contact mode and using a Veeco/Bruker, model RTESP cantilever with a 300 kHz resonant frequency and a nominal force constant near 40 N/m. Topographic images were recorded in the conventional height mode (tapping mode, normal AFM) at a scan rate of 0.5 and 1.5 Hz. The nanoparticles diameter was calculated using the ImageJ software and was the average of 100 nanoparticles.

iii. Study of the chemical structure by Attenuated Total Reflection Fourier Transformed Infra-Red Spectroscopy (ATR-FTIR)

Attenuated Total Reflection Fourier Transformed Infra-Red Spectroscopy (ATR-FTIR) was carried out on freeze-dried samples. ATR-FTIR was performed on a Spectrum One FT-IR Spectrometer of Perkin Elmer. The spectra were scanned over the wave number range of 4000 to 450 cm^{-1} at a resolution of 2 cm^{-1}.

iv. Determination of crystallinity by X-ray diffraction measurements (XRD)

The crystallinity of the chitosan nanoparticles and chitosan nanoparticles loaded with ferrofluid was determined by X-ray diffraction (XRD). The X-ray diffraction (XRD) spectra of chitosan, CS+TPP and NP+Fe 3.2% were performed using a Bruker Advance D8 X-ray diffraction spectrometer with a CuK_{α} target at 40 kV and 50mA. The sample was scanned from 5º to 70º at 2θ.

v. Thermal stability by thermogravimetric analysis (TGA)

Thermogravimetric analysis (TGA) was carried out on a Q500 TA Instruments thermal gravimetric analyzer. Each freeze-dried sample under study (10–15 mg) was placed in the TGA furnace and the measurements were carried out under nitrogen atmosphere with a heating rate of 10 ºC/min from 25 to 700 ºC.

5.2.5 Rheological studies by dynamic oscillatory measurements

Viscoelastic behavior of samples has been performed by dynamic oscillatory measurements. Then, the structural organization of chitosan nanoparticles will be determining by fractal analysis.

i. Dynamic oscillatory study.

Dynamic oscillatory measurements were performed in a AR-G2 rheometer (TA Instruments, USA). The geometry used was 60 mm acrylic parallel plates. Samples under study were dispersed in ultrapure water at concentrations ranging from 0.5 to 2% (w/v). This range was chosen because concentrations higher than 2% (w/v) did not allow the homogeneous dispersion of the samples in water and lower than 0.5% w/v did not allow the rheological characterization due to the torque limit. Strain sweep tests were carried out at a constant, nondestructive 0.5 Hz frequency. All measurements were done at room temperature.

ii. Fractal analysis of chitosan nanoparticles.

In order to understand the gel network formation in suspensions, the scaling concept based on the fractal model was applied. For that, it has been employed the scaling theories developed by Shih et al. and Wu and Morbidelli, described in chapter 2.

5.2.6 *In vitro* studies of chitosan nanoparticles

In order to consider the chitosan nanoparticles prepared in this work for biomedical applications, it is necessary to assess their cytotoxicity. For that, the following analyses were employed.

i. Morphological analysis of Fibroblast treated with NP+Fe by Scanning Electron Microscopy (SEM).

Sample preparation required the seed of approximately $5x10^5$ cells (Fibroblast) per coverslip. After 24 h of incubation, the medium was replaced, as example, with the corresponding aqueous dispersion of NP+Fe3.2% at a concentration of 0.6 mg/mL and incubated at 37ºC for 24 h. Then, samples were washed twice with PBS to remove excess NP+Fe3.2% and then fixed with glutaraldehyde. The dehydration process was conducted using increasing concentrations of ethanol. Samples were then gold-coated and observed using a Nova 200 NanoLab, FEI Company, The Netherlands. SEM images were observed using the electron beam at a voltage of 5 kV and current of 0.4 nA. This experiment was carried out in the Institute of Nanoscience of Aragon, Zaragoza in collaboration with the Professor Gerardo Goya.

ii. Cell culture conditions

The biological response to the materials was tested with fibroblasts of human embryonic skin (FBH).

The culture medium was changed at selected time intervals with little disturbance to culture conditions. Cells without treatment were used as a negative control. NP+Fe samples were dispersed in fresh medium without phenol red at different concentrations. Samples were sterilized with a UV lamp (HNS OSRAM, 263 nm, 3.6 UVC/W) at a power of 11W for 4 h. Sterile plastic was supplied by Sasrtedt, Spain.

iii. Cytotoxicity analysis. Alamar Blue Assay

For determination of cytotoxicity, the Alamar Blue (AB was provided by Serotec, Spain) assay was performed. Cells were seeded at a density of $8x10^4$ cells/mL in complete medium in a sterile 96-well culture plate and incubated to confluence, which means that a monolayer of cells is formed.

After 24 h of incubation, the medium was replaced with the corresponding aqueous dispersions of three NP+Fe samples at different concentrations (Table 5.3) and

incubated at 37 ºC in humidified air with 5% CO_2 for 24 h. After this time, a solution of AB was prepared in warm medium without phenol red and the plates were incubated at 37 ºC for 4 h. Finally, fluorescence was measured with a Biotek Synergy HT detector using an emission wavelength of 590 nm and an excitation wavelength of 530 nm.

In order to determine cell viability, the experiment was performed at different nanoparticles concentration. Cell viability (*CV*) was calculated with the following equation:

$$CV = 100 \times \left(\frac{FD_s - FD_B}{FD_C - FD_B} \right) \qquad \text{Equation 5.1}$$

where FD_S, FD_B, and FD_C are the fluorescence density of the AB for the sample (S), blank (B) (culture medium without cells), and control (C).

Table 5.3. Experimental concentrations (mg/mL) employed in cytotoxicity Alamar blue assay.

D1:	2.50mg/mL	D6:	0,078 mg/mL
D2:	1.250 mg/mL	D7:	0,039mg/mL
D3:	0,625 mg/mL	D8:	0,020 mg/mL
D4:	0,313 mg/mL	D9:	0,010 mg/mL
D5:	0,156 mg/mL	D10:	0,005 mg/mL
		D11	0,002 mg/mL

iv. Lactate dehydrogenase assay

In order to study if the cell death is due to damage in the plasma membrane, lactate dehydrogenase was carried out. For that, LDH cytotoxicity assay kit (Innoprot, Spain) was employed. LDH catalyses the reduction of NAD+ to NADH in the presence of L-lactate, while the formation of NADH can be measured in a coupled reaction in which the tetrazolium salt is reduced to a red formazan product. The amount of the highly colored and soluble formazan can be measured at 490 nm spectrophotometrically.

The protocol is analogous to the Alamar Blue assay. The concentrations employed for the preparation of aqueous dispersions of NP+Fe samples were 1 and 0.05 mg/mL.

5.2.7 Determination of Magnetic Remote Heating.

The specific power absorption (SPA) of the aqueous dispersions of NP+Fe samples at a 5% (w/v) concentration was measured with a commercial AC field applicator (DM100 by nB nanoscale Biomagnetics, Spain) working at f=580 kHz and 24 kA/m (≈300 Oe). Experiments were carried within a thermally -insulated working space of about 1 cm^3, using a closed container of 1.0 mL volume conditioned for measurements in liquid phase. A schematic representation of the equipment is shown in Figure 5.1-a and a photograph of the commercial equipment employed is shown in 5.1-b. This experiment was carried out in the Institute of Nanoscience of Aragon, Zaragoza in collaboration with the Professor Gerardo Goya.

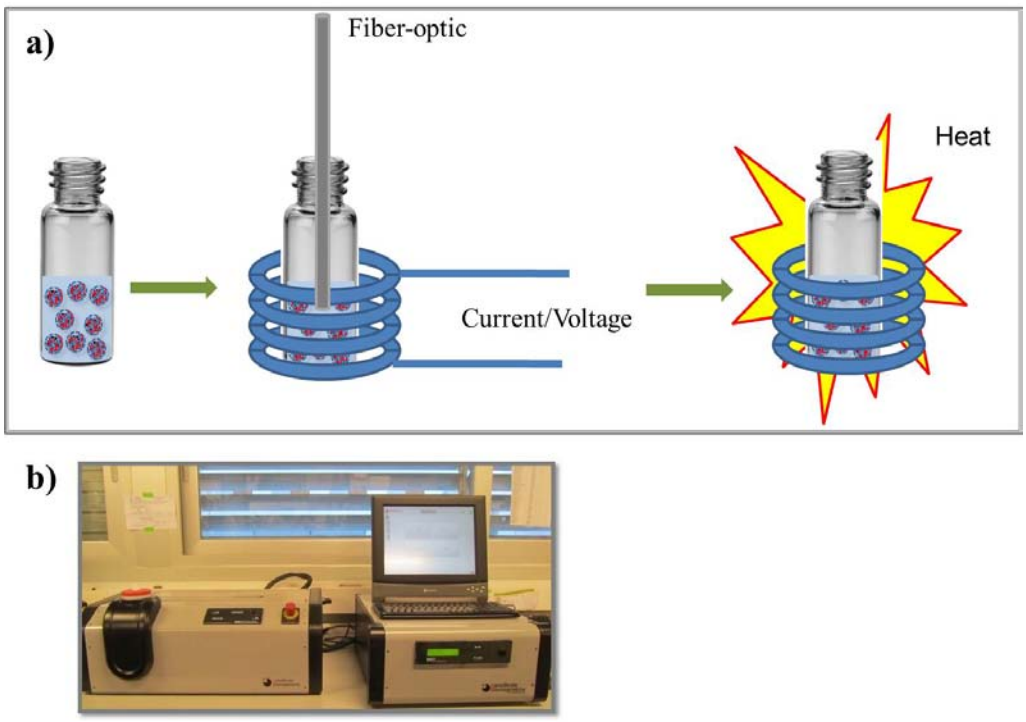

***Figure 5.1**. a) Scheme of hyperthermia experiments and b) commercial equipment AC field applicator (DM100).*

5.3. RESULTS AND DISCUSSION

5.3.1 Optimization of experimental conditions for the preparation of chitosan nanoparticles.

Particle size is one of the most important issues for biomedical applications. For this reason, it was necessary to study the influence of the main experimental parameters such as chitosan and TPP concentrations and volumetric ratios, in order to select the better conditions to obtain nanoparticles with an appropriate size.

Chitosan nanoparticles were synthesized by the ionic crosslinking reaction method between the protonized ammonium groups of chitosan and the tripolyphosphate anions of TPP, as Figure 5.2 shows.

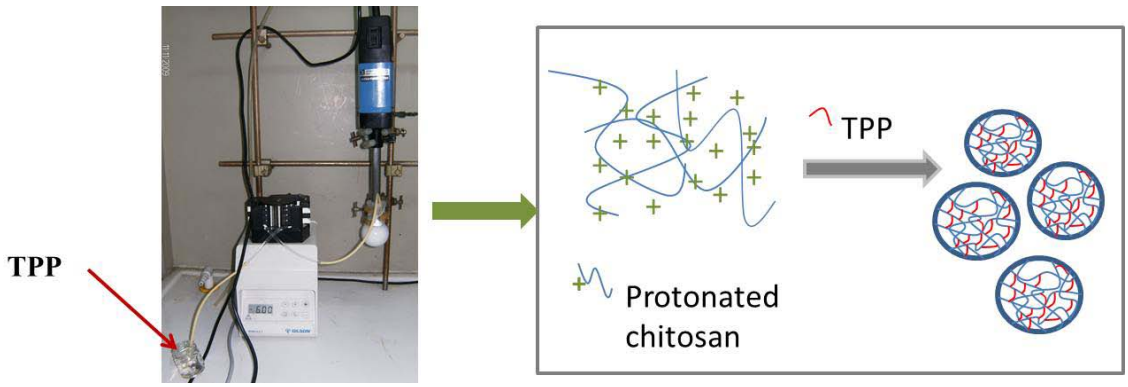

***Figure 5.2**. Scheme of chitosan nanoparticles formation.*

The acid media guarantees the protonation of the amino groups of chitosan. Therefore, only for some speficic ratios among chitosan and TPP were favored the inter and intramolecular linkages created between TPP and the positively charged amino groups of CS, which are responsible of the particles formation. As a previous step, in order to select the most appropiated experimental parameters regarding chitosan and TPP concentration and volumetric rations, we checked the precipitation of aqueous solutions containing different volumetric rations between chitosan and TPP. As known, the apparition of a precipitate indicates the formation of big chitosan nanoparticles. On

the contrary, the presence of transparency indicates that particles were no formed. When the final solution is opalescent, the particles are found to be in the nanometric size. [12] Therefore, based on these assumptions, samples which presented precipitates and or were transparent, were discarded.

Figure 5.3 shows representative photographs of chitosan nanoparticles, specifically for series 0.2CS-0.05TPP (Figure 5.3-a) and 0.2CS-0.5TPP (Figure 5.3-b). In the first photograph, it is possible to observe that final samples are very transparent and on the contrary, from Figure 5.3-b it is evident the different states of samples obtained on function of the volumetric ratio employed, transparent, precipitate and opalescence.

Among of the series prepared, 0.5CS-0.5TPP was found to be the most appropriated in the almost all range of chitosan and TPP concentrations.

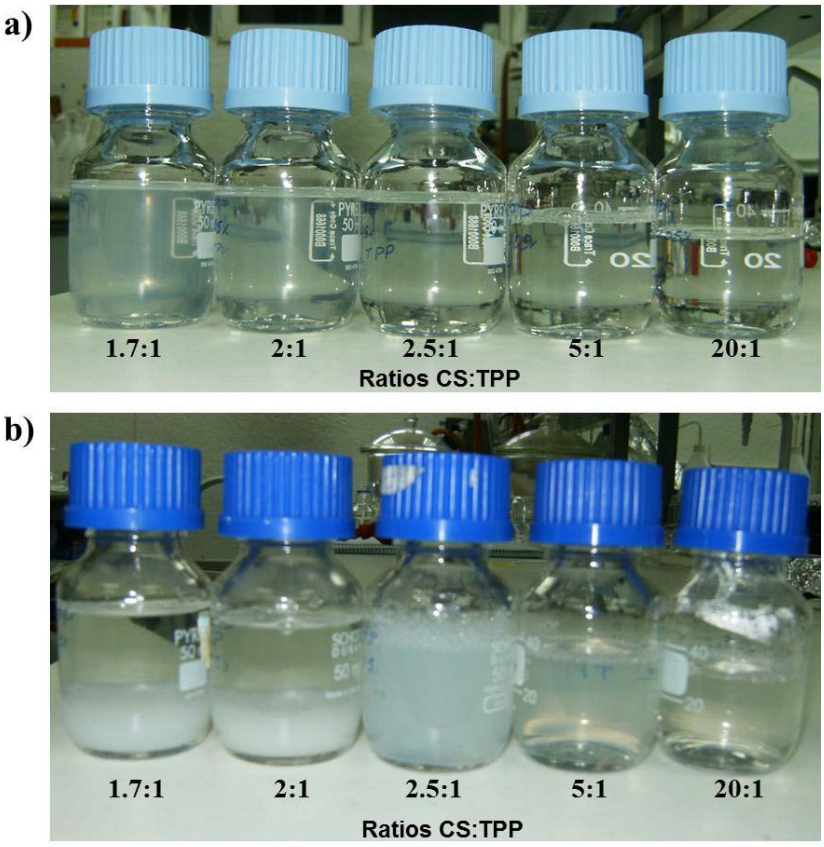

***Figure 5.3**. Photograph of chitosan nanoparticles for a) 0.2CS-0.05TPP and b) 0.2CS-0.5TPP sample.*

Chitosan nanoparticles of series 0.5CS-0.5TPP were analyzed by Scanning Electron Microscopy (SEM). As an example, Figure 5.4 shows, SEM micrographs corresponding to the samples of the series 0.5CS-0.5TPP with three different CS:TPP

volumetric ratios, 20:1, 5:1 and 1.7:1. From these micrographs, it is that particles formations were favored only for some specific volumetric rations of chitosan and TPP. Therefore, sample 0.5CS-0.5TPP with a volumetric ratio of (5:1) presented a good dispersion and small particles size in the order of nanometer, later determined by AFM and dynamic light scattering.

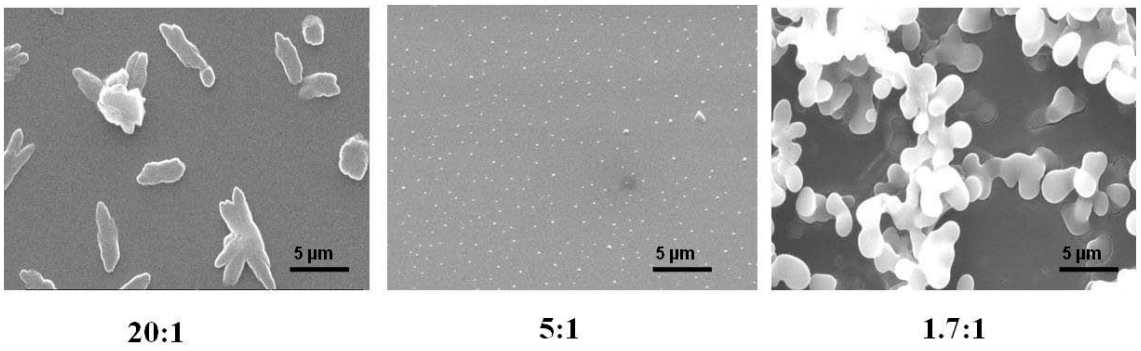

Figure 5.4. *Micrograph corresponding to the sample 0.5CS-0.5TPP with different ratios CS:TPP.*

After to study different volumetric ratios among chitosan and the TPP as crosslinking agent and taking into account their final state (clear, opalescent or precipitate solutions), for the next experiment were select the following conditions: chitosan and TPP concentration of 0.5% (w/v) (0.5CS-0.5TPP) and a volumetric ratio of 5:1. Sample will be denoted as CS+TPP.

Figure 5.5 shows AFM results for CS+TPP nanoparticles. Figure 5.5-a, shows topography with a field of view of 2 × 2 µm and a height range of approximately 15.8 nm, where it is evident its spherical shape and small size. In Figure 5.5-b, is shown the 3D image and Figure 5.5-c corresponds to the frequency of CS+TPP nanoparticles counted from ImageJ and its Gaussian curve. The mean diameter of CS+TPP nanoparticles calculated by ImageJ is approximately 154 nm.

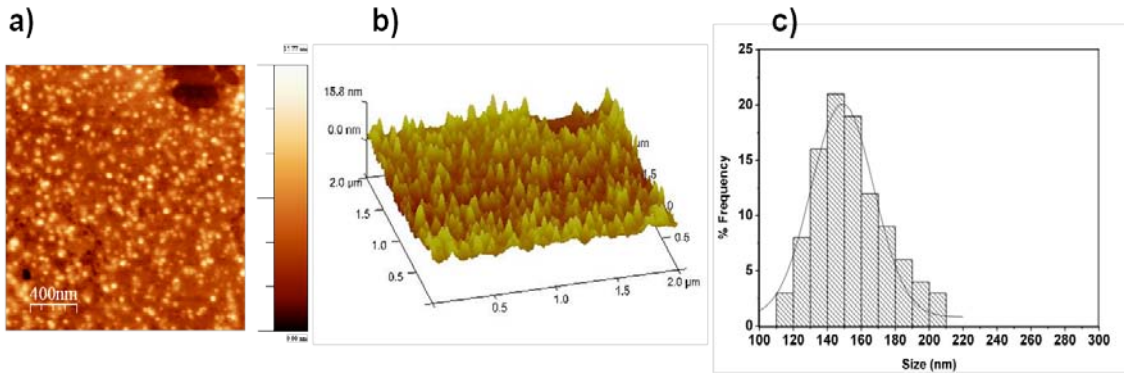

Figure 5.5. *AFM images a) Topography (area 2 × 2 µm), b) 3D images and c) histogram, of CS+TPP.*

The crosslinking degree of CS+TPP nanoparticles was 68% as determined by the ninhydrin test. Ninhydrin is extensively used in the analytical determination of amino acids and related structures because it can react with a variety of primary and secondary amines producing Ruhemann purple color. This product has a maximum absorbance at 570 nm[21].

5.3.2 Preparation of chitosan nanoparticles loaded with ferrofluid.

Chitosan nanoparticles loaded with ferrofluid (NP+Fe) were prepared with concentrations of chitosan and TPP at 0.5% (w/v) selected in the previous section.

NP+Fe were synthesized by the ionic crosslinking reaction between the protonized ammonium groups of chitosan and the tripolyphosphate anions of TPP. Ferrofluid with three concentrations (1, 3.2 and 5.6% (w/v)) were successully encapsulated into chitosan matrix, as later will be corroborated by FESEM. An electrostatic interaction is established in the reaction between chitosan and TPP, enabling the encapsulation of an amount of ferrofluid (negative surface charge) within a positive matrix (chitosan) and negative charge by its phosphate groups of TPP a acting as ionic crosslinking agent [22]. A schematic representation of the preparation of NP+Fe samples is shown in Figure 5.6.

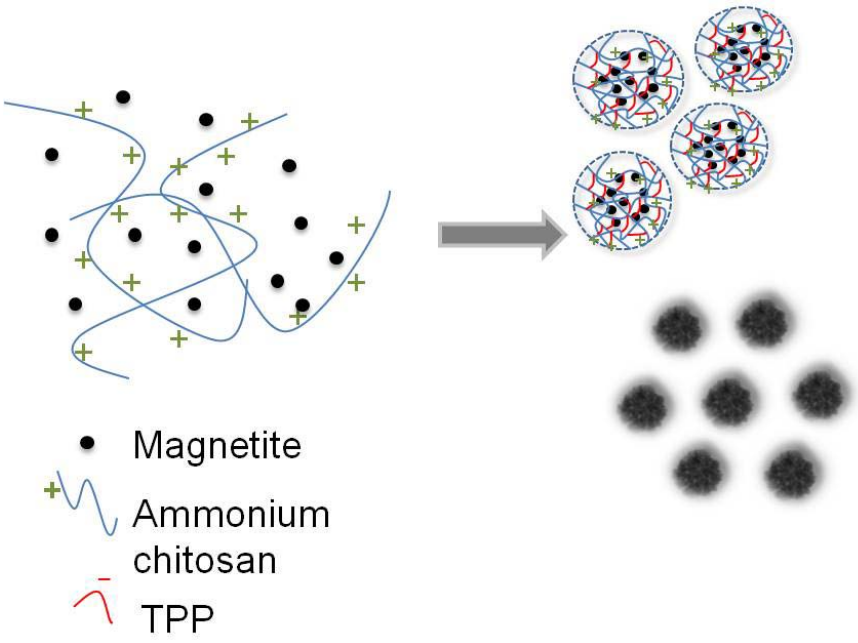

Figure 5.6. *Scheme of preparation of ferrofluid loaded chitosan nanoparticles.*

i. Determination of particle size and zeta potential.

After the ferrofluid loaded chitosan nanoparticles preparation, particles size and zeta potencial were determined by Dynamic Light Scattering (DLS). As can be observed in Table 5.3, ferrofluid encapsulation gives rise to an increase in the size of NP+Fe particles with respect to the CS+TPP particles from 192 to 259 nm, as ferrofluid content is increased from 1 to 5.6%. This result might be attributed to the fact that ferrofluid nanoparticles are subjected to Van der Waals forces and magnetic dipole-dipole interactions generated from residual magnetic moments[23]. Moreover, when compared particle size of CS+TPP obtained by AFM (described in the previous section) and DLS, the size obtained was 154 nm and 140 nm, respectively. The results are very similar and both techniques also corroborate that CS+TPP particles are in the nanometric range, which it is appropiated for biomedical applications.

Table 5.4. Ferrofluid concentration, mean particle size and zeta potential for samples under investigation.

Sample	Ferrofluid concentration* (mg/mL)	Mean Particle Size (nm)	Zeta potencial (mV)
CS+TPP	0	140± 1	63.4 ± 0.8
NP+Fe1%	1.0	192 ± 2	57.2 ± 2.0
NP+Fe3.2%	3.2	205 ± 3	59.3 ± 0.8
NP+Fe5.6%	5.6	259 ± 1	57.9 ± 6.6

*Determined through UV-vis spectroscopy.

Data shown are the mean ± standard deviation

Table 5.4 also reports the zeta potential for samples under investigation. The positive zeta potential encountered for the dispersion of CS+TPP sample (63.4 ±0.8 mV) in Mili-Q water (pH 4.5), it is due to the protonated ammonium groups in the acidic environment. The zeta-potential of all the NP+Fe samples remain positive in the range of 57-63 mV, in close agreement with previous results obtained by Zu et al.,[23]. If we take into consideration that the zeta-potencial corresponding to the commercial ferrofluid is negative (-75.8±3.2 mV). The obtained results suggest its encapsulation into the chitosan nanoparticles as will be corroboted through Scanning Electron Microscopy with electron transmission (FESEM).

ii. Morphological studies

Figure 5.7 shows FESEM micrographs corresponding to the ferrofluid loaded chitosan nanoparticles prepared. As a first general result, it is observed that all samples presented a spherical shape. Nevertheless, it is not possible to ensure if ferrofluid is encapsulated into chitosan matrix. For that a bright field (BF) mode was employed.

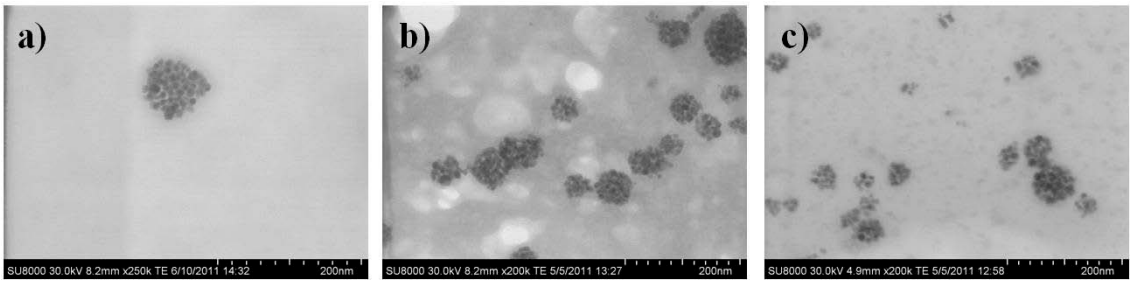

Figure 5.7. *Representative micrograph corresponding to magnetic chitosan nanoparticles: a) NP+Fe1%, b) NP+Fe3.2% and c)NP+Fe 5.6% by field emission scanning electron microscopy.*

Figure 5.8 shows bright field (BF) and SE image obtained for a representative micrograph corresponding to NP+Fe 5.6%.

Bright field image allows confirming the core-shell encapsulation of ferrofluid within a layer of chitosan that constitutes the shell. SE image taken on the same spot shows the smooth surface of the chitosan nanoparticles which confirms the ferrofluid encapsulation with a core-shell morphology[24] A Bright field FESEM microscopy obtained for the sample NP+Fe 5.6% at a high magnification is also shown in the figure 5.8-a, where it is very evident the core-shell morphology of NP+Fe 5.6% nanoparticles.

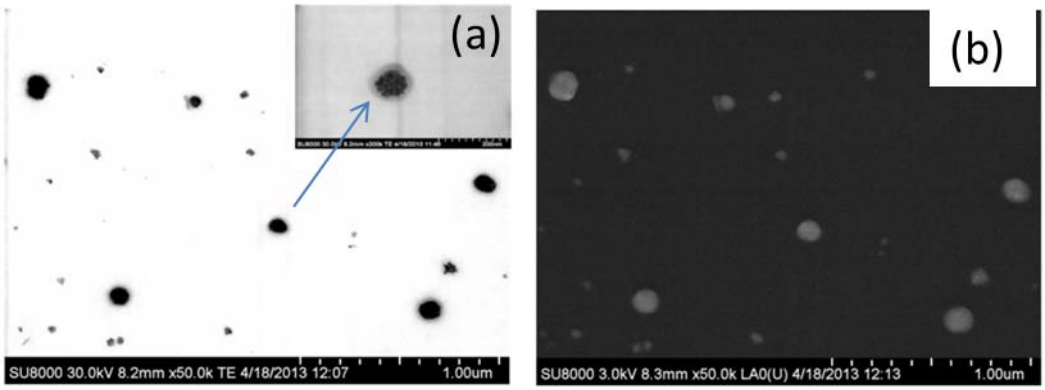

Figure 5.8. *Representative micrograph corresponding to the sample NP+Fe 5.6% by field emission scanning electron microscopy, corresponding to (a) bright field and (b) SE image. The inset in Figure 2a shows a magnification of a core-shell chitosan nanoparticle.*

The crosslinking of TPP and chitosan in the presence of ferrofluid (Figure 5.6) gives rise to its encapsulation into the chitosan nanoparticles. Size measurements performed on images obtained through bright field microscopy allows estimating that the magnetic core size is in the range 75-220 nm whereas the shell size varies in the range 21-39 nm.

iii. Analysis of the chemical structure.

FT-IR spectroscopy is an appropriate technique to study the chitosan-TPP interaction. Figure 5.9 shows ATR-FTIR spectra of pure TPP, chitosan, CS+TPP and NP+Fe 3.2%. In the TPP spectrum (Figure 5.9-a), the following characteristic bands are observed: 1218 cm^{-1} (P=O stretching), 1143 cm^{-1} (symmetric and antisymmetric stretching vibrations in PO_2 group), 1069 cm^{-1} (symmetric and antisymetric stretching vibrations of PO_3 group), 898 cm^{-1} (antisymmetric stretching of the P-O-P bridge).

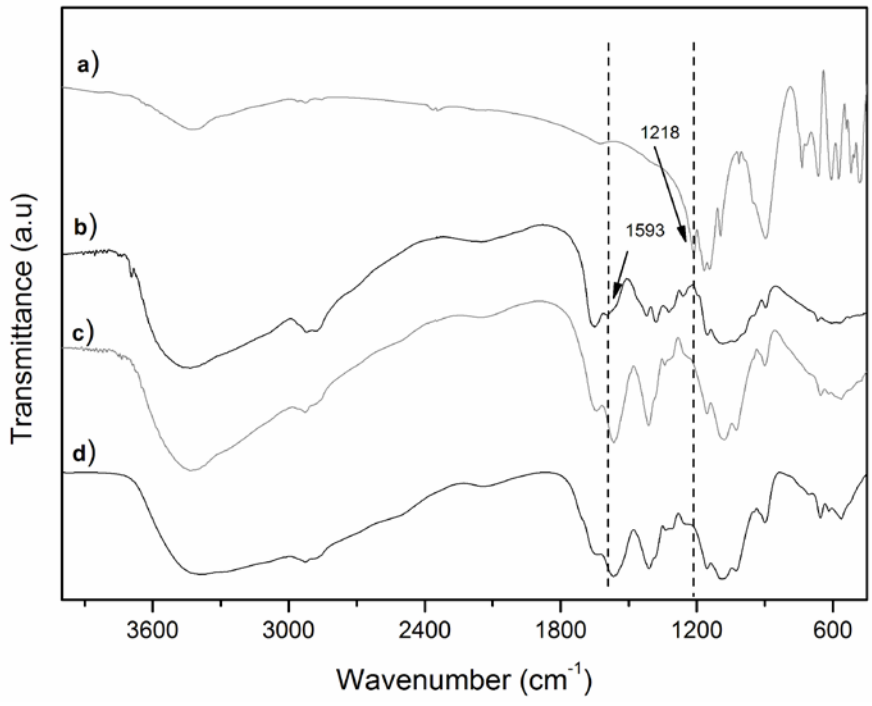

Figure 5.9. *FT-IR spectra corresponding to (a) TPP, (b) chitosan (c) NP+Fe 3.2% and (d) CS+TPP.*

The characteristic vibrational absorption bands observed in the chitosan spectrum (Figure 5.9-b) are the band at 1593 cm^{-1} corresponding to the N-H bending vibration overlapping the amide II vibration and that at 1652 cm^{-1} that corresponds to the amide I vibration[25]. Absorption bands at 1153 cm^{-1} (antisymmetric stretching of the C-O-C bridge), 1089 cm^{-1} and 1033 cm^{-1} (skeletal vibrations involving the CO stretching) are characteristic of the chitosan saccharide structure[26].

Therefore, since a shift in the δ_{NH3} vibration may be expected when NH_3^+ groups interact electrostatically with the negatively charged sites of the TPP as previously shown for chitosan nanocomposites[27]. In fact, a shift of the δ_{NH3} band towards a lower frequency is observed in the spectra corresponding to CS+TPP (Figure 5.9-d) and NP+Fe 3.2% (Figure 5.9-c) spectra for which the band at 1593 cm^{-1} (pointed in Figure 5.9) shifts to 1570 and 1568 cm^{-1} respectively. In both cases, the shift of the band position and the increase of intensity observed could be attributed to the ionic crosslinking between the NH_3^+ from chitosan and the $P_3O_{10}^{5-}$ from TPP [28]. In both spectra, a new band at 1218 cm^{-1} appears that can be assigned to P=O stretching vibrations in phosphate ions (pointed in Figure 5.9). In the spectrum corresponding to NP+Fe 3.2% (Figure 5.9-c), it is not possible to observe the characteristic band of iron oxide[29] centered at 563 cm^{-1} because of the overlapping with characteristic bands from chitosan and TPP.

iv. Determination of crystallinity by X-ray diffraction measurements (XRD)

X-ray diffraction (XRD) was employed to identify the crystallinity properties of the chitosan nanoparticles loaded with ferrofluid. The X-ray diffractograms of chitosan (a), CS+TPP (b) and NP+Fe 3.2% (c) are shown in Figure 5.10. The diffractogram of chitosan shows the diffraction peaks at $2\theta = 9.3°$ and 21.3º indicating its semicrystalline structure[30]. However, after the crosslinking reaction among chitosan and TPP, the CS+TPP diffractogram (Figure 5.10-b), shows reduction of the peak intensity, shift of peak positions and broadness of peaks to respect at chitosan diffractogram (Figure 5.10-a). This fact can be attributed to modification in the arrangement of molecules in the crystal lattice of chitosan by the TPP, which is in agreement with the results reported in the literature [8, 31, 32]. Moreover, new peaks at 8.8º and 11.4º and 26º appear for CS+TPP diffractogram (Figure 5.10-b), associated to the interaction (the crosslinking

reaction) among chitosan and TPP. This suggest new arrangements of molecules in the crystal lattice induced by ionic interaction[31].

As can be observed, chitosan nanoparticles loaded with ferrofluid (NP+Fe3.2%) diffractogram (Figure 5.10-c) are mainly amorphous, because the peaks corresponding to chitosan became much lower and wider. On the other hand, in agreement with the literature, it is observed news peaks at 30.1º, 35.6º, 42.8º, 54.1º, 57.3 and 62.8º which are related with XRD pattern of magnetite[30]. Therefore, this fact confirmed firstly, the presence of magnetite into the chitosan nanoparticles and secondly, that the coating process of chitosan does not result in the phase change of magnetite [33].

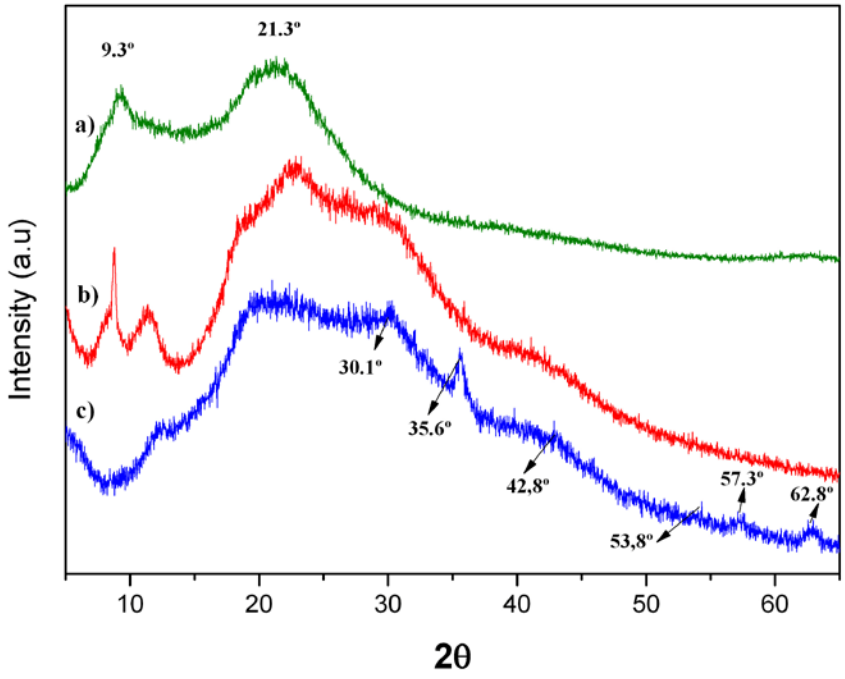

Figure 5.10. *Wide angle X-ray diffractograms of: (a) chitosan, (b) CS+TPP and (c) NP+Fe 3.2%.*

v. Analysis of the thermal degradation of the samples under study.

Thermal degradation of chitosan nanoparticles and ferrofluid loaded chitosan nanoparticles under study (Figure 5.11) was measured using thermogravimetric analysis (TGA). CS+TPP curve (Figure 5.11-a) presented three thermal steps. The first start at 30 ºC and continues up to 80 ºC during which there was 11% of weight loss, due to the loss of water on the surface [34]. Then, a second step is observed, which present an

onset temperature of 115 ºC and continues until 200 ºC, with a weight loss of 8% attributed to dehydration of the sample[35]. This thermal transition is observed as well in TPP thermogram (the inset thermogram). Finally, a third step is observed, with an onset temperature of 240 °C and with a weight loss of ~43%, which may be related to the decomposition of chitosan. Finally, CS+TPP presented a residue of 38% at 600 ºC. Table 5.4, summarizes thermal steps for all samples under study and its corresponding weight loss.

With regard to chitosan nanoparticles loaded with ferrofluid at 1% (Figure 5.11-b), 3.2% (Figure 5.11-c) and 5.6% (Figure 5.11-d) presented similar TGA curves than CS+TPP curve. NP+Fe 1% presented the first steps at 30-100 ºC related with the loss of water on the surface, then a second step is observed as well, with an onset temperature of 125 ºC which suggest the weight loss (6%) attributed to dehydration of the sample. As can be observed, the weight loss of NP+Fe1% is lower than CS+TPP for the second thermal transitions. This fact could be explained for the interaction among ferrofluid and matrix; therefore the number of bonds with water molecules decreases. On the other hand, this interaction among ferrofluid and matrix increase the thermal stability for NP+Fe1% to respect at CS+TPP in this second thermal step. Finally, the last thermal step with an onset temperature of 234 ºC is attributed to decomposition of the organics components with a weight loss of 45%.

However, NP+Fe3.2% and NP+Fe5.6% presented only two steps. The first star at 30 ºC and continues up to 170 ºC with a weight loss of 10% and 11% respectively, related with the loss of water. It is important to highlight that these samples do not present the second steps; this fact can suggest a higher interactions among magnetite and the matrix to respect at NP+Fe1% and CS+TPP. Finally, the last thermal step is observed as well, with an onset temperature of 231ºC and 224 °C, respectively, with a weight loss of 45% and 42%, respectively, attributed to decomposition of the chitosan matrix.

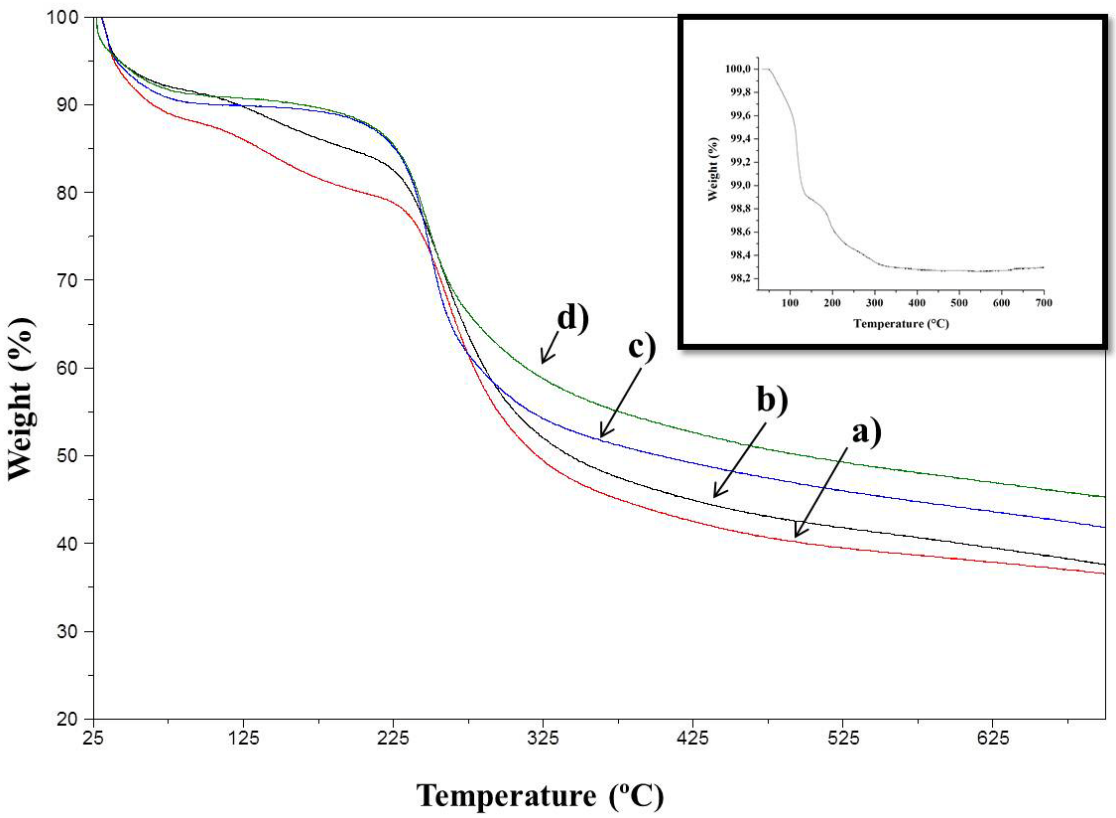

Figure 5.11. *Thermal gravimetric curves of CS+TPP (a), NP+Fe1% (b), NP+Fe3.2% (c) and NP+Fe5.6% (d).*

It is important to highlight the influence of the incorporation of ferrofluid into chitosan nanoparticles. As can be observe in Table 5.5, the third thermal transitions that correspond to degradation of organic components (chitosan matrix) decrease as a function of ferrofluid content, where at higher ferrofluid content the onset temperature decreases. This fact can be explained by the addition of metal nanoparticles into polymers matrix. Previous works reported that the addition of metal nanoparticles may have a catalytic role in the degradation of polymer matrix[36]. On the other hand, XRD results showed that crystallinity property of the sample loaded with ferrofluid decrease. This fact could affect its thermal stability, owing to decrease in degree of crystallinity as a result of cross-linking, as previous works reported [37, 38]. Since, if the crystallinity properties decrease, the thermal stability decreases as well.

The influence of the addition of ferrofluid was observed in the residue at 600 ºC, which was 3%, 6% and 10% for NP+Fe1%, NP+Fe3.2% and NP+Fe5.6%, respectively. This change is directly related with increasing of ferrofluid into chitosan nanoparticles,

however, these values presented a significant difference in comparison with ferrofluid content reported by UV spectroscopy.

Table 5.5. Main thermal steps for samples under study.

Sample	Onset 1º step (º C)	% Weight loss	Onset 2º step (ºC)	% Weight loss	Onset 3º step (ºC)	% Weight loss	Residue at 600 ºC
CS+TPP	30	11	115	8	240	42	38
NP+Fe1%	30	9	125	6	234	45	41
NP+Fe3.2%	30	10	-	-	231	45	44
NP+Fe5.6%	30	11	-	-	224	42	48

5.3.3 Rheological studies. Viscoelastic properties of aqueous dispersions of NP+Fe nanoparticles

Recent results regarding the rheological behavior of aqueous dispersions of poly (acrylamide-acrylic acid) microgels outlined their macroscopic elasticity showing that the material behaves as a colloidal gel[19]. Taking into account these results, the rheological characterization of aqueous colloidal dispersions is of paramount importance, and allows anticipating their behavior under certain conditions of shear.

Shear-thinning of a colloidal suspension could enable a more homogeneous and easy delivery of the material into the body in the case of injectable materials[15]. Moreover, the recovery of the elastic properties immediately after injection may prevent the flow of the colloidal solution and facilitate that the material remains on the target site[39]. A possible recovery of the elastic properties after shear-thinning was explored by comparing up and down strain sweeps carried out, as example on NP+Fe 3.2% sample. Figure 5.12 shows that as the strain diminishes, immediately after shear

thinning, a significant recovery of the elastic properties is observed and the sample recovered almost the initial elastic modulus.

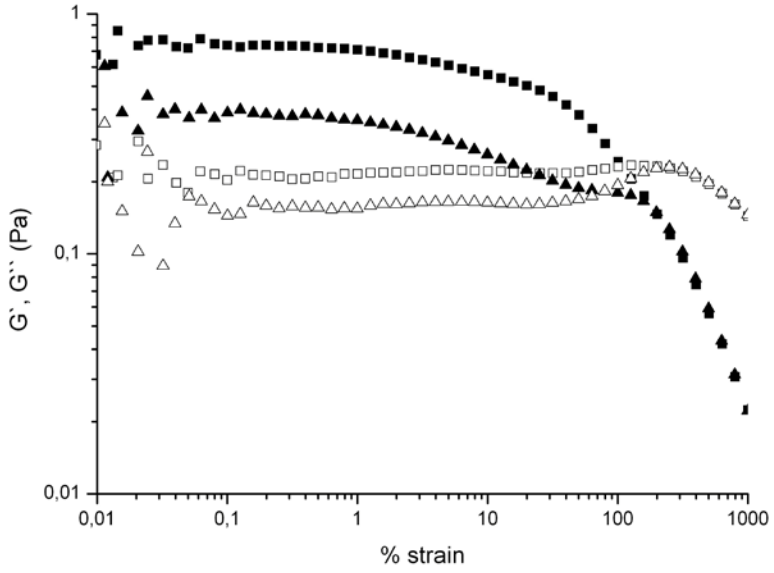

Figure 5.12. *(a) Evolution of the elastic modulus (full symbol) and viscous modulus (empty symbol) as a function of strain for an aqueous dispersion (1% w/v) of the sample NP+Fe 3.2%. First strain sweep (square) and second strain sweep (triangle).*

The results corresponding to the strain sweeps carried out on the samples CS+TPP (Figure 5.13-a), NP+Fe 1% (Figure 5.13-b), NP+Fe3.2% (Figure 5.13-c) and NP+Fe 5.6% (Figure 5.13-d) at different concentrations of the dispersion in water ranging from 0.5% (w/v) to 2% (w/v) are depicted in Figure 5.13. Chitosan nanoparticles and ferrofluid loaded chitosan nanoparticles synthetized, showed that for all the concentrations studied, the samples display a linear viscoelastic regime characterized by the independence of G´ and G´´ on the strain and yield up to a critical shear amplitude, γ_0, above which the samples show a viscoelastic liquid-like behavior followed by apparent shear-thinning. However, for CS+TPP sample, it was not possible to measure concentrations lower than 1% (w/v) due to the inertia of the measurement.

Shear-thinning could be attributed to the breaking apart of clusters formed among the particles at high shear amplitude. The increase in γ_0 that occurs when the concentration of the dispersion increases from 0.5% (w/v) to 2% (w/v) indicates that clusters are less dense at lower dispersion concentrations. Therefore, once some inter-

cluster bond that keep the interconnected network solid break, the sample may flow. The increase in the concentration of the dispersion gives an increase of the corresponding elastic modulus which could be associated to the intrinsic elastic properties of the different nanoparticles or the clusters.

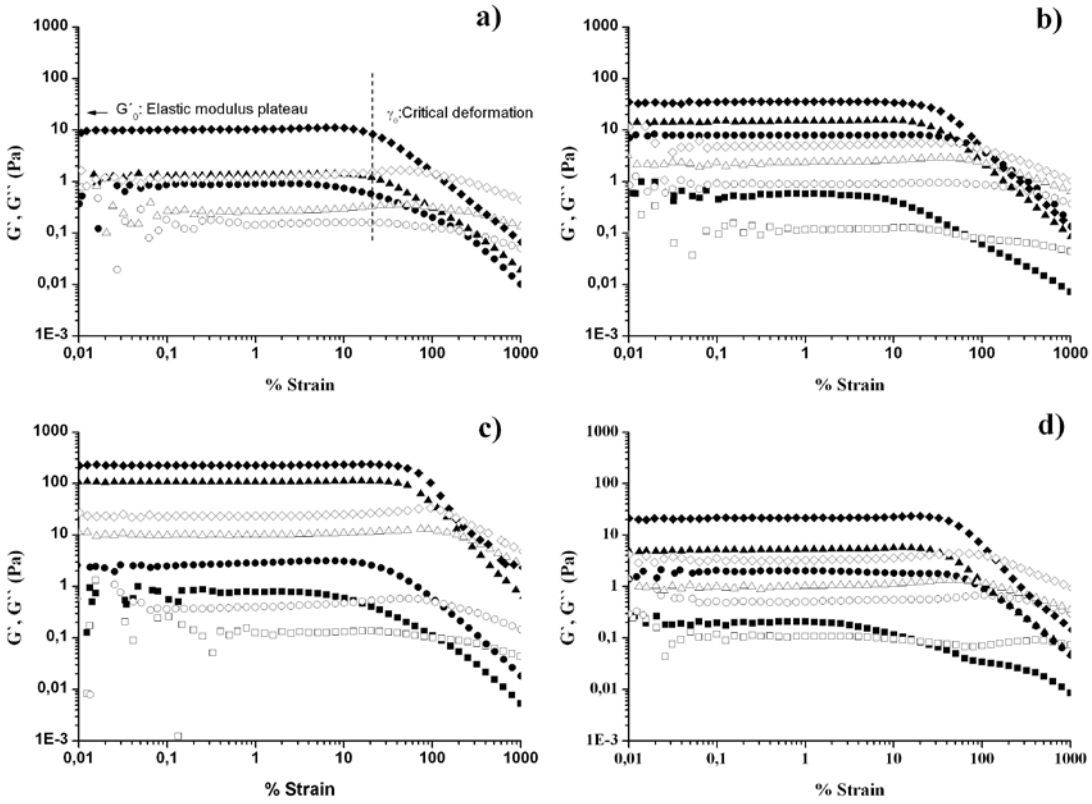

Figure 5.13. *Evolution of the elastic modulus (full symbol) and loss modulus (empty symbol) for 0.5% w/v (square), 1% w/v (circle), 1.5% w/v (triangle), and 2% w/v (diamond) concentration of nanoparticles dispersion: a) CS+TPP; b) NP+Fe 1%; c) NP+Fe 3.2% and d) NP+Fe 5.6%.*

According to Figure 5.13, it is observed the elastic modulus slight dependent of ferrofluid content specifically NP+Fe 5.6%, thus indicating the formation of a relatively weaker structure. This fact could be related with the particle size of these nanoparticles.

i. Determination of aggregating system. Fractal analysis

Results obtained from strain sweeps carried out at different concentrations, reported on Figures 5.14-a and 5.14-b show that both elastic modulus and critical deformations presented dependence with the concentration. These results indicate the occurrence of an aggregating system that may form a gel which can be studied by applying a fractal analysis. As previously studied for the poly(acrylamide-acrylic acid) microgels system, the colloidal gel structure can be related to the rheological properties based on scaling laws[40].

A representation of the plateau values of G_0 and γ_0 already determined from the strain sweep experiments (Figure 5.13) is plotted as a function of concentration in double-logarithmic form in Figures 5.14-a and 5.14-b, respectively.

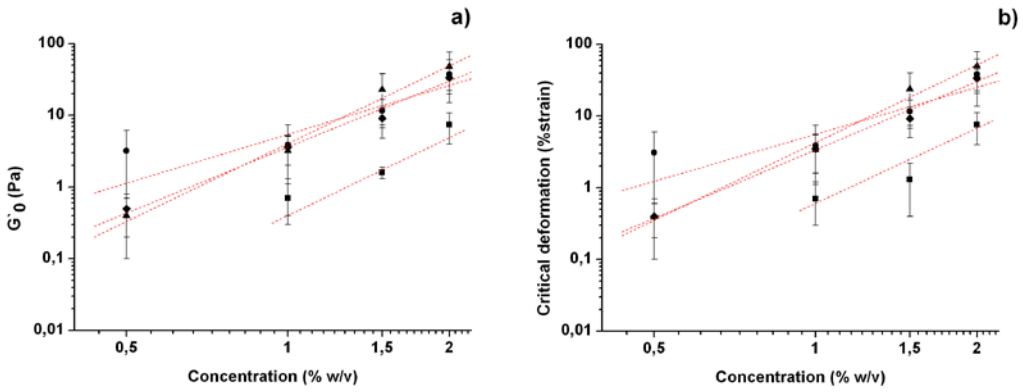

Figure 5.14. *(a) Elastic modulus plateau G_0 and b) critical deformation, γ_0, as a function of concentration of the aqueous dispersion: CS+TPP (■), NP+Fe 1% (●), NP+Fe 3.2% (▲), and NP+Fe 5.6% (♦).*

As can be observe, the elastic modulus plateau, G_0, increases as a function of the concentration of the dispersion for all the samples. The same behavior was observed for the critical deformation γ_0, which indicates that as the concentration of the dispersion increases, it is necessary to apply more deformation to break the clusters. When samples with different ferrofluid contents are compared at the same concentration of the dispersion, an increase of the elastic modulus of the samples with ferrofluid content is observed with respect to the CS+TPP samples.

Both the elastic modulus and the critical deformation can be linearly fitted to relations of the type:

$$G'_0 \approx \varphi^A \qquad \text{Equation 5.2}$$

$$\gamma_0 \approx \varphi^B \qquad \text{Equation 5.3}$$

where φ is the volume fraction and the exponents, *A* and *B* are the slopes corresponding to the fitting lines.

According to the Wu and Morbidelli model[18], A and B have the form:

$$A = \frac{\beta}{3-D} \qquad \text{Equation 5.4}$$

$$B = \frac{2-\beta}{3-D} \qquad \text{Equation 5.5}$$

where D is the fractal dimension and β is an auxiliary parameter defined as:

$$\beta = 1 + (2 + X)(1 - \alpha) \qquad \text{Equation 5.6}$$

where X represents the backbone fractal dimension or tortuosity of the network, whose value for a colloidal gel is in the range of 1-1.3[18]. α is a constant in the range [0, 1] which depends on the relation between the intra and the intermicroscopic elasticity which gives rise to the macroscopic elasticity in colloidal gels. α = 0 corresponds to a strong-link regime where interfloc links are stronger than intrafloc links so that the gel elasticity is dominated by the intramicroscopic elasticity. On the other hand, α = 1 corresponds to a weak-link regime where interfloc links are weaker than intrafloc links, that is, the gel elasticity is dominated by the intermicroscopic elasticity [17]. In Figure 5.15 is shown a representative scheme of interfloc and intrafloc links present in a colloidal gel. According to the Wu and Morbidelli model[18], intermediate regimes are obtained for values of α in the range $0 < \alpha < 1$. These intermediate regimes being between the weak-like and strong-like regime are more real and lead to intermediate situations where both inter- and intrafloc links contribute to the overall elasticity of the gel.

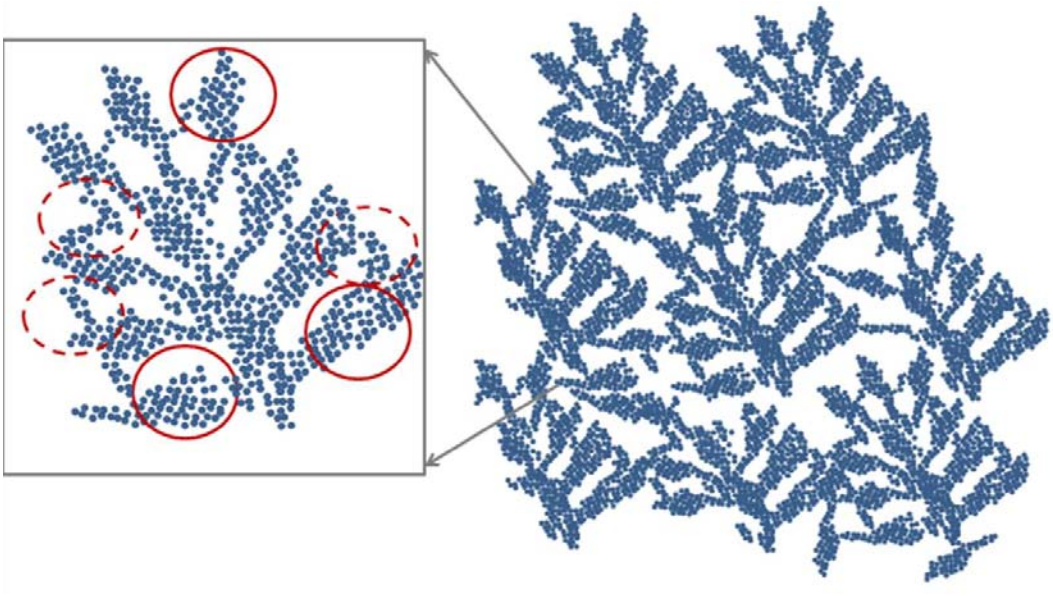

Figure 5.15. *Scheme of interfloc (dash line) and intrafloc (continue line) link in a colloidal gel.*

As can be observed, data represented in Figure 5.14 can be well fitted to a linear regression from which the slope is employed to determine the fractal dimension, D, and α constant. The results are summarized in Table 5.6.

Table 5.6. Summary of the results obtained by applying Wu and Morbidelli's scaling theory

Sample	A	B	D	α	Regime
CS+TPP	6.2	5.9	2.8	0.9	weak
NP+Fe 1%	3.4	3.3	2.7	0.9	weak
NP+Fe 3.2%	5.3	5.3	2.8	1.0	weak
NP+Fe 5.6%	4.4	4.7	2.7	1.0	weak

Values corresponding to α are close to 1 in all cases which indicates that the samples are in the weak-like regime, that is, the interflocs links are weaker than intrafloc links. This implies that the macroscopic elasticity exhibited by the aqueous

dispersions is due to the establishment of interactions between the individual chitosan nanoparticles regardless the presence of ferrofluid. The fact that the interactions regime does not change with the ferrofluid concentration in aqueous dispersions of NP+Fe samples may be a consequence of the efficient encapsulation of ferrofluid inside the chitosan matrix.

A fractal dimension of ~2.8 is found for all samples indicating the occurrence of dense fractal flocs. Interestingly, no change in fractal dimension is observed with the addition of ferrofluid to the material in agreement with the weak-like regime observed for all the samples, and the predominant interactions between the chitosan matrixes of the different nanoparticles.

5.3.4 *In vitro* studies of chitosan nanoparticles

Different kinds of experiments described in experimental part, have been carried out in order to establish the viability of ferrofluid loaded chitosan nanoparticles over Fibroblast. In this way, samples under study can be considered for biomedical applications.

i. Morphological analysis of FBH treated with magnetic chitosan nanoparticles (NP+Fe 3.2%).

Morphological analysis of Fibroblasts (FBH) treated with chitosan nanoparticles was studied by Scanning Electron Microscopy (SEM). As an example, Figures 5.16-a and 5.16-b show SEM images of FBH and FBH treated with NP+Fe 3.2% during 24 h, respectively. As can be observed, FBH is fully spread and well attached to the substrate; also, its surface was relatively smooth. On the other hand, Fibroblast treated with NP+Fe3.2% (Figure 5.16-b) are fully spread as well, which suggest its good cellular viability as will be confirmed trough cytotoxicity assay. However, it is very clear that its surface is rougher (see the inset image). This change is due to addition of chitosan

nanoparticles to the medium, which may suggest a possible uptake or interaction with chitosan nanoparticles.

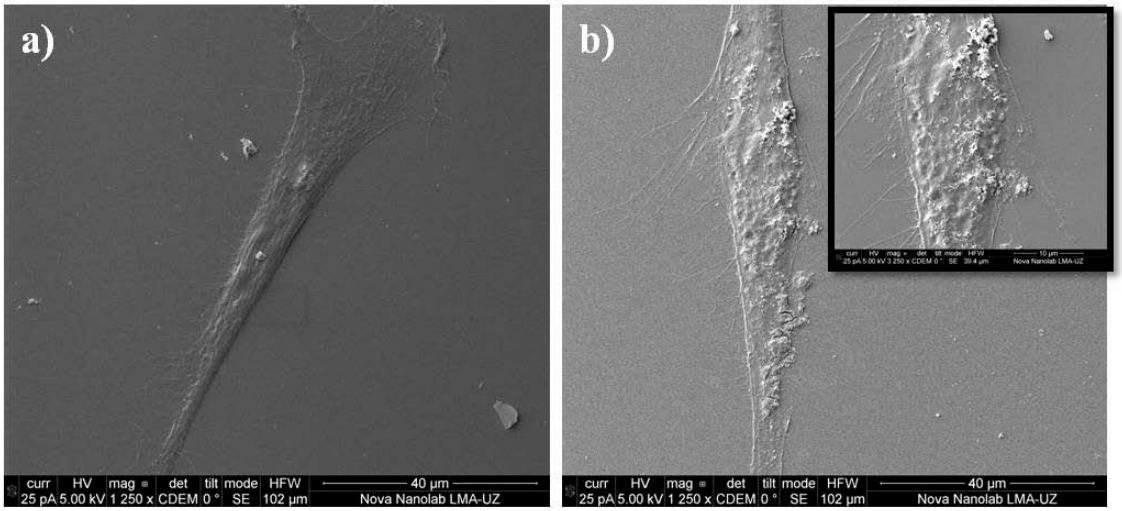

Figure 5.16. *SEM images of a) fibroblast and b) fibroblast treated with NP+Fe3.6%. The inset in Figure 5.15-b shows a magnification of FBH.*

ii. Cytotoxicity study

Figure 5.17 shows the results corresponding to the Alamar Blue assay carried out for all the samples under study dispersed at different concentrations in water.

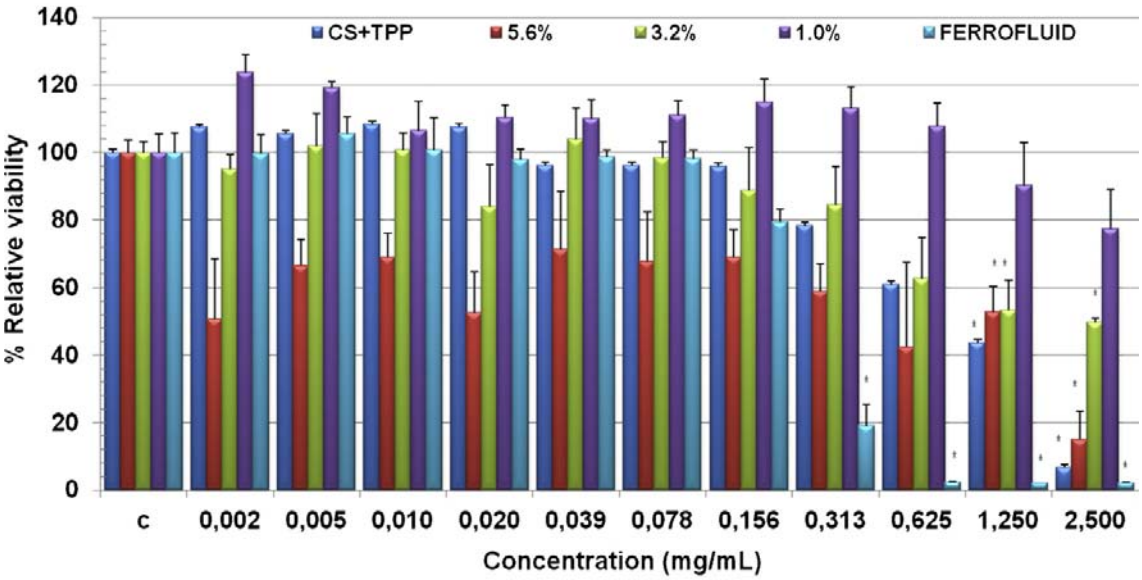

Figure 5.17. *Alamar Blue assay results for all the samples under study and the negative control (c), cells without treatment. All the results are shown as mean 8 S.D. Asterisk (*) depicts a significant difference between the corresponding sample with respect to negative control ($P < 0.05$).*

As can be observed, all the samples, including the ferrofluid exhibit a dose-dependent effect. At high concentrations (2.5-1.25 mg/mL), the toxicity is significantly different between the ferrofluid and NP+Fe 1% and NP+Fe 3.2%. However, in the case of NP+Fe 5.6% a low cellular viability (<70%) is observed in comparison with the control even with CS+TPP or the ferrofluid.

iii. Lactate dehydrogenase (LDH) assay.

Lactate dehydrogenase (LDH), which is a soluble cytosolic enzyme present in most eukaryotic cells, releases into culture medium upon cell death due to damage of plasma membrane. The increase of the LDH activity in culture supernatant is proportional to the number of lysed cells.

In order to establish the mechanism by which the NP+Fe samples tested with the AB assay gives rise to a decrease of the cellular viability, the test of lactate dehydrogenase (LDH) was performed. The LDH test allows determining whether the plasma membrane is damaged. The results plotted in Figure 5.18 indicate that the NP+Fe samples shows a cytotoxicity lower than 20% at the two concentrations tested (1 and 0.05 mg/mL). Therefore, cell death is not due to damage in the plasma membrane.

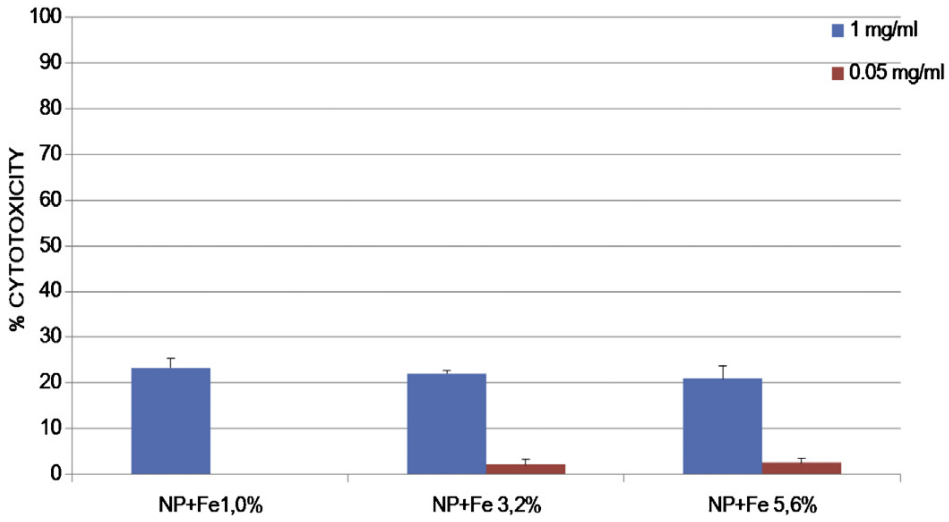

Figure 5.18. *Lactate dehydrogenase assay results for NP+Fe at different concentrations.*

From these results, it can be concluded that the cytotoxic effect of the ferrofluid is decreased when it is encapsulated inside chitosan nanoparticles. Therefore, NP+Fe samples do not compromise *in vitro* viability of this type of cells.

5.3.5 Application ferrofluid loaded chitosan nanoparticles for magnetic hyperthermia

In order to evaluate the potential application of ferrofluid loaded chitosan nanoparticles in magnetic hyperthermia, the heating performance of NP+Fe nanoparticles was carried out when are submitted to an alternating magnetic field. In Figure 5.19 is plotted the temperature increase as a functions of time for the three ferrofluid nanoparticles under study. From the Figure 5.19, we extracted the specific power absorption (SPA) from the initial slope of the temperature vs time curves, as can be observed in Figure 5.19 and explained in the following.

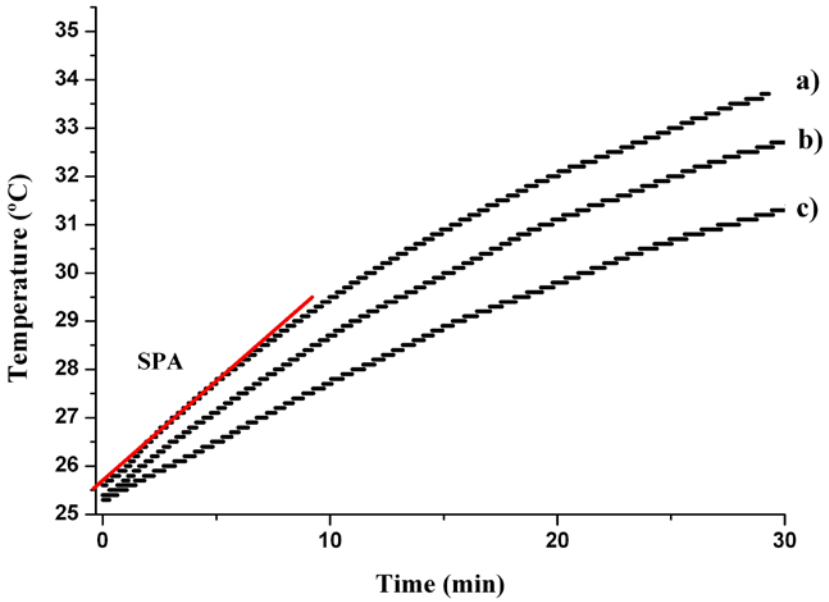

Figure 5.19. *Representative heating performance of a) NP+Fe 5.6%, b) NP+Fe 3.2% and c) NP+Fe 1%.*

The SPA of the colloids was determined from the temperature increase (ΔT) of a given mass of the constituent nanoparticles (m_{NP}) dispersed in a mass of liquid carrier (m_{LIQ}) during the time interval (Δt) of the experiment, using the expression[41]:

$$SPA = \frac{m_{LIQ} c_{LIQ} + m_{NP} c_{NP}}{m_{NP}} \left(\frac{\Delta T}{\Delta t} \right) \qquad \text{Equation 5.7}$$

where c_{LIQ} and c_{NP} are the specific heat capacities of the liquid carrier and the nanoparticles, respectively. Due to the low concentration, around 1% (w/v) of the magnetic material in the colloids we can use the approximation, $m_{LIQ} c_{LIQ} + m_{NP} c_{NP} \approx m_{LIQ} c_{LIQ}$ so that the equation to calculate SPA becomes:

$$SPA = \frac{m_{LIQ} c_{LIQ}}{m_{NP}} \left(\frac{\Delta T}{\Delta t} \right) \qquad \text{Equation 5.8}$$

Since the time dependence of temperature T is not linear, the slope of the T (t) is also a function of time. This is usually due to heat losses of the experimental setup, and thus a criterion is needed in order to extract reproducible and comparative information from experiments. We have chosen the criterion of the maximum derivative for calculating our SPA values, since this criterion has two main advantages: first, the maximum slope ΔT/Δt happens during the first few second of the experiment, and therefore during this short time the heating process can be considered as adiabatic. Second, because it occurs during the first seconds after the magnetic field is turned on, the maximum slope is located at an absolute temperature close to room temperature, irrespective of the final SPA value. Consequently, all SPA values are estimated at nearly the same (room) temperatures.

The SPA values for all NP+Fe samples are shown in Table 5.7 together with the data calculated for the pure ferrofluid.

Table 5.7. Specific power absorption of the samples under study

Sample	ΔT/Δt	Fe (mg/mL)	SPA (W/g)
FF	1,616	69,9	96,6
NP+Fe 1%	0,003	1,9	8,4
NP+Fe 3.2%	0,005	3,1	7,8
NP+Fe 5.6%	0,007	5,6	5,3

As can be observed, there are significant differences between the value reported for the ferrofluid and the values corresponding to the NP+Fe samples. This is a consequence of the low amount of magnetic material of the NP+Fe nanoparticles, as the specific power is given in unit mass of the composite nanoparticles. Therefore, these values could be improved if higher concentrations of ferrofluid within the chitosan nanoparticles can be encapsulated. In spite of the low SPA values reported here in comparison with the usually reported for pure ferrofluids, recent studies have outlined the capability of magnetic nanoparticles of inducing local damage in eukaryotic cells without increasing the macroscopic temperature, resulting in high percentages of cell death[42, 43]. It remains to be investigated whether similar mechanisms could be employed for intracellular drug release using magnetically loaded thermosensitive nanoparticles.

5.4 CONCLUSIONS

In the study of preparation, characterization and evaluation of properties, the following conclusions can be extracted.

Chitosan nanoparticles were successfully prepared by ionic interactions among chitosan and TPP. Appropriated concentrations of reagents, chitosan and TPP were

determined for a success nanoparticles formation, being 0.5% (w/v) and with a volumetric ratio of 5:1, CS:TPP. Their particles size was determinate trough AFM analysis and DLS, where both techniques reported similar size, 154nm and 140 nm, respectively.

Ferrofluid at different concentrations were encapsulated into chitosan nanoparticles, ionically crosslinked with TPP to yield magnetic core-shell chitosan nanoparticles with ferrofluid contents ranging from 1 to 5.6% (w/w). An increase in the size of the NP+Fe from 192 to 259 nm was observed as the ferrofluid content increased with respect to the chitosan nanoparticles without ferrofluid (140 nm). Ferrofluid loaded chitosan nanoparticles presented a positive zeta potential which indicated the encapsulation of ferrofluid into chitosan matrix, fact that was corroborated by FESEM images. Crystallinity properties of NP+Fe confirmed the presence of magnetite into the chitosan nanoparticles, also, evidence that coating process of chitosan did not result in the phase change of magnetite. The final thermal stability of NP+Fe decreased to respect at CS+TPP.

A fractal analysis carried out on the results obtained from dynamic rheological experiments revealed the presence of interactions in between individual chitosan nanoparticles and the absence of formation of aggregates independently from the ferrofluid content. Finally, aqueous dispersions of NP+Fe flow at high strains and recover the initial elastic properties as the strain rate diminishes which demonstrates the shear-thinning properties of these materials.

According the cytotoxicity assay, samples presented a dose-dependent effect and also was observed the cellular viability decreased as a function of ferrofluid content. Experiments on remote magnetic heating carried out on NP+Fe samples have revealed that aqueous dispersions (5% w/v) undergo an increase of temperature when subjected to an alternating magnetic field. Therefore, NP+Fe samples can be considered as potential candidates for magnetic hyperthermia due to their good biocompatibility demonstrated in the cytotoxicity studies and their ability to heat when submitted to an AMF.

5.5 REFERENCES

[1] Zhao D-L, Wang X-X, Zeng X-W, Xia Q-S, Tang J-T. Preparation and inductive heating property of Fe3O4-chitosan composite nanoparticles in an AC magnetic field for localized hyperthermia. Journal of Alloys and Compounds. 2009;477:739-43.

[2] Jordan A, Scholz R, Maier-Hauff K, Johannsen M, Wust P, Nadobny J, et al. Presentation of a new magnetic field therapy system for the treatment of human solid tumors with magnetic fluid hyperthermia. Journal of Magnetism and Magnetic Materials. 2001;225:118-26.

[3] Kim D-H, Kim K-N, Kim K-M, Lee Y-K. Targeting to carcinoma cells with chitosan- and starch-coated magnetic nanoparticles for magnetic hyperthermia. Journal of Biomedical Materials Research Part A. 2009;88A:1-11.

[4] Ur-Rehman T, Tavelin S, Gröbner G. Chitosan in situ gelation for improved drug loading and retention in poloxamer 407 gels. International Journal of Pharmaceutics. 2011;409:19-29.

[5] Gan Q, Wang T, Cochrane C, McCarron P. Modulation of surface charge, particle size and morphological properties of chitosan-TPP nanoparticles intended for gene delivery. Colloids and Surfaces B: Biointerfaces. 2005;44:65-73.

[6] Wu Y, Wang Y, Luo G, Dai Y. In situ preparation of magnetic Fe3O4-chitosan nanoparticles for lipase immobilization by cross-linking and oxidation in aqueous solution. Bioresource Technology. 2009;100:3459-64.

[7] Zhang H, Oh M, Allen C, Kumacheva E. Monodisperse chitosan nanoparticles for mucosal drug delivery. Biomacromolecules. 2004;5:2461-8.

[8] Hosseini SF, Zandi M, Rezaei M, Farahmandghavi F. Two-step method for encapsulation of oregano essential oil in chitosan nanoparticles: Preparation, characterization and in vitro release study. Carbohydrate Polymers. 2013;95:50-6.

[9] Martins AF, de Oliveira DM, Pereira AGB, Rubira AF, Muniz EC. Chitosan/TPP microparticles obtained by microemulsion method applied in controlled release of heparin. International Journal of Biological Macromolecules. 2012;51:1127-33.

[10] Shah S, Pal A, Kaushik VK, Devi S. Preparation and characterization of venlafaxine hydrochloride-loaded chitosan nanoparticles and in vitro release of drug. Journal of Applied Polymer Science. 2009;112:2876-87.

[11] Goycoolea FM, Lollo G, Remuñán-López C, Quaglia F, Alonso MJ. Chitosan-Alginate Blended Nanoparticles as Carriers for the Transmucosal Delivery of Macromolecules. Biomacromolecules. 2009;10:1736-43.

[12] Calvo P, Remuñán-López C, Vila-Jato JL, Alonso MJ. Novel hydrophilic chitosan-polyethylene oxide nanoparticles as protein carriers. Journal of Applied Polymer Science. 1997;63:125-32.

[13] Zhi J, Wang Y, Lu Y, Ma J, Luo G. In situ preparation of magnetic chitosan/Fe3O4 composite nanoparticles in tiny pools of water-in-oil microemulsion. Reactive and Functional Polymers. 2006;66:1552-8.

[14] Jiang D-S, Long S-Y, Huang J, Xiao H-Y, Zhou J-Y. Immobilization of Pycnoporus sanguineus laccase on magnetic chitosan microspheres. Biochemical Engineering Journal. 2005;25:15-23.

[15] Guvendiren M, Lu HD, Burdick JA. Shear-thinning hydrogels for biomedical applications. Soft Matter. 2012;8:260-72.

[16] Wu H, Morbidelli M. Gelation of polymeric nanoparticles. Particuology. 2014;14:1-11.
[17] Shih W-H, Shih WY, Kim S-I, Liu J, Aksay IA. Scaling behavior of the elastic properties of colloidal gels. Physical Review A. 1990;42:4772.
[18] Wu H, Morbidelli M. A Model Relating Structure of Colloidal Gels to Their Elastic Properties. Langmuir. 2001;17:1030-6.
[19] Echeverria C, Peppas NA, Mijangos C. Novel strategy for the determination of UCST-like microgels network structure: effect on swelling behavior and rheology. Soft Matter. 2012;8:337-46.
[20] Hernandez R, Sacristan J, Nogales A, Fernandez M, Ezquerra TA, Mijangos C. Structure and viscoelastic properties of hybrid ferrogels with iron oxide nanoparticles synthesized in situ. Soft Matter. 2010;6:3910-7.
[21] Wu Y, Hussain M, Fassihi R. Development of a simple analytical methodology for determination of glucosamine release from modified release matrix tablets. Journal of Pharmaceutical and Biomedical Analysis. 2005;38:263-9.
[22] Rodrigues S, Costa AMRd, Grenha A. Chitosan/carrageenan nanoparticles: Effect of cross-linking with tripolyphosphate and charge ratios. Carbohydrate Polymers. 2012;89:282-9.
[23] Zhu A, Yuan L, Liao T. Suspension of Fe3O4 nanoparticles stabilized by chitosan and o-carboxymethylchitosan. International Journal of Pharmaceutics. 2008;350:361-8.
[24] Doiron AL, Homan KA, Emelianov S, Brannon-Peppas L. Poly(lactic-co-glycolic) acid as a carrier for imaging contrast agents. Pharmaceutical research. 2009;26:674-82.
[25] Lawrie G, Keen I, Drew B, Chandler-Temple A, Rintoul L, Fredericks P, et al. Interactions between Alginate and Chitosan Biopolymers Characterized Using FTIR and XPS. Biomacromolecules. 2007;8:2533-41.
[26] Pawlak A, Mucha M. Thermogravimetric and FTIR studies of chitosan blends. Thermochimica Acta. 2003;396:153-66.
[27] Darder M, Colilla M, Ruiz-Hitzky E. Biopolymer−Clay Nanocomposites Based on Chitosan Intercalated in Montmorillonite. Chemistry of Materials. 2003;15:3774-80.
[28] Darder M, Colilla M, Ruiz-Hitzky E. Chitosan–clay nanocomposites: application as electrochemical sensors. Applied Clay Science. 2005;28:199-208.
[29] Zhang L-y, Zhu X-j, Sun H-w, Chi G-r, Xu J-x, Sun Y-l. Control synthesis of magnetic Fe3O4-chitosan nanoparticles under UV irradiation in aqueous system. Current Applied Physics. 2010;10:828-33.
[30] Hernández R, Zamora-Mora V, Sibaja-Ballestero M, Vega-Baudrit J, López D, Mijangos C. Influence of iron oxide nanoparticles on the rheological properties of hybrid chitosan ferrogels. Journal of Colloid and Interface Science. 2009;339:53-9.
[31] Yoksan R, Jirawutthiwongchai J, Arpo K. Encapsulation of ascorbyl palmitate in chitosan nanoparticles by oil-in-water emulsion and ionic gelation processes. Colloids and Surfaces B: Biointerfaces. 2010;76:292-7.
[32] Bhumkar DR, Pokharkar VB. Studies on effect of pH on cross-linking of chitosan with sodium tripolyphosphate: a technical note. AAPS PharmSciTech. 2006;7:E50.
[33] Hu B, Pan C, Sun Y, Hou Z, Ye H, Zeng X. Optimization of Fabrication Parameters To Produce Chitosan−Tripolyphosphate Nanoparticles for Delivery of Tea Catechins. Journal of Agricultural and Food Chemistry. 2008;56:7451-8.
[34] Zhu H, Jiang R, Xiao L, Chang Y, Guan Y, Li X, et al. Photocatalytic decolorization and degradation of Congo Red on innovative crosslinked chitosan/nano-CdS composite catalyst under visible light irradiation. Journal of Hazardous Materials. 2009;169:933-40.

[35] Pickup DM, Newport RJ, Barney ER, Kim JY, Valappil SP, Knowles JC. Characterisation of phosphate coacervates for potential biomedical applications. Journal of biomaterials applications. 2014;28:1226-34.
[36] Lee J-Y, Liao Y, Nagahata R, Horiuchi S. Effect of metal nanoparticles on thermal stabilization of polymer/metal nanocomposites prepared by a one-step dry process. Polymer. 2006;47:7970-9.
[37] Pati F, Adhikari B, Dhara S. Development of chitosan–tripolyphosphate fibers through pH dependent ionotropic gelation. Carbohydrate Research. 2011;346:2582-8.
[38] Sarkar SD, Farrugia BL, Dargaville TR, Dhara S. Physico-chemical/biological properties of tripolyphosphate cross-linked chitosan based nanofibers. Materials Science and Engineering: C. 2013;33:1446-54.
[39] Yan C, Mackay ME, Czymmek K, Nagarkar RP, Schneider JP, Pochan DJ. Injectable Solid Peptide Hydrogel as a Cell Carrier: Effects of Shear Flow on Hydrogels and Cell Payload. Langmuir. 2012;28:6076-87.
[40] Echeverria C, López D, Mijangos C. UCST Responsive Microgels of Poly(acrylamideâˆ’acrylic acid) Copolymers: Structure and Viscoelastic Properties. Macromolecules. 2009;42:9118-23.
[41] Lima E, Jr., Torres TE, Rossi LM, Rechenberg HR, Berquo TS, Ibarra A, et al. Size dependence of the magnetic relaxation and specific power absorption in iron oxide nanoparticles. J Nanopart Res. 2013;15:1-11.
[42] Asin L, Ibarra MR, Tres A, Goya GF. Controlled cell death by magnetic hyperthermia: effects of exposure time, field amplitude, and nanoparticle concentration. Pharmaceutical research. 2012;29:1319-27.
[43] Asin L, Goya GF, Tres A, Ibarra MR. Induced cell toxicity originates dendritic cell death following magnetic hyperthermia treatment. Cell death & disease. 2013;4:e596.

Chapter 6

IN VITRO STUDY OF MAGNETIC CHITOSAN NANOPARTICLES LOADED WITH 5-FLUOROURACIL FOR MAGNETIC HYPERTHERMIA APPLICATIONS

This chapter described the preparation of chitosan nanoparticles loaded with ferrofluid and 5-Fluorouracil, a model chemotherapeutic drug. The drug release profile of these nanoparticles is analyzed as a function of pH and ferrofluid content. Moreover, all magnetic chitosan nanoparticles prepared in this study, have been assessed for *in vitro* magnetic hyperthermia applications. In addition, two protocols were proposed for hyperthermia experiments. Finally, cellular damage was analyzed through crystal violet staining and acridine orange and propidium iodide (AO/PI) staining.

6.1. INTRODUCTION

Polymeric based nano-carriers are important materials employed in many biomedical applications and have been developed in an assortment of morphologies including micelles [1, 2], nanoparticles [3-5], nanorods [6, 7], and so on. Specifically, polymeric nanoparticles (NPs) for biomedical applications provide several advantages including small particle size, increased drug efficacy, lowered toxicity, enhanced drug solubility and stability[8]. It is well known that polymeric nanoparticles prepared from biodegradable and biocompatible materials have advantages in biomedical applications [9]. Among them, chitosan is one of the materials that satisfy these requirements and therefore has become particularly attractive, especially when is employed as drug delivery carriers [10-12], permeating vectors for blood–brain barrier (BBB)[13], gene delivery[14] and pH-sensor[15] and hyperthermia agents[16-18].

As mentioned before, chitosan nanoparticles can be used as nano-carriers for drug delivery studies and 5-Fluorouracil (5-FU) was selected as a model drug, because it is well known its effective effect as chemotherapeutic anticancer drugs[19]. 5-FU has been extensively evaluated for its anticancer activity against several cancer models as colon, gastric, breast carcinomas and head and neck cancer[20]. There are also, several studies about 5-FU encapsulated chitosan nanoparticles for application as Ophthalmic delivery[21] or colorectal cancer[22, 23]. However, many of these chitosan nanoparticles loaded with 5-FU are composite matrix, such as chitosan-g-poly(N-vinylcaprolactam) nanoparticles[24] or chitosan-PEG-gelatin[25].

As pointed in the general introduction, this study is also focused on hyperthermia applications for cancer treatment, by heating effectively and locally deep-seated tumors. Moreover, hyperthermia treatment presents some advantages in comparison with other cancer treatments, as for example, chemotherapy, because it has few side effects as it is based on a higher sensibility of cancer cells to heat with regard to normal cells[26]. The latter fact has been explained because in cancer cells after hyperthermia treatment (temperatures achieved around 43 ºC), the oxygen supplied via the blood vessels is not sufficient to maintain the cells alive, whereas normal cells are not damaged even at higher temperatures[27]. In this regard, some studies of magnetic chitosan nanoparticles for hyperthermia applications are reported in the literature. However, in some cases their synthesis includes toxic reagents as example, Fe_3O_4 loaded chitosan nanoparticles crosslinked with glutaraldehyde [28]. Also, other studies can be found as, coprecipitation of Fe^{3+} and Fe^{2+} with an aqueous NaOH solution and then encapsulated into chitosan matrix via a suspension crosslinking method[17], which require several steps.

In recent years, much attention has been focused on development of nanoparticles that combined two or more treatments against different types of cancers by employing multifunctional nanoparticles. Multifunctional nanoparticles are based on materials that can response to external stimulus such as pH, temperature, magnetic and light and act as drug nano-carrier, as well[29]. Therefore, their synergistic effect will improve the cancer therapy. There are some studies that involved multifunctional nanoparticles for combined cancer therapy such as chemotherapy and gene therapy[30], pH-sensitive targeted delivery carriers[31], chemotherapy-biotherapy-hyperthermia[32].

In order to enhance the therapeutic efficacy against cancer cells we propose on objective to develop a nano-carrier loaded with a model drug (5-FU) and ferrofluid into a chitosan matrix that is recognized as pH-sensitive. Moreover, chitosan matrix can help to provide the desirable characteristics of nanoparticles for hyperthermia application such as avoid ferrofluid agglomeration, an appropriated surface charge of nanoparticles for enhance cancer cell interaction[8] for its internalization and achieve the drug release. To the best of our knowledge, no study has been reported on the cancer therapy of 5-Fluorouracil (5-FU) and ferrofluid loaded chitosan nanoparticles for *in situ* magnetic

hyperthermia applications in malignant human glioblastoma (A-172) and Fibroblasts (FBH).

6.2 EXPERIMENTAL PART

6.2.1. Materials

Chitosan and ferrofluid employed in this work were the same described in chapter 3. 5-Fluorouracil (5-FU), acetic acid, sodium tripolyphosphate, acetate buffer (pH 5.2) and phosphate buffered saline (PBS pH 7.4) were purchased from Sigma Company (Sigma Company, St. Louis, MO, USA).

6.2.2. Preparation of hybrid chitosan nanoparticles

i. 5-Fluorouracil loaded chitosan nanoparticles (CS+FU)

First, 5-fluorouracil was dissolved in 6 mL of an aqueous sodium tripolyphosphate (TPP) solution (0.5% w/v), to a final concentration of 0.5% (w/v). CS+FU nanoparticles were formed by dropwise addition of the TPP+5-FU solution into a chitosan stock solution (0.5% w/v) in a ratio chitosan: TPP+5-FU of 5:1, under mechanical stirring at room temperature. After reaction, CS+FU nanoparticles are collected by centrifugation and washed one time with distilled water. Then CS+FU nanoparticles were centrifuged at 5000 rpm, for 20 min. Only the supernatant is collected, because it is where the small CS+FU nanoparticles remain. Finally, the supernatant was separated and then it was dried by lyophilization.

ii. Hybrid chitosan nanoparticles (CS+FU+Fex)

For combined hyperthermia treatment and drug release, 5-FU and ferrofluid loaded chitosan nanoparticles were prepared. First, three different concentrations of ferrofluid (with the same concentration as previous chapter, 1, 3.2 and 5.6% w/v) were dispersed in 5 mL of Milli-Q water. Each of this ferrofluid solution was mixed under mechanical stirring in a N_2 atmosphere with chitosan solution (0.5% w/v) in a volumetric ratio chitosan:ferrofluid of 6:1. Separately, 6 mL of the aqueous TPP+5-FU solution prepared, as described in the previous section for the preparation of CS+FU nanoparticles. CS+FU+Fex nanoparticles were obtained by dropwise addition of 6 mL of TPP+5-FU solution into the solution containing the chitosan (30 mL) and ferrofluid (5 mL) under mechanical dispersion, followed by stirring for 10 min at room temperature. The nanoparticles dispersions were collected by centrifugation at 5000 rpm for 20 min. Finally, the supernatant was separated and then it was dried by lyophilization. 5-FU and ferrofluid loaded chitosan nanoparticles were named CS+FU+Fex, where x correspond to 1, 3.2 and 5.6% (w/v) of ferrofluid, respectively.

6.2.3. Characterization of hybrid chitosan nanoparticles

i. Morphological studies

- Scanning Electron Microscopy with electron transmission (FESEM)

For morphologic visualization of the samples by Scanning Electron Microscopy with electron transmission a Hitachi model SU8000 HRSEM was employed. It was used in the TE (electron transmission) detector bright field mode and SE operated at 0.5-30 KV. The sample preparation was carried out with the same procedure described in chapter 5.

- Atomic Force Microscopy (AFM)

AFM experiments were performed to analyze the morphology of the prepared nanoparticles following the same protocol as employed to characterized NP+Fex in previous chapter and using the same Multimode Scanning probe microscope. All of the images contained 256 × 256 data points. The nanoparticle diameter reported is the average of 100 nanoparticles and was analyzed using the ImageJ software.

The coefficient of variance (CV) of size distribution was calculated as:

$$CV\ (\%) = (\sigma/D)\ x100 \qquad \text{Equation 6.1}$$

where σ is the standard deviation (SD) of the particle size and D is their mean diameter.

ii. Study of the chemical structure by Attenuated Total Reflection Fourier Transformed Infra-Red Spectroscopy (ATR-FTIR)

Attenuated Total Reflection Fourier Transformed Infra Red Spectroscopy (ATR-FTIR) was carried out on freeze-dried samples. Spectra were measured in a Spectrum One FT-IR Spectrometer of Perkin Elmer in the wave number range of 600-4000 cm^{-1} and with 4 cm^{-1} resolution.

6.2.4 Drug release from chitosan nanoparticles

i. Evaluation of drug encapsulation efficiency and loading efficiency.

For the determination of encapsulation efficiency (EE) of 5-FU in CS+FU and CS+FU+Fex, samples were centrifuged at 12000 rpm for 30 min, using centrifuge tubes IVSS Vivaspin 20, with a pore size of 3000 MWCO, to recover the residual fraction containing the 5-FU free. Then, this fraction was measured by ultraviolet spectroscopy (Perkin Elmer Instrument Lambda 35 UV/VIS spectrometer). 5-FU was measured at

265 nm where an intense characteristic peak was displayed. The encapsulation efficiency was calculated according to the following equation[33]:

$$EE = \frac{\text{total amount of 5-FU - amount of free 5-FU}}{\text{total amount of 5-FU}} \quad \text{Equation 6.2}$$

The loading efficiency of 5-FU loaded into CS+FU and CS+FU+Fex samples was determined from the freeze dried samples as follows: a known amount of lyophilized samples was dissolved in acetic acid (1% v/v). Then the drug content was analyzed using UV/Vis spectrometry at 265 nm with the appropriate dilutions. The loading efficiency was calculated as follows:

$$\text{Loading efficiency (LC)} = \frac{\text{Amount of 5-FU incorporated in nanoparticles} \times 100}{\text{Amount lyophilized powder of sample}} \quad \text{Equation 6.3}$$

All measurements were performed in triplicate and the mean value calculated.

ii. Evaluation of *in vitro* drug release.

The release of 5-FU from CS+FU and CS+FU+Fex samples was studied at two different pHs, physiological pH (PBS at pH 7.4) and acidic pH (acetate buffer, pH 5.2) to simulate the tumoral environment[34]. Each of the samples under study was dispersed to a concentration of 0.01% (w/v). Then, each dispersion was placed into a dialysis tubing (MWCO 3500-5000 Da) that was immersed in 10 mL of the respective buffer at 37 ºC with moderate orbital stirring. An aliquot of 1 mL was withdrawn from the release medium at regular times and replaced with equivalent aliquots of fresh medium during 30 days. The kinetics of release of 5-FU from CS+FU and CS+FU+Fex samples was measured by UV/Vis spectroscopy (Perkin Elmer Instrument Lambda 35 UV/VIS spectrometer, at 265 nm). All data reported are an average of three experiments.

6.2.5 Biological studies

i. Cytotoxicity study by Alarmar Blue assay

The cytotoxicity of the CS+FU and three CS+FU+Fex samples was measured through Alarmar Blue (AB) (provided by Serotec, Spain) assays for two cells lines, Fibroblast (FBH-INNOPROT SPAIN) and malignant human glioblastoma cells (A-172-ECACC, UK). Both cells lines were seeded into 96 wells plates at a density of 10×10^4cells/mL in complete medium and incubated to confluence. After being cultured for 24 h, FBH and A-172 cells were treated for different aqueous dispersions of CS+FU and CS+FU+Fex samples and incubated at 37 ºC in humidified air with 5% CO_2 for 24 h. After that, a solution of AB (10% v/v) prepared in a warm medium without phenol red was added to the plate and incubated at 37ºC for 4 h. Finally, fluorescence was measured with a Biotek Synergy HT detector using an emission wavelength of 590 nm and an excitation wavelength of 530 nm.

Cell viability (*CV*) was calculated with the following equation:

$$CV = 100 \times (FDs - FD_B / FD_C - FD_B) \qquad \text{Equation 6.4}$$

where FD_S, FD_B, and FD_C are the fluorescence density of the AB for the sample (S), blank (B) (culture medium without cells), and control (C), respectively.

Samples were sterilized with a UV lamp (HNS OSRAM, 263 nm, 3.6UVC/W) at a power of 11 W for 2 h.

ii. Cellular uptake of chitosan nanoparticles.

The cellular uptake was determined by epifluorescent microscopy, which is a method that allows observing the nanoparticles carrying a fluorescent label (sodium fluorescein dye 20%) in different cells lines (FBH and A-172). The study was carried out for a selected group of chitosan nanoparticles (CS+TPP, NP+Fe5.6%, CS+FU and CS+FU+Fe5.6%) following the next procedure: a dispersion of fluorescent nanoparticles (0.06% (w/v) in medium without phenol red + fluorescein 0.01 % v/v)

was added to the cells seeded onto a glass dish in semi confluence and incubates during 24 h at 37 ºC and 5% of CO_2. The cells were rinsed with phosphate buffered saline (PBS) and fixed with paraformaldehyde 3.7 % in PBS for 10 min at 37 ºC. After that, paraformaldehyde was removed and then rinsed with PBS. Finally, triton (Triton X-100, molecular biology grade, density 1.07 g/cm³) 0.05 % v/v in PBS was added for 20 min at 37 ºC for permeability in the cellular membrane. The samples were rinsed with PBS and the cell nuclei were stained with 10 µL/mL of Hoechst H33342 dye solution. In addition, phalloidin (1 µL/ 100 µL) was used for staining the actin cytoskeleton of the cells and left it for 30 min at room temperature in the darkness. Finally, fluorescence was observed with an epifluorescence microscope (Nikon eclipse TE2000-S) and three different filters. A DAPI filter set (excitation, 387-311 nm, emission bandpass 447-460 nm) was used to detect cell nuclei, a FX RED filter set (excitation, 562-540 nm, emission bandpass 624-640 nm) was used for detect cytoskeleton of the cells and FITC filter set (excitation bandpass, 465–495 nm; emission bandpass, 515–555 nm) was used to detect fluorescent nanoparticles.

6.2.6 *In vitro* magnetic hyperthermia experiments

Two protocols were proposed in order to carry out the *in vitro* magnetic hyperthermia treatment over cancer and normal cells treated with hybrid chitosan nanoparticles.

i. Protocols of study.

- Protocol employing commercial equipment.

The magnetic hyperthermia (MH) experiments were performed using a DM100 equipment (nB nanoscale Biomagnetics, Spain) working at f=580 kHz and 24 kA/m (≈300 Oe). Experiments were carried out within a thermally-insulated working space of about 1 cm^3, using a closed vial of 1 mL volume. The study was carried out on malignant human glioblastoma (A-172) and fibroblast (FBH) loaded with chitosan

nanoparticles: CS+Fe5.6%, CS+FU and CS+FU+Fe5.6%. Sample CS+TPP was used as control.

Both cells lines (FBH and A-172) were seeded onto discs of polystyrene (PS) (6 mm of diameter), at a density of 10×10^4cells/mL in complete medium and incubated to confluence. First, PS discs were sterilized with ethanol and then with a UV lamp (HNS OSRAM, 263 nm, 3.6UVC/W) at a power of 11 W for 2 h. After being cultured for 24 h, FBH and A-172 were treated with each of the corresponding dispersion of chitosan nanoparticles and incubated for 24 h. All nanoparticles dispersions employed were at non toxic concentrations, as determined by the cytotoxicity experiments (chapter 5). Then, both cells lines seeded onto disc of PS were taken and placed carefully into the vial, and after that it was filled with complete medium. In Figure 6.1 a scheme of the experiment is shown.

Samples were exposed to the AC field during 20 min. Then, after the application of the magnetic field, the complete medium was removed and the samples were rinsed with PBS to remove dead cells and free chitosan nanoparticles. Samples were fixed with glutaraldehyde 2.5% (v/v) at 37 °C for 10 min immediately after the MH treatment (t=0). All the experiments were made by triplicate.

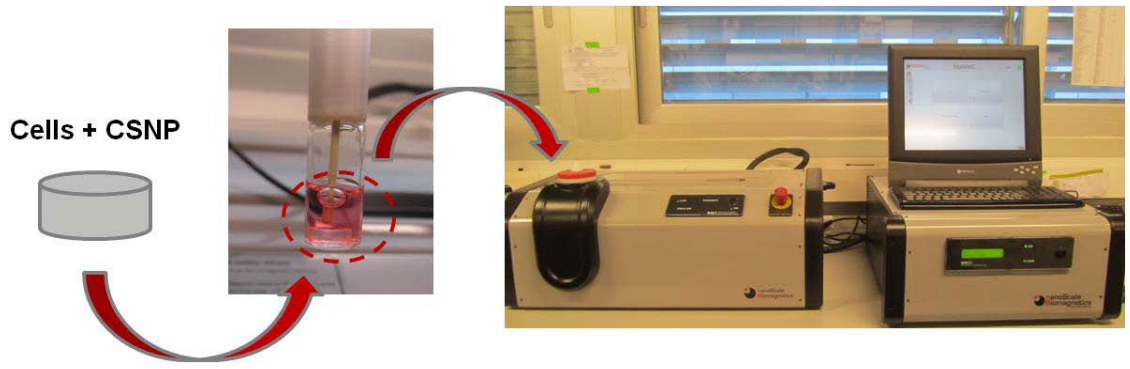

Figure 6.1. *Scheme for the in vitro magnetic hyperthermia treatment using PS discs.*

- Protocol employing homemade equipment.

The magnetic hyperthermia experiments were performed using a Power supply, (EASYHEAT 0224 BENCH) with an external heat station. We study the effect of an Alternative magnetic (AC) field working at 180 KHz and 35 KA/m (450 gauss) on the cell viability of two cells lines, malignant human glioblastoma (A-172) and fibroblast (FBH) loaded with chitosan nanoparticles: CS+Fe5.6%, CS+FU and CS+FU+Fe5.6%.

Figure 6.2 shows the scheme of the experiment. Both cells lines (FBH and A-172) were seeded onto an Ibidi dish (µ-Dish 35 mm, sterile, low wall) at a density of 15 × 10^4 cells/mL in complete medium and incubated to confluence. After being cultured for 24 h, FBH and A-172 Ibidi dishes were treated with the corresponding dispersion of nanoparticles. Finally, after 24 h of incubation samples were exposed to the AC field during 20 min.

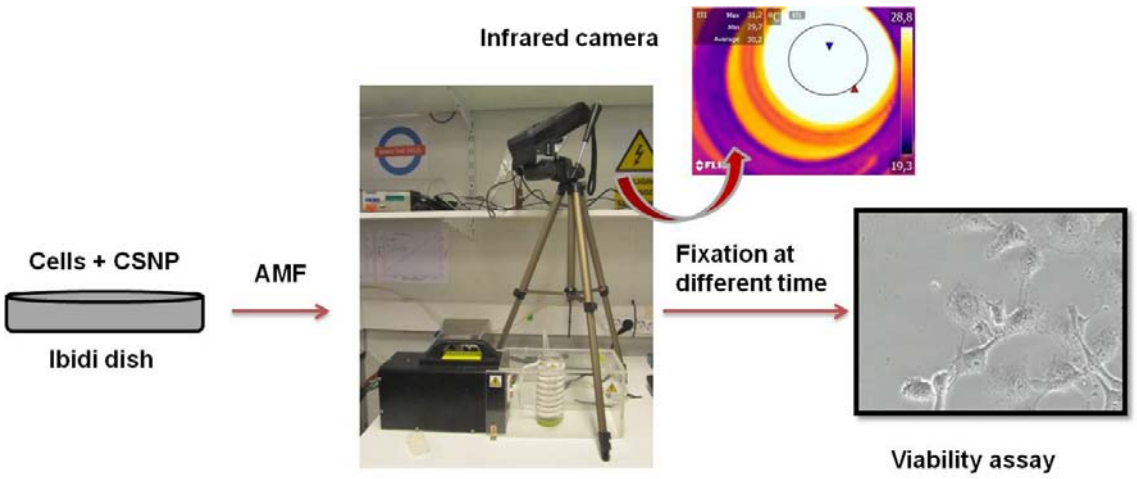

Figure 6.2. *Scheme for the in vitro magnetic hyperthermia treatment using Ibidi dishes.*

After that the samples were rinsed with PBS to remove dead cells and free chitosan nanoparticles. Samples were fixed with glutaraldehyde 2.5% (v/v) at 37 °C for 10 min immediately after the MH treatment (t=0). Then, A-172 were treated again with chitosan nanoparticles and samples were fixed 4 h later (t=4) of the first MH treatment.

In order to study the cell death by several MH treatment, a second doses was applied 24 h latter of the first MH treatment. Samples were fixed 4 hours later (t=24) of the second doses. All the experiments were made for triplicate. During the experiment, the medium temperature was measured with an infrared camera (Jenoptik).

ii. Determination of cell viability after of Magnetic Hyperthermia.

Crystal violet (C.V) staining was used for determining cell viability after magnetic hyperthermia treatment. All the samples fixed, were treated with a 0.1% (w/v) of aqueous solution of crystal violet in PBS pH 7.2. After 10 min of incubation at room temperature under agitation, the staining solution was discarded; the samples were washed with Mili-Q water and then dried at 37 ºC. Finally, aqueous acetic acid (10% v/v) was added to the samples and an aliquot of 200 µL was taken and placed it into a well of plate to determinate the relative viability by a microplate reader at 620 nm-690 nm.

iii. Cell staining procedure.

All the samples after the cell fixation were treated with acridine orange and propidium iodide (AO/PI), which were used to visualize living and dead cells simultaneously. Acridine orange (AO) is permeable to both live and dead cells and stains all nucleated cells to generate green fluorescence. On the other hand, propidium iodide (PI) enters dead cells with compromised membranes and stains all dead nucleated cells to generate red fluorescence.

The procedure was as follows: All the samples fixed after magnetic hyperthermia treatment, were rinsed with PBS and then triton (Triton X-100, molecular biology grade, density 1.07 g/cm^3) 0.05% v/v in PBS was added for 20 min at 37 ºC under low speed orbital shaking. After that, the samples were rinsed with PBS and 10 µL/mL of AO/PI staining solution was added and left it for 30 min at room temperature in the darkness. Finally, the samples were rinsed twice with Tween 20 solution at 0.1% in PBS and left it with Mili-Q water. Samples were observed in an epifluorescence microscope (Nikon eclipse TE2000-S) equipped with a FX RED filter set to detect dead cells, and a FITC filter set to detect live cells.

6.3. RESULTS AND DISCUSSION

6.3.1 Preparation of ferrofluid and 5-Florouracil loaded chitosan nanoparticles.

Chitosan nanoparticles loaded with 5-Fluorouracil and ferrofluid at different concentrations were synthesized as described in experimental section. Chitosan nanoparticles have been prepared using a method based on electrostatic interaction between the positive amino groups of chitosan with the negatively charged phosphate groups of TPP explained in the chapter 5. In this way, these kinds of nanoparticles might act as dual functional material for drug release and magnetic hyperthermia treatment.

6.3.2 Characterization of nanoparticles

i. Morphological studies

Figure 6.3 shows the FESEM micrograph corresponding to CS+FU+Fe3.2% nanoparticles. Bright field image allows corroborating the encapsulation of ferrofluid within a matrix of chitosan. The Figure 6.3, with the use of microscope software, permits obtained an estimation of nanoparticles sizes, which are in the order of 200 nm or less. However, this image suggests a high polydispersity, as will be confirmed by AFM analysis. From this morphological analysis, it is important to highlight that 5-FU and ferrofluid (as was proved in the previous chapter) does not affect the nanoparticles formation.

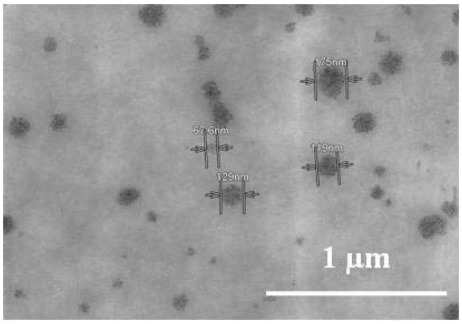

Figure 6.3. *Micrograph corresponding CS+FU+Fe3.2% nanoparticles by field emission scanning electron microscopy.*

The AFM analysis allows determining the morphological appearance and size for chitosan nanoparticles loaded with 5-FU and ferrofluid with different ferrofluid concentration (1, 3.2 and 5.6% w/v). Figure 6.4 shows the topography, the corresponding 3D image and histograms of the samples under study. The nanoparticle size provided by AFM corresponds to CS+FU+Fex nanoparticles spread and dried on a glass surface. As can be observe, all the samples presented a nearly spherical shape and a size in the range of 140-200 nm. The nanoparticles diameter is reported on the Figure 6.4. Coefficient of variance (CV) was calculated according to the data obtained from the histogram and all the samples presented a CV in the range of 15-20%. This parameter describe the dispersion of samples, that can be related with the Gaussian curve (Figure 6.4-c), it is observed that CS+FU+Fe1% and CS+FU+Fe5.6% presented a similar Gaussian curves, on the contrary CS+FU+Fe3.2%. The latter sample presented a slightly lower CV than rest of samples; consequently its Gaussian curve is narrower.

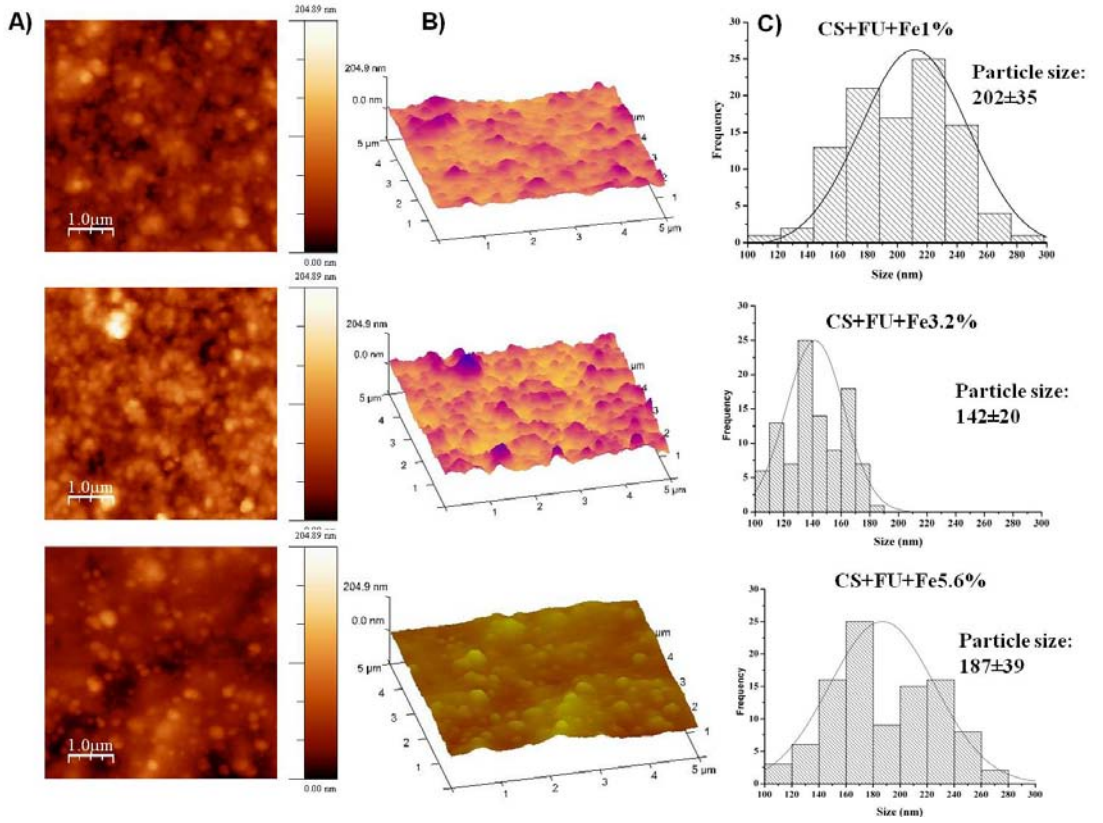

Figure 6.4. *AFM images A) Topography (area 5 × 5 µm), B) 3D images and C) histogram, of CS+FU+Fex with different ferrofluid concentration (x= 1, 3.2 and 5.6% w/v).*

ii. Analysis of the chemical structure.

ATR-FTIR analyses in the region of 600–2000 cm^{-1} was carried out to study the hypothesized interaction among the components of chitosan nanoparticles (chitosan, 5-FU and ferrofluid). The 5-FU chemical structure is shown in Figure 6.5. Its spectrum (Fig 6.6-a) presented well define and sharp peaks at 1651 cm^{-1} attributed to C=O stretching, 1501 cm^{-1} assigned to N-H amine II band, N-H stretching of amide at 1429 cm^{-1}, 1245 cm^{-1} for C-F and 804 cm^{-1} due to C-H out of plane deformation[35].

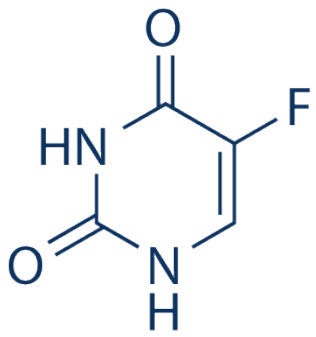

Figure 6.5. *5-Fluorouracil chemical structure.*

CS+TPP spectrum (Figure 6.6-b) as studied in the previous chapter, presents the band at 1570 cm^{-1} corresponding to N-H amine II band, 1218 cm^{-1} attributed to P=O stretching vibrations in phosphate ions of TPP and 1650 cm^{-1} that corresponds to C=O stretching.

Spectra of CS+FU (Figure 6.6-c), CS+FU+Fe3.2% (Figure 6.6-d) and CS+FU+Fe5.6% (Figure 6.6-e) show a strong band at 1246 cm^{-1} and 813 cm^{-1} attributed to the presence of 5-FU (Figure 6.6-a). The band corresponding to the band attributed to N-H stretching of amide in 5-FU spectrum (Figure 6.6-a) which appeared at 1429 cm^{-1} shift to 1407 cm^{-1} for all the samples loaded with 5-FU. Moreover, it was observed a shift corresponding to amino groups for CS+FU (Figure 6.6-c), CS+FU+Fe3.2% (Figure 6.6-d) and CS+FU+Fe5.6% (Figure 6.6-e) to respect at CS+TPP spectrum (Figure 6.6-b). This band in CS+TPP spectrum appeared at 1570 cm^{-1} and shifts to 1551 cm^{-1} for CS+FU and CS+FU+Fe3.2%, while CS+FU+Fe5.6% presented a shift at 1557 cm^{-1}. These shifts could suggest the presence of hydrogen bonding between the polar functional groups in 5-fluorouracil and NH_2 groups of chitosan. In addition, the band located at 804 cm^{-1} in 5-FU spectrum presented a shift to 808 cm^{-1} for CS+FU. With regard to CS+FU+Fe3.2% and CS+FU+Fe5.6% this band appeared at 813 cm^{-1}. The higher shifts observed for samples loaded with ferrofluid, could suggest an interaction among 5-FU and ferrofluid.

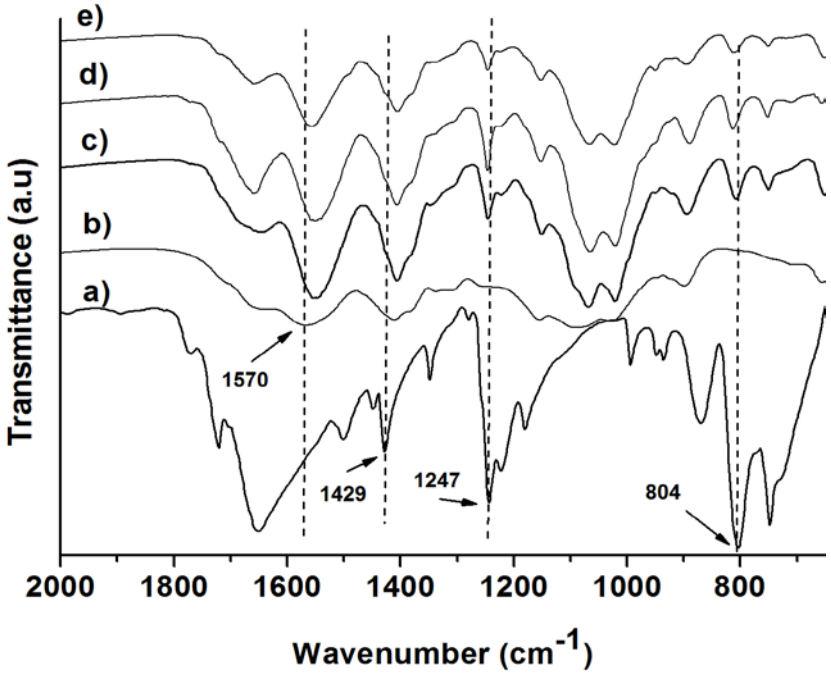

Figure 6.6. *ATR-FTIR spectra of a)5-FU, b)CS+TPP, c)CS+FU, d) CS+FU+Fe3.2% and e) CS+FU+Fe5.6%.*

To explain the above results, it is proposed the formation of a metal complex, based on a central atom or ion (in this case iron), bonded to a surrounding array of molecules or anions (ligands) which could interact with amine groups of the samples. Although, the bands corresponding to iron oxide nanoparticles were not observed by this technique. However, this kind of interaction among 5-FU and iron oxide nanoparticles (IONPs) has been recently reported in the literature[36]. This fact could explain as well, the slight shifts of the N-H amine band between samples loaded with ferrofluid in Figure 6.6. The N-H amine band appeared at 1551 cm^{-1} for CS+FU+Fe3.2% spectrum (Figure 6.6-d) and at 1557 cm^{-1} for CS+FU+Fe5.6% spectrum (Figure 6.6-e). Taking into account this hypothesis, of a metal complex, it could also affect other results, such as, the drug release and the loading efficiency of chitosan nanoparticles, as it will explain ahead.

6.3.3 Drug release from chitosan nanoparticles

i. Drug encapsulation efficiency and loading efficiency.

The encapsulation efficiency (EE) and loading efficiency (LC) of 5-FU in chitosan nanoparticles was determined through UV-spectroscopy, as described in experimental part. The results are summarized on Table 6.1.

With regard to EE, all the samples presented very similar values on the range of 80-82%. These results agree with other investigations which report EE on the range of 80-85%[37]. On the other hand, LC values obtained for all the samples are on the range 33-35% (Table 6.1), with the exception of CS+FU+Fe5.6%, which presented a significant increase in LC. This difference in the LC value obtained for CS+FU+Fe5.6% in comparison to the other ferrofluid loaded chitosan nanoparticles could be explained by the formation of a complex between iron and 5-FU, as was suggested by ATR-FTIR. This would explain why the same concentration of 5-FU (0.5% w/v), the sample with the highest amount of ferrofluid (CS+FU+Fe5.6%) presents the highest LC.

Table 6.1. Loading efficiency (LC) and encapsulation efficiency (EE) of the samples under study.

Sample	EE(%)	LC(%)
CS+FU	81.9±0.6	33.8±7.2
CS+FU+Fe1%	81.4±0.8	37.5±6.4
CS+FU+Fe3.2%	80.8±0.7	34.7±4.0
CS+FU+Fe5.6%	80.6±0.4	70.6±2.0

ii. *In vitro* drug release.

Figure 6.7 shows the *in vitro* drug release of 5-FU from CS+FU and three CS+FU+Fex samples. As can be observed, all the samples presented a burst on the first day caused by diffusion of 5-FU located closer to the surface of chitosan nanoparticles at the two measured pH. Then, there was a controlled diffusion of 5-FU from chitosan nanoparticles during the next 30 days.

From a general overview, there is a very clear dependence of the amount of 5-FU released as a function of pH. For CS+FU, at the cumulative 5-FU release after three days was ~45% and at pH 5.2 was ~20%. However, for CS+FU+Fe1% and CS+FU+Fe3.2% at pH 5.2 the cumulative 5-FU release was similar ~18-23% but at pH 7.4 decreases to ~35%. These results might be explained by considering the major solubility of 5-FU in pH 7.4 than in pH 5.2 as previously reported [38].

In contrast, for CS+FU+Fe5.6% is evident that amount of 5-FU released was independent from the pH, obtaining a percentage of the cumulative 5-FU release of ~10-15%. It is observed the drug delivery is much lower for CS+FU+Fe5.6%. This fact, can be explained by the stabilization of 5-FU for the iron as we demonstrated thorough ATR-FTIR.

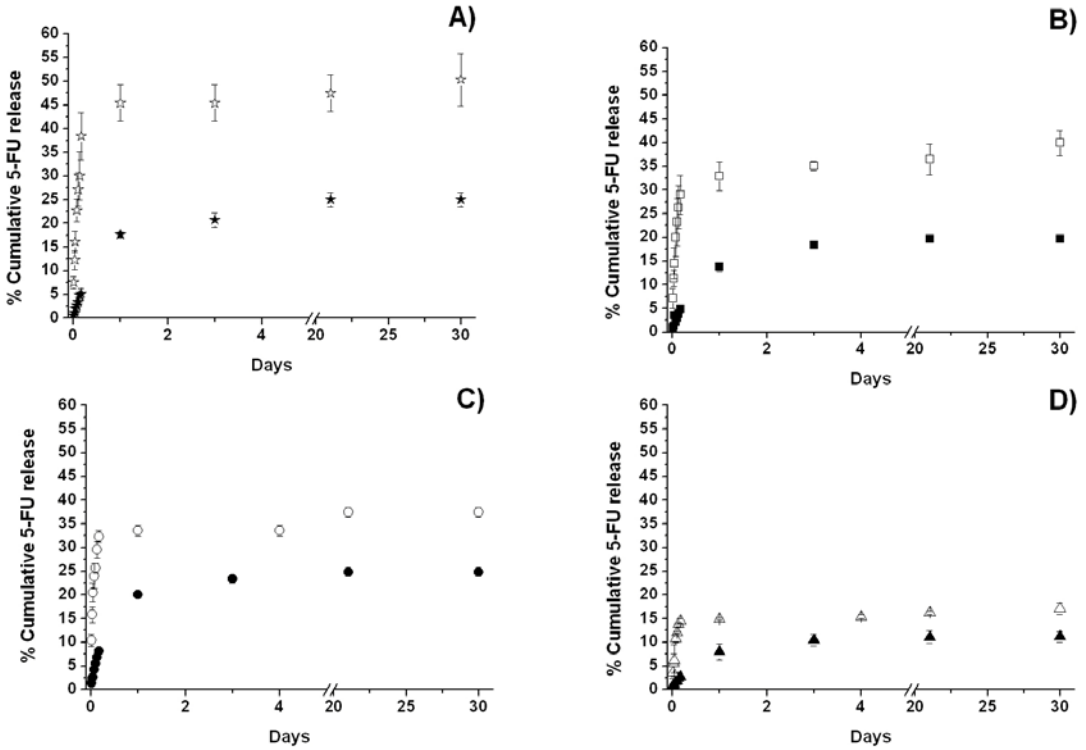

Figure 6.7. *In vitro release of 5-FU from chitosan nanoparticles at pH=7.4 (empty symbols) and pH=5.2 (full symbols) at 37 ºC: A) CS+FU, B) CS+FU+Fe1%, C) CS+FU+Fe3.2% and D) CS+FU+Fe5.6%.*

According to the results obtained, it is possible to modulate the drug release as a function of the ferrofluid concentration and pH for all the samples under study in order to provide a prolonged release of drug.

6.3.4 Biological studies

i. Cytotoxicity assays

The cytotoxicity of samples under investigation CS+FU+Fex (x= 1,3.2 and 5.6% w/v) was evaluated with the Alamar Blue assay. The experiments were tested in two cell lines, Fibroblast and malignant human glioblastoma cells (A-172). Both cells lines were treated with chitosan nanoparticles dispersed at different concentrations in medium without phenol red.

Figure 6.8 shows Alamar Blue assay results, it is observed that all the samples presented a dose-dependent effect for both cells lines, that is, the higher the concentration of nanoparticles in the aqueous dispersions, the lower the cell viability. Specifically for CS+FU+Fe5.6%, at high concentration (5 mg/mL) presented a cell viability of ~10% for both cells lines, but at lower concentrations (0.6 mg/mL), cell viability achieved was almost 100% for FBH (FBH, Figure 6.8-a) and ~70% for A-172 (Figure 6.8-b). This difference of the cell viability as a function of cell line can be attributed at two factors: firstly to the effect of drug action and secondly to intrinsic features of each cell line. Which means that cancer cell with regard to normal cells, loss important features as fast cell proliferation, loss of adhesion, invasion capacities and high resistant to die[39]. In this case, cancer cells (A-172) being sensitive to chitosan nanoparticles can be beneficial for the final application.

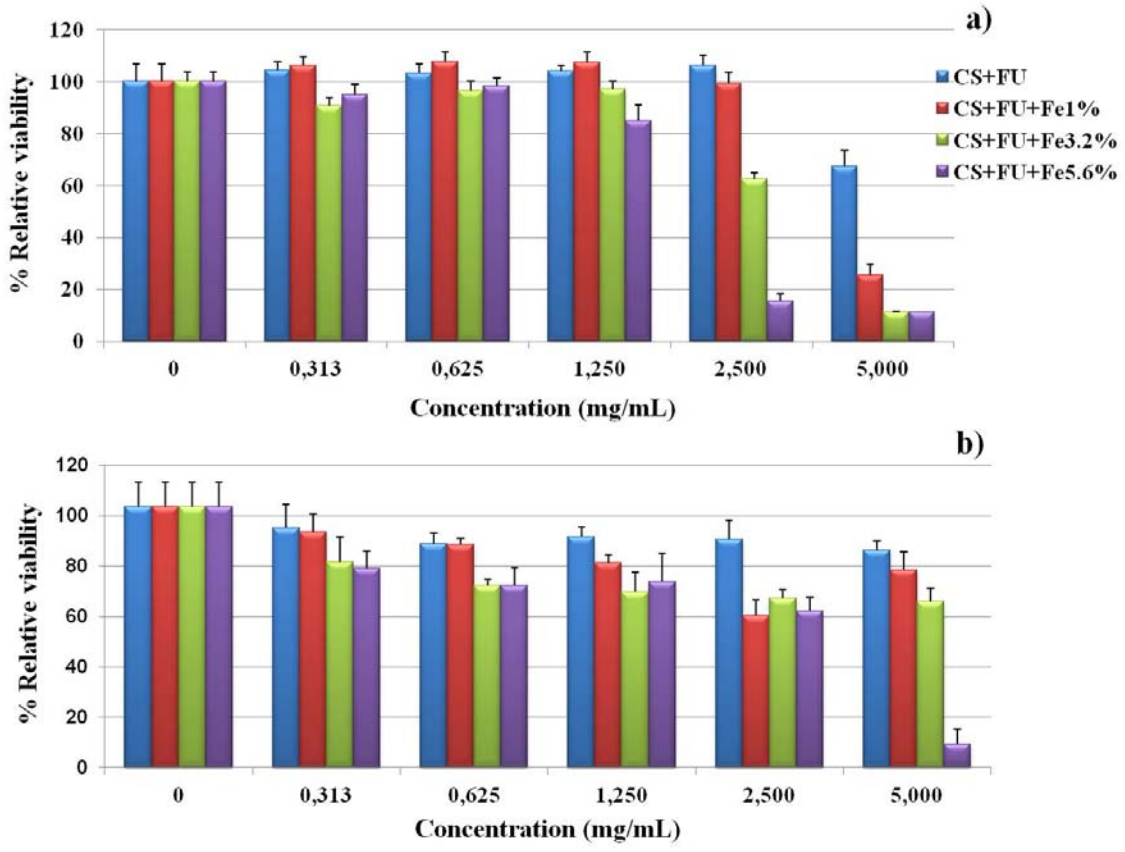

Figure 6.8. *Alamar Blue assay results, A) FBH and B) A-172 for chitosan nanoparticles loaded with 5-FU at different concentrations, and for the negative control, cells without treatment. All the results are shown as mean n=4 ±S.D.*

Based on the results found on AB assay, the concentration proposed for the next biological studies is 0.6 mg/mL, because at this concentration both cells lines showed high viabilities values.

ii. Cellular uptake of chitosan nanoparticles

The cellular uptakes of different chitosan nanoparticles in FBH and A-172 cells lines after 24 h of incubation have been measured through fluorescence technique using an epifluorescence microscope. The study was carried out for the following chitosan nanoparticles: CS+TPP, CS+Fe5.6%, CS+FU and CS+FU+Fe5.6%, at a concentration of 0.6 mg/mL. In Figure 6.9 is shown fluorescence images corresponding to cell lines, FBH and A-172 incubated with sample CS+FU+Fe5.6% for 24 h. To obtain a good observation for the fluorescence images different dyes were used, CS+FU+Fe5.6% were stained with sodium fluorescein dye (green), the cellular nuclei were stained using a Hoechst H33342 dye solution (blue) and the cytoskeleton of the cells were stained using phalloidin (red). The merged image (union of the three stains) shows that after 24 h of incubation, CS+FU+Fe5.6% were successfully internalized into both cells lines. Some agglomeration was observed around the cellular nuclei for both cases.

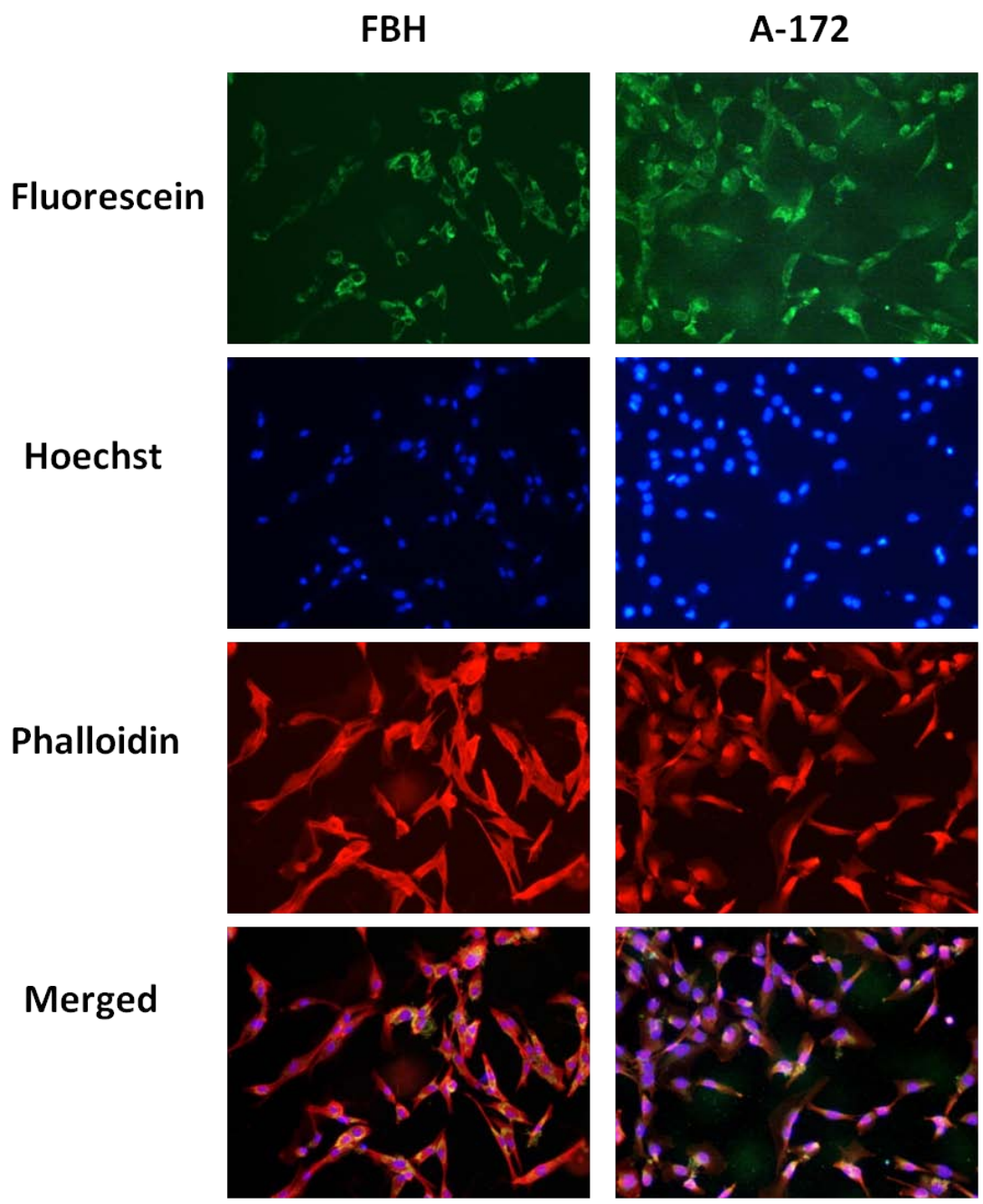

Figure 6.9. *Uptake studies for CS+FU+Fe5.6% after 24 h of incubation, for FBH and A-172 cells lines.*

With regard to the rest of the samples, similar results have been obtained (see Annexed 1). Therefore, the physicochemical properties of chitosan nanoparticles prepared as example, positive surface charge, size, composition and encapsulation of different materials (ferrofluid and 5-FU) allow effective uptake into both cell lines. In

addition, it was observed that cellular uptake was independent of the nanoparticles size (range 140-200 nm) for our samples.

6.3.5 *In vitro* Magnetic hyperthermia experiments

Magnetic hyperthermia treatment was applied over two cells lines, A-172 and FBH treated with chitosan nanoparticles (CS+Fe5.6%, CS+FU and CS+FU+Fe5.6%). For this experiment, two protocols were proposed. Both protocols are based on to avoid the harvesting of such cells and to assure their cellular viability. The first protocol made use of commercial equipment and the second protocol of homemade equipment.

i. Protocols of measurements.

- Protocol employing at commercial equipment.

This experiment was carried out with commercial equipment, DM10. Therefore, it was necessary to select a support to seed the cells with the appropriate dimensions, because, it is introduced into a vial (see Figure 6.1). A small discs of polystyrene (PS) was employed to seed both cells lines (FBH and A-172).

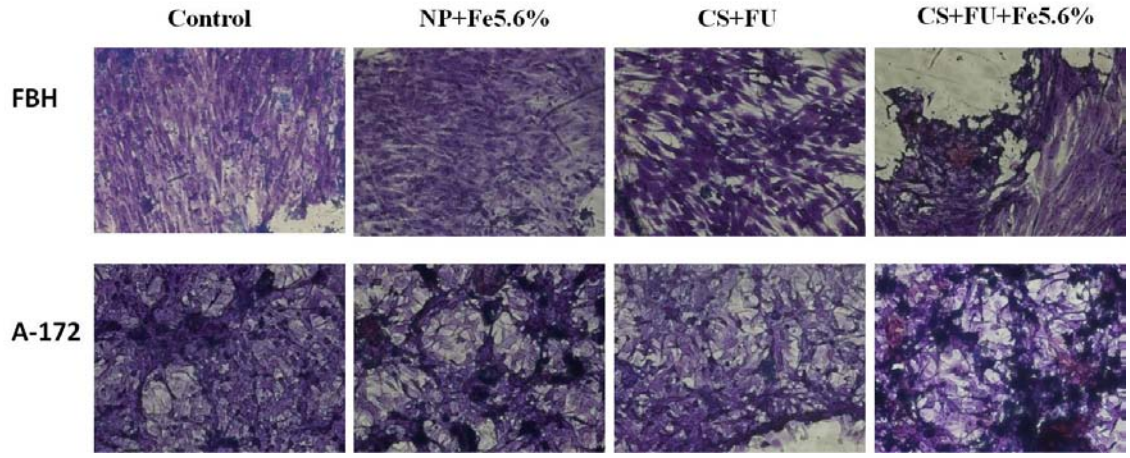

Figure 6.10. *Photograph of crystal violet staining for FBH and A-172 cells lines seeded onto PS discs, after one magnetic hyperthermia treatment.*

Figure 6.10 shows, photographs of crystal violet staining for FBH and A-172 after 20 min of MH treatment. Both cell lines presented an important change in their morphology, attributed to a cellular damage for the two cells lines. In particular, FBH cells treated with all the samples under investigations, mainly for CS+FU+Fe5.6%, samples look like "burn". In the case of A-172 cells, there are some dark areas, which we attributed to cellular death.

Despite of all the experiments were carried out by triplicate, the determination of cell viability by crystal violet was no reproducible and therefore we decided that this protocol is not accurate. Moreover, in some photographs it was observed some empty spaces on their surface (photographs not shown here). This negative result could indicate that PS discs are not the appropriate material for this kind of experiments, because it is not a commercial material for cell culture or need a special covering. So, taking into account these drawbacks, we discard this protocol.

- Protocol employing homemade equipment.

For this second protocol, we keep the same principle of avoiding the harvesting of the cells, as in the previous protocol. In addition, for this experiment Ibidi dishes were employed (see Figure 6.2), that are the material of choice for rest cell studies. Homemade equipment was employed for this experiment and it was possible to recorder the temperature of the samples with an infrared camera.

ii. Determination of cell viability after of Magnetic Hyperthermia.

Figure 6.11 shows photographs of crystal violet staining for FBH and A-172 treated with different samples, after one doses of magnetic hyperthermia (MH) treatment and immediate fixation of cells with glutaraldehyde (t=0). Photographs were taking at 2X magnification (Figure 6.11-a) and 10X magnification (Figure 6.11-b). Figure 6.11-a shows for FBH and A-172 cells an evident cellular damage after the MH treatment, the small spots correspond to dead cells or in apoptosis process. As can be

observed in Figure 6.11-b, for both cell lines there are important changes over cells morphology after the hyperthermia treatment mainly for CS+FU+Fe5.6%. These changes on their morphology are due to cell shrinkage and as a result they presented smaller size, the cytoplasm is dense and the organelles are more tightly packed, thus suggesting that cells undergo on apoptosis process [40]. Therefore, this result demonstrates the ability of chitosan nanoparticles to produce cellular damage after MH treatment which results in a percentage of cell death, despite of low chitosan nanoparticles concentrations employed in these biological studies.

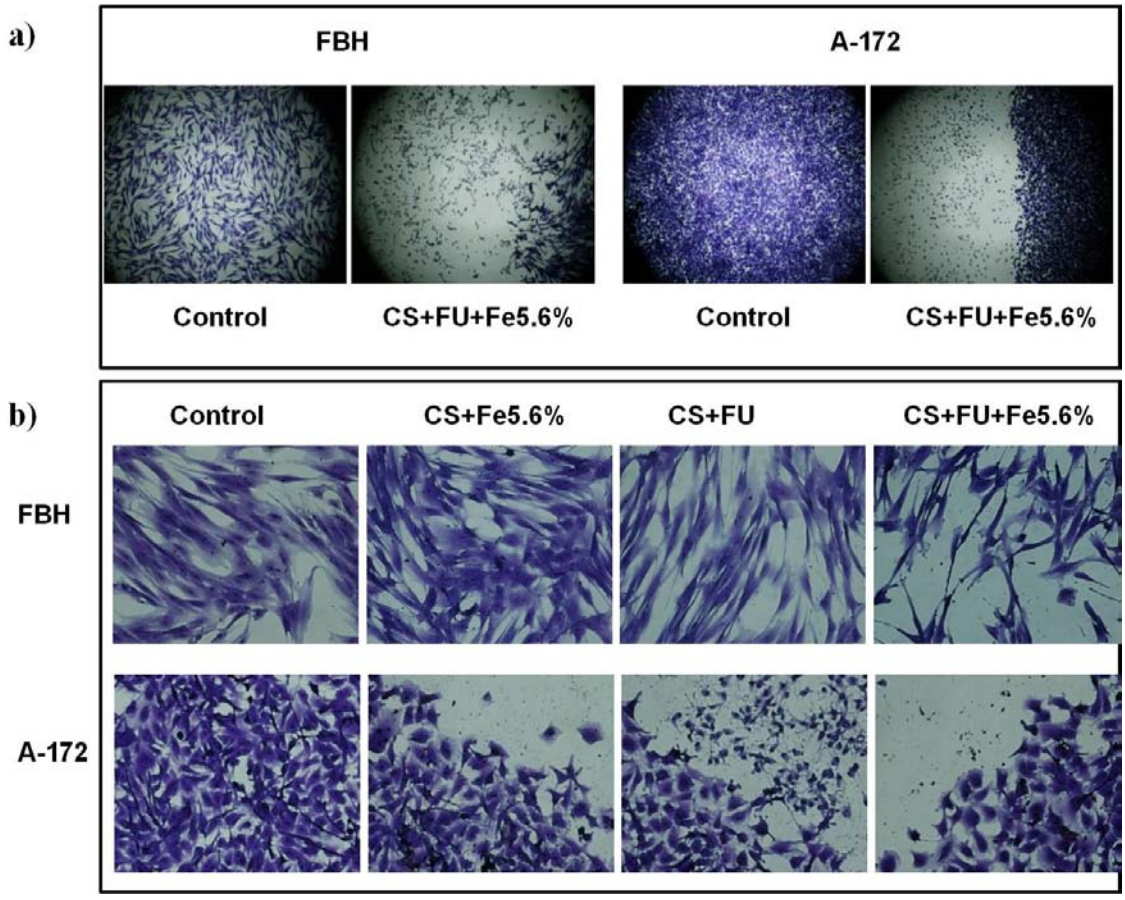

Figure 6.11. *Photograph of a) representative images with a magnification of 2x, of control and CS+FU+Fe5.6% for both cells lines and b) crystal violet staining for FBH and A-172 cells lines (magnification of 10X) after one magnetic hyperthermia treatment and fixed immediately.*

Despite of the cellular damage observed in the photograph (Figure 6.11), it was impossible to observe an increasing of temperatures of the whole cell medium (44-46

°C) necessary to hyperthermia conditions[41]. This fact could be explained due to the low concentration of nanoparticles used for the experiment (0.6 mg/mL). In the experiment there was no increasing of temperature detectable with the infrared camera (Figure 6.12), although, temperature was homogeneous on the Ibidi dish, as can we observed in Figure 6.12.

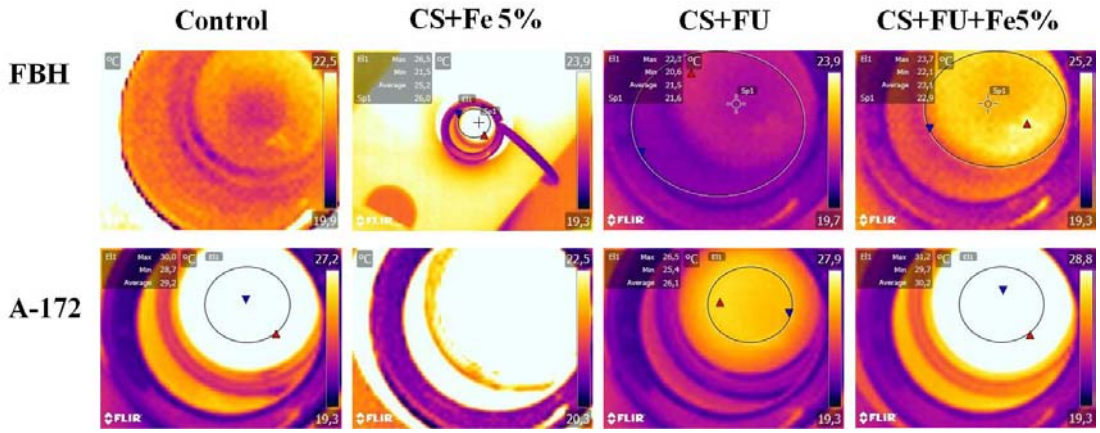

Figure 6.12. *Photograph of infrared camera of FBH and A-172 cells lines in the moment of magnetic hyperthermia treatment was applied.*

Despite, that there was no increasing detectable of temperature during the MH experiments, Figure 6.11 shows a cellular damage of the samples under study. It has been reported some hypothesis that could explain this fact and to conclude that cellular death, after MH treatment, can be related to cluster formation of several cells fully loaded with magnetic nanoparticles and not to the temperature increase of a single cell[41].

In order to quantify the impact of MH over both cells lines, cell viability was determined through crystal violet staining for samples subjected to one MH treatment. As can be observed in Figure 6.13, after the first MH treatment, there is a significant reduction of the cell viability as a function of cell type being malignant human glioblastoma (A-172) more sensitive to MH treatment than normal cells (FBH). In fact, FBH treated with all the samples under study presented cell viability higher than ~94 %, which indicates than MH treatment does not have an important effect on these cells. On

the contrary, A-172 treated with chitosan nanoparticles presented an important decrease in the cell viability on the range of 67-75%. Therefore all chitosan nanoparticles were effective for A-172 after MH treatment achieving a reduction of cell viability. This difference could be related with loss of properties of cancer cells with regard to normal cells and it is a key issue for hyperthermia.

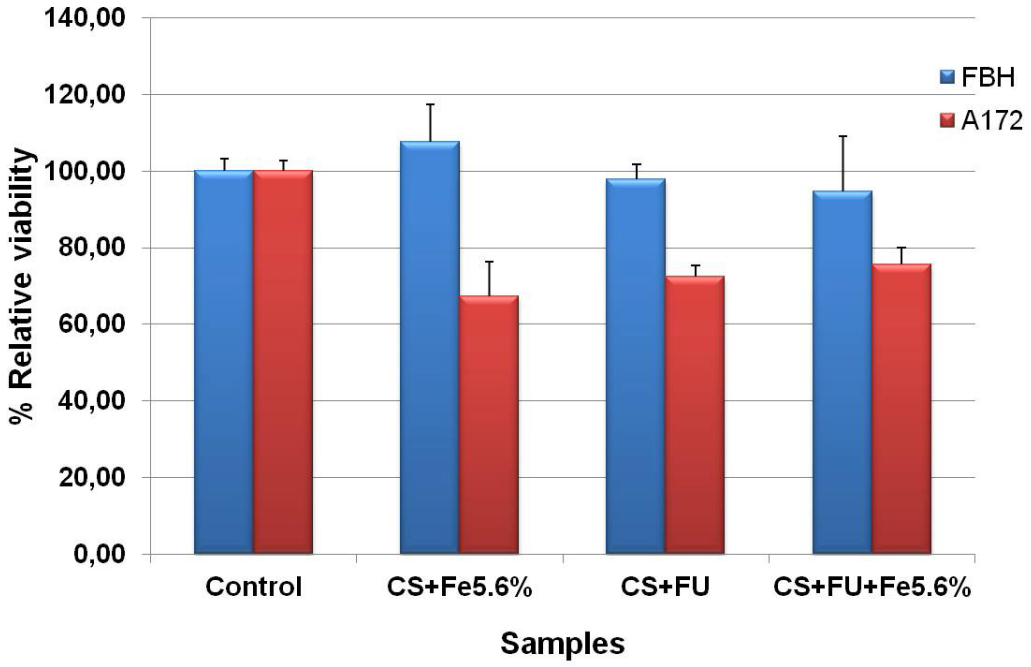

Figure 6.13. *Crystal Violet results, cell viability for FBH and A-172 cell lines after one MH treatment (t=0).*

In principle, no significant differences are observed between the cell viability calculated after the first MH treatment with crystal violet and the cell viability obtained by Alamar Blue assay (see Figure 6.8). This fact could be explained because crystal violet procedure stained all the cells including those that are in apoptosis process, which artificially increase the relative viability reported. This few selectivity in the stain process over different the states of the cells could mask, the effect of chitosan nanoparticles over both cells lines and hence the effect of the MH treatment over cell viability.

Taking into account this, as there is no literature study concerning the optimum time to fix the cells, the same MH experiment was applied to A-172 cell line but samples were fixed 4 h later of the first MH treatment, instead of being fixed immediately.

In Figure 6.14 is shown crystal violet staining for A-172 cell lines photographs after the MH treatment and fixed 4 h later, taking at 2X magnification (Figure 6.14-a) and at 10X magnification (Figure 6.14-b). In Figure 6.14-a is observe a clear evidence of the cellular damage after the MH treatment. In Figure 6.14-b, it is possible to observe in detail how samples look. As can be observed, some of the cells in apoptosis process were removed after rinsing the samples before of their fixation. However, if we analyze the morphology of the cells that are still on the Ibidi dish, they look as healthy cells or in recuperation process. This fact is based on their long filopodia, which suggest that cells are growing and in recuperation process, however, it is still possible to observe some cell shrinkage.

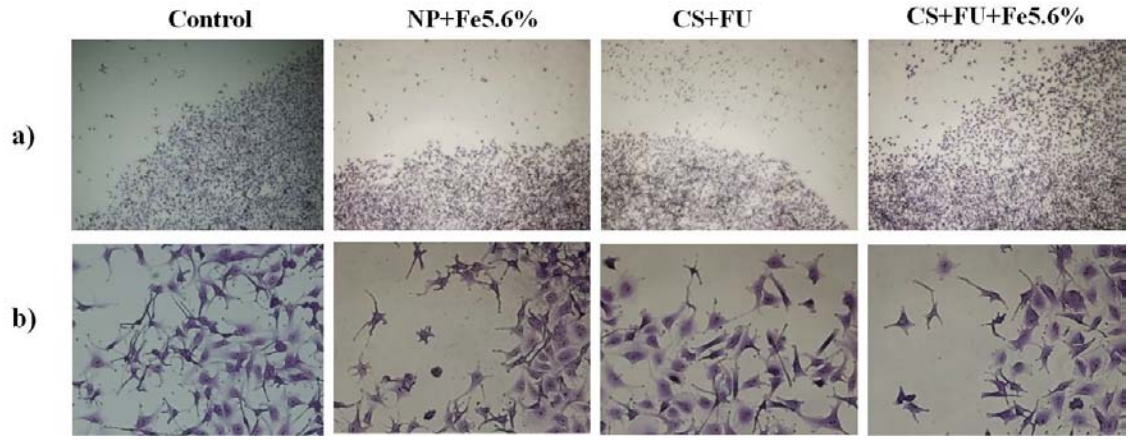

Figure 6.14. *Photograph of crystal violet staining for A-172 cells lines after one magnetic hyperthermia treatment and fixed 4 h later, a) photograph taken at 2X, b) photograph with 10X of magnification.*

This hypothesis of the cell regeneration, 4 h later, of the MH treatment, was quantified trough crystal violet. The comparison of cell viability of samples fixed at t=0 and t=4 is shown in Figure 6.15. On the one hand, it is very evident that cell viability decreased as a function of type of chitosan nanoparticles. In fact, cells treated with

CS+FU+Fe5.6% presented the lowest cell viability (~93%). On the other hand, cell viability of sample fixed at 4 h later of the MH treatment, increased to respect at samples fixed at t=0. This increase indicates cell regeneration during this 4 h. Therefore, this cell regeneration and their fast proliferation rate, mask the effect of chitosan nanoparticles over the A-172 cell line.

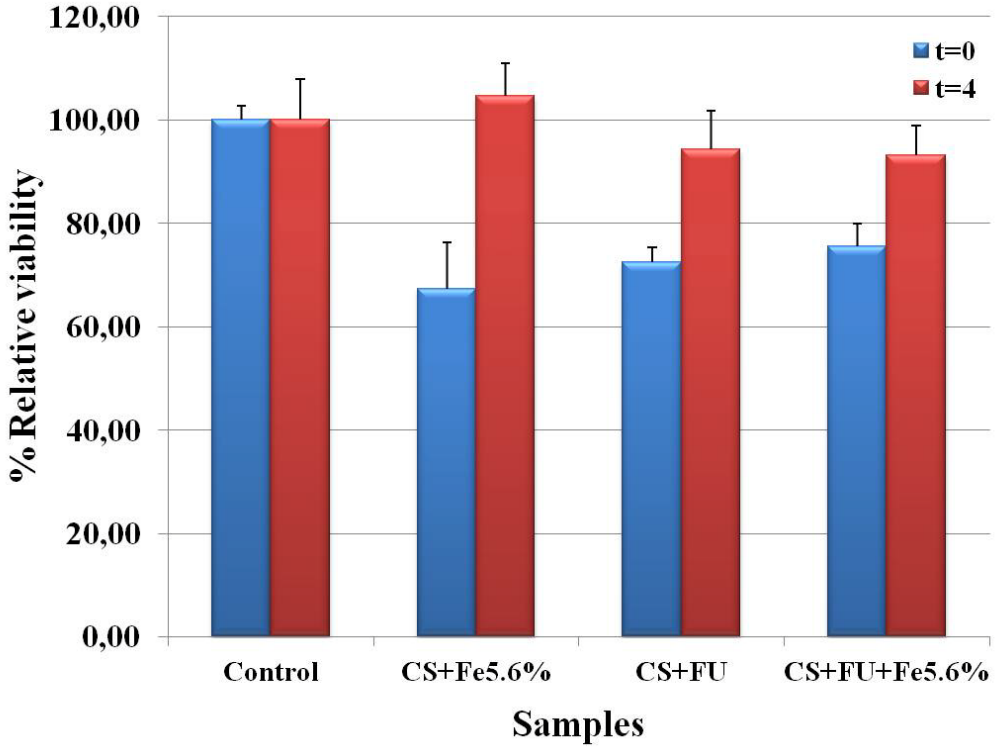

Figure 6.15. *Comparison of cell viability for A-172 cell line after one MH treatment fixed a different times. (t=0 and t=4).*

iii. Cell staining.

AO/PI staining (Figure 6.16) allows recognizing easily dead cells (red fluorescence), lived cells (green fluorescence) and cells in the process of death (orange fluorescence) after MH treatment. In Figure 6.16 fluoresce images for FBH at t=0 and A-172 at t=0 and t=4 are show. It is observed for A-172 cell line dead cells, while for FBH was not abundant. This effect is also evident for A-172 cells fixed at t=4 where red fluorescence highly increases for cells treated with CS+FU+FE5.6%. This indicates a higher number of dead cells in this case.

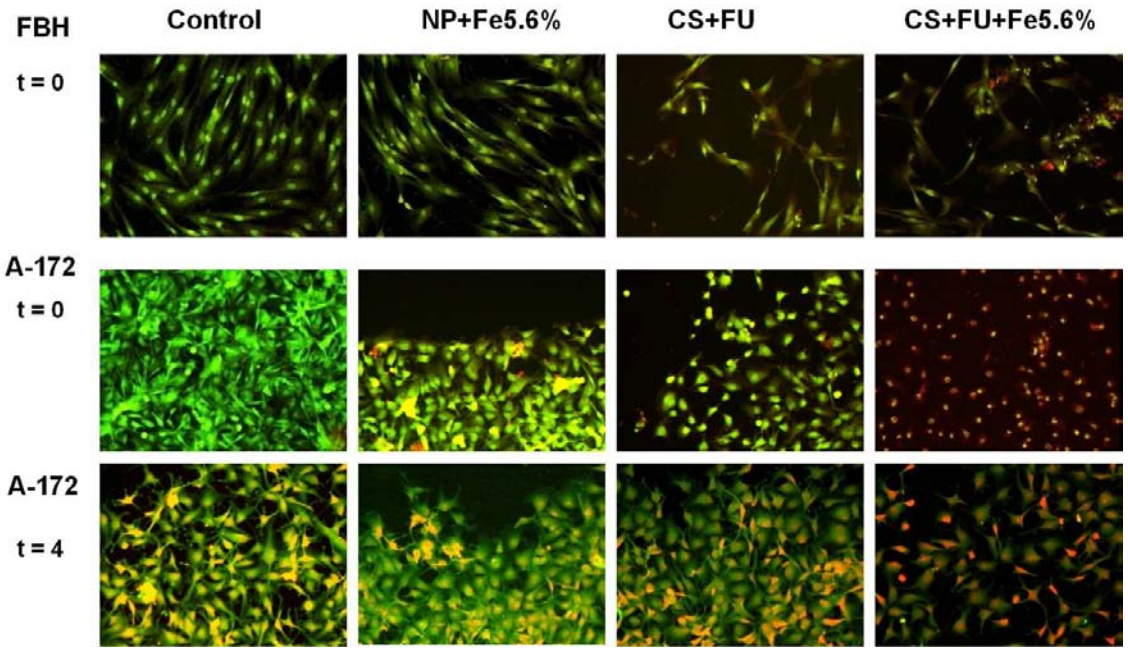

Figure 6.16. *Fluoresces images for FBH and A-172 cells lines treated with samples under study, obtained after AO/PI staining after one magnetic hyperthermia treatment and fixed at different times.*

iv. Effect of two Magnetic Hyperthermia treatments

A second magnetic hyperthermia (MH) treatment was applied to A-172 cell line and samples were fixed 4 h later (t=24). Cell viability was determined by crystal violet as in the previous MH treatment. Their corresponding photographs of crystal violet staining see Annexed 2.

Figure 6.17 shows a comparison of the cell viability of cancer cells (A-172) with after one and two MH treatments and samples fixed 4 h latter of each treatment. As can be observed, the cell viability after a second MH treatment increases to respect at t=4 for cells treated with NP+Fe5.6%. This fact can be explained, for the cell proliferation rate of A-172, which overcomes the cellular death. Also, these results suggest that some of the cells damaged during the MH treatment exposure appear as 'healthy' cells within few hours after (4h). In the case of cells treated with CS+FU the cell viability did not

present a significant change. Nevertheless, for samples treated with CS+FU+Fe5.6% cell viability decreased with regard to t=4 overcomes the cell proliferation.

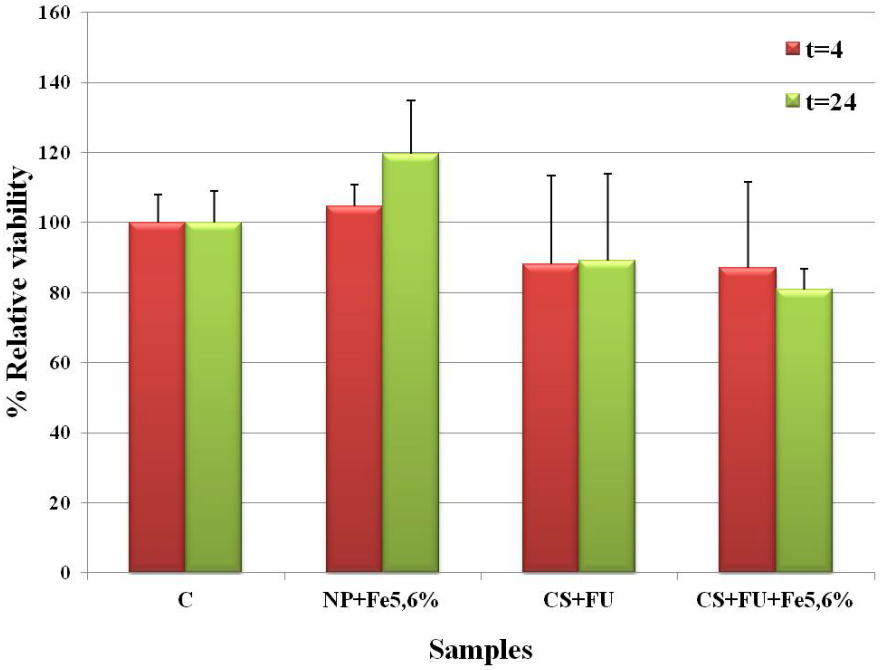

Figure 6.17. *Comparison of cell viability for A-172 cell line determined by crystal violets at t= 4 and after a second MH treatment (t=24).*

AO/PI staining was made as well for this experiment, which it was possible to observed death cells (the results are show in Annexed 3). Figures 6.18 shows a representative images for A-172 cell line treated with CS+FU, obtained after AO/PI staining (Figure 6.18-a) and crystal violet staining (Figure 6.18-b) after a second MH treatment. In both images, it is observed a vacuolization process (circles) by the appearance of empty bags into cytoplasm, which indicated than cells are in process death. All this bags are enclosed within an intact plasma membrane, as can be observed in both images, which it is an important feature for apoptosis[40]. Also, typical nuclei separation and chromatin condensation related with apoptosis was observed (arrows). These results suggested that chitosan nanoparticles are capable of inducing apoptosis in A-172 cells. Same results were obtained for the other samples.

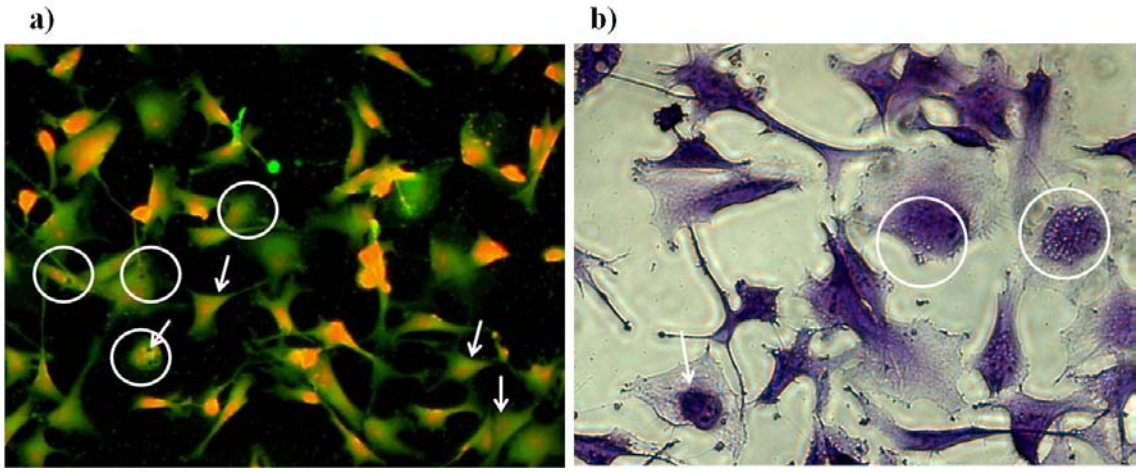

Figure 6.18. *a) Fluoresce images obtained after AO/PI staining and b) crystal violet staining for A-172 cell line treated with CS+FU, where is observed the vacuolization process (circles) and chromatin condensation (arrows).*

Taking in account, all the biological studies performed after the magnetic hyperthermia applications, chitosan nanoparticles loaded with ferrofluid and 5-FU, arise as potential dual functional system against cancer.

6.4 CONCLUSIONS

In the study of preparation and characterization of 5-FU and ferrofluid loaded chitosan nanoparticles for *in vitro* Magnetic Hyperthermia, the following conclusions can be drawn:

5-FU and ferrofluid loaded chitosan nanoparticles with dual properties for magnetic hyperthermia treatment and drug release were successful obtained by electrostatic interaction among chitosan and TPP. From the ATR-FTIR analysis, it was demonstrated on one hand, the electrostatic interaction between matrix (chitosan) and drug (5-FU) and on the other hand, drug with ferrofluid.

The loading efficiency (LC) and encapsulation efficiency (EE) calculated for chitosan nanoparticles are comprised on the range of 30-36% and 80-85% respectively.

It was demonstrated that drug delivery profile of 5-FU from chitosan nanoparticles can be modulated as a function of ferrofluid concentration and pH. Moreover, drug delivery was faster at pH physiological than acid pH (pH 5.2). Therefore, these results evidence that chitosan nanoparticles and magnetic chitosan nanoparticles are an efficient nano-carrier for drug release applications.

Cytotoxicity assays by Alamar Blue showed that all the samples presented a dose-dependent effect for both cells lines and that as a function of cell line, cancer cells were more sensitive to chitosan nanoparticles loaded with 5-FU and ferrofluid than normal cells.

Chitosan nanoparticles were successfully internalized over normal cells (Fibroblast) and malignant human glioblastoma (A-172). Physicochemical properties of all chitosan nanoparticles (size 140-200 nm) were optima for their uptake with both cells lines.

Magnetic Hyperthermia (MH) treatment was applied over Fibroblast and malignant human glioblastoma cells (A-172) and treated with chitosan nanoparticles using two different protocols. A protocol was designed making use of commercial equipment. This protocol presented several drawbacks, as not reproducible results and PS disc used to seed the cells presented irregularities on its surface. Therefore, a second and definitive protocol was employed based on homemade equipment. A-172 cell line is more sensible to MH treatment than FBH. Cell viability for A-172 was on the range of 67-75%. Samples fixed 4 h later of the first MH treatment, presented a cell regeneration which masked the effect of chitosan nanoparticles.

The effect of a second MH treatment over A-172 was evaluated and it was evident the regeneration of some cells damaged after the treatment and therefore increased cell viability, however it was observed a reduction of ~20% with regard to control. Also, AO/PI staining and crystal violet staining leaded analysis morphologies changes over both cells lines after MH treatment and where was evident apoptosis process.

In view of the entire characteristic, 5-Fluorouracil and ferrofluid loaded chitosan nanoparticles after an optimization process can be considered as potential nano-carrier

for hyperthermia application, achieving a reduction of cell viability and incite the apoptosis after MH treatment.

6.5 REFERENCES

[1] Talelli M, Rijcken CJF, Lammers T, Seevinck PR, Storm G, van Nostrum CF, et al. Superparamagnetic Iron Oxide Nanoparticles Encapsulated in Biodegradable Thermosensitive Polymeric Micelles: Toward a Targeted Nanomedicine Suitable for Image-Guided Drug Delivery. Langmuir. 2009;25:2060-7.

[2] Ding G, Guo Y, Lv Y, Liu X, Xu L, Zhang X. A double-targeted magnetic nanocarrier with potential application in hydrophobic drug delivery. Colloids and Surfaces B: Biointerfaces. 2012;91:68-76.

[3] Dilnawaz F, Singh A, Mohanty C, Sahoo SK. Dual drug loaded superparamagnetic iron oxide nanoparticles for targeted cancer therapy. Biomaterials. 2010;31:3694-706.

[4] Devanand Venkatasubbu G, Ramasamy S, Ramakrishnan V, Kumar J. Folate targeted PEGylated titanium dioxide nanoparticles as a nanocarrier for targeted paclitaxel drug delivery. Advanced Powder Technology. 2013;24:947-54.

[5] Gamboa JM, Leong KW. In vitro and in vivo models for the study of oral delivery of nanoparticles. Advanced Drug Delivery Reviews. 2013;65:800-10.

[6] Alkilany AM, Thompson LB, Boulos SP, Sisco PN, Murphy CJ. Gold nanorods: Their potential for photothermal therapeutics and drug delivery, tempered by the complexity of their biological interactions. Advanced Drug Delivery Reviews. 2012;64:190-9.

[7] Zhou Z, Ma X, Jin E, Tang J, Sui M, Shen Y, et al. Linear-dendritic drug conjugates forming long-circulating nanorods for cancer-drug delivery. Biomaterials. 2013;34:5722-35.

[8] Venkatesan P, Puvvada N, Dash R, Prashanth Kumar BN, Sarkar D, Azab B, et al. The potential of celecoxib-loaded hydroxyapatite-chitosan nanocomposite for the treatment of colon cancer. Biomaterials. 2011;32:3794-806.

[9] Shukla SK, Mishra AK, Arotiba OA, Mamba BB. Chitosan-based nanomaterials: A state-of-the-art review. Int J Biol Macromol. 2013;59:46-58.

[10] Goycoolea FM, Lollo G, Remuñán-López C, Quaglia F, Alonso MJ. Chitosan-Alginate Blended Nanoparticles as Carriers for the Transmucosal Delivery of Macromolecules. Biomacromolecules. 2009;10:1736-43.

[11] Yuan Q, Shah J, Hein S, Misra RDK. Controlled and extended drug release behavior of chitosan-based nanoparticle carrier. Acta Biomaterialia.6:1140-8.

[12] Zhang H, Oh M, Allen C, Kumacheva E. Monodisperse chitosan nanoparticles for mucosal drug delivery. Biomacromolecules. 2004;5:2461-8.

[13] Lien C-F, Molnár É, Toman P, Tsibouklis J, Pilkington GJ, Górecki DC, et al. In Vitro Assessment of Alkylglyceryl-Functionalized Chitosan Nanoparticles as Permeating Vectors for the Blood–Brain Barrier. Biomacromolecules. 2012;13:1067-73.

[14] Gan Q, Wang T, Cochrane C, McCarron P. Modulation of surface charge, particle size and morphological properties of chitosan-TPP nanoparticles intended for gene delivery. Colloids and Surfaces B: Biointerfaces. 2005;44:65-73.

[15] Wu W, Shen J, Banerjee P, Zhou S. Chitosan-based responsive hybrid nanogels for integration of optical pH-sensing, tumor cell imaging and controlled drug delivery. Biomaterials. 2010;31:8371-81.

[16] Zamora-Mora V, Fernández-Gutiérrez M, Román JS, Goya G, Hernández R, Mijangos C. Magnetic core–shell chitosan nanoparticles: Rheological characterization and hyperthermia application. Carbohydrate Polymers. 2014;102:691-8.

[17] Zhao D-L, Wang X-X, Zeng X-W, Xia Q-S, Tang J-T. Preparation and inductive heating property of Fe3O4-chitosan composite nanoparticles in an AC magnetic field for localized hyperthermia. Journal of Alloys and Compounds. 2009;477:739-43.

[18] Dias AMGC, Hussain A, Marcos AS, Roque ACA. A biotechnological perspective on the application of iron oxide magnetic colloids modified with polysaccharides. Biotechnology Advances. 2011;29:142-55.

[19] Zhu L, Ma J, Jia N, Zhao Y, Shen H. Chitosan-coated magnetic nanoparticles as carriers of 5-Fluorouracil: Preparation, characterization and cytotoxicity studies. Colloids and Surfaces B: Biointerfaces. 2009;68:1-6.

[20] Bruton Laurance L. LJS, Parker Keith L. Goodman and Gilman´s The Pharmacological Basis of Therapeutics. Eleven ed. United States: McGraw-Hill 2006.

[21] Nagarwal RC, Nath Singh P, Kant S, Maiti P, Pandit JK. Chitosan Nanoparticles of 5-Fluorouracil for Ophthalmic Delivery: Characterization, in-Vitro and in-Vivo Study. Chemical and Pharmaceutical Bulletin. 2011;59:272-8.

[22] Ganguly K, Aminabhavi TM, Kulkarni AR. Colon Targeting of 5-Fluorouracil Using Polyethylene Glycol Cross-linked Chitosan Microspheres Enteric Coated with Cellulose Acetate Phthalate. Industrial & Engineering Chemistry Research.50:11797-807.

[23] Ashwanikumar N, Kumar NA, Asha Nair S, Vinod Kumar GS. Methacrylic-based nanogels for the pH-sensitive delivery of 5-Fluorouracil in the colon. International Journal of Nanomedicine. 2012;7:5769-79.

[24] Rejinold NS, Chennazhi KP, Nair SV, Tamura H, Jayakumar R. Biodegradable and thermo-sensitive chitosan-g-poly(N-vinylcaprolactam) nanoparticles as a 5-fluorouracil carrier. Carbohydrate Polymers.83:776-86.

[25] Rajan M, Raj V, Al-Arfaj AA, Murugan AM. Hyaluronidase enzyme core-5-fluorouracil-loaded chitosan-PEG-gelatin polymer nanocomposites as targeted and controlled drug delivery vehicles. International Journal of Pharmaceutics. 2013;453:514-22.

[26] Laurent S, Dutz S, Häfeli UO, Mahmoudi M. Magnetic fluid hyperthermia: Focus on superparamagnetic iron oxide nanoparticles. Advances in Colloid and Interface Science. 2011;166:8-23.

[27] Kawashita M, Tanaka M, Kokubo T, Inoue Y, Yao T, Hamada S, et al. Preparation of ferrimagnetic magnetite microspheres for in situ hyperthermic treatment of cancer. Biomaterials. 2005;26:2231-8.

[28] Qu J, Liu G, Wang Y, Hong R. Preparation of Fe3O4-chitosan nanoparticles used for hyperthermia. Advanced Powder Technology.21:461-7.

[29] Cheng R, Meng F, Deng C, Klok H-A, Zhong Z. Dual and multi-stimuli responsive polymeric nanoparticles for programmed site-specific drug delivery. Biomaterials. 2013;34:3647-57.

[30] Li Y, Huang G, Zhang X, Li B, Chen Y, Lu T, et al. Magnetic Hydrogels and Their Potential Biomedical Applications. Advanced Functional Materials. 2013;23:660-72.

[31] Deng Z, Zhen Z, Hu X, Wu S, Xu Z, Chu PK. Hollow chitosan–silica nanospheres as pH-sensitive targeted delivery carriers in breast cancer therapy. Biomaterials. 2011;32:4976-86.

[32] Mi Y, Liu X, Zhao J, Ding J, Feng S-S. Multimodality treatment of cancer with herceptin conjugated, thermomagnetic iron oxides and docetaxel loaded nanoparticles of biodegradable polymers. Biomaterials. 2012;33:7519-29.

[33] Papadimitriou S, Bikiaris D, Avgoustakis K, Karavas E, Georgarakis M. Chitosan nanoparticles loaded with dorzolamide and pramipexole. Carbohydrate Polymers. 2008;73:44-54.

[34] Kim B, Lee E, Kim Y, Park S, Khang G, Lee D. Dual Acid-Responsive Micelle-Forming Anticancer Polymers as New Anticancer Therapeutics. Advanced Functional Materials. 2013.

[35] Zamora-Mora; V, Fernandez-Gutierrez; M, Roman; JS, Goya; G, Hernandez; R, Mijangos C. Magnetic core-shell chitosan nanoparticles: rheological characterization and hyperthermia application. Carbohydr Res. 2013, DOI information: 10.1016/j.carbpol.2013.10.101.

[36] Banerji B, Pramanik SK, Mandal S, Maiti NC, Chaudhuri K. Synthesis, characterization and cytotoxicity study of magnetic (Fe3O4) nanoparticles and their drug conjugate. RSC Advances. 2012;2:2493-7.

[37] Wang Z, Zeng R, Tu M, Zhao J. Synthesis, characterization of biomimetic phosphorylcholine-bound chitosan derivative and in vitro drug release of their nanoparticles. Journal of Applied Polymer Science. 2013;128:153-60.

[38] Rao KSVK, Chung I, Reddy KM, Ha C-S. PMMA-based microgels for controlled release of an anticancer drug. J Appl Polym Sci. 2009;111:845-53.

[39] Esteve AA. Lo que hay que saber sobre el cáncer de colon y recto. 1 ed. Spain: Marge Médica Books; 2009.

[40] Elmore S. Apoptosis: A Review of Programmed Cell Death. Toxicologic Pathology. 2007;35:495-516.

[41] Asin L, Ibarra MR, Tres A, Goya GF. Controlled cell death by magnetic hyperthermia: effects of exposure time, field amplitude, and nanoparticle concentration. Pharmaceutical research. 2012;29:1319-27.

Chapter 7

GENERAL CONCLUSIONS AND PERSPECTIVES

The present work has been focused on the *Development of hybrid chitosan hydrogels for combined application in magnetic hyperthermia and drug delivery***.** Considering this objective, different chitosan hydrogels have been prepared: hydrogels with different size scale: macrogels, microgels and nanogels; composite chitosan/agarose hydrogels and ferrofluid loaded chitosan hydrogels. A systematic investigation on the preparation of each type of chitosan gel has been carried out and the effect of different experimental factors such as polymer concentration, crosslinking process, incorporation of the second polymer, addition of ferrofluid, flow rates, over their final properties has been analyzed. A deep characterization of the different chitosan systems by techniques such as Attenuated Total Reflection Fourier Transformed Infra-Red Spectroscopy (ATR-FTIR), thermogravimetric analysis (TGA), Scanning Electron Microscopy (SEM), X-ray diffraction measurements (XRD), and rheology was carried out. From the results obtained, the next general conclusions can be established:

i. In the study of chitosan macrogels, the following general conclusions can be extracted:

- **In the synthesis of alkali chitosan macrogels** obtained by precipitation in alkali media, hydrogen bonding and hydrophobic interactions are the responsible of their formation. From the viscoelastic study and fractal analysis, it can be concluded that all the samples present typical gel behaviour, in which the dynamic elastic modulus (G´) is relatively independent of the frequency of deformation, and that gels are constituted of flexible chains linked each other through the formation of cooperative hydrogen bonds.

- **In the synthesis of chitosan ferrogels** prepared by *in situ* synthesis of iron oxide nanoparticles within chitosan matrix, chitosan concentration had a direct influence over the formation of iron oxide nanoparticles and chitosan ferrogels presented a higher thermal stability with regard to alkali chitosan macrogels. From the viscoelastic study, it is observed that elastic modulus of the chitosan

ferrogels depends on the concentration of chitosan and on the concentration of iron oxide nanoparticles.

- **Composite chitosan/agarose macrogels** prepared by agarose gelification in the presence of a chitosan solution presented higher temporal stability (mass loss) than agarose macrogels. Temporal stability increased as a function of agarose concentration. Temperature and pH are two external parameters that also influence the temporal stability of composite chitosan/agarose macrogels. Samples were more stable at 37 ºC than at 45 ºC and with regard to pH, samples were more stable at physiological pH than in acid pH (pH=5.2). The melting point and elastic modulus increased as a function of agarose concentration; therefore chitosan addition improved the properties (mechanical properties and temporal stability) of the resulting composite gels.

- **Composite chitosan/agarose macrogels loaded with ferrofluid** presented a porous microstructure. Their thermal stability increased with the ferrofluid content. Ferrofluid loaded chitosan/agarose macrogels presented lower melting point and elastic modulus with regard to composite chitosan/agarose macrogels, although no significant difference was observed with the ferrofluid content. Moreover, composite chitosan/agarose macrogels loaded with ferrofluid had the capacity to heat when submitted to an alternative magnetic field. With regard to their drug release profile, chitosan/agarose gels assured that 5-FU can be released along time (96 days) under the conditions employed in this work and the 5-FU release was higher at physiological pH than at acid pH (pH=5.2).

ii. In the study of the preparation of chitosan microgels through microfluidics technique employing different microfluidic devices, it is possible to conclude that:

- **Microfluidics technique** allowed both the emulsification of chitosan through T-junction and flow-focusing droplet generator and the formation of chitosan microgels.

- **In the study of flow-focusing droplet generator,** two crosslinking processes in order to obtain chitosan microgels crosslinked with tripolyphosphate salts were assessed: off-chip and on-chip. The first process allowed the formation of chitosan droplets with diameters of 16 μm with a CV of 4.6%; however, a jetting regime was obtained accompanied of satellite droplets.

- **For on-chip crosslinking process** of chitosan, two devices were proposed. A device with three inlets leads to fiber formation due to the fast crosslinking reaction among chitosan and sodium tripolyphosphate (TPP). A fourth inlet device, consisted in the incorporation of another dispersed phase, acetic acid, that favoured the chitosan microgels formation. In this case, the average diameter of the chitosan microgels decreased with the flow rate of the oil phase and the residence time of the chitosan microgels in the MF device affected the microgel size.

- **Composite chitosan/agarose microgels** were successfully obtained by microfluidics technique using a flow-focusing device yielding transparent microgels with a well-defined round shape and polydispersity below 1.5%. Agarose concentration and the flow rate had a direct effect over their size, at higher agarose concentration the microgels size increased. The average diameter of microgels was smaller than the diameter of the corresponding precursor droplets, owing to microgel shrinkage upon gelation. Moreover, composite chitosan/agarose microgels loaded with ferrofluid can be also successfully obtained by microfluidics technique.

- In general, **for all the microfluidic devices** designs studied, flow rate of the oil phase had a direct influence over the droplet size, the increase of the flow rate of the oil phase leads to a decrease of the droplets sizes.

iii. In the study of ionic crosslinking reaction of chitosan with sodium tripolyphosphate (TPP) to generate chitosan nanoparticles, it is possible to extract the next conclusions:

- **The crosslinking reaction** between chitosan and TPP was influenced by three main experimental parameters: chitosan and TPP concentrations and volumetric ratios. The final state (clear, opalescent or precipitate solutions) allowed a first selection of the experimental conditions suitable to obtain chitosan particles of nanometric size. Then, size was corroborated by AFM or DLS techniques.

- **Chitosan nanoparticles loaded with ferrofluid** were successfully obtained. These nanoparticles presented core-shell morphology and sizes in the range of 192 to 259 nm. The encapsulation of ferrofluid within chitosan matrix was corroborated by field emission scanning electron microscopy and zeta-potencial. The zeta-potencial of all samples remained positive in the range of 57-63 mV. All samples presented a linear viscoelastic regime and from fractal analysis of the nanoparticles dispersions, a weak-like regime was obtained. Chitosan nanoparticles loaded with ferrofluid can act as hyperthermia agents due to their ability to heat when subjected to an alternative magnetic field.

iv. In the study of chitosan nanoparticles for combined therapies against cancer, the following conclusions can be established:

- **5-Fluorouracil was successfully encapsulated** into chitosan nanoparticles loaded with ferrofluid. The sizes obtained are in the range of 140-200 nm, which proved to be suitable to be internalized in connective cells (Fibroblast) and malignant human glioblastoma cells (A-172) as demostrated through uptake studies.

- **The drug release profile** of 5-Fluorouracil from chitosan nanoparticles loaded with ferrofluid was modulated as a function pH and ferrofluid content. For all the samples under study the drug release was higher at physiological pH than at pH 5.2. Moreover, the sample with the highest amount of ferrofluid presented

the lowest drug release. A controlled diffusion of 5-FU from chitosan nanoparticles was obtained during 30 days.

- **From cytotoxicity assays** carried out on Fibroblast and cancer cells (A-172) it can be concluded that ferrofluid loaded chitosan nanoparticles presented a dose-dependent effect. That is, the cell viability decreased with the concentration of the nanoparticles. Cancer cells (A-172) were more sensitive to chitosan nanoparticles than normal cells.

- ***In situ*** **magnetic hyperthermia (MH) experiments** were carried out in a homemade equipment and the experimental protocol employed offered reproducibility on the results. The effect of the application of the magnetic hyperthermia treatment on cell viability was evaluated as a function of the number of doses of MH and the protocol employed for cell fixation. Cellular damage, changes over cells morphology and a reduction of cell viability was observed after the application of one MH treatment. When cells were fixed 4 h after the first MH treatment, cell regeneration masked a possible effect of the chitosan nanoparticles over the A-172 cell line. A second magnetic hyperthermia treatment did not induce a significant change over cell viability. From the results obtained it was demonstrated that cancer cells (A-172) were more sensitive than Fibroblast cells to MH treatment.

From this PhD work several fruitful national and international collaborations have been established with different groups as for example with E.Kumacheva (U. Toronto, CANADA), J. San Román (CSIC, SPAIN) and G. Goya (INA, SPAIN).

Considering the results obtained in the present PhD work, new challenges arise for other PhD and Master projects. Future work is focused in the development of new biomaterials that can combine different cancer therapies with the objective to have a synergistic effect and reduce the side effects.

ABBREVIATIONS

5-Fluorouracil	5-FU
Phosphate buffer saline	PBS
Specific power absorption	SPA
Temperature of the maximum weight loss rate	T_p
Linear Viscoelastic Regions	LVR
Elastic modulus	G´
Loss modulus	G´´
Elastic modulus plateau	G_0
Critical deformation	γ_0
Melting temperature	T_m
Temperature increase	ΔT
Time interval	Δt
Microfluidic	MF
Triple interpenetrating network	3XN
oxidized dextran	Odex
N-carboxyethyl chitosan	CEC
Poly(dimethylsiloxane)	PDMS
Silicon	Si
Flow rate of the oil phase	Q_o
Flow rate of the dispersed phase	Q_d
Sodium tripolyphosphate	TPP
Coefficient of variance	CV
Mean diameter	D

Generally recognized as safe	GRAS
Food and Drug administration	FDA
Alamar Blue	AB
Chitosan–sodium tripolyphosphate nanoparticles	CS+TPP
Ferrofluid loaded chitosan nanoparticles	NP+Fe
5-Fluorouracil loaded chitosan nanoparticles	CS+FU
Hybrid chitosan nanoparticles	CS+FU+Fe
Fibroblasts	FBH
Malignant human glioblastoma	A-172
Cell viability	*CV*
Lactate dehydrogenase	LDH
Acridine orange and propidium iodide	(AO/PI)
Polymeric nanoparticles	NPs
Blood−Brain Barrier	BBB
Standard deviation	SD
Encapsulation efficiency	EE
Loading efficiency	LC
Magnetic Hyperthermia	MH
Polystyrene	PS
Alternative magnetic	AC
Crystal violet	C.V
X-ray diffraction measurements	XRD
Differential thermogravimetric curves	DTG
Scanning Electron Microscopy	SEM
Dynamic light scattering	DLS

Scanning Electron Microscopy with electron transmission	FESEM
Electron transmission	TE
Atomic Force Microscopy	AFM
Attenuated Total Reflection Fourier Transformed Infra-Red Spectroscopy	ATR-FTIR
Thermogravimetric analysis	TGA
Bright field	BF

ANNEXES

Annexe 6.1. Uptake studies

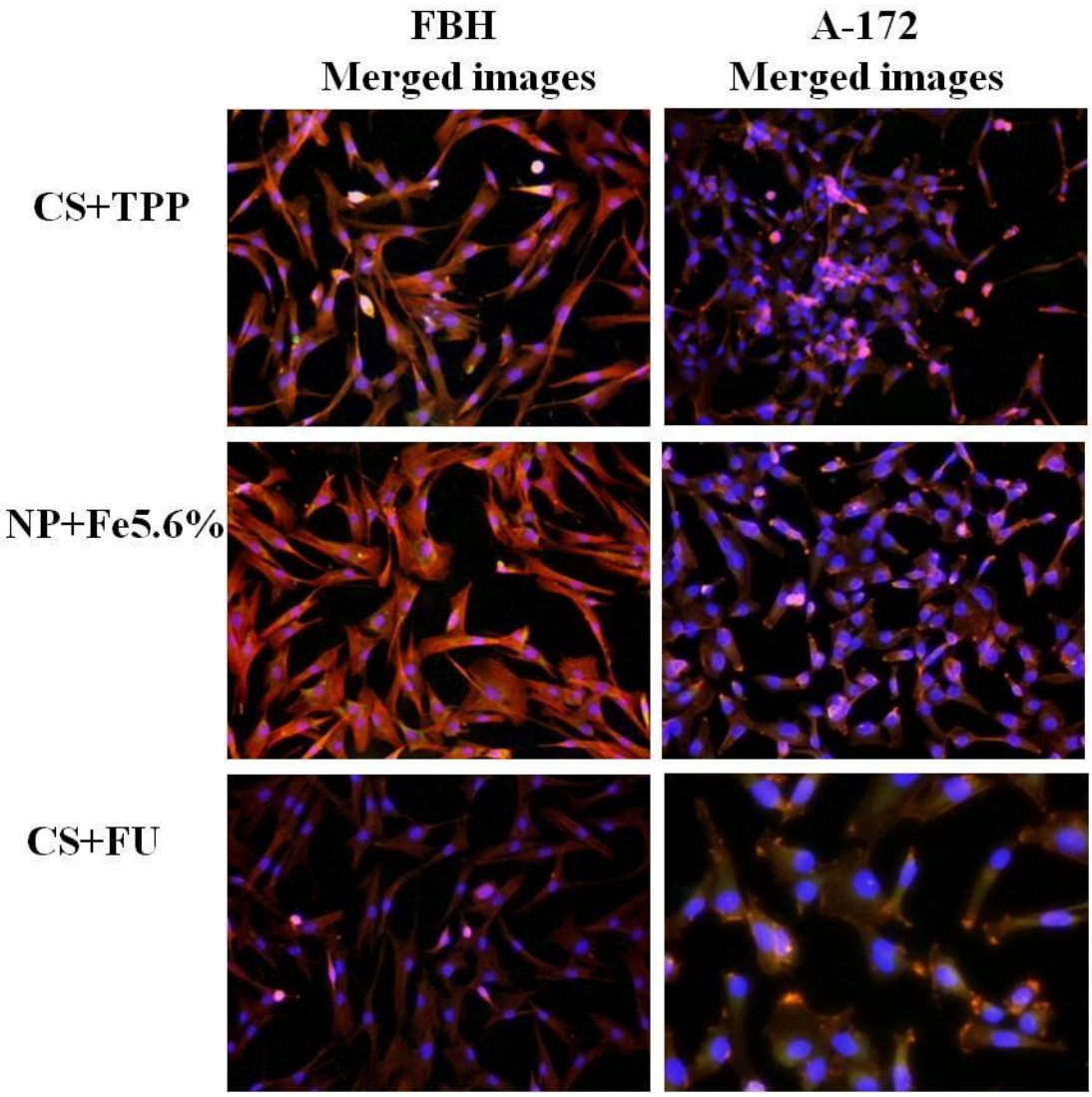

Figure A-6.1. *Uptake studies for different chitosan nanoparticles after 24 h of incubation, for FBH and A-172 cells lines.*

Annexe 6.2. Determination of cell viability by crystal violet after a second magnetic hyperthermia treatment.

Figure A-6.2 shows, photograph of crystal violet for A-172, after a second MH treatment and fixed 4 h later (t=24). As can be observe, it is evident the cellular damage by changes in its morphology, where A-172 cells look smaller than control cells and appear as a round or oval mass. To compare these photographs with the first MH treatment (Figure 6.15-b), these samples look more damaged. This is more evident for cells treated with CS+FU and CS+FU+Fe5.6%, On the other hand, for cells heated with NP+Fe5.6%, it is possible to observe cell regeneration at four hours after the MH treatment, for its long filopodia.

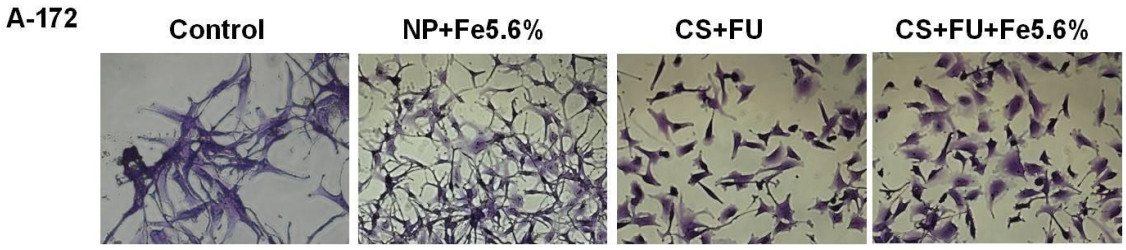

Figure A-6.2. *Photograph of crystal violet staining for A-172 cell line after a second magnetic hyperthermia treatment (t=24).*

Annexed 6.3. AO/PI staining after a second magnetic hyperthermia treatment.

In Figure A-6.3 is shown AO/PI staining, for A-172 cell treated with our chitosan nanoparticles after a second MH treatment (t=24), which suggest a significant evidence of cellular death and cells in process of death, recognized by the orange cells. These photographs indicate that cells treated with CS+FU and CS+FU+Fe5.6% have a more effect over A-172 cells.

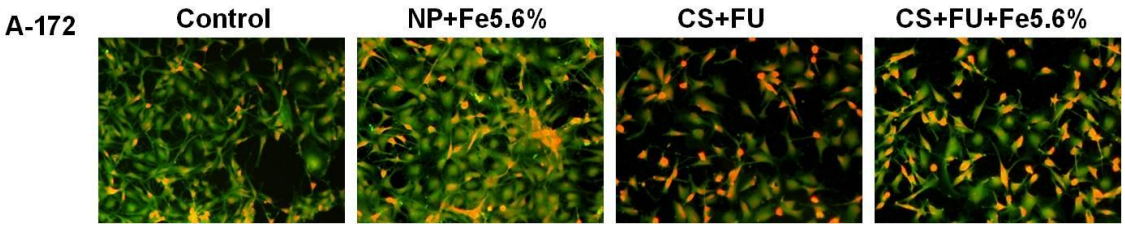

Figure A-6.3. *Fluoresce images for A-172 cell line, obtained after AO/PI staining after a second magnetic hyperthermia treatment.*

LIST OF PUBLICATIONS

1. Hernández, R.; Zamora-Mora, V.; Sibaja-Ballestero, M.; Vega-Baudrit, J.; López, D.; Mijangos, C., Influence of iron oxide nanoparticles on the rheological properties of hybrid chitosan ferrogels. *Journal of Colloid and Interface Science* **2009,** *339* (1), 53-59.

2. Zamora-Mora V, Fernández-Gutiérrez M, Román JS, Goya G, Hernández R, Mijangos C., Magnetic core–shell chitosan nanoparticles: Rheological characterization and hyperthermia application. *Carbohydrate Polymers*. **2014**, 102:691-8.

3. Zamora-Mora, V.; Velasco, D.; Hernández, R.; Mijangos, C.; Kumacheva, E., Chitosan/agarose hydrogels: Cooperative properties and microfluidic preparation. *Carbohydrate Polymers* **2014,** *111* (0), 348-355.

4. Zamora-Mora, V.; Velasco, D.; Hernández, R.; Mijangos, C., Chitosan microgels obtained by on-chip crosslinking reaction employing a microfluidic device. *Optofluidics Microfluidics and Nanofluidics Journal* **2014.**

5. Zamora-Mora V, Fernández-Gutiérrez M, González Gómez A, Sanz B, Román JS, Goya G, Hernández R, Mijangos C. Chitosan nanoparticles for combined drug delivery and Magnetic Hyperthermia treatment. *Biomacromolecules*. **In preparation.**

6. Zamora-Mora, V.; Echeverria, C.; Hernández, R.; Mijangos, C.; Ferrofluid loaded composite chitosan/agarose hydrogels. Performance in Magnetic Hyperthermia. **To be sent**

7. Zamora-Mora, V.; Hernández, R.; Mijangos, C.; Uptake studies of chitosan nanoparticles through Raman spectroscopy. **To be sent**